Modélisation de la dégradation chimique de membranes dans les piles à combustibles à membrane électrolyte polymère

Romain Coulon

UNIVERSITÉ DE GRENOBLE

THÈSE

Pour obtenir le grade de

DOCTEUR DE L'UNIVERSITÉ DE GRENOBLE

Spécialité : **Physique**

Arrêté ministériel : 7 août 2006

Présentée par

Romain COULON

Thèse dirigée par **Alejandro A. Franco** et

préparée au sein du **Laboratoire des Composants pour les piles à combustibles, les électrolyseurs et de modélisation.** (Commissariat à l'Energie Atomique et aux Energies Alternatives) et de l'**Institut de thermodynamique technique** (Deutsches Zentrum für Luft und Raumfahrt)
dans **l'École Doctorale de Physique**

Modélisation de la dégradation chimique de membranes dans les piles à combustible à membrane électrolyte polymère.

Thèse soutenue publiquement le **31 janvier 2012**,
devant le jury composé de :

Michael EIKERLING
Professeur, Simon Fraser University, Vancouver, Rapporteur
Gérald POURCELLY
Professeur d'Universités, Université de Montpellier 2, Rapporteur
Thierry DEUTSCH
Docteur chercheur, Université Joseph Fourier, Grenoble, Président
Jochen KERRES
Docteur chercheur, Universität Stuttgart, Examinateur
Gwenaelle RENOUARD-VALLET
Ingénieur, Airbus, Hambourg, Examinateur
Wolfgang G. BESSLER
Co-encadrant de thèse, ingénieur chercheur, DLR Stuttgart
Alejandro A. FRANCO
Directeur de thèse, ingénieur chercheur senior, CEA Grenoble

Abstracts

Resumé en français :

Cette thèse propose une approche de modélisation de la dégradation chimique par attaque radicalaire de la membrane dans les piles à combustibles à membrane électrolyte polymère, ainsi que à son impact sur la dégradation de la performance électrochimique.

La membrane considérée dans cette étude est de type perfluorosulfonique, avec une structure dépendant fortement de son humidification et conditionnant les propriétés de transport. Afin d'étudier la dégradation de la membrane, il faut dans un premier temps établir un modèle de transport, qui sera utilisé aussi bien dans le modèle de dégradation que par les modèles de performance de cellule déjà existants. Une fois ce modèle établi, nous nous focalisons sur la partie dégradation chimique. Après une compréhension globale des phénomènes physico-chimiques se déroulant lors de la dégradation, une mise en équation détaillée est nécessaire. Même les concepts utilisés sont relativement simples, le besoin de nombreux paramètres nous a contraint à simplifier le modèle sur certains points, notamment le mécanisme de dégradation chimique, tant la complexité du phénomène est un frein à la paramétrisation du modèle. Ce modèle, avec ses simplifications et ses hypothèses, est ensuite validé, aussi bien d'un point de vue performance que d'un point de vue dégradation.

Il est pour finir exploité dans différents cas de figures, allant de l'utilisation ininterrompue à courant constant (test purement utilisé en laboratoire) à un cyclage plus représentatif de conditions de fonctionnement réelles.

PEMFC, Pile à combustible, Fenton, Dégradation, Modélisation, Membrane, Nafion®

Abstract in English:

This thesis proposes a modeling approach of the chemical degradation by radicals attack of the membrane in polymer electrolyte membrane fuel cells, as well as its impact on the electrochemical performance degradation. The work considers a perfluorosulfonated acid type membrane. Its structure is strongly influenced by humidification, which also impacts the transport properties of mass and charge within the membrane. In order to study the degradation of the membrane, we first established a multi-species transport model for protons, water, and dissolved gases, radicals and ions. We then included detailed chemical reaction mechanisms of hydrogen peroxide formation, hydrogen peroxide decomposition, and radical attack of the membrane. Finally, a feedback between degradation, structure, and performance was established. Parameters were identified and the model was validated using literature experimental data both under performance and degradation aspects.

The model was then exploited under different conditions, from pure laboratory conditions (constant current kept over a long time) to working conditions which are more representative of the use of a PEMFC for stationary applications (performance cycles).

Polymer electrolyte membrane fuel cell (PEMFC), Fenton, Degradation, Modeling, Nafion®

Remerciements / Danksagung

Trois ans c'est le temps nécessaire à terminer le lycée. C'est aussi le temps nécessaire à terminer une école d'ingénieur. Mais ce fut également le temps nécessaire à l'aboutissement de ce projet de thèse.

En premier lieu, je tiens ici à remercier les membres du jury. Mes rapporteurs, Michael Eikerling et Gerald Pourcelly, pour le temps qu'ils m'ont accordé, à la fois lors de la révision de mon manuscrit et également lors de leur présence à ma soutenance. Ich bedanke mich auch bei Jochen Kerres, für seine Anwesenheit bei der Verteidigung und sein große Interesse an meiner Arbeit. Je voudrais également remercier Gwenaelle Renouard-Vallet et Nicolas Fouquet pour le temps qu'ils m'ont accordé à lors de l'examen de mon manuscrit. Et merci à Thierry Deutsch, qui fut un temps mon directeur de thèse.

Ensuite viennent ceux qui me soutiennent et supportent depuis 3 ans (voire plus). Alejandro et Wolfgang, merci pour votre soutien au cours de cette aventure, et merci surtout pour la chance que vous m'avez donnée il y a trois ans, alors que je n'avais jamais programmé, ni su ce qu'était une pile à combustible. Vos contributions et toutes les discussions enrichissantes que nous avons pu avoir ont grandement contribué à combler mes lacunes.

Nun meine Gedanken an meiner deutschen Kumpel ! Danke Dir Christian fürs vieles Lachen, Brainstorming und Freitags-LKW! Danke auch der Modellierungsgruppe und alle, die mal dabei waren: Jonathan, David, der kleine Wolfgang, Vitaliy Cheng, Max, Florian, Moritz, Wendelin, Christoph und noch viel mehr, da es viele waren.

Ensuite les „français", parce que pas beaucoup ne sont français. Obrigado les brésiliens Luiz, Daiane et Rodriginho pour m'avoir fait découvrir les paçoquinha et pour votre bonne humeur au labo. Alegato Yoshinori, your help was first quality in solving physical issues the last months. Grazie Valentina, je note que je dois arrêter les T shirt moches et me mettre aux chemises. Thank you professeur Cheah. Greetings Senthilnathan. Gracias Pablo, don't forget that fairy wear boots in a locomotive breath. Merci également à Fus Ro Dah Benjamin, pour les quizz, les séquences vintage et sa contribution dans ma quête de faire découvrir la culture française à nos brésiliens. Merci ensuite aux « autres », ceux qui font des expériences… Nicolas, Olivier, Zhe, Federico, Anne-Gaëlle, Galdric, Samir, Mohamed, etc etc. Merci à mes secrétaires successives, qui ont dû endurer ma présence plus qu'envahissante dans leur bureau. Donc merci à vous, Gégé, Kim, Aline et Charline ! Un merci tout particulier également à Mathias, tu as beau faire des modèles, tu n'en restes pas moins un bon vosgien et merci à Jenny pour les heures passées à discuter et à rigoler.

Pour terminer, les derniers remerciements mais non les moindres, je remercie mon papa, ma maman, mon brud et ma ninette pour leur soutien moral non scientifique depuis toutes ces années passées et à venir. Je leur dédie ce manuscrit qu'ils ne comprendront jamais.

« La théorie, c'est quand on sait tout et que rien ne fonctionne. La pratique, c'est quand tout fonctionne et que personne ne sait pourquoi. Ici, nous avons réuni théorie et pratique : Rien ne fonctionne... et personne ne sait pourquoi! »

Albert Einstein

«C'est pas faux»

Perceval, Kaamelot

Table of Contents

List of Tables

List of Figures

List of Abbreviations

Abbreviation	Meaning
AST	Accelerated Stress Test
CCV	Closed Circuit Voltage
CL	Catalyst Layer
CV	Cyclic Voltammetry
DAE	Differential algebraic equation
DENIS	Detailed Electrochemistry Numerical Impedance Simulation
DFT	Density Functional Theory
DMFC	Direct Methanol Fuel Cell
DMPO	5,5'-dimethyl-1-pyrroline-*N*-oxide
EDL	Electrochemical Double Layer
EIS	Electrochemical Impedance Spectroscopy
EoL	End-Of-Life
ENMR	Electrophoretic NMR
EPR	Electron Paramagnetic Resonance
ESR	Electron Spin Resonance
EW	Equivalent Weight
FC	Fuel Cell
FER	Fluoride Emission Rate
GDL	Gas Diffusion Layer
GSSEM	Generalized Steady State Electrochemical Model

HOR	Hydrogen Oxidation Reaction
HT-PEM	High Temperature PEMFC
IEC	Ion-Exchange Capacity
iN	impregnated Nafion®
IV	Intensity – Voltage
MEA	Membrane Electrode Assembly
MEMEPhys®	Modèle Electrochimique Multi-Echelle Physique
MS	Mass Spectroscopy
NMR	Nuclear Magnetic Resonance
OCV	Open Circuit Voltage
ORR	Oxygen Reduction Reaction
PBI	PolyBenzImidazole
PDE	Partial Differential Equation
PEMFC or PEM	Polymer Electrolyte Membrane Fuel Cell
PFSA	PerFluoroSulfonated Acid
PSSA	Poly(StyreneSulfonic Acid)
RHE	Reversible Hydrogen Electrode
ROP	Rate Of Progress
RRDE	Rotating Ring-Disc Electrode
SANS	Small-Angle Neutron Scattering
SAXS	Small-Angle X-Ray Scattering
SEM	Scanning Electron Microscope
SOFC	Solid oxide fuel cell
TFE	TetraFluoroEthylene

WAXD	Wide-Angle X-Ray Diffraction

List of Symbols

Greek

α_{memb}	Ratio between water flux and effective water flux in the membrane / -
β^e	(DENIS) Symmetry factor for the transition state / -
β_{memb}	Proportionality coefficient between water flux into the membrane and water content difference over electrode / membrane interface / $mol \cdot m^{-2} \cdot s^{-1}$
Γ	(MEMEPhys®) Dipolar surface density / $D \cdot m^{-2}$
$\Delta G_i^{\neq}$	Gibbs activation energy for reaction i / $J \cdot mol^{-1}$
δ	Distance between proton in hydronium ion an proton-accepting water molecule / m
ε	Porosity of the membrane / -
ε_0	Electric permittivity of free space ($=8.85 \cdot 10^{-12}$ $C^2 \cdot J^{-1} \cdot m^{-1}$)
ε_r	Relative permittivity of the membrane / -
$\zeta[3]$	(MEMEPhys®) Riemman's function evaluated at 3 (≈ 1.20)
η	Viscosity of water / $Pa \cdot^{-1}$
η	(MEMEPhys®) Electrostatic surface potential across the adsorbed layer / V
η_s	(DENIS) Electrostatic potential difference across the double layer / V
θ_F	Final angle diffusing proton and an adjacent water molecule / -
θ_I	Initial angle between diffusing proton and adjacent water molecule / -
θ_i	Covering fraction of species i
λ	water content or local ratio H_2O/SO_3 in the membrane / -
λ_{eq}	Water content in the membrane in equilibrium with the humidity in the gas phase / -
μ_W	(MEMEPhys®) Dipole moment of liquid water / $C \cdot m^{-1}$
ξ	Bruggeman correction factor / -

ρ_i	Density of specie *i* / kg·m^{-3}
σ_{H^+}	Proton conductivity / S·m^{-1}
σ	(MEMEPhys®) Electronic surface density / C·m^{-2}
τ	Tortuosity of the membrane / -
$v_{i,j}$	Reaction order of specie *j* for the reaction *i* / -
$\phi_{electrode}$	(DENIS) Electrode potential / V
Φ	(MEMEPhys®) Electrostatic potential in the diffuse layer / V
ψ	(MEMEPhys®) Electrode potential / V

Latin

a_{H_2O}	Activity of water / -
c_i	Concentration of specie *i* / mol·m^{-3}
d	(MEMEPhys®) Thickness of ad-layer / m
D_i	Diffusion coefficient of specie *i* / m²·s^{-1}
e	Elementary charge (=1.60·10^{-19} C)
$E_{act,i}^{j}$	Activation energy for process *j* of species *i* / J·mol^{-1}
EW	Equivalent weight of the membrane / kg·eq^{-1}
F	Faraday's constant (= 96500 C·mol^{-1})
F_i	Flow rate of species *i* / mol·s^{-1}
h	Planck constant (=6.62·10^{-34} J·s)
i	Current density / A·cm^{-2}
I	Absolute value of current / A
J_i	Flux of specie *i* / mol·s^{-1}·m^{-2}
$J(s)$	Leverett J-function / -

k_B	Boltzmann constant (=1.38·10^{-23} J·K^{-1})
k_i	Rate constant of reaction i / s^{-1}
K_i	i^{th} acidity constant of sulfuric acid / -
$L_{membrane}$	Membrane length / m
l_G	Mean step distance for Grotthus diffusion / m
l_Σ	Mean step distance for surface diffusion / m
M_i	Molar mass of substance i / kg·mol^{-1}
n_i	Amount of substance i / mol
n_s	number of free sites per unit area of the metallic phase / m^{-2}
P_i	Partial pressure of species I / Pa
R	Ideal gas constant (= 8.314 J·K^{-1}·mol^{-1}) / Resistance of the membrane / Ω
r	$\overline{V_{NAFION}}/\overline{V_{H_2O}}$
R_f	Effective radius of fixed anion groups / m
R_i	Radius of hydronium ion / m
R_w	Radius of water molecule / m
s	Swelling coefficient of the membrane
$\dot{S}_j$	production term of specie j / mol·m^{-3}·s^{-1}
$S_{electrode}$	Geometric area of electrode / m²
t_{H_2O}	Drag coefficient of water / -
T	Temperature / K
U_{cell}	Cell voltage / V
v	number of water molecules surrounding one sulfonate acid group / -
$\overline{V}_i$	Molar volume of species i / m^3·mol^{-1}
v_i	Rate of reaction i / mol·m^{-3}·s^{-1}

V_i	Volume of phase i / m^3
X	Molar fraction / -
z_i	Charge of specie i / -

Sub-/superscript

A, an	Anode
C, ca	Cathode
CL	(MEMEPhys®) Compact layer
DEG	Degradation
Diff Nafion®	Diffusion in Nafion®
DL	(MEMEPhys®) Diffuse layer
Dmj	Damjanovic
dry	Dry Nafion®
elde	Electrode
elyt	Electrolyte
EO	Electro-osmotic
Far	Faradic
Fick	Related to Fickian diffusion
G	Grotthus
gas	Entire gas phase
HEY	Heyrovsky
liq	Liquid
m	en masse
ref	Reference

sat	Saturation
TAF	Tafel
$v \rightarrow l$	Vaporization
vap	Water under vapor form
VOL	Volmer
Σ	Surface (vicinity of the side chain in the membrane)

CHAPTER 0

Introduction

La modélisation scientifique permet de comprendre des processus via des modèles conceptuels, graphiques ou mathématiques en les partitionnant sous des formes simples.

Cette thèse aborde la thématique des piles à combustible (PAC) à membrane électrolyte polymère (PEMFC), qui autant d'un point de vue théorique qu'expérimental, intéresse de nouveaux groupes de recherche depuis les années 1960. Cependant les premiers travaux de modélisation ne sont apparus que 30 ans après les premiers systèmes réels, travaux réalisés par Bernardi et Verbrugge [1]. Depuis, beaucoup de modèles simulant les performances de la PAC ont été proposés ; en revanche les travaux s'intéressant aux évolutions à long-terme des performances sont minoritaires, ce genre d'évolution faisant plutôt l'objet d'une approche expérimentale en effectuant des tests de PAC sur des durées de l'ordre de 1000 heures.

La compréhension des phénomènes de dégradation est un aspect essentiel dans le développement de nouveaux matériaux, de nouvelles structures ou dans l'établissement de modes de fonctionnement optimisés visant à améliorer la durée de vie des systèmes. Les outils analytiques disponibles permettent d'identifier les origines des défaillances. A partir de ces observations, il est possible d'établir des modèles permettant de simuler un comportement de plusieurs centaines d'heures en un temps réduit, ce qui est le vrai atout de la modélisation. De plus la modélisation permet d'obtenir des informations relatives à des phénomènes apparaissant à une faible échelle spatiale et temporelle.

Dans la littérature, peu de modèles proposent la prise en compte de l'évolution des propriétés structurales et de l'évolution des performances de la cellule. Franco *et al.* a propose une approche prenant en compte l'interaction de processus de dégradation et de l'évolution des performances de la cellule [2-5]. Peu de travaux de modélisation traitent de la dégradation de la membrane dans les PAC, et ceux proposés montrent de grandes différences dans les résultats, et leur domaine de validité reste restreint.

L'objectif de cette thèse est de fournir à la communauté scientifique un modèle physique décrivant la dégradation chimique des membranes acide perfluorosulfonique lors de leur application

dans des PAC. Elle propose également de coupler ce modèle de dégradation avec l'évolution de la structure de la membrane et enfin de coupler le modèle de membrane avec un modèle d'électrodes, permettant ainsi de simuler l'évolution des performances de la PAC au cours du temps pour différentes conceptions de cellule et de conditions opératoires.

0.1 What is modeling? Why using modeling in fuel cell technology?

Scientific modeling is the process of generating abstract, conceptual, graphical and/or mathematical models. Science offers a growing collection of methods, techniques and theory about all kinds of specialized scientific modeling. A scientific model can provide a way to read elements easily which have been broken down to a simpler form [6].

When this thesis started in 2009 and still now 3 years later, there was still a large diversity of experimental and modeling efforts made by different scientific groups all around the world to understand the chemical degradation of the membranes during the operation of polymer electrolyte membrane fuel cell (PEMFC). Modern PEMFC were founded at the beginning of the 1960s, but the first complete modeling work was published 30 years later, at the beginning of the 1990s by Bernardi and Verbrugge [1]. Since then, many performance models were published and presented. However modeling efforts to study degradation phenomena were not so numerous, groups focusing rather on modeling instant performance than long-term performance loss [7]. This field was let to experimental groups who performed tests over more than 1000 hours in order to observe the impact of the degradation on the cell performance.

The understanding of the degradation phenomena in PEMFC technology is a key aspect towards the proposal of solutions in the choice of new materials, new components structures, manufacturing processes or operating conditions for enhanced system durability. Over the years, analytic tools became more and more precise and allow nowadays identifying the causes of the cell failure. The main drawback of this remains the time required to perform one single experiment, as unlike in modeling simulations, one minute in real life last one minute. Modeling proposes, in a shorter time, to provide an approached result to that one obtained by experiment. Indeed, where experimental work requires a certain amount of time and costs, a simulation, once it has been validated, proposes predictions and trends of the results within hours and is a way to reduce the “try-and-error” of experimental work and thus to save money.

Moreover, some phenomena are still unknown or are taking place on such a small temporal and spatial scale and space scale, that they cannot be seen by direct experimental observation. Modeling in such cases provides an interesting solution as well.

0.2 Scope of this thesis

In the published literature we were aware about only few models proposed accounting to predict the structural evolution of the cell components induced by the materials degradation as well as the associated cell performance evolution. Franco *et al*. proposed a modeling approach to account the feedback between the degradation processes and the instantaneous performance of the cell. Within this framework, PEMFC catalyst degradation, carbon corrosion and contamination and the associated long-term cell performance evolution and durability have been predicted based on multiscale simulations [3, 4, 8, 9]. To date very few of the available models treated membrane degradation. Different types of membrane degradation models can be found in literature all of them laying on certain assumptions and focused on an aspect of the whole chemical degradation, but none dealing with a complete description of the different observables. This limits their uses and validity.

The first goal of this thesis is to provide a physical model describing the chemical degradation of a perfluorosulfonated acid (PFSA) membrane for fuel cell use (for example Nafion®). Then a second objective is to couple this chemical degradation model with the structural and physical parameters which are characteristic of the membrane. Finally, a third objective is to include the two submodels into a complete cell model so that makes possible to get a feedback between instantaneous performance, degradation and evolution of the membrane structure. We try to build up the model as precise as possible so that different operating conditions and cell designs can be simulated and that the results and trends given by the model are as reliable as possible.

CHAPTER 1

Context and motivation of this thesis: Degradation of the membrane in PEMFCs

La PAC est un système convertissant l'énergie chimique des réactions d'oxydation de l'hydrogène à l'anode et de réduction de l'oxygène à la cathode en énergie électrique et en énergie thermique. Cette technologie est considérée comme propre en raison de la seule présence d'eau comme sous-produits. Elle est constituée de deux électrodes (l'anode et la cathode) séparées par une membrane permettant entre autre le transport de protons entre les électrodes. L'acheminement des gaz à la surface des électrodes ainsi que le transport des électrons vers l'extérieur est assuré par la présence conjointe des plaques bipolaires dans lesquelles sont gravés des canaux ainsi que de couches de diffusion des gaz.

Selon les utilisations faites de la PAC, différents types de membrane peuvent être utilisés. Celles-ci présentent des températures de fonctionnement différentes. Dans le cadre de la PEMFC fonctionnant à basse température (jusqu'à 90 °C), une des familles de membrane les plus utilisés est celle des membranes à acide perfluorosulfonique, dont le représentant le plus ancien et le plus connu est le Nafion, inventé dans les années 1960. Ces membranes sont composées d'un squelette similaire au Téflon sur lequel sont branchés des chaînes pendantes portant une fonction acide perfluorosulfonique. Ces membranes présentent une grande stabilité chimique, thermique et mécanique, sont imperméables à la diffusion des gaz et permettent un transport optimal des protons.

Bien que largement utilisée dans la technologie actuelle, ces membranes n'en demeurent pas moins une énigme pour les scientifiques pour toutes les questions relatives à l'organisation des chaînes de polymère au sein de la membrane et les mécanismes exacts de diffusion observés dans la membrane. Dans la littérature, plusieurs modèles ont été proposés afin de rendre compte le plus fidèlement possible de la structure exacte du Nafion et des membranes PFSA d'une manière générale, structure qui demeure à ce jour toujours inconnue [10-14]. Le fait de ne pas connaître la structure nanoscopique exacte des membranes n'est cependant pas un frein à l'étude macroscopique des membranes, plus particulièrement dans le cadre de cette thèse des aspects de dégra-

dation de la membrane.

D'un point de vue expérimental, il existe différentes méthodes analytiques afin de mettre la dégradation de la membrane en évidence. La dégradation chimique peut se traduire par l'observation de différents phénomènes. La dégradation chimique de la membrane va entraîner une perte de matière, ce qui va se traduire par une diminution de l'épaisseur de la membrane. Cette diminution d'épaisseur s'observe lors d'analyse post-mortem par exemple par observation directe au microscope électronique à balayage [15, 16]. Comme lors de toute réaction chimique, des produits, sous-produits et intermédiaires de réaction sont impliqués et peuvent donc être observés. Le premier de ces produits est le peroxyde d'hydrogène. Celui-ci peut résulter d'une réduction partielle de l'oxygène à la cathode ou d'une réaction chimique entre l'hydrogène et l'oxygène à l'anode. La présence d'oxygène est expliquée par le caractère partiellement imparfait de la membrane, celle-ci laissant diffuser entre les électrodes une partie des gaz. Quelques groupes de recherche se sont penchés sur la quantification du peroxyde d'hydrogène produit dans une cellule lors de son fonctionnement ainsi que lors de manipulation ex-situ, en particulier grâce à la technique d'électrode tournante [17-19].

En présence d'ions fer, dont l'origine dans la PAC reste discutée, le peroxyde d'hydrogène se décompose en radicaux, entre autre hydroxydes. L'étude de cette décomposition fait l'objet de nombreuses études, elle est utilisée notamment dans le traitement des eaux usées, les radicaux étant des espèces extrêmement réactives et pouvant oxyder la matière organique réfractaire dans les eaux usées [20-26]. L'étude de ces réactions entre ions fer et peroxyde d'hydrogène se nomme la chimie de Fenton. La durée de vie de ces espèces étant extrêmement courte (de l'ordre de la microseconde), leur mise en évidence et quantification ne peut se faire qu'en piégeant les radicaux en les faisant réagir avec des molécules spécifiques [27-30]. La quantification se fait ensuite par des méthodes spectroscopiques.

Lors de la synthèse de membranes PFSA, il est possible que des fonctions intermédiaires de réaction soient encore présentes. Ces fonctions peuvent pas exemple être de type acide carboxylique. De telles fonctions sont sujettes à réagir avec les radicaux. Ce genre de réaction est l'initiation de la dégradation chimique de la membrane. Les produits ultimes de dégradation sont le dioxyde de carbone, les ions sulfates et les ions fluorure [31, 32]. La méthode classique de suivi de la dégradation de la membrane est la mesure de la concentration des ions fluorures dans l'eau en sortie de piles.

D'un point de vue modélisation, peu de travaux ont été proposés, la plupart du temps se focalisant sur un des points mentionnés précédemment. Xie et Hayden proposent un mécanisme réactionnel basé sur l'analyse de fragments organiques dans la membrane [32]. Ce mécanisme reflète bien les observations expérimentales et est à ce jour le mécanisme communément admis par la

communauté. Ces travaux ne permettent cependant pas de relier le fonctionnement de la pile à combustible à la dégradation même de la membrane. Chen et Fuller ont publié de nombreux travaux sur la dégradation chimique dans les piles à combustibles [33-37]. Un de leurs axes de recherche est la formation de peroxyde d'hydrogène dans la PAC [33, 36]. Ils ont publié entre autres un modèle de production de H_2O_2, incluant transport d'oxygène, en utilisant une structure d'agglomérats pour les électrodes. Cependant ce modèle ne prend pas en compte le devenir des molécules de peroxyde d'hydrogène dans la cellule. Gubler *et al.*, quant à eux, ont publié des travaux se focalisant sur le devenir de ces molécules de peroxyde d'hydrogène, notamment lors de leur décomposition en radicaux selon plusieurs réactions lors de la chimie de Fenton puis de l'attaque de ces radicaux sur la membrane PFSA en elle-même [38]. Cependant, ces précédents modèles ne reflètent pas le fonctionnement complet d'une cellule. Shah *et al.* ont publié des travaux prenant en compte à la fois les aspects thermique, fluidiques ainsi que les phénomènes de dégradation chimique dans la membrane [39]. Ce modèle discrétisé 1D leur permet de faire des prédictions de profils de concentration selon l'épaisseur de la membrane. Cependant, la prise en compte de cette dégradation sur les performances de la cellule n'est pas prise en compte, ce qui justifie l'utilité de cette thèse aux yeux de la communauté scientifique.

1.1 A clean energy conversion device: The PEMFC

1.1.1 General presentation

A PEMFC (and fuel cell (FC) more generally) is an energy converter: it converts the chemical energy of the Reaction 1.3 below into electricity and heat. The only reaction product is water, which make PEMFC one of the cleanest technologies currently available to obtain electricity. Reaction 1.1 and Reaction 1.2 are the half-cell reactions occurring in the electrodes, leading to Reaction 1.3 (Figure 1.1).

Half-cell reaction at the anode $H_2 \longrightarrow 2\,H^+ + 2\,e^-$ Reaction 1.1

Half-cell reaction at the cathode $O_2 + 4\,H^+ + 4\,e^- \longrightarrow 2\,H_2O$ Reaction 1.2

Global reaction in the cell $H_2 + \frac{1}{2}\,O_2 \longrightarrow H_2O$ Reaction 1.3

PEMFCs have a broad application field. Even if currently their usage is still limited to prototypes and niche markets, they have a promising future. They can be used at all sizes and power ranges:

- Transport applications: Power supply in automotive, aircraft and space
- Stationary applications: Power supply for, for example, small houses (remote locations)
- Portable applications: Power source for, for example, cell phones or digital camera

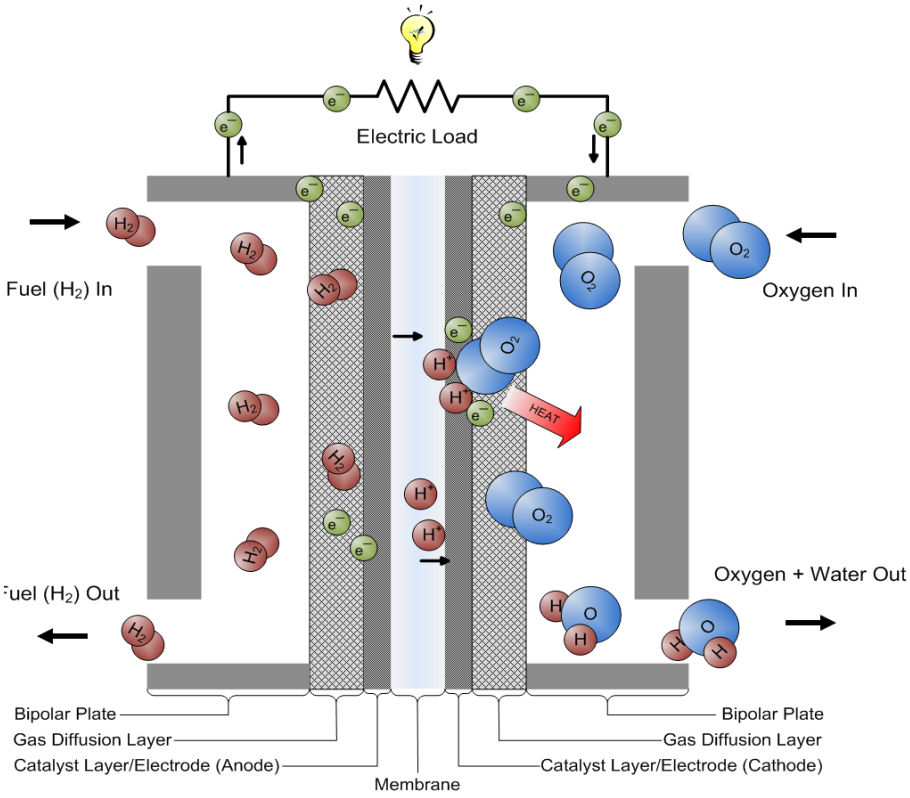

Figure 1.1: Basic diagram of a PEMFC [40]

1.1.2 Components of a PEMFC

Materials and design of a cell are very important because they are the main factors determining the performance and the life-time of a cell.

We can identify three groups of components in a typical cell:

- Components providing a good fuel feed: Bipolar plate and gas diffusion layer (GDL)
- Components allowing the reaction of the gases: Electrodes
- Component ensuring isolation and proton exchange between the electrodes: Electrolyte (or membrane)

The combination of the membrane and the electrode is abbreviated under membrane electrode assembly (MEA).

Every component is made of a different material or combination of materials. Table 1.1 summarizes the different types of material that can be used in the PEMFCs.

Component	Material	Properties
GDL	• Carbon cloth • Carbon paper	• Porous • Electrical conductivity
Bipolar plate	• Metal • Carbon • Conductive composite polymer	• Impermeable to gases • Electrical conductivity • Corrosion resistant
Electrode	• Catalyst : Platinum and platinum alloys supported on carbon black • Ionomer: same material as the corresponding electrolyte	• HOR and ORR • Electrical conductivity • Protonic conductivity
Membrane / Electrolyte / Separator	• PFSA: Nafion®, Hyflon… • Phosphoric acid doped polybenzimidazole (PBI)	• Impermeable to gases • High protonic conductivity • Chemical, thermal and mechanical stability

Table 1.1: Materials and properties of the PEMFC components

GDLs, whose thickness lies in generally between 100 and 300 µm, have two functions. Firstly they allow a good diffusion of the gases to the active site in the electrodes and secondly they are one of the links in the chain of the conduction of electron from the anode to the cathode. Thus they have to be conductive and porous. Moreover they have a key role in the water management in the membrane because they must both humidify the membrane and allow water removal (prevention of the water flooding at the cathode side at high current density).

Bipolar plates are often made of high-density graphite, but gold-coated steel can be for example used as well. Their main role is the distribution of gases over the whole surface of the electrode and the conduction of the excess water outside of the system. They are also current collectors. Electrons flow through the GDL at the anode to the bipolar plate, then go through an external circuit and arrive at the bipolar plate at the cathode. At a stack level, it is the junction element separating the cathode of a cell from the anode of the following one. The fluid transport is achieved through micro-channels (width ≈ 0.8 mm). The geometry of the channel is very important because it will ensure a homogenous gas supply in the cell, as it can be seen in Figure 1.2.

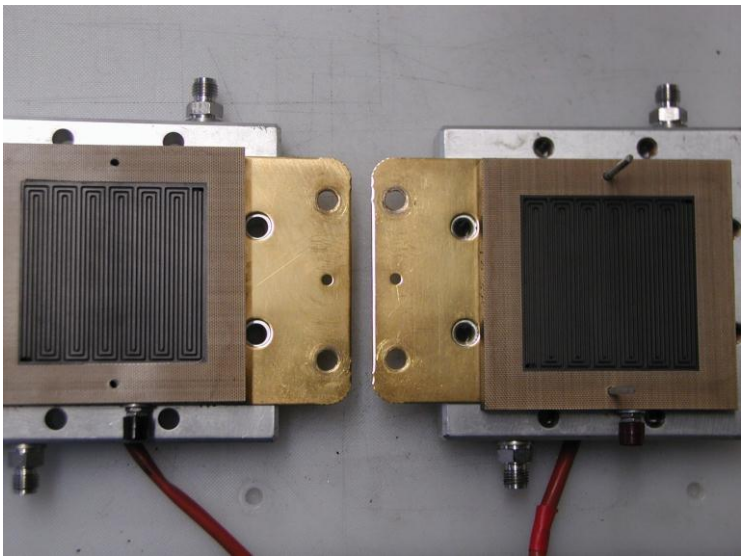

Figure 1.2: Examples of flow field used at the laboratory scale

In PEMFCs, the electrodes are based on precious metals. These precious metals represent the lightest part of the whole electrode material but they are the most important because of their catalytic properties. The most commonly used catalyst is platinum Pt. The amount of Pt in a single cell varies from 0.1 to 1 $mg \cdot cm^{-2}$. It could be used under a pure form, but for economic reasons, it is deposited on small particles of active coal with very high specific area. Their role is to catalyze the hydrogen oxidation reaction (HOR) (resp. oxygen reduction reaction (ORR)) at the anode (resp. cathode). Electrodes are very expensive because of the use of Pt (on 2nd of February 2012 39.50€/g). However, only a small area of Pt is effectively used (20 % to 30 % of the metal). Therefore efforts are made to control and to improve the geometry of the electrode structural properties (for example by electrode deposition) [41]. One other area of research is the development of Pt-based alloys in order to reduce the cost without reducing performances.

The electrolyte is characteristic for each kind of fuel cell. We focus our attention only on the PEMFC thus we will mention here only its electrolyte. For low-temperature fuel cells, PFSA membranes are mostly used. The first materials available in the early 60s were sulfonated polystyrene membranes. These were rapidly replaced from 1966 by Nafion®, developed by the company Du Pont de Nemours, but over the years many other companies developed their own PFSA membrane (for example Solvay Solexis, 3M, Gore…). These membranes are ion exchanger. They permit the permeation of cations, like hydronium ions H_3O^+ and water can move within the membrane. Another essential function of the membrane is the separation of the gases to prevent any chemical short circuit (that means ORR and HOR taking place at the same electrode, in that case electrons will not have to flow through the external circuit). Moreover the membrane should not be electrically conductive. PFSA membranes operate

up to 90 °C. Above this temperature, other materials have to be used. Indeed water management is a key challenge for a successful operation of PEMFCs. Above 100 °C, liquid water cannot ensure its role in proton conduction anymore and thus no proton transport can occur, leading to the failure of the cell. For High-Temperature PEMFCs (HT-PEM), PBI membranes are used. In these membranes, proton transport occurs through a rapid proton exchange (hopping mechanism) between phosphate and amidazole moieties and self-diffusion of phosphate moieties [42].

1.2 Nafion®: The most famous electrolyte for PEMFC

1.2.1 An enigma for modelers and polymer scientists

Nafion® ionomers are developed by the company Du Pont de Nemours since the early 1960s. These materials are the result of the copolymerization of tetrafluorethylene (TFE, also known as Teflon) with a perfluorinated vinyl ether comonomer. A common representation for an elementary unit of Nafion® polymer is given in Figure 1.3. This copolymerization is not well-controlled and there is no clue to determine if the distribution of the side chain is uniform on the back bone [43, 44]. For this reason, the concept of equivalent weight (EW) has been introduced. It is defined as the weight of dry Nafion® per mol of sulfonate acid groups and corresponds to the quantity of polymer needed to neutralize one equivalent of base. This value is linked to the ion-exchange capacity (IEC) through

$$EW = \frac{1000}{IEC}. \qquad \text{Equation 1.1}$$

The official nomenclature chosen for Nafion® membrane is following: The two first numbers correspond to the *EW*. For example for Nafion® 112, the *EW* is 11·100 g·eq^{-1}, 1100 g/eq. The last number (in this example 2) corresponds to the membrane thickness in milli-inches (mil). 1 mil represents 25.4 µm, thus Nafion® 112 has a thickness of about 50 µm.

Experimentally the *EW* can be for example measured by acid-base titration. From the Figure 1.3, we see that the structure of Nafion® is governed by the choice of 4 indices, determined by the comonomer chosen during the synthesis. *x* indicates also how many –CF_2- groups are present on the back bone between two carbon atoms wearing a side chain.

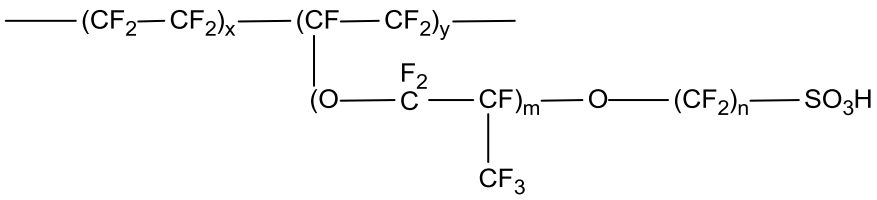

Figure 1.3: General formula of a PFSA membrane

Usually, *y* is taken equal to 1, *n* as well. The value of *n* depends on the comonomer which was used. From the value of the equivalent weight and the knowledge of the formula of the monomers, one can obtain the value of *x* via Equation 1.2. The establishment of this relation is given in Appendix A.

$$x = \frac{\mathrm{EW} - (81 \cdot y + 166 \cdot m + 50 \cdot n + 81)}{100} \qquad \text{Equation 1.2}$$

In the literature, there is no report about measuring the molecular weight of the membrane as it is common to be done for macromolecules and polymers, for example with the technique of gel permeation chromatography. This impossibility is due to the property of Nafion® that it does not form true solutions: Nafion® is rather a suspension and thus cannot permeate in chromatography [45].

In the following parts of this thesis, we will use the previously explained nomenclature for Nafion® designation. Table 1.2 shows the properties of some commercial membranes. We see that the range of thickness, equivalent weight and structure is very broad.

Parameters	Manufacture	Name	*EW* / g·mol^{-1}	Thickness / µm
m=1; *x*=5-13.5; *n*=2; *y*=1	DuPont	Nafion® 120	1200	260
		Nafion® 117	1100	175
		Nafion® 115	1100	125
		Nafion® 112	1100	80
m=0.1; *n*=1-5	Asashi Glass	Flemion-T	1000	120
		Flemion-S	1000	80
		Flemion-R	1000	50
m=0; *x*=1.5-14; *n*=2-5	Asashi Chemicals	Aciplex-S	1000-1200	25-100
m=0; *x*=3.6-10; *n*=2	Dow Chemicals	Dow	800	125
m=0; *x*=5-13.5; *n*=2; *y*=1	Solvay Solexis	Aquivion E87-03	870	30
		Aquivion E87-05	870	50
		Aquivion E87-10	870	100
		Aquivion E79-03	790	30
		Aquivion E79-05	790	50

Table 1.2: Parameters of some commercial PFSA membranes (when no value for a parameter is given, this means that the parameter is not present in the chemical structure of the ionomer)

While macroscopic properties give some insight into the microstructure, no direct precise observation is to date available concerning the exact microstructure of Nafion®. Such knowledge would be a real breakthrough for researchers on PEMFC. Indeed, key parameters for PEMFC operation such as water management, proton conductivity, and electro-osmotic drag are closely linked to the chemical structure and the morphology of the electrolyte. As no direct observation or analytical method can be used to see behavior of Nafion®, indirect methods are carried out to derive models and assumptions on Nafion® structure.

1.2.2 Analytical methods for morphology determination of Nafion®

Nafion® is a very complex material. As seen in Figure 1.3, Nafion® is composed of hydrophobic back

bones (Teflon skeleton) and hydrophilic side chains (the ionic sulfonate head). Thus the study of the morphology of Nafion® has to be done in regards to the water content in the membrane.

Many analytical methods have been used to analyze structural properties of Nafion®, but scientists always kept in mind that their conclusions about the structure of Nafion® are relevant only if they are put into correlation with the hydration of the membrane.

The first step after having synthesized a new material is its characterization. The molecular formula can be determined by nuclear magnetic resonance (NMR). In the case of Nafion®, such measurements were presented in the literature [46-49]. This technique is used since the beginning of the 80s to determine the molecular structure of synthesized Nafion® [47]. NMR allows knowing which atom groups are located in the molecule and which groups are locate in their vicinity. In fact, the structure of Nafion® was assumed knowing the comonomer and the Teflon structure, and, NMR confirmed the molecular formula. This technique is still not sufficient to advance conclusions about the morphological structure of this polymer.

A powerful technique to inquire indirectly through Nafion® is the uses of X-rays and neutrons. This technique is since the 70s one of the most used to study Nafion®. Such measurements were carried out under every possible experimental condition [11, 50-54]. But it is here neither the purpose to present an exhaustive list of the every paper dealing with small-angle X-ray scattering (SAXS), small-angle neutron scattering (SANS) and wide-angle X-ray diffraction (WAXD) nor detailing these very complex analytical methods.

We rather focus on some of the most cited and recognized papers which offered new insights and proposals about the Nafion® structure.

Gierke *et al*. were one of the pioneer researchers in this field [10]. He examined and compared the morphological features of Nafion®, having a range of EW, in the unhydrolyzed sulfonyl fluoride precursor form, the hydrolyzed sulfonyl acid form and the neutralized metal sulfonate form. From SAXS experiment they observed evidences for crystalline structure within the fluorocarbon matrix. With a hydrolyzed form of Nafion®, they found evidences characteristic of a system containing ionic clusters within a semicrystalline matrix [55]. Based on further SAXS and WAXD analysis with the observation of two scattering peaks on the profiles and considering the three most prevalent models for the morphology of ionomers at the time, including a model of spherical clusters on a paracrystalline lattice, a core-shell model, and a lamellar model, Gierke and co-workers concluded that the water-swollen morphology of Nafion® was best described by a model of ionic clusters that were approximately spherical in shape with an inverted micellar structure [10, 56]. In consideration of the high ionic permselectivity and the requirement of a percolation pathway for ionic transport in Nafion® membranes, the spherical ionic clusters were further proposed to be interconnected by narrow chan-

nels, constituting a morphology referred to as the cluster-network model as displayed Figure 1.4 [57, 58].

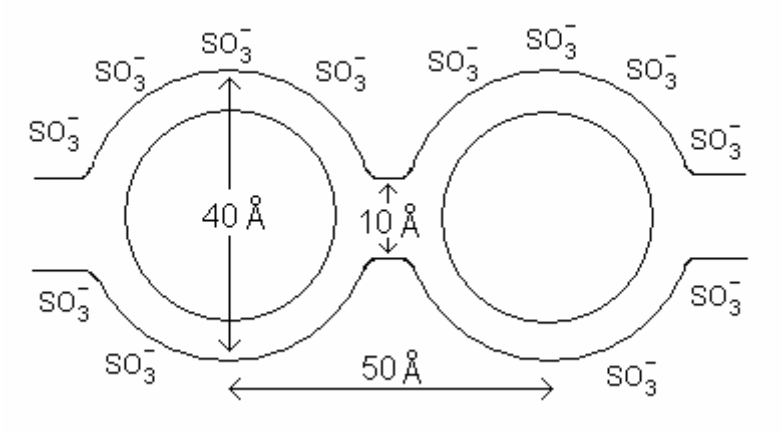

Figure 1.4: Cluster-network model from Gierke [59].

Fujimura *et al*. performed SAXS and WAXD experiments as well in order to define the morphological origins of the two scattering peaks. In order to analyze the effect of ionic interactions due to the side chain, they neutralized chemically the sulfonated groups of the side chain into sulfonyl chloride, similar to Nafion® but nonionic [60, 61]. Like Gierke, Fujimura found two scattering maxima at s = 0.07 nm and 0.3 nm^{-1} (s is scattering vector, defined as $s= 2\cdot\sin(\theta) / \lambda$) which were attributed to crystalline and ionic domains. They also concluded from their measurements that the crystallinity of a Nafion® whose EW is 1100 $g\cdot mol^{-1}$ was 23% and 18-14% crystalline in the nonionic and carboxylated forms, respectively. The low angle scattering maximum at s = 0.07 nm^{-1} was supposed to be an average spacing between crystalline lamellar plate. At higher humidification, the cluster dimension is shown to increase. Fujimura *et al* concluded that the observed behavior can be the best described by an intraparticle core-shell model [60]. A schematically representation is given in Figure 1.5.

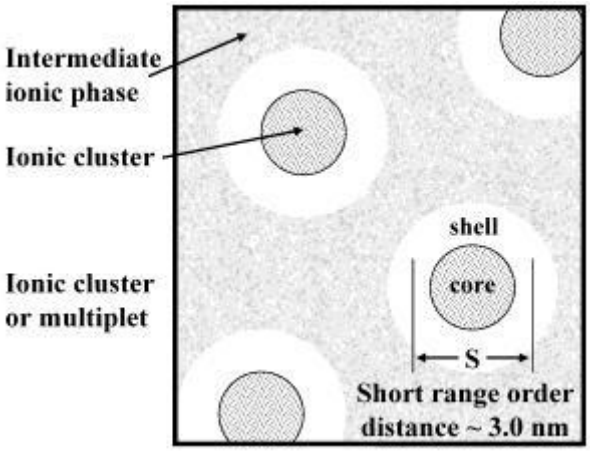

Figure 1.5: Modified core-shell model for Nafion® [60].

Haubold *et al*. proposed a variation of the lamellar model of Litt as presented in Figure 1.6 [11, 62]. They performed SAXS studies for that. They observed the usual peak at 1.4 nm^{-1}. The scattering cross section data was fitted to a layered model whose structure element is a "sandwich". The outer portion (shell) is composed by the side chains and the core is a liquid phase with water (and methanol in their case – Direct Methanol Fuel Cell (DMFC) conditions). In order to provide channels for the proton transport along the membrane, the "sandwiches" were stacked in a linear fashion so that the liquid core regions are contiguous as shown in Figure 1.7 [58].

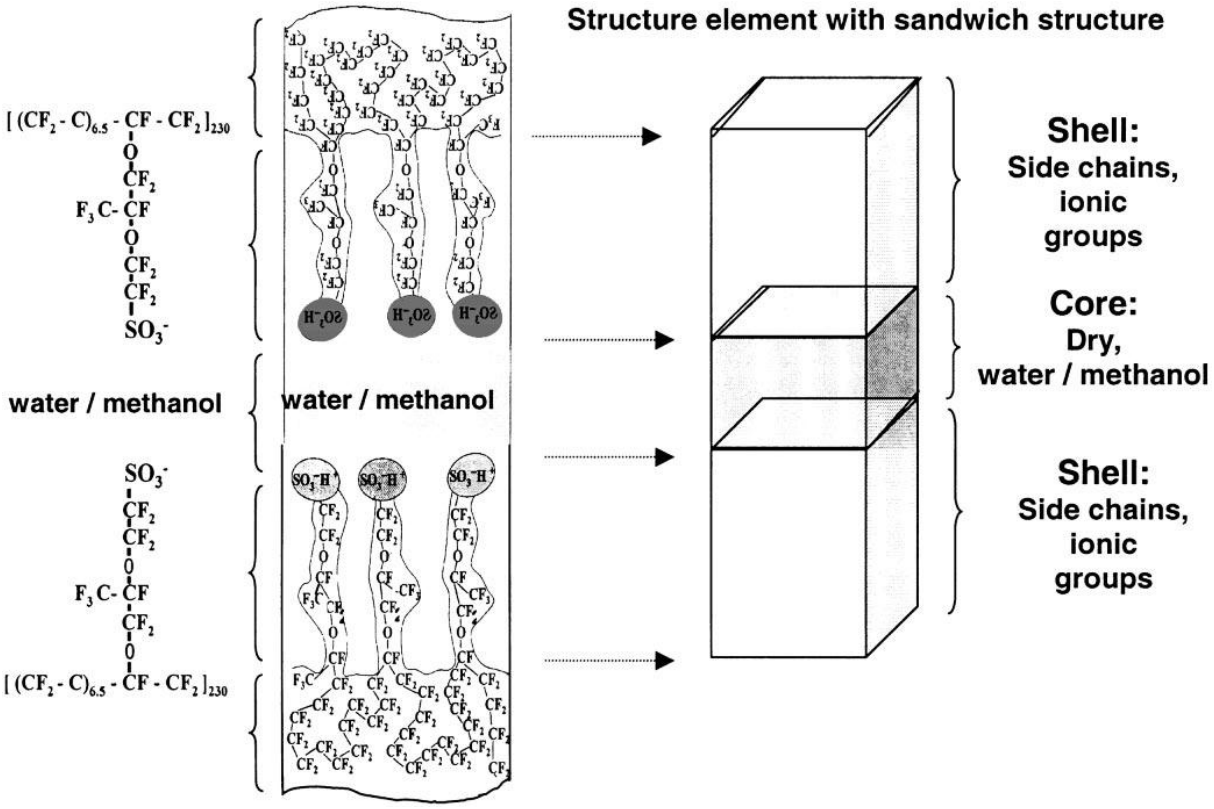

Figure 1.6: Haubold's sandwich-like structure for Nafion® [11]

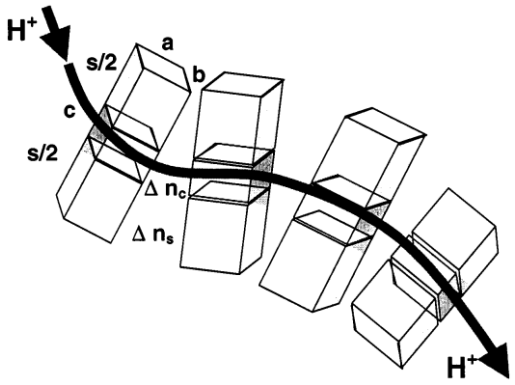

Figure 1.7: Stack of element to describe proton conductivity in Nafion® [11]

Most of these models regard fully-humidified membranes. Gebel proposed a conceptual description for the swelling and dissolution process, as shown in Figure 1.8. In this qualitative model, the dry membrane is considered to contain isolated, spherical ionic clusters with diameters of 1.5 nm and a center-to-center separation distance of 2.7 nm. With the absorption of water, the clusters swell to hold pools of water surrounded by ionic groups at the polymer water interface in order to minimize the interfacial energy. As the water content increases to a water volume fraction between 0.3 and 0.5, structural reorganization occurs to keep constant the specific surface area, and the onset of percolation is achieved by the formation of connecting cylinders of water between the swollen, spherical clusters. At water volume fraction values greater than 0.5, an inversion of the structure occurs such that the structure resembles a connected network of rods (inverted micelles). Finally, as the membrane "dissolves" into solution, the rodlike structures separate to yield a colloidal dispersion of isolated rods [58].

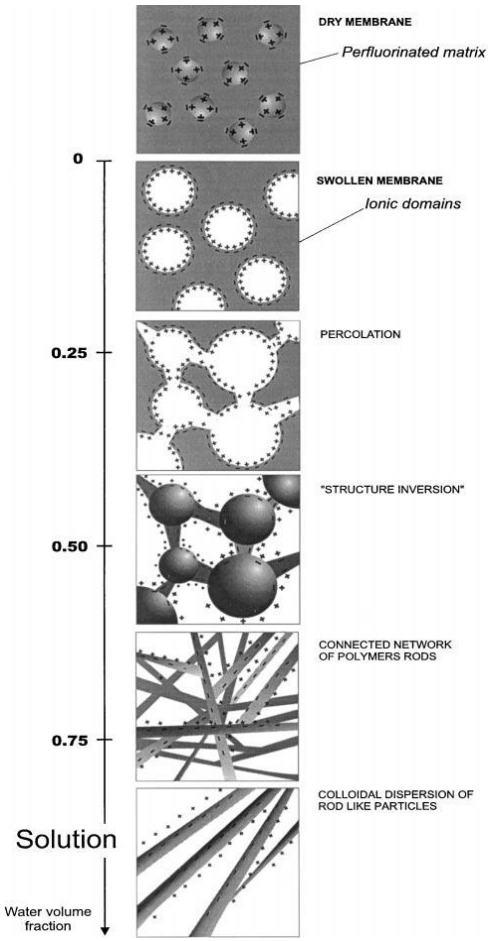

Figure 1.8: Schematic evolution of the Nafion® structure depending on the water content [63]

In the continuity of this work, Rubatat *et al* combined neutron and X-ray scattering techniques, and extended the range of X-ray scattering by using Ultra SAXS [12]. They collected scattering data from Nafion® samples at various water contents. Maxima positions and shapes of scattering profiles were similar to what other groups previously reported in the literature. This observation supported the assumption that the swelling process involves a dilution of the scattering entities, and not a strong structural reorganization as previously proposed [63]. This dissociation was partial and continuous over the whole swelling process [64]. Although the real description should be more complex, the assumption of Rubatat that the Nafion® membrane was composed of an assembly of bundles of fibrils (as displayed in Figure 1.9) allowed them to analyze the anisotropic scattering spectra observed when a strain is applied on the membrane. They assumed the morphology of Nafion® as a mixture between amorphous phases and ordered phases, whose dimensions were derived from USAXS and organization by the ionomer peak on measured profiles.

Figure 1.9: Schematic view of correlated polymeric aggregates domains [65]

Weber and Newman treated the Hsu and Gierke cluster-network model as an idealization of the Yeager and Steck model, where the pathways between the clusters are the interfacial regions [14, 57, 66]. The main focus of the model is how the membrane structure changes as a function of water content, where λ is the moles of water per mole of sulfonic acid sites (Figure 1.10). In the first step, the dry membrane absorbs water in order to solvate the acid groups. The initial water is associated strongly with the sites, and with the addition of more water in the membrane, the water becomes less bound, and inverted micelles form in the polymer matrix. With more water uptake, these clusters grow and form interconnections with each other. The connections, or collapsed channels, are transitory and have hydrophobicities comparable to the matrix. The cluster-channel network forms based on a percolation-type phenomenon of the clusters; therefore, to form a transport pathway, the clusters must grow and be close enough together to be linked by the collapsed channels [67].

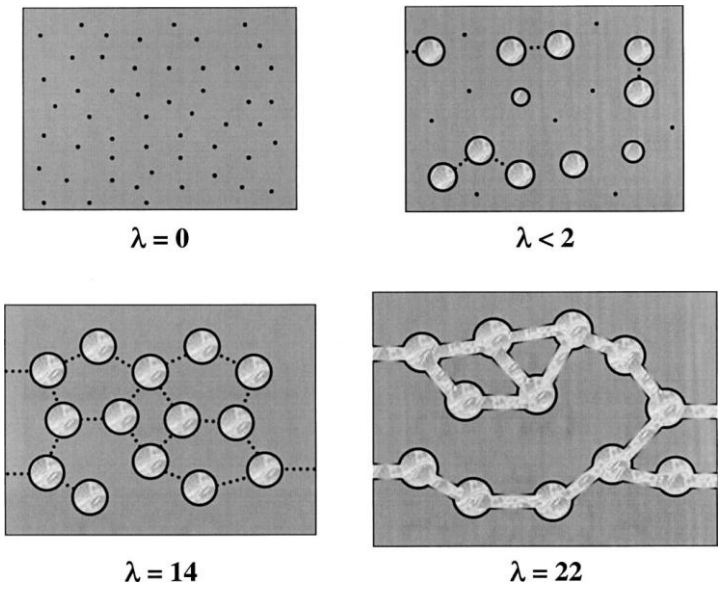

Figure 1.10: Evolution of the membrane structure as a function of water content λ (moles of water per mole of sulfonic acid sites). The pictures are cross-sectional representations of the membrane where the gray area is the fluorocarbon matrix, the black is the polymer side chain, the light gray is the liquid water, and the dotted line is a collapsed channel [67].

A more recent structure was proposed by Schmidt-Rohr and Chen, as schematically presented in Figure 1.11 [13]. Using simulations tools (they developed a new algorithm for simulating SAXS measurements), they proposed a novel structure named the parallel water-channel model. This model explains the scattering data of unoriented samples and of oriented films or fibers with their exclusively meridional intensity for both the ionomer peak and the small-angle upturn. The stiffness of the helical backbone segments, which has been confirmed by NMR, can stabilize the long cylindrical structures [48, 49, 68, 69]. A rationale for the supposed regular alternation between clusters and channels in Gierke's model was never given. The parallel water-channel model shows that the previously elusive channels by themselves fully account for the ionomer peak, without spherical clusters. The water-channel model naturally accounts for many of the outstanding properties of Nafion®, in particular its high proton conductivity and water permeability.

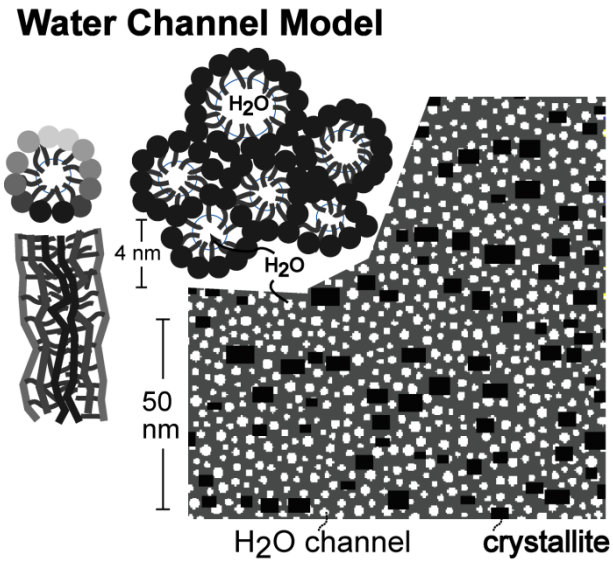

Figure 1.11: Schematically representation of the water-channel model [13].

1.3 Chemical degradation of the electrolyte in PEMFCs: Experimental evidence

The performance decay or the failure of a PEMFC may have several causes. Each part of the cell may be the cause of the failure and it is almost impossible to predict a priori which component would fail at first. This explains why lot of efforts have been made to separate each degradation phenomena and its effects on the cell, from the mechanical stresses on the GDL under the gas channel of the end plate to the electrochemical degradation of the catalyst and the carbon support within the electrodes. We focus here on the experimental work carried out in order to observe and underline the effect of the chemical degradation on the membrane and the global effect induced to the performance of the cell.

Several analytical techniques are currently used in the research on chemical degradation of membrane. It is possible to distinguish these methods with different criteria, for example, destructive / non-destructive methods, in-situ / ex-situ methods, direct / indirect methods, dynamic / post-mortem methods. We present here some of the evidences of the chemical degradation and the analytical tools necessary to the observation and explanation of the degradation phenomena.

1.3.1 Loss of cell performance over time

Most of the experimental reports which can be find reports that the degradation is more important under open-circuit condition (OCV) than under a current load [70]. For this reason, most of the work made on chemical degradation of PFSA membrane was carried out at OCV. However some groups studied the impact of the cell potential on the chemical degradation.

Young *et al*. published the results of a complete study about the impact of the electrode composition over the chemical degradation of the cell [16]. They investigated two compositions of cathode, with respectively 23 wt% and 33 wt% of Nafion®. They performed a test with optimized conditions to observe faster the degradation of the cell. After several experimental times, they plotted polarization curves. These are represented in Figure 1.12 and Figure 1.13.

From Figure 1.12 and Figure 1.13, they justify a well-known observation; the slow kinetics at the cathode side (due to the high complexity of the ORR) is the major contributor to the performance loss in a PEMFC. Cathode with higher Nafion® content seems to be more degraded chemically than a cathode with less Nafion®. The ohmic losses are due to an increase of the membrane resistance, that is, a decrease of the membrane conductivity. This conductivity is directly linked to the side chain presence and water distribution.Considering that at a given current density, the humidification remains unchanged, it was concluded that the radical reaction responsible of the chemical degradation involves not only an attack on the Teflon back bone but on the side chain as well (known as side chain unzipping).

Tang *et al*. studied both mechanical and chemical degradation of Nafion® in PEMFC and performed an electrochemical characterization of Nafion® 111 [71]. They tested a single cell (25 cm^2 active area, 0.2 $mg_{Pt} \cdot cm^{-2}$ in both electrodes, 50 h under feed H_2/O_2) at OCV conditions and observed a decay of the cell potential, as represented in Figure 1.14. To identify the origin of this dramatic decay, they applied at the anode and the cathode polarization under N_2/O_2 and then under H_2/N_2. The cell potential was found to be constant, which confirmed that both hydrogen and oxygen have to be present to observe degradation. Even if the potential decay they observed remains abnormally high, it confirms that the chemical degradation induces losses in the cell performance.

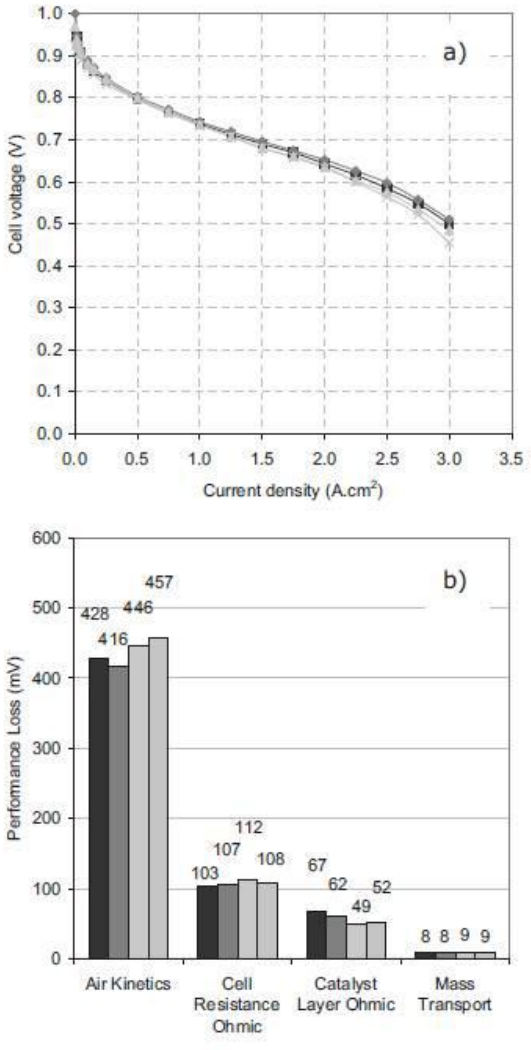

Figure 1.12: IV-curve (a) 23 wt% Nafion® in cathode and repartition of losses (b) at 2.5 A·cm^{-2} taken at (■) 0, (♦) 150, (▲)300, and (x) 440 h [16]

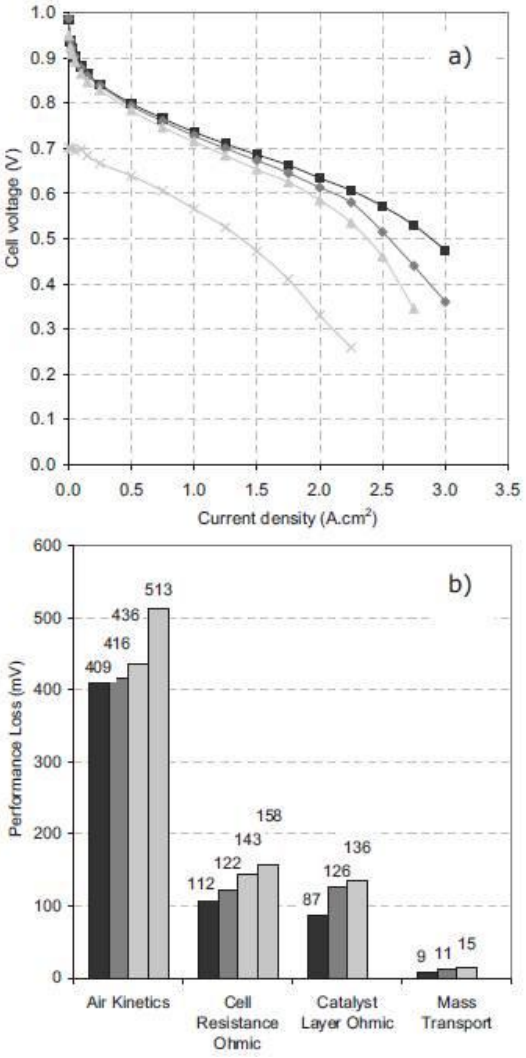

Figure 1.13: IV-curve (a) 33 wt% Nafion® in cathode and repartition of losses (b) at 2.5 A·cm^{-2} taken at (■) 0, (♦) 150, (▲)300, and (x)440 h [16]

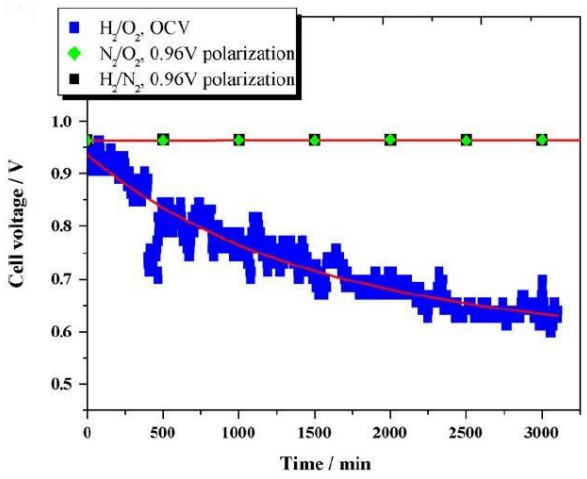

Figure 1.14: Evolution of the cell potential under OCV conditions [71].

Similar behavior was observed by Inaba *et al*. [72]. The potential loss is not so large than in the experiment of Tang but a decrease is observed. In Figure 1.15, we can see at the OCV, the potential is decreasing. This potential loss is to be compared with the temporal evolution of the hydrogen crossover from the anode to the cathode (Figure 1.16).

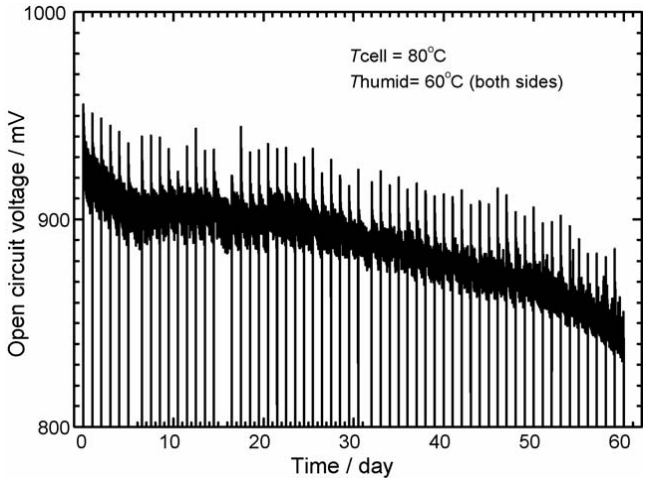

Figure 1.15: Variation of the open-circuit voltage of H_2/air cell during OCV durability test at 80 °C [72].

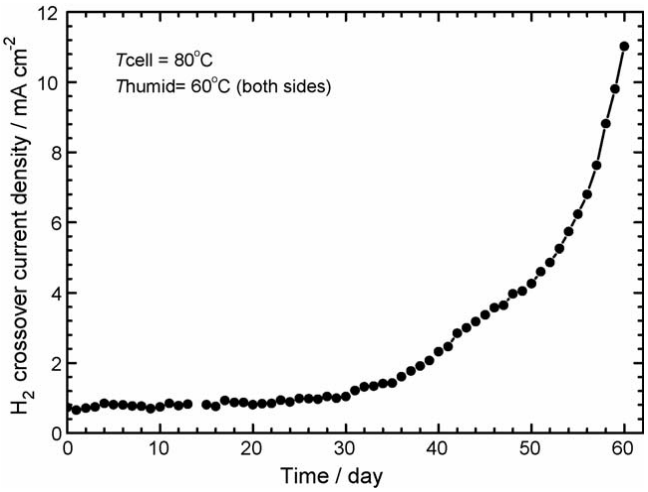

Figure 1.16: Variation of the H_2 crossover current density during OCV durability test at 80 °C [72].

At every 24 h, air was replaced with argon to measure hydrogen crossover current, where the OCV dropped down to about 100 mV in. In each 24 h, the OCV was the highest just after air was introduced in the cell, and then dropped gradually with time. This phenomenon is attributed by the authors to reversible oxide film formation on the cathode Pt catalyst and hence is a reversible degradation phenomenon. The OCV (just after air was introduced at every 24 h) slowly decreased to about 840 mV after 60 days. The average voltage degradation rate was ca. 83 $\mu V \cdot h^{-1}$, which is much faster than that in normal operation (a few to several $\mu V \cdot h^{-1}$) under fully humidified conditions. Consequently, the open-circuit condition accelerates the degradation of the MEA [72].

Based on the work of Young *et al*., the performance loss remains low compared for example to ohmic losses due to the degradation of the carbon catalyst support [16]. Schulze *et al*. analyzed the effect of degradation on a fuel cell and observed through electrochemical impedance spectroscopy (EIS) measurement an increase of the carbon-support resistance of about 14 mΩ, whereas the increase of the membrane resistance was barely measurable [73]. However, the degradation strongly depends on the experimental conditions, materials and cell design (e.g. channels geometry) used.

1.3.2 Membrane thinning

As the loss in performance is not a reliable tool to quantify and identify the chemical degradation of the membrane, experimentalists had to find other ways to characterize the chemical degradation of Nafion®. The chemical degradation "removes" atoms from the membrane, thus we can expect that the membrane slowly vanishes into the liquid phase. An effect would then be the decrease of the membrane thickness. The most common way to observe it is the use of high resolution microscopes.

Tang *et al*. put the membranes into bottles under conditions of dry, atmospheric humidity, saturated humidity and 1 mol·l^{-1} H_2SO_4 [71]. These bottles were then fed with 100 sccm H_2 and 100 sccm O_2 respectively. They measured the membrane thickness after 1000 h in different operations conditions that would exist in the fuel cell. Table 1.3 sums up the result of these measurements

	Thickness / µm
Original Nafion®111	25.4 ±0.1
1000 h H_2	
Absolute dry	25.1 ±0.1
Atmospheric humidity	24.8 ±0.1
100 % RH	25.2 ±0.1
Acidic condition	24.3 ±0.1
With Fe^{2+}	22.4 ±0.1
1000 h O_2	
Absolute dry	25.2 ±0.1
Atmospheric humidity	24.3 ±0.1
100 % RH	24.2 ±0.1
Acidic condition	23.9 ±0.1
With Fe^{2+}	23.4 ±0.1

Table 1.3: Evolution of membrane thickness of Nafion® membranes exposed in H_2 or O_2 for 1000 h (after [71])

They noticed no significant decrease of Nafion® thickness. This indicated that the Nafion® membrane is chemically stable vis-a-vis oxygen and hydrogen. This means that the chemical degradation occurs only in presence of both gases, which was already suggested by the OCV electrochemical experiments.

Healy *et al*. presented an interesting overview of PFSA chemical degradation in fuel cell utilization [15]. They performed in-situ and ex-situ experiments in order to understand better the origin of the degradation. In their investigation, they ran a fuel cell over 1000 h and followed the release of fluoride ions in drain water, an important by-product of the chemical degradation. They correlated a high fluoride production with a decrease of the membrane thickness. They observed it by comparison of elec-

tron probe X-ray imaging on MEA before and after the operation of the cell. The imaging is shown in Figure 1.17. The left picture is the imaging of a fresh MEA, the one on the right is a MEA after 1000 h utilization.

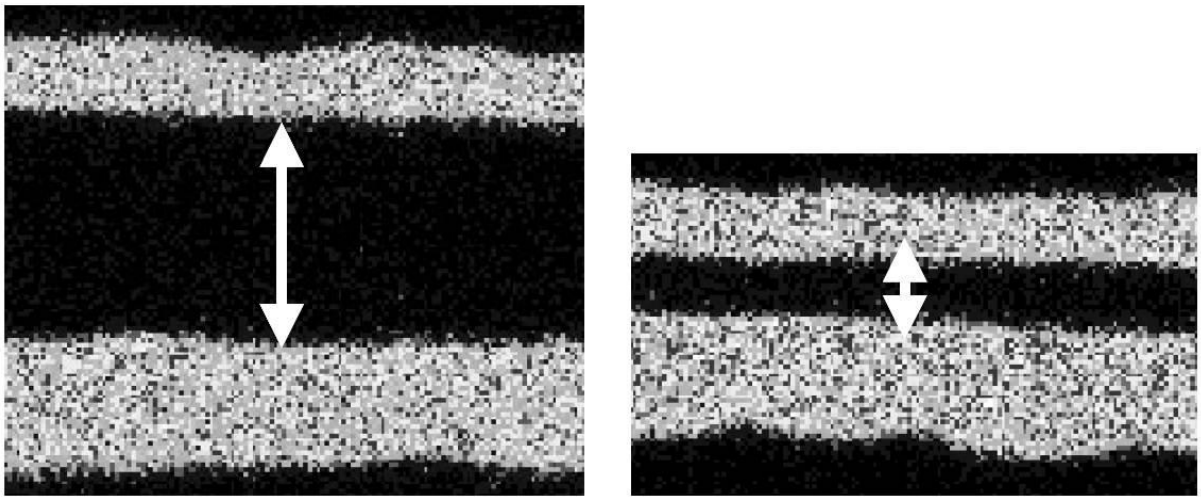

Figure 1.17: Electron probe acquired X-ray images of cross-sectioned new and used MEAs (the white arrow represents the membrane thickness) [15]

The significant decreasing of the membrane thickness is supposed to be caused by the chemical degradation but no quantification was given.

Young *et al*. observed a decrease of the membrane thickness as well. They performed accelerated stress tests (AST) on a fuel cell (90 °C, 2 bar pressure anode and cathode, 0.3 slpm anode and cathode flow rate, 120 % RH, 1 V). These conditions are extremely severe and are used rather to study the effect of the degradation than to get precise hints on the durability of the cell. Within several hundreds of hours, degradation states are reached which would take several thousands of hours under normal conditions. Their SEM observations are shown in Figure 1.18.

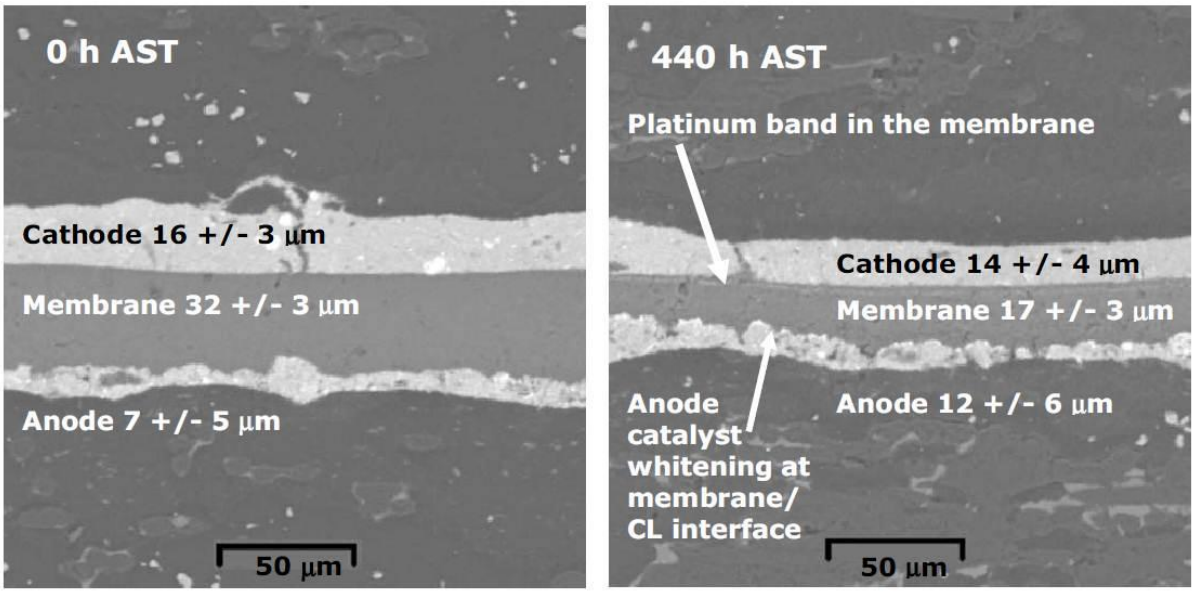

Figure 1.18: Comparison of SEM micrographs for the MEA with 33 wt % Nafion® in the cathode CL before and after AST testing at 1.0 V_{RHE} [16].

Operating condition	Temperature (°C)	Cathode / anode pressure (kPa)	Cathode flow rate (slpm)	Anode flow rate (slpm)	Relative humidity (%)
AST	90	200	0.3 (air)	0.3 (H_2)	120

Table 1.4: AST used by Young *et al*. [16].

Figure 1.18 shows no significant thinning of the cathode or anode electrodes, whereas the Nafion® membrane thinned 40–50% over the 440 h degradation period [16]. It is to notice that a platinum band has been founded in the membrane, evidence for platinum catalyst degradation through a dissolution-reduction scheme [4, 74]. Young *et al* studied the correlation between the fluoride emission (see Section 1.3.5) and the decrease of the membrane thickness. Figure 1.19 shows their conclusion. No linearity is observed between the amount of released fluoride and the thickness of the membrane. At the beginning of the degradation, the membrane thickness dramatically decreases of about 40 %, and then the membrane thickness seems to remain constant. That suggests that both uniform and localized membrane degradation occurred [16]. First the degradation may rather occur at the interfaces electrodes/electrolyte, then inside the membrane.

After an ex-situ test where the membrane was soaked in a hydrogen peroxide / metal cations solution, Tang *et al*. reported the formation of voids and later of pinholes in SEM micrographs, whereas such observation has never been reported after aging of membrane in fuel cell conditions [71].

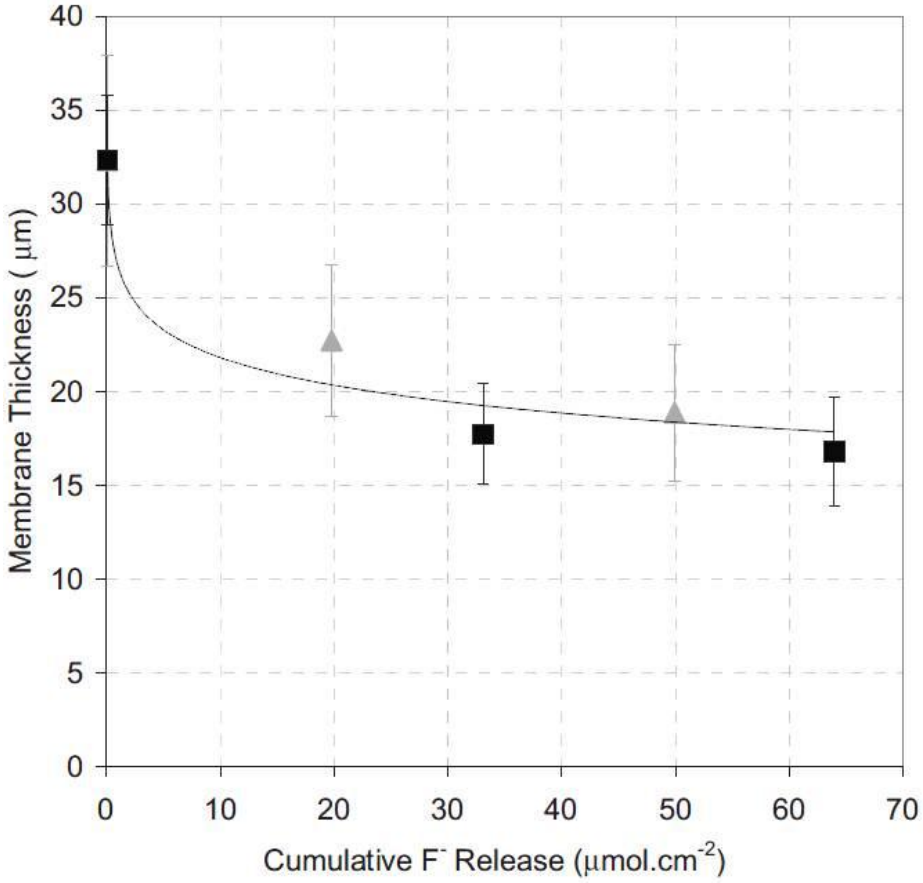

Figure 1.19: Membrane thinning measured from SEM micrographs as a function of cumulative fluoride release (▲ 23 wt % and ■ 33 wt % Nafion® content in the cathode CL) [16]

1.3.3 Production of hydrogen peroxide in the electrodes

One of the role of the membrane is to separate the gases at the electrode (methanol / air in DMFC or hydrogen / air in PEMFC). However, it has been often reported that permeation of reactant through the membrane occurs [27, 72, 75-77]. This shows that Nafion® is not a perfect gas separator has it ought to be. The presence of oxygen at the anode can lead, among other things, to the chemical production of hydrogen peroxide following Reaction 1.4. Moreover, it is possible to imagine an oxygen reduction at the cathode involving two electrons (see Reaction 1.5).

H_2O_2 production (anodic case) $\quad H_2 + O_2 \longrightarrow H_2O_2$ Reaction 1.4

H_2O_2 production (cathodic case) $\quad O_2 + 2\,H^+ + 2\,e^- \longrightarrow H_2O_2$ Reaction 1.5

However there is still debate in the literature to see if the major location of H_2O_2 production is at the anode or the cathode side [17, 18, 78]. The understanding of ORR mechanism was already experimentally studied by Davies *et al*. and Yeager [79-83]. Davies *et al*. proposed several mechanisms for the oxygen reduction in their study on the oxygen electrode in 1959 [79]. They proposed three possible mechanisms for this reaction on carbon in alkaline solution as shown in Figure 1.20 In a modern PEMFC, the pH of the cell is strongly acidic. But we could assume that the mechanism is not deeply influenced as basic species appear on the product side of the reactions. Yeager studied the oxygen reduction reaction on several surfaces [82]. In our case, the surfaces of interest are platinum and carbon, as they are the active constituents of the considered electrodes. Using the rotating ring-disc electrode (RRDE) technique on Pt, they get evidence that the O_2 reduction is carried out principally through the 4-electron pathway in both acid and alkaline aqueous electrolytes under conditions where adsorbed impurities are minimal. However on his study on graphite and carbon he considered peroxide as a possible intermediate in the ORR, a mechanism was published by Morcos *et al*. [81].

Mechanism 1

$$H_2O + e \rightarrow H\ (ads) + OH^-$$
$$O_2\ (gas) \rightarrow O_2\ (ads)$$
$$O_2\ (ads) + H\ (ads) \rightarrow HO_2\ (ads)$$
$$HO_2\ (ads) + e \rightarrow HO_2^-$$

Mechanism 2

$$H_2O + e \rightarrow H\ (ads) + OH^-$$
$$O_2\ (gas) \rightarrow O_2\ (ads)$$
$$O_2\ (ads) + H\ (ads) \rightarrow HO_2\ (ads)$$
$$HO_2\ (ads) + H\ (ads) \rightarrow H_2O_2$$
$$OH^- + H_2O_2 \rightarrow H_2O + O_2H^-$$

Mechanism 3

$$O_2\ (gas) \rightarrow O_2\ (ads)$$
$$O_2\ (ads) + H_2O + 2e \rightarrow HO_2^- + OH^-$$

Figure 1.20: Oxygen reduction on carbon under alkaline conditions [79].

Ab initio calculations, within the Density Functional Theory -DFT- approach, are also carried out to elucidate ORR mechanism on different catalysts and the different pathways leading to H_2O_2 formation [84-88].

Mittal *et al*. showed that hydrogen peroxide is formed in PEMFC [78]. They could not answer the question whether the production occurs at the anode or the cathode because of diffusing effects in the

cell but they made a complete study about the influence of reactant, humidity and temperature.

Liu and Zuckerbrod set up an experimental device to detect in situ the production of hydrogen peroxide [18]. This clever experiment uses two Pt microelectrode embedded in different types of membrane and assembled in a fuel cell. After determining the electrochemical signature of H_2O_2 through cyclic voltammetry (CV) and calibrating the height of its peak with the concentration, they could interpret the electrochemical response during the operation of the fuel cell, displayed in Figure 1.21.The H_2O_2 concentrations they calculated are estimation by comparison of H_2O_2 peak on CV with references. It appears that despite differences between ionomer type, EW, and membrane processing, the concentration of H_2O_2 was mostly influenced by membrane thickness, the thinner the membrane, the higher the concentration of H_2O_2. To produce H_2O_2, O_2, a catalyst, and a reducing environment such as low potential are required. In a PEMFC, low potential areas are located at the anode side, and oxygen is provided through permeation from the anode to the cathode. Obviously, the thinner the membrane, the higher the cross-over is.

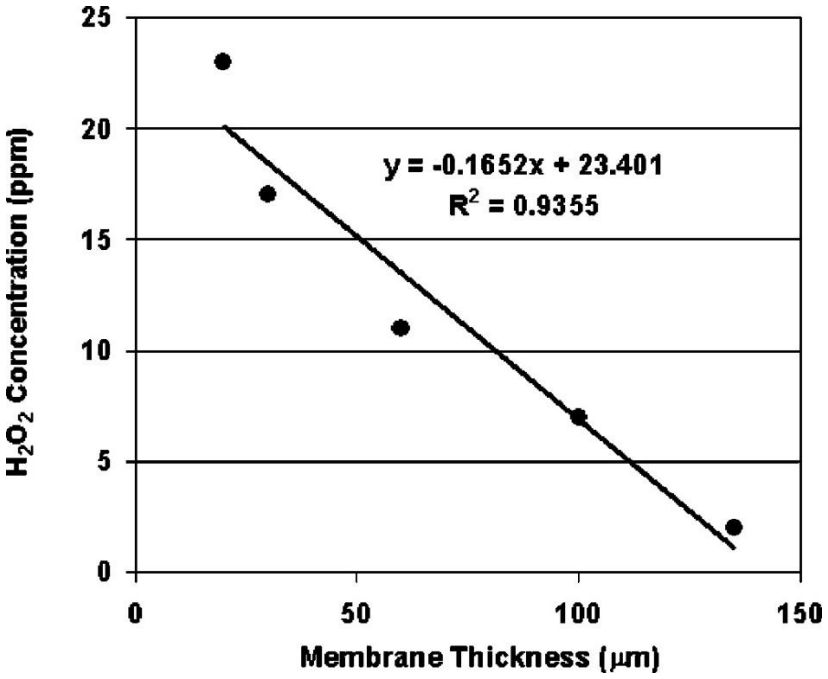

Figure 1.21: Estimation of H_2O_2 concentration in fuel cells with different membrane thickness [18]

However, a high concentration of hydrogen peroxide does not automatically mean a large degradation. One of the key factors is the presence of so-called Fenton's ions (for example Fe^{2+} or Cu^{2+}) in the fuel cell which will initiate the decomposition of H_2O_2 in radicals. One of the most plausible origins of these ions is the degradation of iron containing end-plate which is used in the fuel cell technology [89, 90]. Some clues indicated that this degradation is due to the use of oxygen at the cathode. Mittal *et al.* supplied H_2O_2 as reactant at the cathode and no degradation was observed, which would suggest that

no iron was produced in the system [78].

1.3.4 Formation of radicals

Hydroxyl radicals are highly reactive and consequently short-lived. They are really difficult to be observed because of their low life-time (about 10^{-9} s). Two solutions may be envisaged to solve this problem: trapping the radical under a more stable form or cool down (77 K) the membrane to make direct observations.

Aoki *et al*. used 5,5'-dimethyl-1-pyrroline-*N*-oxide (DMPO) was added in a H_2O_2 solution suspending various types of membrane as a spin trap reagent to form DMPO-OH adduct [91]. After 5 min, they then measured by electron spin resonance (ESR), technique also known as electronic paramagnetic resonance (EPR) the amount of hydroxyl radical which has been produced. Figure 1.22 shows the amount measured under several conditions.

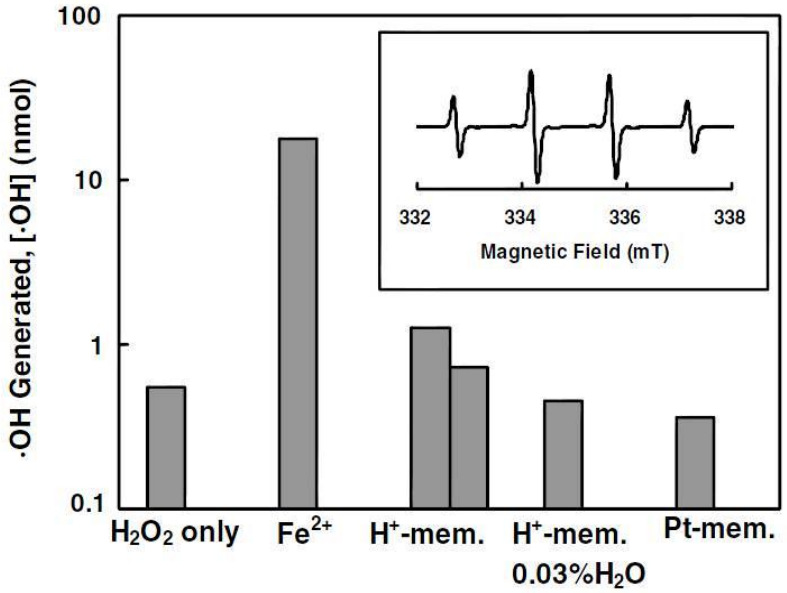

Figure 1.22: Hydroxyl radical generated in membrane in different solutions [91]

The essential role of ferrous iron is here confirmed. A self-decomposition of H_2O_2 is really low. But the presence of Fe^{2+} increases the amount of produced hydroxyl radicals.

Panchenko *et al*. developed a cell capable of operating in the resonator of an X-band EPR-spectrometer [92]. This method was used by Vogel *et al*. to observe in-situ formation of radical during the operation of a fuel cell [93]. They concluded to the role of hydroxyl radicals in the attack of membrane.

Kadirov *et al*. analyzed by ESR membrane neutralized with different metal cations (Cu^{2+}, Fe^{2+}, Fe^{3+}) [28]. Their measurement at 77 K lead to the conclusion that the presence of Fe^{2+}, Fe^{3+}, or Cu^{2+} in combination with hydrogen peroxide and UV irradiation leads to extensive radical formation on PFSA membranes.

Danilczuk *et al*. performed in situ ESR measurement of a PEMFC at 300 K [27]. They concluded that the production of hydrogen peroxide (and thus of radicals) occurred at the cathode side only in closed circuit voltage (CCV), which suggests an electrochemical production of hydrogen peroxide through a two electron reduction step of oxygen in these conditions. However the possibility of a radical production at the anode is not excluded [18, 94-96].

1.3.5 Chemical analysis of the degradation of PFSA membranes

The most reported method to underline the PFSA membrane degradation is the measurement of fluoride ions (fluoride emission rate FER) in the drain water of the cell. One of the products of the degradation of Nafion® is fluoride ions. As the initial conditions of a cell do not include the presence of fluoride in ionic form, their presence in the drain water is a direct measure of the chemical degradation. Many analytical methods have been developed to measure the quantity of fluoride in the produced water or on the contrary, the remaining fluoride in the membrane.

Healy *et al*. found through ^{19}F NMR a fluoride peak in the drain water (water which leaves the system through the gas channels) of a severely degraded membrane which was not present in an unused MEA [15]. It was assigned to perfluoro(3-oxapentane)-1-sulfonic-4-carboxylic diacid (later named molecule A) displayed in Figure 1.23. This was confirmed by mass spectrometry (MS). This molecule is a sort of acidic form of side chain, resulting of the side chain unzipping during degradation.

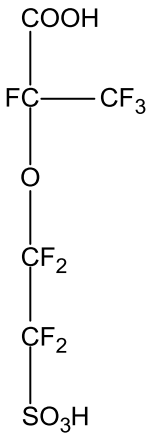

Figure 1.23: Semi-developed formula of perfluoro(3-oxapentane)-1-sulfonic-4-carboxylic diacid (molecule A)

The total amount of fluoride ions which have been released has been determined through ionic chromatography. The amount of fluoride is a parameter which should not linearly assimiled to the rate of degradation of the membrane. Indeed it strongly depends to the experimental conditions, the amount of produced hydrogen peroxide, the presence of iron ions, membrane thickness and a part of the degraded fluoride may remain under organic form [15, 16, 37, 72, 97-99]. Thus experimental results are very difficult to be interpreted.

Another possibility is to follow the evolution of the mass of the membrane [100]. Kundu *et al*. performed two accelerated degradation test and compared them. The first method exposes the membrane to a solution of peroxide and metal ions (solution method) while the second method exchanges the metal ions with the acid sites of the polymer before exposure to peroxide (exchange method) [15, 97]. They started from different iron ions concentrations in the cell and measured the weight loss after a certain period of degradation. It seemed that the mass loss is independent of the quantity of iron ions, as after the same periods of time the same mass loss had been observed. However the amount of fluoride produced was different, which was due to the fact that organic fragment of Nafion® remained in the membrane in one case and could not be then observed by anorganic fluoride sensitive analytic methods. They found out, depending on the degradation test they used, that the loss of weight lays by 25 % after 120 h, when the amount of fluoride loss was only 0.5 % to 1.5 % of the total amount of fluoride.

All of these experimental observations are specifically to a single experiment, as some experimental cannot be controlled (ratio between organic fluoride in degraded products to anorganic fluoride for example). This explains why experimental works are sometimes linked to a specific model. The next part deals with relevant modeling work currently available in the literature.

1.4 Chemical degradation of the electrolyte in PEMFCs: Available modeling work

Modeling is a broad field and several works are available in the existing literature. Some of them inquire through atomistic calculations the pathways of the chemical degradation; other uses continuum approaches to make predictions on the behavior the fuel cell or the membrane.

First of all, it is important to know the chemical pathway leading to the chemical degradation of the membrane. Indeed, no model can be effective if the phenomenon is not perfectly clearly defined. Xie and Hayden proposed a mechanism of membrane degradation, which is now regarded as the most plausible approach, exhibing good agreement with experimental works [32].The highly reactive radical species produced after the permeation of oxygen to the anode side may either react following one of the reactions described in Section 2.3.1 (Reaction 2.3, Reaction 2.4 and Reaction 2.5) or attack the

PFSA membrane.

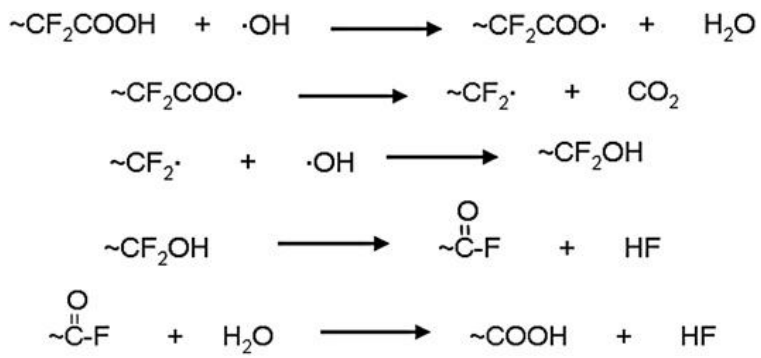

Figure 1.24: Individual degradation reaction steps via end group unzipping [32]

The carboxylic acid groups present in the membrane are either a direct by-product of the synthesis of the membrane or the result of reactions of others weak groups (for example $–CH_2F$) with radical species. This carboxylic acid reacts with two radicals and through this step, carbon dioxide and HF are released and the carboxylic acid group is transformed into a fluoride acid group which is then hydrolyzed, releasing another HF molecule and regenerating the carboxylic acid group. After each degradation process, the membrane back bone is reduced by one carbon atom.

During the degradation process it occurs that the carboxylic acid group is located in α of a carbon atom supporting a side chain. In such a case, we have to consider a parallel degradation pathway, as presented by Xie and Hayden [32].

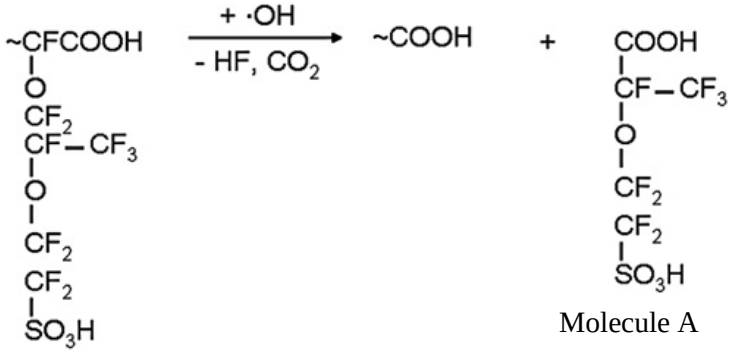

Figure 1.25: Secondary degradation reaction via end group unzipping [32].

As mentioned previously in Section 1.3.5, the organic molecule resulting from the unzipping of a side chain is called molecule “A” in order to simplify the discussion, as shown in Figure 1.25. This molecule A has been observed experimentally thus confirming this parallel process [15]. The molecule A can itself be degraded under radical attack and be decomposed into HF, CO_2 and sulfate ions, as shown in Figure 1.26.

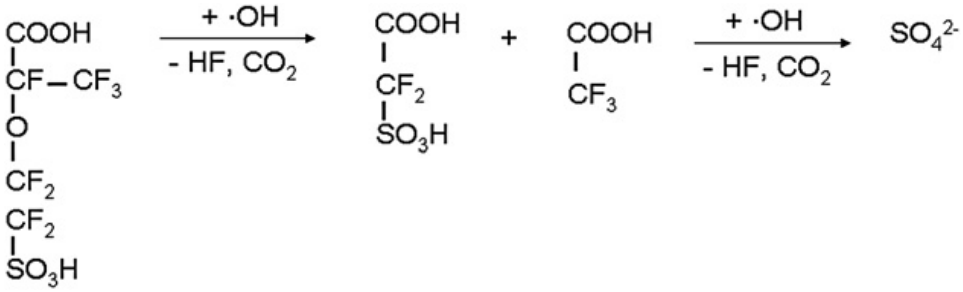

Figure 1.26: Unzipping degradation reaction of molecule A [32].

Ishimoto *et al*. performed DFT calculations to understand the chemical degradation mechanism of side chain by attack of hydroxyl radical [101]. They came to the same conclusions and provided potential energy profiles as a function of the bond of the side chain which is attacked by the hydroxyl radical.

The two previous modeling works included assumptions about the origin and the quantity of radicals and hydrogen peroxide and therefore, these works have to be completed by more models focused on the origin of hydrogen peroxide and its decomposition. Chen and Fuller proposed a H_2O_2 formation model based on catalyst agglomerate model [36]. They modeled both the production of H_2O_2 at the anode and at the cathode through chemical and electrochemical pathways. The H_2O_2 formation model is linked to an oxygen permeation model and described the diffusion of H_2O_2 in the agglomerate, as displayed in Figure 1.27. Figure 1.28 shows a comparison between Chen's model and experimental measurements. The trend observed between simulation and experiment is good. However, on a quantitative point of view, the model strongly underestimates the concentration of H_2O_2, more particularly at low humidity..

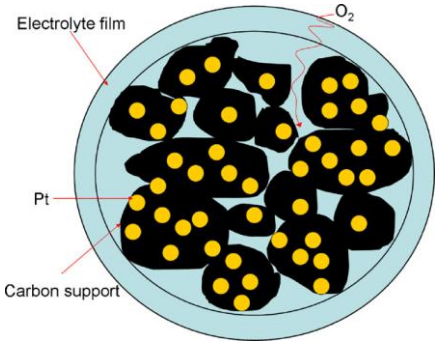

Figure 1.27: Catalyst agglomerate model [36]

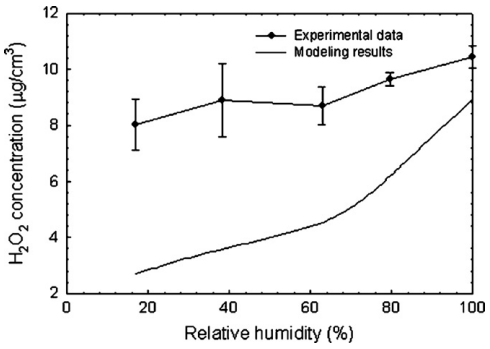

Figure 1.28: Comparison between experimental and simulated H_2O_2 concentrations under different relative humidities. Operating conditions:H_2//O_2; T_{cell} =65 °C; ambient pressure [36]

To complete this H_2O_2 production, it is necessary to describe the decomposition of the peroxide into radicals. Gubler *et al*. presented a model for the radical formation and the ionomer degradation [38]. They reused the rate constants from the work of Dockheer *et al*. [102]. Figure 1.29 shows the pathway that Gubler *et al*. studied.

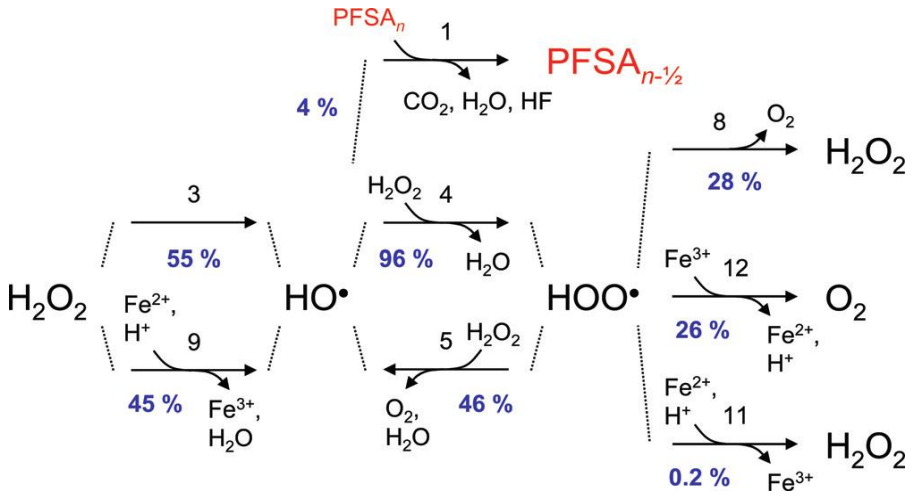

Figure 1.29: Reaction pathways involving radical species in an environment containing iron ions and PFSA membrane [38].

In Figure 1.30, we get an overview of the reaction rate of every reaction which was considered by Gubler *et al*. compared to the global iron concentration in the system. In their model, reaction 1 is the most important because it includes all the chemical degradation reactions occurring in the PFSA membranes. They used their model for other kind of membranes as well, a poly(styrenesulfonic acid) (PSSA) membrane, in order to compare the stability of these membrane against radical attack.

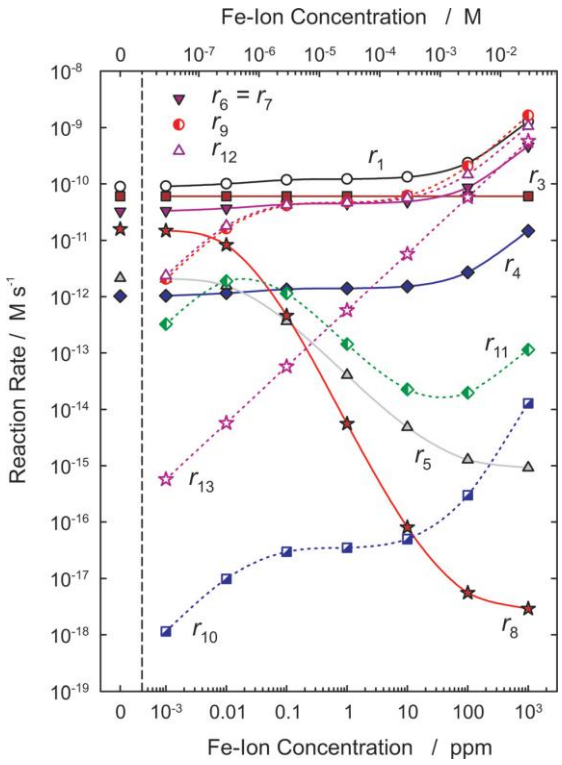

Figure 1.30: Reaction rates of reactions 1 and 3–13 (Figure 1.29, 13 is the reaction between ferric ions and hydrogen peroxide) at a H2O2 concentration of 0.5 mM in the presence of PFSA ionomer with a reactive end-group concentration [38].

To date, the most complete model describing the phenomena involved in the ionomer degradation has been presented by Shah *et al*. [39]. Transport phenomena, thermal effects and charge conservation were taken into account. They showed an interesting parametric study with discretization along the membrane, as displayed in Figure 1.31. But in their model they ignore the side chain unzipping, which means a constant conductivity of the membrane, and thus no effect of the degradation on the transport phenomena and the cell performance can be simulated. If we compare this results with the values experimentally observed in Figure 1.28, we see a certain difference between the simulations of Shah and Chen. This shows how important it is to validate a model (even partially) to give more reliability to the simulation results which are difficult / impossible to get experimentally.

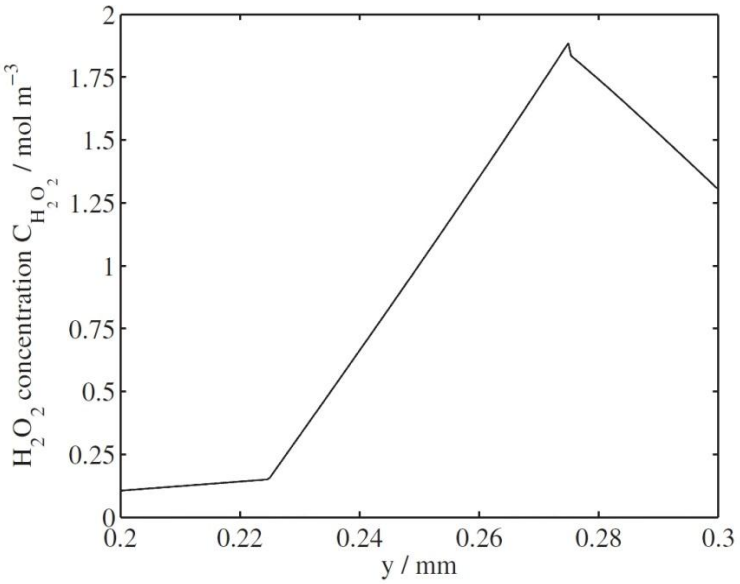

Figure 1.31: Evolutions of H_2O_2 concentrations for the base-case parameter values at the OCV: T_{Anode} = $T_{Cathode}$ = 60 °C, P_{Anode} = $P_{cathode}$ = 300 kPa, no side-chain cleavage, and a constant Fe^{2+} concentration of 5 ppm [39].

It has been experimentally observed that the potential decreases during operation. One contributor to this decrease is the increasing of the membrane resistance. Fowler *et al*. used a so-called generalized steady state electrochemical model (GSSEM) [103]. The ohmic losses are modeled by the use of Ohm's law. Figure 1.32, showed a comparison between a long-time experiment and simulation they carried out. It presents a very good agreement but this kind of modeling has a drawback: It lays on the use of empirical fitting of experiment. The simulations can only be carried out after getting the empirical equations required by the model. Such a model can unfortunately not be predictive, which means that the model cannot be adapted to an another experiment without running it.

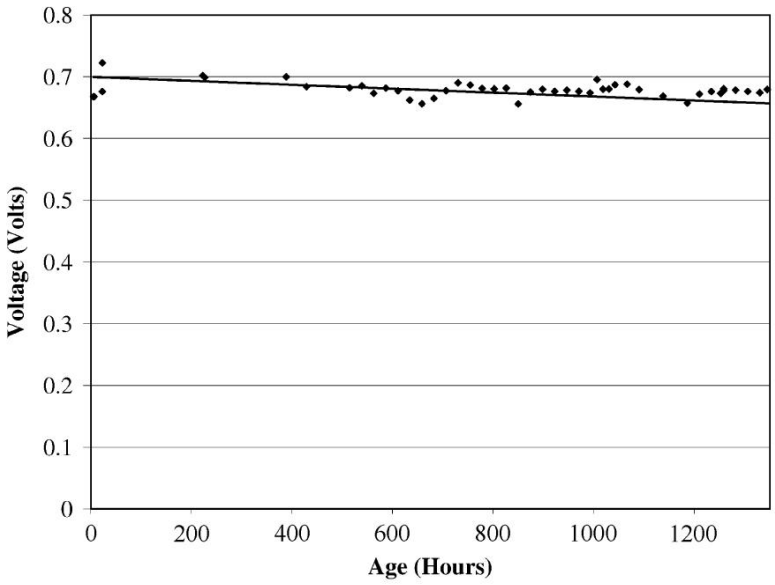

Figure 1.32: Voltage degradation curve of a single cell operated at 80 °C and 0.4 A·cm^{-2} [103]

1.5 Summary

This lack of complete and validated modeling work to understand membrane degradation in PEMFCs justifies the purpose of the present PhD thesis. We propose here to establish a model which intends to take into account as good as possible the available experimental results and observations: the objective is to develop an analytical model for the prediction of the evolution of membrane resistance and thus of the evolution of the ohmic losses due to the membrane in the cell.

The next two chapters will establish the complete set of physical and chemical concepts used in the model.

Chapter 2 deals with the chemical degradation model of the membrane. Chapter 3 is dedicated to the description of the electrode models used in the performance and durability calculations at the cell level.

CHAPTER 2

Modeling of the chemical degradation of the PFSA membrane

Une modélisation précise de membrane PFSA représente un réel challenge pour la science, tant sa nanostructure reste en partie incomprise. Pour cette raison, nous nous contentons dans cette approche de considérer la membrane comme un objet microscopique, en restant cependant cohérant avec les observations nanoscopiques qui ont été mentionnées dans le chapitre précédent.

Notre approche de la modélisation de la dégradation de la membrane se divise en deux parties, la description des phénomènes de transport dans la membrane, et ensuite son extension et son couplage aux phénomènes propres à la dégradation de la membrane.

La gestion de l'eau dans la membrane est un des aspects essentiels à maîtriser pour garantir une durée de vie et des performances optimales de la pile. Lors du fonctionnement normal d'une PAC, les protons sont produits à l'anode lors de la réaction d'oxydation de l'hydrogène, diffusent le long de la membrane et sont ensuite consommés à la cathode lors de la réaction de réduction de l'oxygène. En solution aqueuse, les protons n'existant pas seuls, ceux-ci protonent les molécules d'eau. Lorsqu'il est demandé à la cellule de produire du courant, celles-ci sont donc transportées de l'anode à la cathode induisant un flux d'eau couplé à celui de protons. Ce flux induit une accumulation partielle d'eau au niveau de la cathode, entraînant un déséquilibre dans la répartition de l'eau dans le long de la membrane, déséquilibre d'autant plus grand que le courant demandé est élevé. La cellule va naturellement tendre vers un état d'équilibre, se traduisant par un flux inverse d'eau de la cathode à l'anode. Ces deux phénomènes permettent de traiter les aspects de la gestion de l'eau dans la membrane. L'équation transcrivant le flux d'eau en tout point de la membrane est

$$J_{H_2O} = -t_{H_2O} \cdot \frac{i}{F} - D_{H_2O}^{Fick} \cdot \frac{\partial c_{H_2O}(y,t)}{\partial y} .$$

où le premier terme traduit le flux électroosmotique (mouvement des molécules d'eau avec les protons) et le second terme le terme de diffusion retour, diffusion dite Fickienne. Afin de déter-

miner la répartition d'eau dans la membrane, nous résolvons la première loi de Fick en tout point de la membrane. Afin de déterminer la valeur du paramètre λ une relation reliant ce paramètre à la concentration en eau dans la membrane est établie

$$c_{H_2O} = \frac{\lambda \cdot \rho_{Nafion}}{(1 + s\lambda) \cdot EW}$$

et l'équation de diffusion peut être réécrite en terme de λ.

$$\frac{\partial \lambda}{\partial t} = -\frac{(1+s\lambda)^2 \cdot EW}{\rho_{Nafion}} \cdot \frac{\partial J_{H_2O}(y,t)}{\partial y} .$$

Ainsi, il est possible de connaître précisément la teneur en eau dans la membrane. La teneur en eau conditionnant les propriétés de transport dans la membrane, il est possible de relier cette quantité aux différents paramètres de transport d'espèces dissoutes dans la membrane en appliquant des corrections dites de Bruggeman aux grandeurs de transport impliquées dans les équations de Fick exprimant les mouvements des différentes espèces dans la membrane (constantes de Henry et coefficients de diffusion). Cette correction fait intervenir certains paramètres structuraux de la membrane (la porosité et la tortuosité) dans le calcul des constantes de transport.

La dégradation chimique de la membrane est un phénomène complexe, faisant intervenir de nombreuses espèces et dont le déroulement précis n'est pas connu de manières précises. Certaines constatations expérimentales ont cependant permis de valider certaines théories. Dans le cadre de cette thèse, nous limitons les phénomènes intervenant dans cette dégradation au schéma suivant

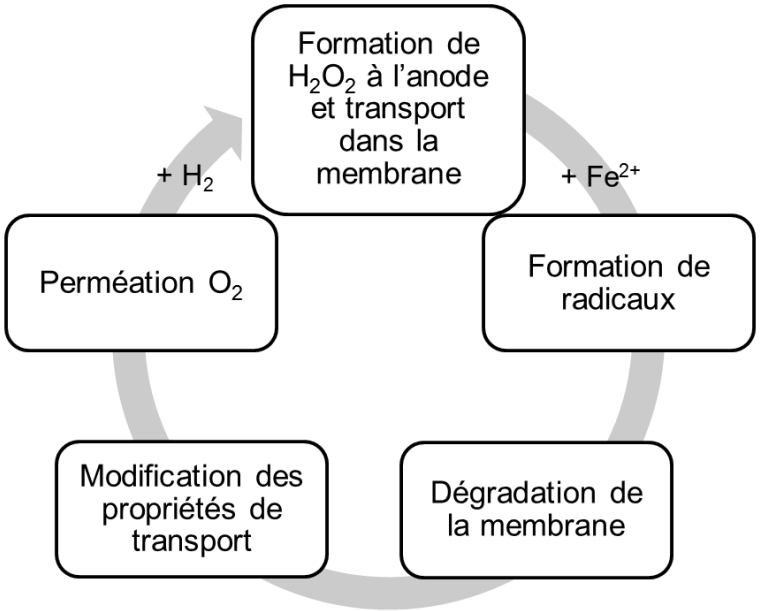

Chaque étape de la dégradation est modélisée et les conditions de frontières d'une étape sont

définies par l'état précédent dans la dégradation, comme l'indique le schéma précédent.

Dans ce modèle, nous considérons que la perméation de l'oxygène se fait dans l'eau de la membrane sous forme dissoute. La loi de Henry nous permet donc de définir des conditions de frontières pour la résolution de la seconde loi de Fick pour la diffusion et ainsi calculer en tout point la concentration en espèces dissoutes dans la membrane.

Dans notre modèle, la formation de peroxyde d'hydrogène n'est considérée qu'à l'anode, résultat d'une réaction chimique entre l'hydrogène et l'oxygène arrivant de la cathode. Le mécanisme supposé et les énergies d'activation associées pour cette réaction est issu de résultats de calculs *ab-initio* et permet un calcul approché des vitesses de réaction et la résolution des équations de conservation pour chaque espèces adsorbée intervenant dans la production de H_2O_2.

Lors du fonctionnement d'une cellule, il est possible que des cations Fe^{2+} soient produits, bien que leurs sources restent encore soumises à discussion. Une source possible est la corrosion des plaques bipolaires du côté cathodique. En présence de ces cations, le peroxyde d'hydrogène se décompose en radicaux (hydroxyle et peroxyle), espèces hautement réactives. L'ensemble de ces réactions entraînant la formation de radicaux à partir du peroxyde d'hydrogène et les ions fer entrent dans le cadre de la chimie dite « de Fenton » dont l'étude est notamment d'un grand intérêt dans la dépollution des eaux à forte demande chimique en oxygène dure. D'un point de vue cinétique, les différentes réactions mises en jeu dans la production de radicaux sont très bien documentées dans la littérature et les données cinétiques relatives à ces réactions sont donc directement utilisables [104-108].

Après la synthèse du Nafion®, il est possible que des groupements chimiques indésirables subsistent sur le squelette Téflon, notamment des groupements acide carboxylique. Ces groupes fonctionnels sont réactifs et ils peuvent être attaqués par les radicaux produits lors de la réaction de Fenton. Ceci constitue une initiation supposée de la dégradation chimique, comme présenté par Xie et Hayden [32]. Chaque étape de dégradation chimique du squelette le raccourcit d'un groupement $–CF_2–$ et translate ainsi la position du groupement –COOH. Lorsque le groupement acide carboxylique est proche d'une fonction éther liant une chaîne pendante au squelette, l'attaque radicalaire se fait sur cette fonction éther et on observe ainsi la scission d'une chaîne pendante. D'un point de vue modélisation, nous considérons que cette étape, ayant la probabilité d'occurrence la plus faible (un certain nombre d'étape de dégradation du squelette doit d'abord avoir lieu), est l'étape cinétiquement déterminante. Aussi nous exprimons la dégradation chimique complète de la membrane en fonction de cette étape de scission de chaînes pendantes et réduisons ainsi un mécanisme chimique complexe à une seule réaction.

Afin de relier la dégradation à la structure de la membrane, il est nécessaire de dériver une ex-

pression de la porosité et la tortuosité en fonction de la structure chimique de la membrane. Ceci est possible en faisant intervenir le concept de masse équivalente dans le calcul de la porosité et d'utiliser une approche classique pour relier la tortuosité à la porosité (Equations 2.28 **à** 2.32**). La masse équivalente étant en relation directe avec la quantité de groupement acide sulfonique dans la membrane, une évolution de cette quantité impactera directement sur la porosité.**

A partir de cette évolution et compte tenu de la correction de Bruggeman utilisée, il est possible de déterminer l'évolution de la résistance de la membrane au cours du fonctionnement de la pile et de l'avancée de la dégradation. Il est ainsi possible de déterminer l'évolution des chutes ohmiques dues à la résistance de la membrane et ainsi l'évolution de la tension de cellule.

2.1 Introduction

As mentioned in Section 1.2.1, it is a real challenge to model a PFSA membrane in an exact way. To get rid of the problem of an accurate description of membrane nanostructure, we consider the membrane as a microscopic system, but with underlying concepts still consistent with observations from the nano / microscale.

This chapter is divided into two main parts. First we will present the model used to describe the transport processes in the membrane and then the concepts and equations behind the chemical degradation model.

2.2 Modeling the transport processes in the membrane

2.2.1 Modeling of water management and transport

The proton conductivity of Nafion® is strongly dependent on the water content in the membrane. Indeed a fully hydrated membrane will exhibit excellent proton conductivity, but when water content decreases, the proton conductivity decreases. Thus water management in the membrane and in the whole cell is one of the key aspects leading to efficient fuel cell operation. Two coupled mechanisms are leading to dehydration of the membrane during fuel cell operation:

- electro-osmotic drag, pulling water from anode to cathode,
- a loss of water to fuel or air streams.

There is a considerable literature on the first mechanism, which focuses primarily on the water transport mechanism within the membrane, assuming either a diffusive mechanism or a convective one based upon phenomenological determined capillary pressure isotherms [109, 110]. In practical applications the problem of a dry anode is solved by the use of a thin membrane (25 to 50 µm), which facilitates the back diffusion of water and thus rehydrating the anode.

For a seek of simplicity we assume here:

a) isothermal conditions. The same temperature is set at both electrodes. No thermal exchanges are taken into account.

b) GDL and electrodes are considered as hydrophobic, so that liquid water can be carried out of the system.

c) If nothing else specified, the model is 1D across the thickness of the MEA+GDL. The membrane model includes the description of the transport phenomena along the *y* axis between cathode and anode.

d) Gases are considered as ideal gases and follow the ideal gas law.

e) PFSA membranes are superacid; the protons are entirely dissociated from the side chain and are free to move.

Figure 2.1 summarizes the cell structure we take into account.

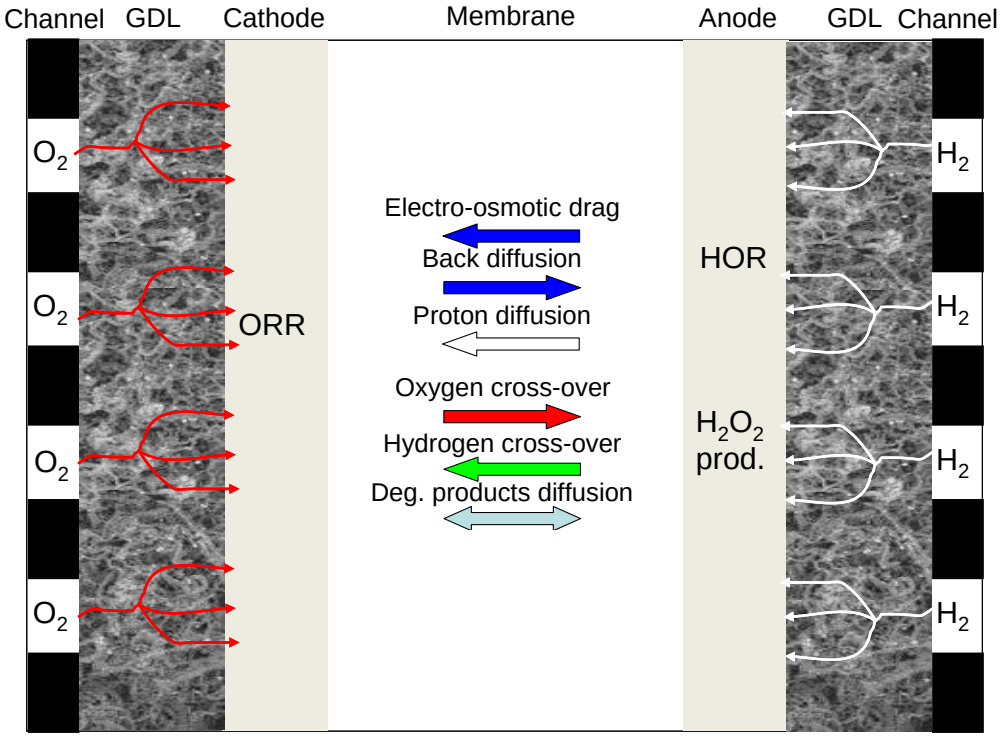

Figure 2.1: Schematic representation of the cell model

2.2.1.1 General model for water transport in the membrane

Water management is the key for a good operation of a PEMFC: A dry cell will exhibit low proton conductivity, a good humidified cell will have good performance and an excess of water will flood the electrodes and block the diffusion of hydrogen or air from the gas channel to the electrodes through the GDL. The first source of water in a PEMFC is the vapor mixed with the reactant gases. Vapor condensates into the ionomer present in the electrodes and humidifies it. At a given temperature, the amount of water liquid water is directly linked to the relative humidity of the gas. Concerning humidification in PEMFC technology, water content is usually expressed in term of water concentration but

as a local ratio between water and sulfonic acid groups in the membrane and is noted λ. By assuming equilibrium between the water into the gas phase and the ionomer, the water content within the ionomer is given through the equation

$$\lambda_{eq} = 0.3 + 10.8 \cdot a_{H_2O} - 16 \cdot a_{H_2O}^2 + 14.1 \cdot a_{H_2O}^3 \qquad 2.1$$

obtained from thermodynamical measurement of water adsorption in Nafion membrane.A graphical representation for Equation 2.1 is shown in Figure 2.2 [109].

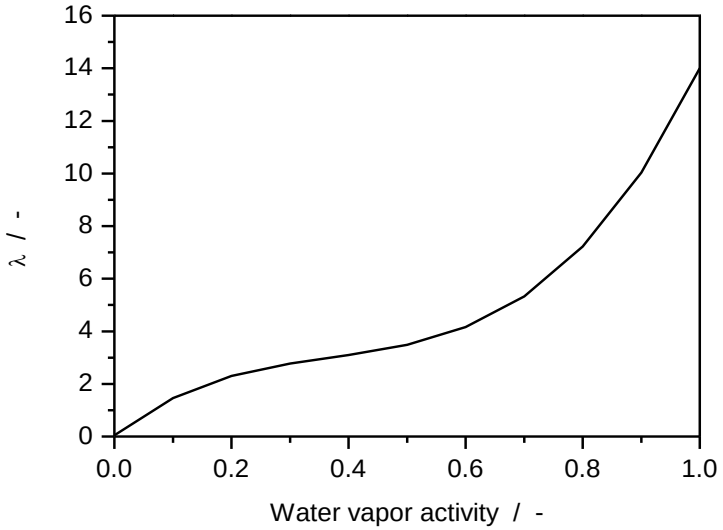

Figure 2.2: Simulated membrane water content versus water activity for a Nafion® 117 at 30 °C.

Considering the small thickness of the Nafion® layer in the electrodes, we consider no gradient of water content in this Nafion® and thus Equation 2.1 represents our boundary conditions at the interfaces anode / membrane and cathode / membrane. For a better understanding, we provide in Figure 2.3 a scheme of the electrode / membrane interface.

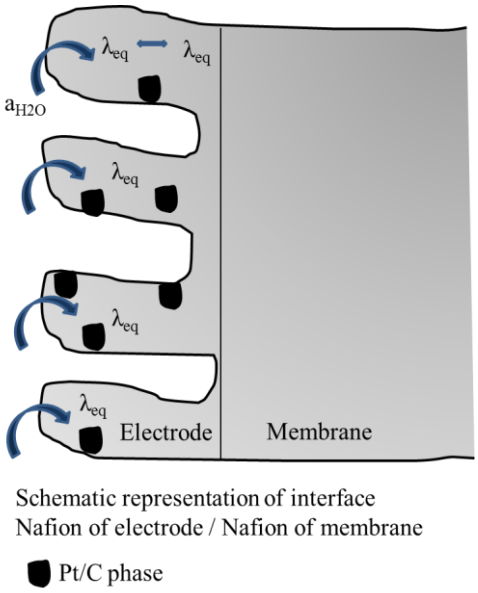

Figure 2.3: Schematic representation of the interface Electrode / Membrane (in gray color: ionomer).

The conservation equation of the water transport in a one dimensional coordinate within the membrane is given by the second Fickian law

$$\frac{\partial J_{H_2O}(y,t)}{\partial y} = -\frac{\partial c_{H_2O}(y,t)}{\partial t}, \qquad 2.2$$

where J_{H_2O} represents the local water flux and c_{H_2O} the local concentration of water. As λ represents the water content in the membrane, it is possible to link it to the water concentration in the membrane. Springer *et al*. derived such an expression, considering that the Nafion® swells with increasing water uptake, which we assume as well [109].

$$c_{H_2O} = \frac{\lambda \cdot \rho_{Nafion}}{(1+s\lambda)\cdot EW} \qquad 2.3$$

is the relation established by Springer, where ρ_{Nafion} is the density of dry Nafion®, s is the swelling coefficient and EW is the equivalent weight of the membrane. Equation 2.3 can be included into Equation 2.2. The simplification of the partial derivative leads to

$$\frac{\partial \lambda}{\partial t} = -\frac{(1+s\lambda)^2 \cdot EW}{\rho_{Nafion}} \cdot \frac{\partial J_{H_2O}(y,t)}{\partial y}. \qquad 2.4$$

We have now an explicit equation between the water content and the water flux in the membrane. The next point is to get an expression for the water flux in the membrane (constitutive equation). Different approaches are possible for that purpose. In our work, we use a semi-phenomenological one. When a

current load is applied to a PEMFC, protons are required at the cathode side for the ORR. As protons are always bound in complex cations in water (H_3O^+, $H_5O_2^+$, etc.), their motion from the anode to the cathode induces a motion of water as well. A so-called drag coefficient (noted t_{H_2O}) is introduced to link this water flux to proton flux from the anode. If we assume no accumulation of protons within the membrane, the Faraday's law can be written

$$J_{H^+} = \frac{i}{F}, \qquad 2.5$$

where *i* is the current density and *F* the Faraday's constant. From the last remark and Equation 2.5, we get the expression of the electro-osmotic contribution in the model. As this flux is oriented from the anode to the cathode, and our coordinate system is oriented from the cathode to the anode, we have to correct with a negative sign and thus,

$$J_{H_2O}^{EO} = -t_{H_2O} \cdot \frac{i}{F}, \qquad 2.6$$

which represents the electro-osmotic flux of water in the membrane. When no current is applied, no protons are required and obviously this flux is equal to zero.

At the cathode side, water is produced by the ORR as shown on Reaction 1.2. From this production and the electro-osmotic flux, the water balance in the membrane in not equilibrated anymore. This means that a water gradient appears along the membrane. The anode becomes dryer and the cathode trends to be flooded. This gradient causes a back flux of water from the cathode to the anode, in order to equilibrate the water balance in the membrane [111]. This can be mathematically expressed by the first Fickian law for the diffusion as

$$J_{H_2O}^{BD} = -D_{H_2O}^{Fick} \cdot \frac{\partial c_{H_2O}(y,t)}{\partial y}, \qquad 2.7$$

where D_{H_2O} is the diffusion coefficient of water in Nafion®.

Adding Equations 2.6 and 2.7, we get the expression of the net water flux within the membrane, as

$$J_{H_2O} = -t_{H_2O} \cdot \frac{i}{F} - D_{H_2O}^{Fick} \cdot \frac{\partial c_{H_2O}(y,t)}{\partial y}. \qquad 2.8$$

Combining Equation 2.8 in Equation 2.4, we can simulate water content profile along the membrane. To get a precise profile of the water content, it is however necessary to define precisely boundary conditions for the system. These boundaty conditions will be slightly different depending on the simulation environment which is used (see Section 3). Indeed, as MEMEPhys® includes an adapted version of the membrane model of DENIS, the model must return water flow at interfaces membrane / elec-

trodes as boundary for Equation 2.4. DENIS computes a water flux from the equivalent water content calculated from Equation 2.1 and the value of the water content in the membrane close to the interface.

At the anode / membrane interface, the inlet flow is driven by the difference in water content between the membrane at $y = L_{membrane}$ and the anode (where the water content is supposed to be equal to λ_{eq}). There is here no difference between MEMEPhys® and DENIS, as no water is produced in the anode. The same assumptions are made at the cathode / membrane interface (at $y = 0$). Moreover, water is produced in the cathode catalyst layer and this has to be then linked with the cathode model. In DENIS, the flux of produced water can be expressed through the Faraday's law, giving

$$J_{H_2O}^{prod} = \frac{i}{2 \cdot F}. \qquad 2.9$$

In MEMEPhys®, water is produced during the ORR by Reaction 3.14 (see Section 3.2.4.2). The rate of the reaction determines the flux of water production by the ORR.

As in a real fuel cell not all of the produced water at the cathode is released in the membrane but can leave the cell through the GDL and gas channel, we assume that the net water inlet due to the water production is equal to

$$J_{H_2O}^{prod,eff} = \alpha_{memb} \cdot J_{H_2O}^{prod}, \qquad 2.10$$

where α_{memb} is an arbitrary coefficient between 0 and 1, and which indicates the fraction of water produced during the ORR, which remains in the membrane.

We can now define the boundary conditions at the interfaces anode catalyst layer / membrane and membrane / cathode catalyst layer concerning the water flux. At the anode side, neglecting the evacuation of water through the GDL / gas channel pathway, the only water movement that has to be considered is the water dissolution for the gas phase into the ionomer contained into the anode. The corresponding water content is calculated through Equation 2.1. Assuming a uniformity of the water content in the anode catalyst layer, the water flux at the anode / membrane interface is driven by the gradient in the water content between the anode and the membrane at $y = L_{membrane}$. The boundary condition is then

$$J_{H_2O}^{anode/membrane} = \beta_{memb} \cdot \left(\lambda_{eq}^{anode} - \lambda^{y=L_{membrane}} \right). \qquad 2.11$$

At the cathode side, as previously said, water is produced. The flux of produced water can be quantified as shown on Equation 2.10. Considering the water flux between the gas channel and the ionomer in the cathode, we get a second boundary condition for the water flux,

$$J_{H_2O}^{cathode/membrane} = \beta_{memb} \cdot \left(\lambda_{eq}^{cathode} - \lambda^{y=0} \right) + \alpha_{memb} \cdot J_{H_2O}^{prod} \qquad 2.12$$

.

Thus from Equations 2.4, 2.8, 2.11 and 2.12, we can now determine the water profile distribution in the membrane.

2.2.1.2 Closing equations for the water transport

In order to perform water content profile simulations, some parameters are still needed to be explained. Equation 2.8 requires knowing two more parameters for the calculation: The diffusion coefficient of water and the drag coefficient of proton in water. The measurement of these two parameters is widely discussed in the literature and thus diverse approaches are available for their calculations. Motupally *et al*. presented a work on experimental and simulated data for the diffusion of water across Nafion® membranes as a function of the water content gradient [112]. It is shown in this paper that the Fickian diffusion coefficient can only be determined with a certain error, depending on the experimental setup. Such differences in the results lead to differences in the fitting equations for the diffusion coefficient of water. As the code is written in a modular way, it is possible for us to implement several equations in order to compare them. The first model is derived from water self-diffusion coefficient measurements, carried out by Zawodzinski *et al*. at 30 °C [113]. Motupally *et al*. extended the work to derive from this self-diffusion coefficient a Fickian diffusion coefficient. No electron transport is involved in the diffusion of water, thus the Fickian and self-diffusion coefficient of water are linked through the Darken factor

$$D_{H_2O}^{Fick} = D_{H_2O}^{self} \cdot \left[\frac{\partial \ln(a_{H_2O})}{\partial \ln(\lambda)} \right], \qquad 2.13$$

as demonstrated by Weppner and Huggins [111]. Using Equation 2.1, Motupally *et al*. rewrote Equation 2.13. By taking the reciprocal of the differential of Equation 2.1, they determined the Darken factor. It leads to the following equations for the Fickian diffusion coefficient of water, depending on the water content,

$$D_{H_2O}^{Fick} = 3.10 \cdot 10^{-7} \cdot \lambda \cdot \left(e^{0.28 \cdot \lambda} - 1\right) \exp\left(\frac{-2436}{T}\right), \text{ for} \qquad 2.14$$

$$0 \le \lambda \le 3,$$

$$D_{H_2O}^{Fick} = 4.17 \cdot 10^{-8} \cdot \lambda \cdot \left(161 e^{-\lambda} + 1\right) \exp\left(\frac{-2436}{T}\right), \text{ for} \qquad 2.15$$

$$3 \le \lambda \le 17.$$

The discontinuity observed in Equations 2.14 and 2.15 results from the functional dependence of the

Darken factor in terms of λ.

Nguyen and White report the Fickian diffusion coefficient in terms of the activity of water. Using Eq. 7, their expression can be converted to a function of λ to given, [114]

$$D_{H_2O}^{Fick} = 10^{-4} \cdot \left(1.76 \cdot 10^{-5} + 1.94 \cdot 10^{-4} \cdot \lambda\right) \exp\left(\frac{-2436}{T}\right) \qquad 2.16$$

As the measurements were carried out at 30 °C and in order to take into account the influence of temperature on the diffusion coefficient, the last equations are corrected with a factor exp(-2436/*T*), representing the enthalpy for Fickian diffusion [112].

A graphical representation of these two approaches is given on the Figure 2.4.

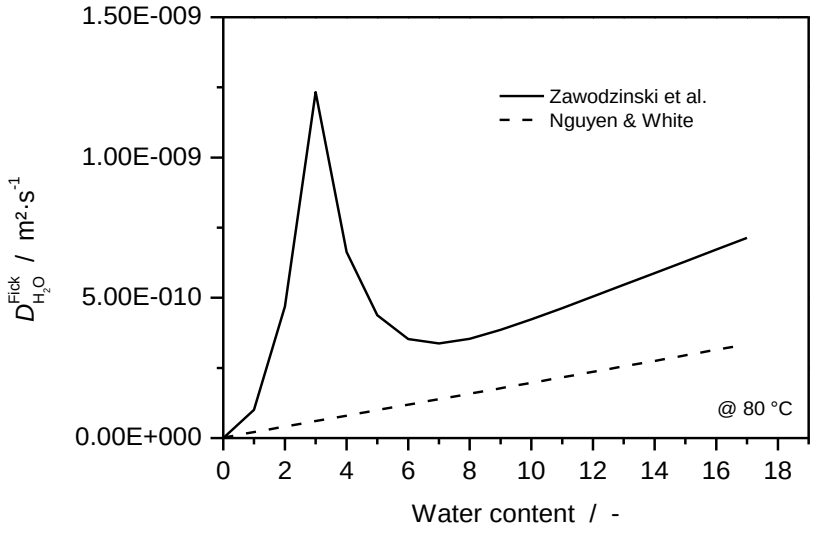

Figure 2.4: Fickian diffusion coefficient values calculated with Equations 2.14, 2.15 and 2.16.

We observe a strong difference depending on which approach is used for the diffusion coefficient of water. To make our choice for the approach we will use in our further simulations, we referred to the literature. Comparing the experimental setup used by Zawodzinski *et al.* and the one used by Nguyen and White, we considered the first one as the moste accurate and rigourous in the measurement and we used the approach of Zawodzinski in our further calculations.

The second parameter which has to be defined from experimental measurements is the electro-osmotic drag coefficient. Similar to Fickian diffusion coefficient, the experimental setup has an important influence on the measured values. Several research groups took a precise interest in their study [115-118]. Because of the uncertainty of the measurements, we did not want to favor one work or the other. Thus we focus on two of the main work concerning the determination of electro-osmotic drag coeffi-

cient in Nafion®.

The first one was published by Fuller and Newman [118]. Their set up was based on the generation of a water activity gradient between two sides of a membrane and measuring the potential difference which arises between two reversible H^+/H_2 electrodes on each side of the membrane.

Zawodzinski *et al*., inspired by the work of Fuller and Newman, improved the experimental set up of the former [116]. They found out that the electro-osmotic drag coefficient is independent of the water content and is equal to the unity as long as the membrane is in equilibrium with vapor (water under gaseous form). However in presence of liquid water, the maximum water uptake is increased from 14 to 22, which impacts on the value of the drag coefficient (so-called Schroeder's paradox)[119, 120]. The electro-osmotic drag coefficient is calculated by

$$t_{H_2O} = 1, \quad \text{for } 0 \le \lambda \le 14, \tag{2.17}$$

$$t_{H_2O} = 1.0 + 1.5\frac{\lambda - 14.0}{8}, \quad \text{for } 14 \le \lambda \le 22. \tag{2.18}$$

A later work for the determination of the electro-osmotic drag was reported by Ise, Kreuer and Meier [115]. They applied electrophoretic NMR (ENMR) for the first time, in order to measure electro-osmotic drag coefficients in polymer electrolyte membranes [121]. With this method, it is possible to determine t_{H_2O} as a function of water content (without the requirement of different pretreatments of the samples) and as a function of temperature. They measured the electro-osmotic drag coefficient at several water content from 5 to 20. We interpolate linearly their results to get our last equation for the calculation of the electro-osmotic drag,

$$t_{H_2O} = 4.6 \cdot 10^{-2} \cdot \lambda + 1.44 \tag{2.19}$$

As it can be seen in Figure 2.5, the value of the electro-osmotic drag strongly varies with water content and analytical methodology. Thus it is interesting to further compare them and see how their impact on the water management and cell performance is.

Both experimental setups provide drastically different results. To solve the problem of knowing which results are the more representable of reality, we agree with a work of Meier and Eigenberger about transport in Nafion® membrane [122]. They performed their own measurements of drag coefficient for water content in membrane beyond 12. The results were in quite good agreement with the results of Ise *et al.* and then they correlated their measurements with respect to the work of Zawodsinski when λ trends to zero. Thus the correlation for drag coefficient which is used in our model is

$$t_{H_2O} = 1 + 0.028\lambda + 0.0026\lambda^2 . \qquad 2.20$$

This section showed how difficult it is, to establish a transport model for water in a PEMFC. Even if the physics used to describe the motion of water molecule is only a sum of an EO drag and a Fickian diffusion, the determination of the transport parameters needed to solve this equation is far more complex and it is a real challenge for a modeler to decide, which measurement and approach could be the closest from the modeled system.

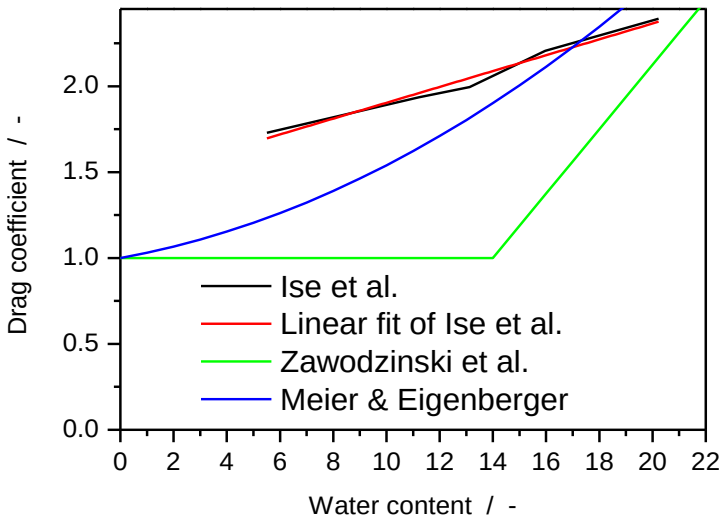

Figure 2.5: Evolution of the electro-osmotic drag coefficient with water content

2.2.1.3 Motion of species through the membrane

As previously mentioned in Section 1.1.2, one role of the membrane is the separation of gases between anode and cathode side, in order to prevent any short circuit. However, it has been experimentally shown (as mentioned in Section 1.3.3) that Nafion® cannot prevent the oxygen or hydrogen to permeate between the electrodes. It has been experimentally shown that the highest permeation of gases between the electrodes occurs when the membrane is humidified (for example, the oxygen cross-over is 10 time higher as for a dry membrane) [122]. Thus for a poorly hydrated membrane, the cross-over is low. This value will increase with rising water content. This part will deal with the mathematical formulation for the diffusion of non-charged hydrated species in the membrane.

As oxygen (resp. hydrogen) is present under gas form only at the cathode (resp. anode), a concentration gradient appears once the gases are dissolved in the ionomer phase. This concentration gradient induces an oxygen flux from the cathode to the anode and a hydrogen flux from the anode to the cathode. We first have to estimate the concentration of gases which effectively come into the ionomer at

the GDL / electrode interfaces. As reactants are under a gaseous form in the channel but react in dissolved form in the electrodes, we have to express the dissolution process into the ionomer. For that purpose we use the Henry's law, (at a constant temperature, the amount of a given gas that dissolves in a given type and volume of liquid is directly proportional to the partial pressure of that gas in equilibrium with that liquid)[40]. A mathematical formulation for this is

$$c_i^{\mathrm{liq}}(\mathrm{elec/pore}, t) = H_{0,i} \cdot \exp\left(-\frac{E_{\mathrm{act},i}^{\mathrm{Henry}}}{R \cdot T}\right) \cdot P_i(\mathrm{elec/pore}, t) \quad 2.21$$

,

where $H_{0,i}$ is the reference Henry's constant of species *i*, $E_{\mathrm{act},i}^{\mathrm{Henry}}$ its activation energy, $c_i^{\mathrm{liq}}(y,t)$ and $P_i(y,t)$ are the concentration and the partial pressure of species *i* in the ionomer phase at the interface pore / ionomer. A part of these dissolved gases will react, depending on the power demanded to the cell. The rest will be available to eventually diffuse along the membrane.

The motion of dissolved species in the membrane follows the conservation equation

$$\frac{\partial c_i^{\mathrm{liq}}(y,t)}{\partial t} = D_{0,i} \cdot \exp\left(-\frac{E_{\mathrm{act},i}^{\mathrm{Diff\ Nafion}}}{R \cdot T}\right) \cdot \frac{\partial^2 c_i^{\mathrm{liq}}(y,t)}{\partial y^2}, \quad 2.22$$

where $D_{0,i}$ is the diffusion coefficient in Nafion® of solved species *i* and $E_{\mathrm{act},i}^{\mathrm{Diff\ Nafion}}$ its activation energy. The boundary conditions of the Equation 2.22 are given by the Equation 2.21. However, as the concentration of dissolved oxygen at the anode and dissolved hydrogen at the cathode are zero when the cell starts, boundary conditions have to be time-dependent. It is not certain that the parasitic gas will pass from the ionomer phase to the gas phase in the electrode. To solve this problem we assume continuity in the ionomer at the membrane / electrode interface for parasitic gases and we set following continuity equations at the interfaces membrane / electrode:

$$c_{\mathrm{O_2}}^{\mathrm{liq}}(y = L_{\mathrm{membrane}}, t) = c_{\mathrm{O_2}}^{\mathrm{liq}}(y = \mathrm{anode}, t), \quad 2.23$$

$$c_{\mathrm{H_2}}^{\mathrm{liq}}(y = 0, t) = c_{\mathrm{H_2}}^{\mathrm{liq}}(y = \mathrm{cathode}, t). \quad 2.24$$

From Equation 2.21, linked to Equations 2.22, 2.23 and 2.24, we can now get the oxygen and hydrogen profile through the membrane.

This cross-over of oxygen from the cathode to the anode constitutes the first step in the chemical degradation of the membrane.

2.3 Modeling of chemical degradation of Nafion®

2.3.1 Chemical mechanism for Nafion® degradation

As shown in Section 1.2.2, the structure of Nafion® is very difficult to be defined and direct observations during operation of a PEMFC need a heavy and complicate experimental set up. This consideration of the FC as a black box complicates the understanding of chemical degradation processes. Therefore, experiments could give rise and quantify the presence of fluoride ions in the waste water of the cell, as well as perfluorosulfonic acid and complex fluorated organic molecules [16, 31, 98, 100, 123-125]. Assuming that in such experiment the eventual PTFE as additive in the GDL is stable, the only possible fluoride source is the PFSA membrane. That would imply that the membrane has been degraded. After the analysis of several literature sources, we concluded to a series of steps explaining the mechanism of the degradation, which is summed up in Figure 2.6.

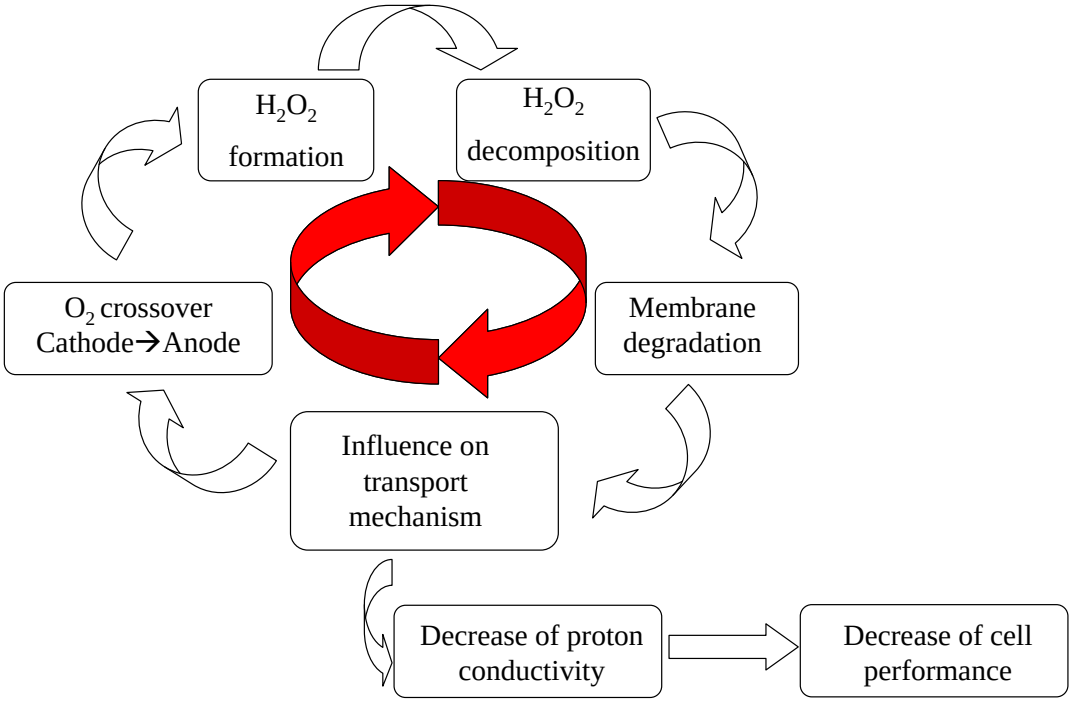

Figure 2.6: Schematic representation of the causes-consequences of the chemical degradation

Hydrogen peroxide and anodic reactions – In the previous part, we described the permeation of oxygen across the membrane from the cathode to the anode. It is to be noticed that at the same time, hydrogen can permeate from the anode to the cathode. As any further reaction of hydrogen at the cathode is not taken into account, we do not consider it in our degradation scheme. The second part which has to be regarded is the production of hydrogen peroxide from this oxygen. This reaction is linked to the electrochemical reactions occurring at the anode. Thus the description of this phenomenon is explained in Section 3.2.4.1.

Radical formation – Hydrogen peroxide is used as a radical initiator [126]. In presence of so-called Fenton's ions (Fe or Cu), hydrogen peroxide is decomposed into hydroxyl or peroxide radicals. Its action has already been discovered at the end of the 19th century by Henry Fenton and further studied by Haber and Weiss [21, 127]. The decomposition of hydrogen peroxide into radicals belongs to a broad field called Fenton chemistry. It includes a complete set of parallel reactions which have widely been studied and whose kinetics coefficients have been measured (see also Appendix B). To simplify our simulation and reduce the calculation time, we restrain all these reactions to five reactions which we assumed as the major ones to describe the generation and consumption of radicals in the membrane.

H_2O_2 decomposition – F1 (1st step) Reaction 2.1

$$H_2O_2 + Fe^{2+} + H^+ \rightleftharpoons Fe^{3+} + HO^{\cdot} + H_2O$$

H_2O_2 decomposition – F2 (2nd step) Reaction 2.2

$$H_2O_2 + Fe^{3+} \rightleftharpoons Fe^{2+} + HOO^{\cdot} + H^+$$

H_2O_2 decomposition – F3 (3rd step) Reaction 2.3

$$HOO^{\cdot} + Fe^{3+} \rightleftharpoons Fe^{2+} + O_2 + H^+$$

H_2O_2 decomposition – F4 (4th step) Reaction 2.4

$$H_2O_2 + HO^{\cdot} \rightleftharpoons H_2O + HOO^{\cdot}$$

H_2O_2 decomposition – F5 (5th step) Reaction 2.5

$$HO^{\cdot} + Fe^{2+} + H^+ \rightleftharpoons Fe^{3+} + H_2O$$

From Reaction 2.1 and Reaction 2.2, we see the catalytic action of iron ions. In acidic media (like in Nafion®), ferrous irons (Fe^{2+}) are oxidized by hydrogen peroxide into ferric irons (Fe^{3+}), hydroxyl radicals and water. Fe^{3+} can be then reduced back to Fe^{2+}, a peroxide radical and a proton by hydrogen peroxide (disproportionation of hydrogen peroxide – H_2O_2 is simultaneously reduced and oxidized).

The essential requirement for the decomposition of H_2O_2 is the presence of transition-metal ions in the system. As this system is closed, these ions can only come from an internal source. Pozio *et al*. showed that a PEMFC with stainless steel end-plates significantly degraded after 960 h of continuous operation. By changing these end-plates with iron-free one, a little degradation was observed after 1200 h [89]. This point makes the modeling so difficult. The oxidation of the end-plate is a high random phenomenon whose occurrence cannot be precisely known.

Membrane chemical degradation mechanisms –

As previously mentioned in Section 1.4, the chemical degradation mechanism is now well-known and accepted. Even if it is theoretically possible to implement in the model, the kinetics parameters related to each step would then have to be fitted if not known, which represents an irksome work compared to the relative validity of the results. For this reason, we need to reduce the mechanism. To the steps proposed by Xie and Hayden, it is also possible to imagine a degradation initiation via side chain cleavage, which they presented as well. They presented schematically a possible reaction pathway as shown in Figure 2.7 [32].

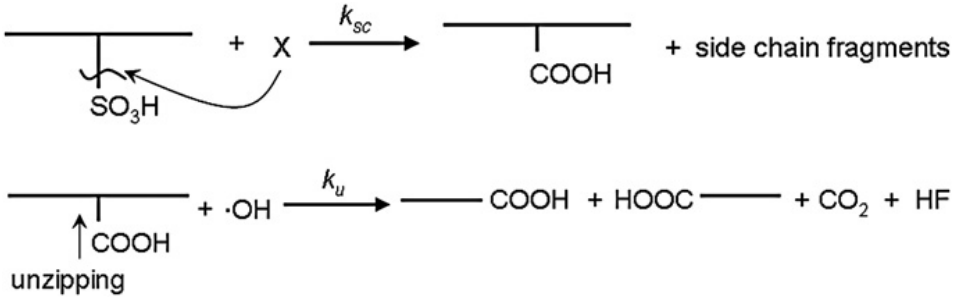

Figure 2.7: Degradation initiation via side chain cleavage [32].

However the degradation initiation via side chain cleavage is poorly understood both in terms of its occurrence under certain degradation conditions and the nature of the attacking species, if it does occur. In this work, we assume that such a degradation initiation is not occurring. The only possible degradation initiation comes from the attack of radical on weak end groups.

As displayed in Figure 1.24, after every degradation step the backbone loses one carbon atom. That implies that the backbone becomes shorter during the chemical degradation. That would mean, a loss of matter occurs, which has an impact on the transport properties of the membrane. Moreover, due to the side chain scission, the amount of sulfonic acid groups will decrease. As it has been explained in Section 1.2.1, these groups are responsible for the proton conduction along the membrane. Consequently, a decrease of the protonic conductivity ought to be expected.

To sum up qualitatively the effects of chemical degradation on PFSA membranes, we can say that the membrane will see its density decreasing, which induces increased gas permeation between the electrode, implying more hydrogen peroxide, more radicals and more degradation, impacting on the lifetime of the membrane. To this effect, it should be add the reduction of the protonic conductivity, and thus an increase of the ohmic losses in the membrane, as schematized in Figure 2.6.

Now that the physical and chemical concepts have been explained, the degradation has to be mathematically established.

The degradation mechanism is highly complex and for every step, kinetic parameters would be need-

ed. Such an approach would be very time consuming and approximate, as we would have fitted every kinetic parameters we used. For this reason, we have to find a way to simplify the system. As mentioned in the previous chapter, the degradation is initiated by a radical attack on weak end group, and during the degradation, it occurs that a side chain are cut from the backbone every time the backbone degradation step is reached a certain time. Thus we assume in our model that regarding the whole chemical degradation, the side chain unzipping is the rate-determining step. Thus we express the kinetic of the back bone degradation as a linear function of the side chain degradation.

2.3.2 Mathematical formulation of the chemical degradation

The first step of the modeling of the chemical degradation is to determine the evolution and the spatial distribution of the species involved during the degradation. For that we apply first the law of mass action (Equation 2.25) for the expression of reaction rates,

$$v_i(y,t) = k_i \cdot \prod_{j=\text{species involved in reaction } i} \left(c_j^{\text{membrane}}(y,t)\right)^{\nu_{i,j}} \qquad 2.25$$

,

where $r_i(y,t)$ is the reaction rate of the reaction i at time t and at the coordinate y in the membrane, k_i the reaction rate constant of the reaction i, $c_j^{\text{membrane}}(y,t)$ the concentration of the species j at time t and at the coordinate y in the membrane, and $\nu_{i,j}$ is the reaction order relate to species j in reaction i. The reactions considered by the index i are the step of the Fenton chemistry (Reaction 2.1 to Reaction 2.5) and the degradation step related to the side chain unzipping. The temporal evolution of the concentration in the membrane is then given by solving an equation system constituted by the mass balance equation of each species (Equation 2.26)

$$\frac{\partial c_j^{\text{membrane}}(y,t)}{\partial t} = \dot{S}_j + \sum_{i=\text{reaction involving species } j} \delta_{i,j} \cdot v_i(y,t) \qquad 2.26$$

,

where $\dot{S}_j$ is the production term of species j used for example in the case of hydrogen peroxide, whose concentration is given by the electrochemistry at the anode and ferrous ions, whose production is arbitrary set by the user of the model (see Section 4.2.3.4).

From Equations 2.25 and 2.26, it is possible to determine the evolution of species concentration along the membrane. This will be the starting point for the rest of the modeling. From the evolution of the concentration, we will be able to define the evolution of structural parameters of the membrane (poros-

ity and tortuosity), which will impact on the performance of the cell.

As mentioned in Section 1.3.5, fluoride ion is a degradation product which is easy to measure and follow over time with simple analytical methods (for example ionic chromatography or with a fluoride sensitive sensor). As we consider in our approach only the kinetic of the side chain scission, we need a way to however estimate the global amount of released fluoride. If we assume that the back bone is degraded on a linear way, it will occur that the carboxylic acid group of the backbone is located on a α-position of a side chain. That would imply that the steric factor becomes negligible and it is possible for the radical to attack the ether function of the PFSA membrane. Considering this, we assume that the rate determining step of the membrane degradation is the side chain scission, and thus, the kinetic of release of fluoride ions is driven by the velocity of side chain scission. When the scission of a side chain occur, that mean that roughly 15 $–CF_2–$ and one –CF– groups of the back bone have been cut, thus 31 fluoride atoms are released into the membrane through the backbone. As a side chain contains 10 fluoride atoms, we come to an estimated ratio side chain to fluoride of 1 to 41 in Nafion®. In term of mass balance equation, it comes

$$\frac{\partial c_{\text{sidechain}}^{\text{membrane}}(y,t)}{\partial t} = 41 \cdot \frac{\partial c_{\text{Fluoride}}^{\text{membrane}}(y,t)}{\partial t} . \qquad 2.27$$

Evolution of structural parameters – In the following parts and in the rest of this work, we will speak about the porosity ε of the membrane even if this concept does not really suit to a PFSA membrane. Indeed no porous structure can be identified. This porosity refers rather to the volume fraction of water. We can then write

$$\varepsilon = \frac{\lambda}{\lambda + r} , \qquad 2.28$$

where $r = \overline{V_{\text{NAFION}}} / \overline{V_{\text{H}_2\text{O}}}$ is the ration of partial molar volume of membrane to that of water.

The partial molar volume of membrane can be expressed as a function of the equivalent weight of the membrane *EW* and the density of the dry polymer ρ_{dry} as $\overline{V_{\text{NAFION}}} = EW / \rho_{\text{dry}}$. As the equivalent weight can be expressed as

$$EW = \rho_{\text{dry}} / \left((1 + s \cdot \lambda)^3 \cdot c_{\text{sidechain}} \right), \qquad 2.29$$

where *s* is the swelling coefficient of the membrane (factor showing the variation of the membrane volume by water uptake), and the side chain concentration depends on the position in the membrane and time (when degradation occurs), we can simplify the expression for the partial molar volume of the membrane in

$$\overline{V_{\mathrm{NAFION}}(y,t)} = \left((1+s\cdot\lambda)^3 \cdot c_{\mathrm{sidechain}}(y,t)\right)^{-1}. \qquad 2.30$$

Tortuosity and porosity are two parameters whose evolutions are dependent on each other: when the porosity of the cell decreases, the tortuosity will increase. Several expressions for tortuosity have been proposed for porous media and membranes based on the statistical analysis of diffusion coefficients, free volume theory and power series expansion etc. [128-130]. These models provide similar values of tortuosity factors for Nafion® for the sorption range of interest. Here, we adopt Prager's model which has been previously used for Nafion® by Koter and by Choi *et al* [130, 131]

$$\tau = \frac{2\cdot(1-\varepsilon) + 2\cdot\varepsilon\cdot\ln\varepsilon - 0.5\cdot\varepsilon\cdot(\ln\varepsilon)^2}{\varepsilon\cdot(1-\varepsilon) + \varepsilon^2\cdot\ln\varepsilon}. \qquad 2.31$$

We see in Figure 2.8 that with Prager's model, the tortuosity increases to values which are unrealistic when the porosity trend to zero. To check the validity of this approach, we compared the results we obtained with a more common equation used to describe the relative evolution of porosity and tortuosity,

$$\tau = \frac{1}{\sqrt{\varepsilon}}. \qquad 2.32$$

From a porosity of 0.2, results of Prager's model are in a range which is more consistent with the value of a tortuosity. From a porosity of about 0.4, we see that both approaches have comparable results. After each simulation, we controlled these two parameters. The porosity never decreases under 0.2; therefore, we kept Equation 2.31 in our simulations.

From Equations 2.28, 2.30 and 2.31, it is now possible to determine the structural evolution of the membrane. It ought now to link these evolutions with their impact on the transport and the performance of the cell. A comparison of the relative evolution is plotted in Figure 2.8. As we can see, a high porosity in the membrane will induce a low tortuosity, which means degraded transport properties.

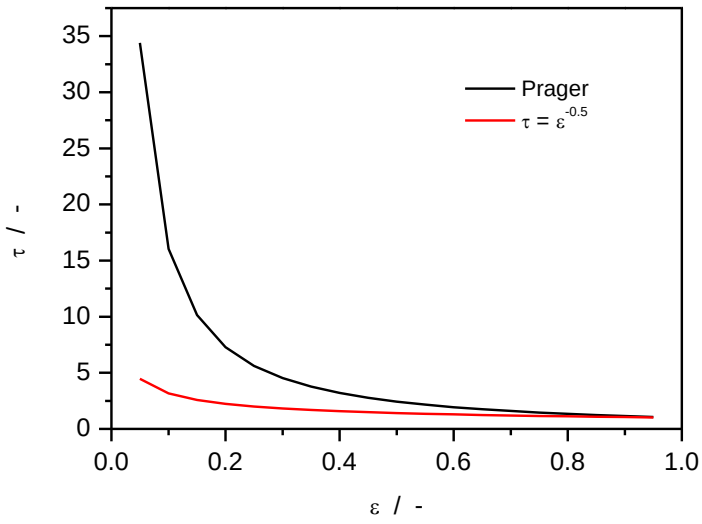

Figure 2.8: Evolution of the tortuosity with porosity

Evolution of the transport properties and performance – If we consider diffusion processes in porous media, it is obvious that the diffusion coefficient will depend on the pathways available for the diffusion. This assumption is accurate for solid porous media (like the GDL in a PEMFC), but it can be applied to a PFSA membrane when assuming it as a porous media. In order to take into account this influence of the material structure, we correct the transport parameter through a function depending on tortuosity and porosity of the media, so-called Bruggeman correction. Several empirical functions are used in the literature. As previously mentioned, the code is written on a very modular way. As it is difficult to prefer one function to another, we regard two possibilities for the Bruggeman correction. We note the Bruggeman correction factor ξ

$$\xi(y,t) = \frac{\varepsilon(y,t)}{\tau(y,t)}, \qquad 2.33$$

$$\xi(y,t) = \varepsilon(y,t)^{\tau(y,t)}, \qquad 2.34$$

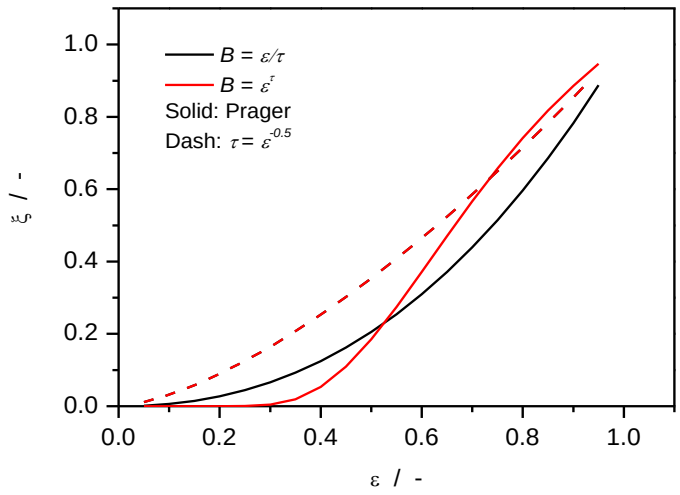

Figure 2.9: Evolution of Bruggeman correction factor with porosity

Figure 2.9 shows the value of the Bruggeman factor depending on which equation is used for its calculation and which assumption was made to calculate the tortuosity factor. We see that the shape is similar in every case. If we use the assumption of Equation 2.32, we notice no difference. A quick calculation shows that under assumption of Equation 2.32, we have $\varepsilon(y,t)/\tau(y,t) = \varepsilon(y,t)^{\tau(y,t)}$. For the other assumption for the tortuosity calculation, we notice slight difference in the evolution depending how we calculate the correction factor but when the porosity trends to 1, this factor trends to converge to the same value. As no really significant difference is however seeable, we decided to keep the approach used by Choi *et al* in their paper, that is to say Equations 2.31 and 2.33 for the calculation of the Bruggeman correction factor.

From Equation 2.33 and 2.34, it is now possible to express effective diffusion coefficients $D^{\text{eff}} = \xi \cdot D_0$ for the species in the membrane and improve Equation 2.22 as

$$\frac{\partial c_i^{\text{liq}}(y,t)}{\partial t} = \xi(y,t) \cdot D_{0,i} \cdot \exp\left(-\frac{E_{\text{act},i}^{\text{Diff Nafion}}}{R \cdot T}\right) \cdot \frac{\partial^2 c_i^{\text{liq}}(y,t)}{\partial y^2} \qquad 2.35$$

2.3.3 Proton transport in the membrane

The last transport which takes place in the membrane and has to be regarded is the related to the transport of proton. Of course protons are present in the membrane as counter ions of the sulfonic acid groups but are produced during the ORR and consumed during the ORR. A motion of proton is thus needed. This motion is usually modeled by the proton conductivity in the membrane. In the literature, several approaches are available. We selected two, whose fundaments are completely different: one phenomenological and one purely physical.

The first one, published by Meier and Eigenberger, is the empirical one, based on the work of Zawodzinski *et al*. and completed with their own results, where we add a Bruggeman correction [113, 122].

$$\sigma_{H^+} = \frac{\varepsilon}{\tau} \cdot (0.46 \cdot \lambda - 0.25) \cdot \exp\left(-1190\left(\frac{1}{T} - \frac{1}{298.15}\right)\right) \qquad 2.36$$

,

where σ_{H^+} is the proton conductivity.

On the contrary, Choi *et al*. used only physical principle to describe the proton conductivity [131]. They split the transport of water into three contributions. As displayed in Figure 2.10, the proton conduction can occur either through a surface diffusion mechanism occurring close to the pore wall or under low water activity in a layer of around 1 nm from the pore wall (grey arrows) or a bulk diffusion mechanism prevailing in the central region of the pore or under high water activity condition. In the bulk, proton diffusion is predominantly via the Grotthuss mechanism (dotted arrows), but H_3O^+ ions also undergos traditional mass diffusion (black arrows).

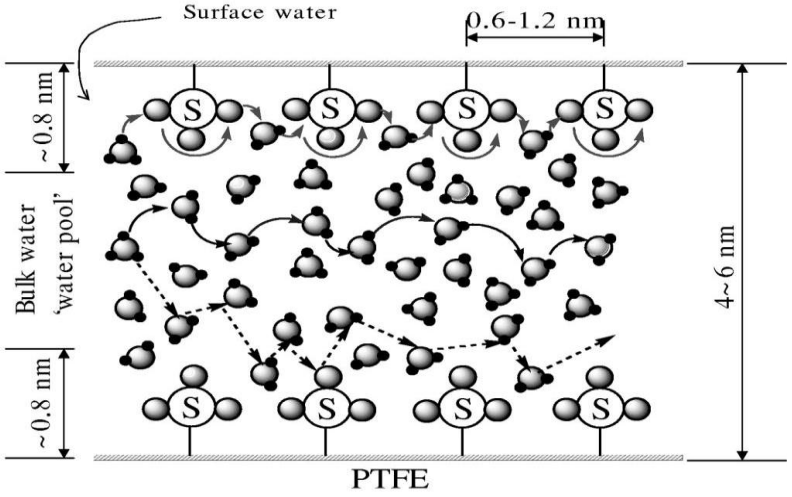

Figure 2.10: Simplified picture of structure and proton transfer in Nafion® in fully hydrated state [131].

Combining Nernst-Einstein equation with a Bruggeman correction, we obtain

$$\sigma_{H^+}(y,t) = \frac{\varepsilon}{\tau} \cdot \left[\frac{F^2}{RT}\left(D^{\Sigma}_{H^+} \cdot c^{\Sigma}_{H^+} + D^{G}_{H^+} \cdot c_{H^+} + D^{m}_{H^+} \cdot c_{H^+}\right)\right] \qquad 2.37$$

,

where subscript Σ refers to surface; *G* to Grotthuss and *m* to mass diffusion. Choi explained each dif-

fusion coefficient using Einstein-Smoluchowski equation and obtained

$$D_{H^+}^{\Sigma} = \frac{k_B \cdot T}{h} \cdot \frac{l_\Sigma}{4} \cdot \exp\left[- \frac{e^2}{4 \cdot \pi \cdot \varepsilon_0 \cdot \varepsilon_r \cdot k_B \cdot T} \cdot \left(\frac{l_\Sigma}{(R_f + R_i + l_\Sigma)(R_f + R_i)} \right) \right], \quad 2.38$$

$$D_{H^+}^{G} = \frac{l_G^2 \cdot \mu_W \cdot (z_{H^+} \cdot e)}{192 \cdot \pi^2 \cdot \eta \cdot \varepsilon_r \cdot \varepsilon_0 \cdot R^3 \cdot \delta^2} \Bigg/ \ln\left(\frac{\tan\left(\theta_I / 2\right)}{\tan\left(\theta_F / 2\right)} \right), \quad 2.39$$

$$D_{H^+}^{W} = \frac{k_B \cdot T}{6 \cdot \pi \cdot \eta \cdot R_i}, \quad 2.40$$

the parameters related to each equation and their value are given in Symbols parts [131].

For comprehension purpose, how all those parameters can be used in the calculation of diffusion coefficients of protons, some figures can be used to illustrate the theory.

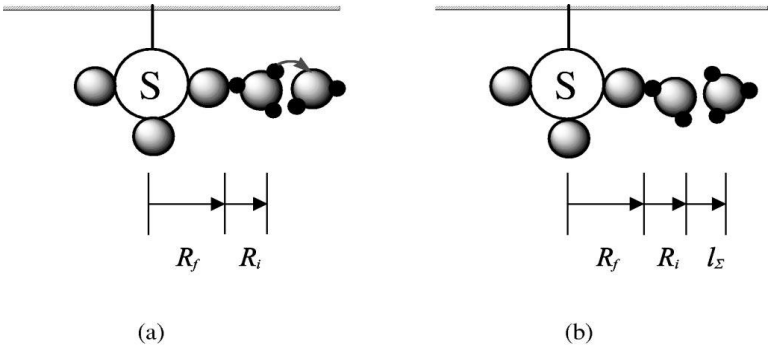

Figure 2.11: A schematic representation of the first proton hopping at the surface of Nafion® (a) before and (b) after the first jump [131].

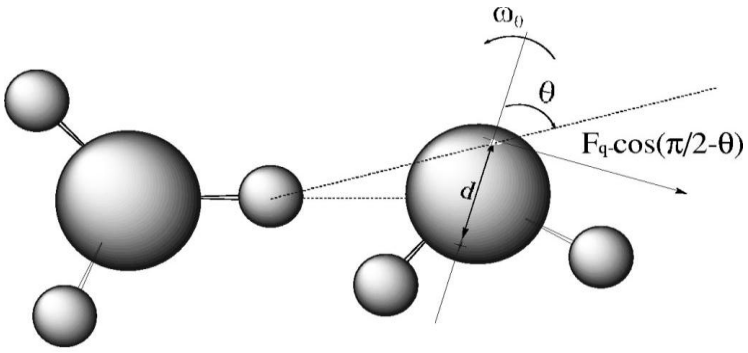

Figure 2.12: The hydrodynamic model of Grotthuss diffusion mechanism of protons in the pore bulk [131].

Figure 2.11 shows schematically the proton transfer in Nafion® from the sulfonate group of a side chain to a close located water molecule (state (a) to state (b)). Then the proton will hop from a "free" hydronium ion to a water molecule bond to a side chain, making the surface diffusion possible.

Figure 2.12 present the geometrical requirement for a proton to be able, in the bulk water area of a channel, to hop from a hydronium ion to a water molecule. As the water is omnipresent in the membrane at a sufficient state of humidification and considering the entropy of the system high enough, the probability that one water molecule is ideally located compared to a hydronium ion is high and make the contribution of this diffusion as major in good humidified membrane. The *en masse* expression is the expression of the Stockes-Einstein equation considering hydronium ion as a diffusing entity a continuum of water.

Now we have all relationship for the calculation of proton conductivity in Equation 2.37 except the one for the concentration of proton in at the surface of the pore and in the bulk water.

Because of the electroneutrality principle applied to the membrane, the concentration of hydronium ions is equal to the one of sulfonic acid groups. But its distribution has to be cleared. Choi used an approach in which the dissociated acid sites with up to two water molecules are assumed to remain close to the surface and are designated as surface water, while those with more than two water molecules are assumed to move away from the surface into the pore bulk, based on the hypothesis that sulfonic acid groups are sufficiently strong acids so that ion pairs $SO_3^-H_3O^+$ or $SO_3^-H_5O_2^+$ are formed [131]. It comes out the following expressions for the proton distribution, depending on water content and relative humidity (activity of water vapor)

$$c_{H^+}^{\Sigma} = \frac{1}{\lambda \cdot \overline{V}_{H_2O}} \cdot \frac{K_1 \cdot a \cdot (1-a) \cdot (1+K_2 \cdot a)}{(1-a) \cdot (1+K_1 \cdot a) + K_1 \cdot K_2 \cdot a^2 \cdot (1-a^{v-1})}, \quad 2.41$$

$$c_{H^+} = \frac{1}{\lambda \cdot \overline{V}_{H_2O}} \cdot \frac{K_1 \cdot K_2 \cdot a^3 \cdot (1-a^{v-2})}{(1-a) \cdot (1+K_1 \cdot a) + K_1 \cdot K_2 \cdot a^2 \cdot (1-a^{v-1})}, \quad 2.42$$

where K_1 and K_2 are the equilibrium constants for proton dissociation in the membrane, *a* the activity of water, $\overline{V}_{H_2O}$ the molar volume of water and v the amount of water molecules surrounding one hydronium. From Equations 2.38 to 2.42, it is now possible to calculate the proton conductivity through Equation 2.37.

The use of this local conductivity is then used by DENIS in the calculation of the ionic potential across the membrane through the solving of Laplace equation (see Section 3.3.2).

However, for MEMEPhys®, a local value of the proton conductivity in the membrane is not used. The transport parameter which is effectively used in the potential calculation is the membrane resistance.

So it is needed to compute equivalent proton conductivity for the whole membrane to be able to compute the global resistance of the membrane. In a general 1D case, we have to consider a series circuit with conductance. The resulting equivalent conductance will be

$$\left(\sigma_{\text{eq}}(t)\right)^{-1} = \frac{1}{L_{\text{membrane}}} \cdot \int_{y=0}^{y=L_{\text{membrane}}} \frac{dy}{\sigma_{H^+}(y,t)} . \qquad 2.43$$

From the equivalent proton conductivity, we calculate the membrane resistance as

$$R(t) = \frac{E_{\text{membrane}}}{S_{\text{electrode}} \cdot \sigma_{\text{eq}}(t)} . \qquad 2.44$$

It is now possible to evaluate the evolution of the membrane ohmic losses $\eta_{\text{ohm}}(t)=R(t)\cdot I$ and thus evaluate the impact of the chemical degradation of the membrane on the cell performance.

2.4 Summary

We presented in this chapter first a transport model for water and dissolved species in the membrane of a PEMFC. Water management is one of the key of the operating of the cell, as water is involved among other in proton conduction and species diffusion. This model is based on classical work published in the literature, extended with a permeation model for dissolved gases in the membrane. The approach allows then a feedback between membrane degradation and membrane micro-structure, through the calculation of the evolution of the porosity and the tortuosity.

CHAPTER 3

Coupling of the membrane model with the cell models

La section précédente présentait le modèle de membrane incluant la dégradation chimique. Il convient maintenant de coupler ce modèle avec des modèles d'anode et de cathode afin de simuler le fonctionnement complet d'une PAC. Le modèle de membrane a été développé conjointement entre le centre aérospatial allemand (DLR) à Stuttgart et le Commissariat à l'Energie Atomique et Energies Alternatives (CEA) à Grenoble. Les groupes de travail au sein desquels le travail a été effectué, bien qu'utilisant à terme le même modèle de membrane, ont développé séparément leurs propres modèles d'électrodes.

Pour cette raison, notre modèle de membrane a été codé de sorte à être utilisable dans les deux environnements de simulation, le modèle CEA étant développé sous MATLAB/Simulink, le modèle DLR en langage C. Cet aspect a été traité grâce à la souplesse de Simulink, qui peut intégrer dans ces modules des fonctions codées en C. Ainsi un modèle de membrane codé en langage C permet à la fois d'être intégré directement dans les environnements développés au CEA et au DLR.

Au CEA, le modèle d'électrodes développé, appelé MEMEPhys® (Modèle Electrochimique Multi-Echelle Physique) se base sur une approche multiphysique et multiéchelle des phénomènes se déroulant dans les électrodes d'une PAC. Ce modèle se base sur une description précise de la double couche électrochimique se formant à la surface du catalyseur. Cette approche permet un calcul de la tension de cellule à partir du courant demandé à la cellule. Une description complète du modèle ne fait pas l'objet de ce résumé, mais celui-ci est disponible dans de nombreuses sources dans la littérature [132-134]. Le couplage du modèle de membrane au modèle d'électrodes se fait via la calcul de la résistance de la membrane.

Le modèle développé au DLR, nommé DENIS (Detailed Electrochimistry and Numerical Impedance Simulation), fut à l'origine conçu pour la simulation du fonctionnement de PAC de type SOFC. Ce modèle a été maintes fois éprouvé et validé dans la littérature [135, 136]. Le principe a été transposé au PEMFC et un modèle de performance a été établi et validé [137]. Cet environ-

nement a connu ces dernières années d'importantes modifications, notamment au niveau de l'approche utilisée dans les calculs électrochimiques. Le code utilise l'environnement CANTERA pour la définition des phases dans les électrodes et le calcul des potentiels et compositions des différentes phases. Une description complète de l'approche physique utilisée dans CANTERA est détaillée dans sa documentation [138].

Ces deux modèles ont chacun leurs points forts et faiblesse dans l'approche. Afin d'effectuer une comparaison des deux approches physiques mises en jeu dans les modèles, le modèle de membrane est intégré dans chaque environnement. Cependant sur la durée de cette thèse, la membrane n'a pu être couplée que dans l'environnement MEMEPhys®. Un couplage complet avec DENIS fait l'objet de projets en cours.

3.1 Why cell models?

As said at the beginning of Chapter 0, the membrane model aims to be integrated into two different simulation packages. Both have their own specificities, in particular on the level of detail of the physics used to describe the electrochemical and transport phenomena in the PEMFC components.

3.1.1 DENIS

DENIS (detailed electrochemistry and numerical impedance simulation) is a C code that is developed since 2003 within the group of Wolfgang Bessler successively at the Interdisciplinary Center for Scientific Calculation (IWR) of the University of Heidelberg and at the Institute for Technical Thermodynamics at the German Aerospace Center in Stuttgart. Simulations are carried out, based on conveniently editable text input files for all modeling and simulation parameters. The software allows the automated generation of current/voltage curves and electrochemical impedance spectra. Finite-volume discretization techniques are used to convert the partial differential equations (PDE) occurring in the transport models to a differential algebraic equation (DAE) system. Discretization is needed for the two dimensions (x: along the gas channel, y: through MEA). The 1D+1D mesh can be set arbitrarily, i.e. variable numbers and sizes of discretization compartments, so that a dense number of grid points can be used for regions of strong gradients. Based on text input files of chemical reaction mechanisms (pre-exponential factors, activation energies, thermodynamic properties), chemical source terms are calculated using algorithms from the CANTERA software package. CANTERA is also used to calculate gas-phase transport properties [139]. For numerical integration of the DAE system, the fully implicit solver LIMEX is implemented [140, 141] . The implementation is carried out in a flexible and modular way. Different sub-models can be coupled in user-defined ways. The software package can be used for detailed or global chemistry, for 0D, 1D, quasi-2D or quasi-3D simulations where arbitrary transport models can be coupled, for dual-chamber and single-chamber setups, for full-cell and reference electrode setups.

3.1.2 MEMEPhys®

The group headed by Alejandro Franco develops since 2002 at CEA-LITEN a transient, multi-scale and multiphysics single PEMFC model (called MEMEPhys® –French abbreviation for Multiscale electrochemical-physical model) accounting for the coupling between self-consistent physical mechanistic

descriptions of the physicochemical phenomena (e.g., reactants, water and charge transport and detailed electrochemistry, materials aging mechanisms) taking place in the electrodes, the PEM, the GDLs and the channels [5, 133, 134]. This model was designed to connect atomistic phenomena (elementary kinetic processes) with macroscopic electrochemical observables (e.g. polarization curves, Electrochemical Impedance Spectra, cyclic voltammetry, cell potential decrease over time…) with reasonable computational effort by using *ab initio* and surface science databases [3-5, 133, 134]. Such a model is a multi-scale one in the sense that it is made of a set of interconnected sub-models describing the phenomena occurring at different scales in the PEMFC. However, this description remains at the continuum level in the sense that it is based on irreversible thermodynamics concepts particularly adapted for the description of non-equilibrium physicochemical systems, as they are extensively used in chemical engineering: use of conservation laws coupled to closure equations (e.g. flux expressions, chemical rate models, thermodynamic models).

To the best of our knowledge, this model is the unique in published literature allowing describing the feedback between the instantaneous performance and the intrinsic MEA aging processes: that means that the model takes into account, at each simulated time step, both the effect of performance on aging and the effect of aging on performance [3-5, 8]. The model is constituted by a hybridation between a set of C modules and a Matlab/Simulink environment. It allows discretizing the cell into 1D (across the cell thickness) + 1D (along the channels).

3.1.3 Membrane simulation code

DENIS and MEMEPhys® do not have anything in common concerning the implementation. As we wanted to develop a generic module to limit the programming work and allow a direct comparison of the physics used in electrodes with both their advantages and drawbacks, we needed a solution so that the membrane model can be used by both simulation environments with minimum adaptation efforts.

Matlab proposes in its Simulink package the possibility to execute functions written in C through the so-called S-functions. An S-function is a computer language description of a Simulink block written in MATLAB®, C, C++, or FORTRAN. As DENIS was developed in C as well, the use of S-Function is an elegant solution to use as a module in MEMEPhys®. The challenge is to provide to Matlab the tools needed by the membrane module (called polymermembrane.c) to work correctly. In the membrane module, arrays are defined and in DENIS, the allocation of array is done in an external module (called memory.c). As polymermembrane.c is developed for the solving of DAE, mathematical functions are required. These are contained in DENIS in a module called mathlib.c. For all other functions which are used in polymermembrane.c but which refer to another module (for example to the module responsible for thermal calculation etc.), the needed function are put into a specific module.

DENIS works with specific input files, where all the parameters (diffusion coefficients, discretization of the membrane, physical and chemical parameters for the cell etc.) are entered. As it is not possible to use it directly with Simulink, we had to create a new module integrating all the parameters which are used by polymermembrane.c.

Last polymermembrane.c needs and returns information from and to the Simulink model. These are the inputs and outputs of the S-Function. A specific module ensures the communication between Simulink and the S-Function.

A schematically representation of the architecture of our S-Function is displayed in

Figure 3.1.

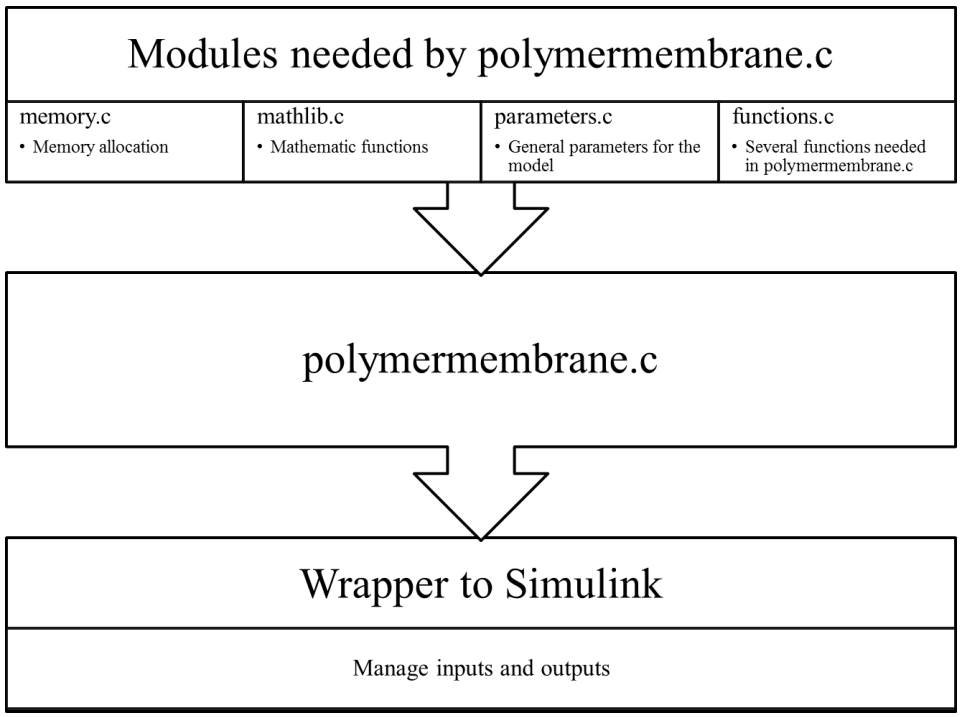

Figure 3.1: Structure of the S-Function implemented in Simulink to run our membrane module

3.2 Physics underlying the MEMEPhys® model

3.2.1 Presentation of the model

Since 2002, Franco and his successive collaborators have developed a dynamic numerical multiscale model of a single PEMFC, based on non-equilibrium thermodynamics and electrodynamics, as presented in Figure 3.2 [3, 4, 85, 133, 134]. The model calculates, dynamically, the potential difference between the two electrodes in response to a time dependent current demand. The major work concerning the electrode models were published by Franco et al. since 2005 where they presented the under-

lying physics in the description of the cell [3, 4, 85, 132-134]. This will be the main basis for the next chapter. We will first present the structure of the electrode models with their assumptions. Then how the membrane model can be included and coupled to the electrodes model.

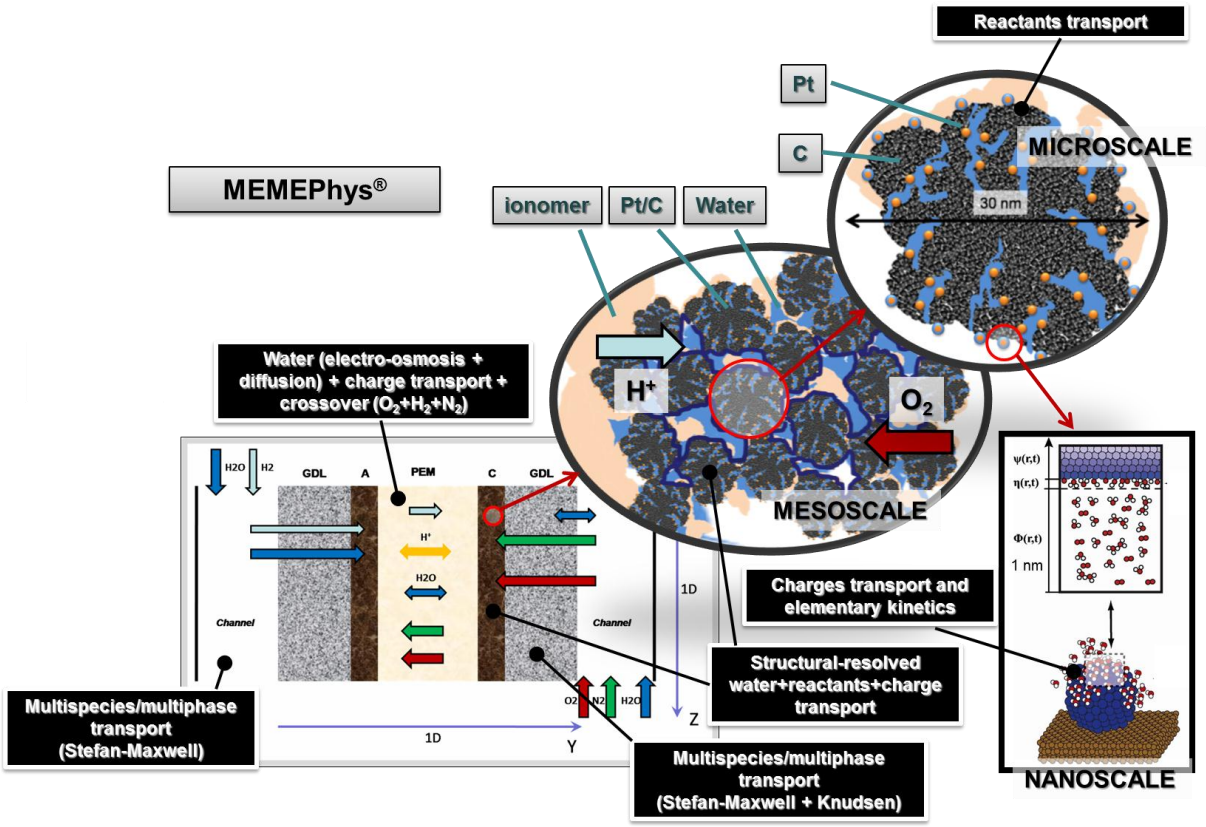

Figure 3.2: MEMEPhys® model in its most evolved version [2].

3.2.2 Description of the multi scale model of the electrodes

PEMFC electrodes are formed by catalyst/electronic conductor particles (called the electronic conductor phase) immersed in an ionic conductor medium (called the electrolyte phase) and a void fraction (called the pore phase) (Figure 3.3) [142]. This ionic conductor contains negatively charged sulfonate sites (in this case Nafion®). The electrodes, which are several micrometers thick, are separated by a 20 to 100 micrometer electrolyte phase. The particles that constitute the electronic conductor phase, usually particles deposed on carbon support, have a typical diameter of 100 nm and are presumed to be uniformly distributed in the electrode volume, as well as homogeneously covered with the impregnated electrolyte layer of 0.1 µm maximum thickness [143]. Within the catalyst and the ionomer interface, an electrochemical double layer (EDL) is formed. As discussed by Franco *et al*. [33], it is constituted of a diffuse layer (also known under Gouy-Chapman layer) and of an inner layer (also known under Stern layer). The diffuse layer consists of moving ions, counter-ions from the electrolyte phase,

and of water molecules. The inner layer is formed from adsorbed water molecules and intermediate reaction species at the catalyst surface. A schematical representation is presented in Figure 3.4

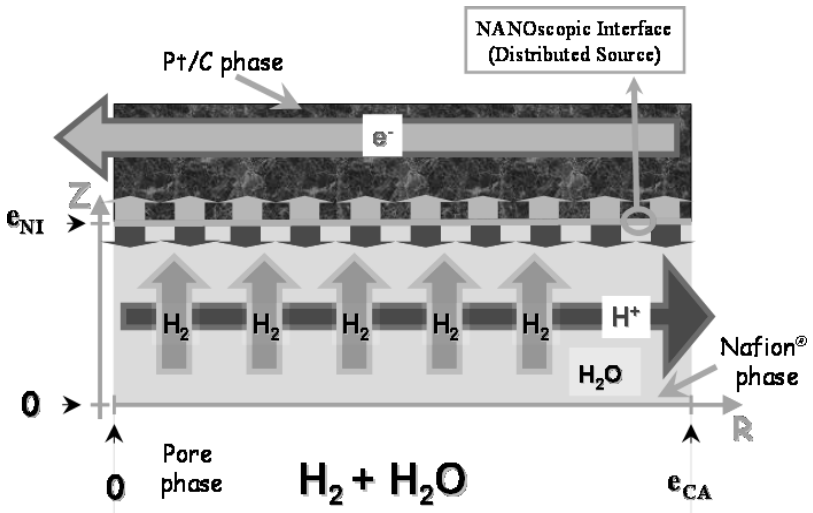

Figure 3.3: Electrode morphology and geometrical model. The Nafion® phase can be seen as an "effective Nafion®/water phase" [134].

The microscopic scale model includes the description of the transport phenomena in the ionomer, as described in the Chapter 0. We note here *Z* the microscopic thickness coordinate for the impregnated Nafion® (iN). The nanoscale description is based on the dynamic model of the EDL structure, coupled with the electrochemical reactions (Figure 3.4).

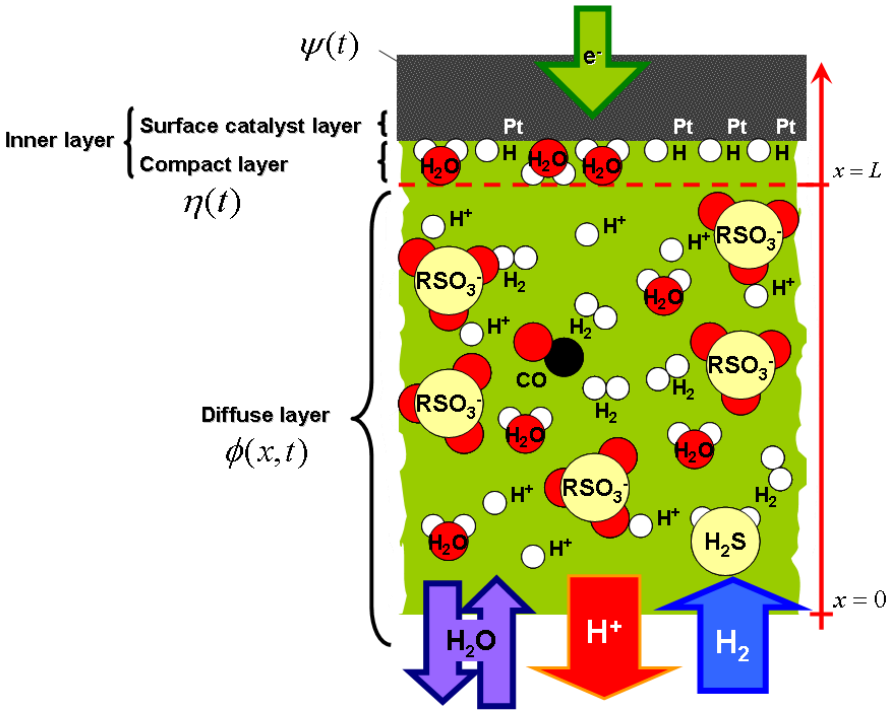

Figure 3.4: Schematic representation of the non-equilibrium EDL model within MEMEPhys®. Example of the anodic case: The hydrogen species arrives to the inner layer where the electron transfer reaction takes place. The proton species is produced at $x = L$ and evacuated through $x = 0$. (the eventual contamination by CO and H2S pollutants is also shown but they are not treated in this PhD thesis work).

Nanoscale model: diffuse layer – In this layer, diffusion and electro-migration transport phenomena are assumed to occur. The species which are present can be either non-charged (e.g. oxygen or hydrogen) or charged (e.g. proton).

In the case of non-charged species, the diffusion process is assumed to be Fickian. Thus we use Equation 2.22 for the calculation of the concentrations in the diffuse layer. Regarding the low thickness of the iN (about 10 nm), we consider no Bruggeman correction in the equation of diffusion, as the structure effect is assumed here as negligible.

In the membrane, the electroneutrality is respected, but in the vicinity of the catalyst, protons are produced (anode side) or consumed (cathode side). This induces an ionic potential spatial heterogeneity in the diffuse layer within the iN. Thus the transport of proton will result from two contributions, one due to the diffusion effect, and the other one to the electromigration effect. The proton are considered as punctual (diluted solution theory), so that interparticle electrical interactions can be neglected.

Nanoscale model: inner layer – In MEMEPhys® inner layer approach we consider the presence in the layer of:

- adsorbed water molecules, modeled by punctual electric dipoles responsible for the generation of an interfacial potential discontinuity,
- adsorbed reaction intermediates.

The modeling of this layer is based on a non-equilibrium thermodynamics and electrodynamics approach [134]. With this approach, it is possible to describe the evolution of the surface dipolar density, directly linked to the adsorption of water molecules (and the direction of the dipole) and of reaction intermediates. From the calculation of the surface dipolar density, it is possible to evaluate the potential drop between the diffuse layer and the catalyst. This potential is called by Franco *et al.* the surface or Frumkin potential and noted χ *(or* η_F *in their publications).* According to the superposition principle, this potential can be written as the addition of two contributions, first the drop due to the thickness of the adsorbate layer and secondly to the drop related to the surface dipolar density of the adsorbates layer. These contributions are noted respectively $\Delta\varphi_1$ and $\Delta\varphi_2$. They are both related to the electronic surface density σ, calculated by the charge conservation law at the catalyst / electrolyte interface.

Table 3.1 summarizes the different potentials which are calculated in the MEMEPhys® model.

Surface potential at the cathode	χ_{cathode}
Electrostatic potential in the diffuse layer at the cathode	Φ_{cathode}
Catalyst electrostatic potential at the cathode	$\psi_{\text{cathode}} = \Phi_{\text{cathode}} + \chi_{\text{cathode}}$
Surface potential at the anode	χ_{anode}
Electrostatic potential in the diffuse layer at the anode	Φ_{anode}
Catalyst electrostatic potential at the anode	$\psi_{\text{anode}} = \Phi_{\text{anode}} + \chi_{\text{anode}}$
Cell potential	$U_{\text{cell}} = \psi_{\text{cathode}} - \psi_{\text{anode}}$

Table 3.1: Summary of the potentials calculated in the MEMEPhys® model

The purpose of the following section is not the demonstration for the calculations of the several potentials (which have already been published by Franco *et al.*) but rather present the underlying physics and the main equations required for the simulation studies done in this PhD thesis.

3.2.3 Calculation of the potential in the MEMEPhys® approach

3.2.3.1 Calculation of the potential in the diffuse layer

In the anode catalyst layer, protons are produced. In the vicinity of the catalyst sites, hydrogen molecules adsorb on the platinum surface and split into protons, which stay in the ionomer phase of the catalyst and electrons, which are conducted to the cathode through the carbon phase. As the protons are in the Nafion® phase and the electrons in the metallic phase, locally the electroneutrality of the ionomer phase cannot be assumed. An electrostatic potential distribution is induced in the electrolyte at the vicinity of the catalyst. This potential distribution is calculated through the numerical resolution of Poisson's equation,

$$\frac{F}{\varepsilon_{DL}}\cdot\left(C_{H^+}-C_{SA}\right)=-\frac{\partial^2\Phi}{\partial x^2}\,, \qquad 3.1$$

where ε_{DL} is the electric permittivity in the diffuse layer, C_{H^+} the concentration of protons and C_{SA} the concentration of sulfonic acid groups. Indeed far from the platinum surface, the electroneutrality is respected and thus the concentrations of sulfonic acid groups and protons are equal [134].

This electrostatic potential is strongly related to the transport of protons, assumed to be governed by the Nernst-Planck equation,

$$\frac{\partial C_{H^+}}{\partial t}=D_{H^+}\cdot\frac{\partial^2 C_{H^+}}{\partial x^2}+\frac{F}{R\cdot T}\cdot\left(D_{H^+}\cdot\frac{\partial C_{H^+}}{\partial x}\cdot\frac{\partial\Phi}{\partial x}+D_{H^+}\cdot C_{H^+}\cdot\frac{\partial^2\Phi}{\partial x^2}\right) \qquad 3.2$$

.

For the coupled solution of Equations 3.1 and 3.2, the used boundary conditions are for the anode side an electrical potential set to 0, and at the cathode side, the electrical potential value is set as the value at the boundary between the membrane and the cathode as calculated by the membrane model (see Section 3.5.3.3).

3.2.3.2 Calculation of the electronic surface density

As previously mentioned in Section 3.2.2, the electronic surface density value is a key parameter, as it is involved in the calculation of the surface potential of the catalyst. By writing a charge conservation law at the catalyst / electrolyte interface, we obtain

Anode case
$$-\frac{\partial\sigma(r,t)}{\partial t}=J(r,t)-J_{FarA}(r,t)\,, \qquad 3.3$$

Cathode case
$$\frac{\partial\sigma(r,t)}{\partial t}=J(r,t)-J_{FarC}(r,t)\,, \qquad 3.4$$

where $J(r,t)$ is the local electronic current density at the catalyst surface, $J_{Far}(r,t)$ are the faradic current at the anode or cathode side. These current are linked to the electrochemical reaction rate which will be presented later in Section 3.2.4.1 and Section 3.2.4.2.

3.2.3.3 Calculation of the catalyst surface potential

As mentioned in Section 3.2.2, the surface potential can be split into two contributions due to different physical phenomena both related to the electronic surface density (see Section 3.2.3.2).

The first contribution is due to the thickness of the adsorbed water layer. If we consider the closed surface including the inner layer and the charge included in this surface noted as σ, we can write the Gauss's law in order to get the electric field at the surface as

$$\frac{\partial \Phi(r,t)}{\partial x} = -\frac{\sigma(r,t)}{\varepsilon_{CL}}, \qquad 3.5$$

where ε_{DL} is the electric permittivity in the inner layer.

Regarding the low thickness of the inner layer, Equation 3.5 can be reduced to

$$\Delta\varphi_1 = -\frac{\sigma(r,t)}{\varepsilon_{CL}} \cdot d, \qquad 3.6$$

where d is the thickness of the inner layer.

From Equation 3.6, we have the first contribution to the surface potential. The second one is calculated explaining the dipolar nature of water molecule adsorbed at the catalyst surface.

The water layer is considered as a layer of punctual dipoles, the interfacial potential drop can thus be calculated by

$$\Delta\varphi_2 = -\frac{\Gamma(r,t)}{\varepsilon_{DL}}, \qquad 3.7$$

where Γ is the dipolar surface density.

We need to establish an analytical expression for Γ. For this, Franco used the two states hypothesis for the description of the adsorption of water molecule. A water molecule can either be adsorbed with the hydrogen atoms oriented toward the catalyst surface (state 1) or with the lone pairs of water toward the catalyst surface (state 2) [134]. It is possible to express the dipolar surface density as

$$\Gamma(r,t) = \mu \cdot (n_1 - n_2), \qquad 3.8$$

where n_i is the number of diploes per unit of area in the state 1 or 2. The objective is now to quantify

the amount of water in each state.

This is possible through the description of the water adsorption step at the catalyst surface (Reaction 3.1).

Water adsorption $H_2O + Pt \rightleftharpoons H_2O\text{–}Pt$ Reaction 3.1

Two orientations are possible and the mass action law gives

$$\frac{n_1}{n_s \cdot a_{H_2O}} = \exp\left(-\frac{\Delta G^0_{c,1} + \Delta G^0_{e,1} + \Delta G^0_{i,1}}{R \cdot T}\right), \quad 3.9$$

$$\frac{n_2}{n_s \cdot a_{H_2O}} = \exp\left(-\frac{\Delta G^0_{c,2} + \Delta G^0_{e,2} + \Delta G^0_{i,2}}{R \cdot T}\right), \quad 3.10$$

where n_s is the number of free sites per unit area of the metallic phase, $\Delta G^0_{c,i}, \Delta G^0_{e,i}$ and $\Delta G^0_{i,i}$ are respectively the dipolar chemical adsorption energy, the dipolar electrostatic adsorption energy and the dipolar interaction adsorption energy for the adsorption in the state *i* (state 1 or 2) and *a* is the activity of water.

Knowing the adsorption energy, it is possible to calculate the n_i and thus the surface potential. Franco demonstrated that the coverage of both state can be calculated through

$$n_1 = n_s \cdot a_{H_2O} \cdot \frac{A}{2} \cdot \exp(-X), \quad 3.11$$

$$n_2 = n_s \cdot a_{H_2O} \cdot \frac{A}{2} \cdot \exp(X), \quad 3.12$$

where X is the solution to the transcendental equation

$$\frac{A \cdot \sinh(X)}{\frac{n^*}{n_s \cdot a_{H_2O}} + A \cdot \cosh(X)} = \kappa \cdot \sigma - \xi \cdot X, \quad 3.13$$

where n* is the sum of free sites and sites covered by intermediate reaction species per unit area of the metallic phase, $\kappa = \frac{d^3}{\varepsilon_{CL} \cdot \vartheta \cdot \mu}$, $\vartheta = \frac{\zeta[3]}{2 \cdot \pi \cdot \varepsilon_{DL}}$ and $\xi = \frac{k \cdot T \cdot d^3}{\vartheta \cdot \mu^2}$.

The combination of Equations 3.7, 3.8, 3.11 and 3.12 leads to

$$\varphi_2 = -\frac{A \cdot n_s \cdot a_{H_2O} \cdot \mu \cdot \sinh(X)}{\varepsilon_{DL}}. \quad 3.14$$

Adding $\Delta\varphi_1$ and $\Delta\varphi_2$ (Equations 3.6 and 3.14), it follows

$$\chi_{\text{electrode}} = -\frac{\sigma \cdot d}{\varepsilon_{\text{CL}}} - \frac{A \cdot n_s \cdot a_{\text{H}_2\text{O}} \cdot \mu \cdot \sinh(\text{X})}{\varepsilon_{\text{DL}}} . \qquad 3.15$$

3.2.4 Coupling of the MEMEPhys® electrode model with electrochemistry

The power produced by a PEMFC is due to the electrochemical reactions occurring in the electrodes. Thus it is obvious that we have to link the electrochemical reactions with the calculations of the cell potential. Regarding the Equation 3.15, the only missing parameter which has to be calculated is the evolution of n^* and n_s. These parameters are directly related to the reactions occurring in the electrode, thus a precise description of the electrochemical phenomena will allow completing the electrical equations.

3.2.4.1 Electrochemistry at the anode

Franco *et al*. considered the HOR in their first model [134]. In our case, we consider in a parallel way the production of hydrogen peroxide. The mechanism which was used by Franco *et al*. for the HOR description was based on the so-called Tafel – Heyrovsky – Volmer mechanism, one of the most reported in the literature [144-148].

Tafel reaction (abb. TAF) $\quad \text{H}_2 + 2\,(\text{Pt}) \rightleftharpoons 2\,\text{H(Pt)}$ Reaction 3.2

Heyrovsky reaction (abb. HEY) $\quad \text{H}_2 + (\text{Pt}) \rightleftharpoons \text{H(Pt)} + \text{H}^+ + \text{e}^-$ Reaction 3.3

Volmer reaction (abb. VOL) $\quad \text{H(Pt)} \rightleftharpoons \text{H}^+ + \text{e}^- + (\text{Pt})$ Reaction 3.4

Reaction 3.2 to Reaction 3.4 are the elementary steps used for the description of the HOR. For each step, the rates (noted *r*) are written as a function of the coverage, the kinetic constant, the activities at the interface and the surface potential [134]

$$v_i = k_i \cdot \prod_{j=\text{species involved in reaction i}} \theta_j \cdot \prod_{j=\text{species involved in reaction i}} a_i \cdot f(\chi) - k_{-i} \cdot \prod_{j=\text{species involved in reaction -i}} \theta_j \cdot \prod_{j=\text{species involved in reaction i}} a_{-i} \cdot f(\chi) \qquad 3.16$$

with the kinetic paramters k_i that can be calculated thanks to the activation energies as determined from *ab initio* calculation or fitted from experimental data. The kinetic parameters are needed in the expression of the reaction rate constant k_i of the Reactions 2.25 and 3.17. These coefficients are calculated from Eyring's equations, derived from the activated-complex theory (known as transition state

theory as well) [149].

$$k_i = \frac{k_B \cdot T}{h} \cdot \exp\left(-\frac{\Delta G_i^{\neq}}{R \cdot T}\right), \qquad 3.17$$

where $\Delta G_i^{\neq}$ is the Gibbs activation energy, k_B is Boltzmann's constant, and h is Planck's constant.

On a parallel and competitive way, we observe, through the simultaneous presence of oxygen and hydrogen at the cathode, the production of hydrogen peroxide. Thus we added to the existing reactions as second set, describing this production.

As previously discussed in Section 1.3.3, it is still an open question to decide if H_2O_2 is produced at the anode side or at the cathode side. In the case which the hydrogen peroxide is produced at the cathode, the supposed involved mechanism is a 2-electron reduction of the oxygen as shown on Reaction 1.5. The standard electrode potential of this reaction is 0.77 V. As the potential at the cathode side lay by 1 V, H_2O_2 is an unstable species and is quickly reduced into water. For this reason, we assume that hydrogen peroxide is only produced at the anode side, following a detailed mechanism similar to Figure 1.20, which will be defined in this section. The second step of the degradation, once the oxygen diffused to the catalyst site of the anode, is the production of hydrogen peroxide. The mechanism we used for this is

H_2O_2 production (1^{st} step) 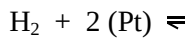 Reaction 3.5

H_2O_2 production (2^{nd} step) 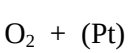 Reaction 3.6

H_2O_2 production (3^{rd} step) 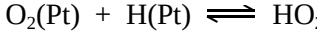 Reaction 3.7

H_2O_2 production (4^{th} step)  Reaction 3.8

H_2O_2 production (5^{th} step) 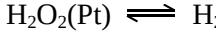 Reaction 3.9

as proposed by Davies [79].

Reaction 3.5 is the first step of the HOR (see Section 3.2.4.1). It is widely known that H_2O_2 formation on a Pt/C catalyst is greatly enhanced in an anode potential region below 0.2 V, where atomic hydro-

gen is adsorbed on platinum [17, 150, 151]. These facts supported the mechanism proposed by Davies.

From the expressions of these reactions rate, it is now possible to express the different boundary conditions needed for the calculation of the equations of the previous parts (diffusion and electronic surface density).

The net flux of hydrogen into the inner layer is

$$J_{\mathrm{H_2}}(r,L,t) = -(v_{\mathrm{TAF}} + v_{\mathrm{HEY}}), \tag{3.18}$$

which takes into account the consumption of hydrogen through the Volmer and the Heyrovsky steps. This will constitute the boundary for diffusion equation of hydrogen in the diffuse layer.

The net flux of protons gives the value of the faradic current and is calculated by

$$J_{\mathrm{H^+}}(r,L,t) = (v_{\mathrm{TAF}} + v_{\mathrm{HEY}}) = \frac{J_{\mathrm{FarA}}}{F}. \tag{3.19}$$

The next point which has to be treated is the expression of the different coverage rates of reaction intermediates on the catalyst layer. As mentioned, we consider a simultaneous and competitive production of H_2O_2. The mechanism we assume for the hydrogen peroxide production is given in Section 2.3.1, Reaction 3.6 to Reaction 3.9. This means that we have in our model more reaction intermediates than in the work of Franco [134]. On a similar calculation way as Franco, we obtain the following expression for the transcendental equation

$$\frac{A\cdot\sinh(\mathrm{X})}{\frac{1}{a_{\mathrm{H_2O}}}\left(1+\frac{\theta_{\mathrm{intermediate}}}{\theta_s}\right)+A\cdot\cosh(\mathrm{X})} = \kappa\cdot\sigma - \xi\cdot\mathrm{X} \tag{3.20}$$

.

where $\theta_{\mathrm{intermediate}}$ is the covering fraction of the reaction intermediates and θ_s the covering fraction of free sites. In our case we have

$$\theta_{\mathrm{intermediate}} = \theta_{\mathrm{PtH}} + \theta_{\mathrm{PtO_2}} + \theta_{\mathrm{PtHO_2}} + \theta_{\mathrm{PtH_2O_2}}. \tag{3.21}$$

Covering fraction of each intermediate can be calculated by solving the balance equations

$$\frac{n^{\max}}{N_A}\cdot\frac{d\theta_i}{dt} = \sum_{i=\mathrm{production}} r_i - \sum_{j=\mathrm{consumption}} r_j, \tag{3.22}$$

where $n^{\max}$ is the maximal quantity of free site per unit area of the metallic phase.

The still unknown parameters θ_s and n_s can then be calculated through the unity of the sum of the coverage

$$\theta_s + \theta_{\text{intermediate}} + \frac{n_1 + n_2}{n^{\max}} = 1 \text{ and} \qquad 3.23$$

$$n_s = \theta_s \cdot n^{\max}. \qquad 3.24$$

The coupling between the transport model and the electrochemical model in the electrode is now complete for the anode and it is possible to calculate the anodic potential.

3.2.4.2 Electrochemistry at the cathode

On a similar way as for the anode, elementary kinetic steps are written for the ORR. We use here the model proposed by Franco, as we consider no parasitic reaction at the cathode side [134]. The mechanism which is assumed was proposed by Damjanovic and is [152]

ORR Reaction 1 $\quad O_2 + 2\,(Pt) \rightleftharpoons 2\,O(Pt)$ Reaction 3.10

ORR Reaction 2 $\quad O(Pt) + H^+ + e^- \rightleftharpoons OH(Pt)$ Reaction 3.11

ORR Reaction 3 $\quad O_2 + H^+ + (Pt) + e^- \rightleftharpoons O_2H(Pt)$ Reaction 3.12

ORR Reaction 4 $\quad O_2H(Pt) + H_2O + 2\,(Pt) \rightleftharpoons 3\,OH(Pt)$ Reaction 3.13

ORR Reaction 5 $\quad OH(Pt) + H^+ + e^- \rightleftharpoons H_2O + (Pt)$ Reaction 3.14

(ab initio –based mechanisms can be also be implemented instead, as recently published by Ferreira de Morais *et al*. [153]).

In the cathode case, we write the different fluxes as function of the reaction rates of the ORR mechanism.

The net flux of oxygen into the inner layer is

$$J_{O_2}(r, L, t) = -v_{\text{Dmj1}}, \qquad 3.25$$

which takes into account the consumption of hydrogen through Volmer and Heyrovsky steps. This will constitute the boundary for diffusion equation of hydrogen in the diffuse layer

The net flux of protons gives the value of the faradic current and is calculated by

$$J_{H^+}(r, L, t) = (v_{\text{Dmj1}} + v_{\text{Dmj3}}) = -\frac{J_{\text{FarC}}}{F}. \qquad 3.26$$

As we wrote the transcendental equation on a generic way, this remains unchanged. Only the expression of the reaction intermediates is modified as

$$\theta_{\text{intermediate}} = \theta_{PtHO_2} + \theta_{PtOH}. \qquad 3.27$$

The missing coverage rates can easily be computed on a similar way as in the anodic case using Equa-

tions 3.22 to 3.24 and then it is possible to calculate the potential of the cathode.

It should be precise that in the cathode case, the boundary condition for Equation 3.1 is calculated through

$$\phi = R_{\text{membrane}} \cdot I \ . \qquad 3.28$$

Through this last relationship, the impact of the degradation and the membrane model impact also on the cathode performance are taken into account.

3.2.5 Channel and GDL model

In order to represent the best way the feed of the reactant to the electrodes, the model includes also a channel and GDL model. This model allows the calculation of partial pressure from flux values [154]. This chapter presents the general equations which are used in the model. This model has been implemented discretized, therefore we simplify our simulation with only one compartment, as the electrode model is not discretized and the membrane model is only discretized from the cathode to the anode in MEMEPhys®.

In the model, mass balances are calculated, input and output fluxes are known. From molar flow rates and temperatures of gases (hydrogen or air) and from the presence and amount of liquid water as inputs, the model calculates the pressure, the temperature of the mix, the molar fraction of the gases and the volume saturation in liquid water. As one of our model assumptions is an isothermal system, the temperature effects are not taken into account.

The mass balance on the different elements gives

$$\frac{dn_{O_2}}{dt} = \sum F_{O_2} \ , \qquad 3.29$$

$$\frac{dn_{N_2}}{dt} = \sum F_{N_2} \ , \qquad 3.30$$

$$\frac{dn_{vap}}{dt} = \sum F_{vap} - F_{v \to l} \ , \qquad 3.31$$

$$\frac{dn_{liq}}{dt} = \sum F_{liq} + F_{v \to l} \ , \qquad 3.32$$

where F_i represents the flow rate and n_i the amount of component i.

The molar fraction of water is given by the ratio between the saturation pressure of water and the total pressure

$$X_{sat} = \frac{P_{sat}(T)}{P}. \quad 3.33$$

$$X_{vap} = \frac{n_{vap}}{n_{vap} + n_{O_2} + n_{N_2}} \quad 3.34$$

where X represents the molar fraction in the gaseous phase.

In order to calculate the pressure of the different gas components, the following equations are used:

$$V_{liq} = \frac{n_{liq} \cdot M_{liq}}{\rho_{liq}}, \quad 3.35$$

$$V_{gas} = V - V_{liq}, \quad 3.36$$

$$P_{gaz} = \frac{\left(n_{O2} + n_{N2} + n_{vap}\right) \cdot R \cdot T}{V_{gaz}}, \quad 3.37$$

$$P_{cap} = k_{Pc} \cdot J(s), \quad 3.38$$

$$P_{liq} = P_{gas} - P_{cap} \quad 3.39$$

where V_i is the volume of phase i, n_i is the amount of substance i, P_i the pressure of phase i and $J(s)$ the Leverett J-function, a dimensionless function of water saturation describing the capillary pressure [153].

From these results on the channel, the model then calculates the concentration of the different gas components in the pore of the GDL, which are reused in the mass balance equation of the electrode model.

3.3 Physics underlying in the electrode model of DENIS

3.3.1 Presentation of the model

Bessler and co-workers develop the DENIS model since 2003. Even if the initial conception of DENIS was designed in a way that simulations of solid-oxide fuel cell (SOFC) were possible, the modularity of the C-programmed model and the similarities in the architecture of a SOFC and PEMFC made it possible to adapt the model to the PEMFC system [137, 155]. The following chapter will present the DENIS model, the way it treats the electrodes and the transport phenomena.

3.3.2 Calculation of the cell potential in DENIS

3.3.2.1 General aspects

As in MEMEPhys®, the calculation of the cell voltage in DENIS is given by the difference of the electric potentials in the cathode and in the anode. This allows to the model to calculate on a quasi 2D way the distribution of the gas-phase species, the current, the potential, as well as the pressure and the flow velocities. We will recall here the main equations needed for the computation of the cell potential.

In Figure 3.6, we present the global architecture of DENIS. For a better understanding how the cell potential is calculated, we plot schematically the contribution of anode, cathode and electrolyte on the cell voltage in Figure 3.7.

Like in the MEMEPhys® approach, the cell voltage is calculated after

$$U_{\text{cell}} = \phi_{\text{ca}} - \phi_{\text{an}}, \qquad 3.40$$

the difference will be in the calculation of the electrode potentials.

The formalism we used here is the one as in the original work of Bessler *et al*. [155]. Indeed so that the reader could refer to the original work, we keep the consistency in the notation. This explains why some symbols conflicts may occur with the previous parts.

The driving equations used in the DENIS model for the calculation of every contribution of the cell voltage (as displayed in Figure 3.7) are given in Figure 3.5.

Physicochemical process	Model equation	Boundary conditions
Electrochemistry and surface chemistry (all x, y within electrodes)		
Surface chemistry (anode, all $i \in S_s$)	$\frac{\partial \theta_i}{\partial t} = \frac{\sigma_i}{\Gamma_k} \dot{s}_i^{\mathrm{A}}$	–
Species production rates (anode, all $i \in S_s$)	$\dot{s}_i^{\mathrm{A}} = \sum_m \nu_{i,m} \left(k_{\mathrm{f},m} \prod_{j \in R_{\mathrm{f},m}} c_j^{\nu'_j} - k_{\mathrm{r},m} \prod_{j \in R_{\mathrm{r},m}} c_j^{\nu''_j} \right)$	–
Total current density (anode and cathode)	$i = \int_{y=0}^{L_{\text{electrode}}} (i_{\mathrm{F}}^{\mathrm{V}} + i_{\mathrm{dl}}^{\mathrm{V}}) \mathrm{d}y$	–
Current density due to electrical double layer (anode and cathode)	$i_{\mathrm{dl}}^{\mathrm{V}}(t) = A_{\mathrm{dl}}^{\mathrm{V}} C_{\mathrm{dl}}(\Delta\phi) \frac{\partial(\Delta\phi)}{\partial t}$	–
Relationship anode $i_{\mathrm{F}}^{\mathrm{V}} - \Delta\phi_{\mathrm{an}}$	$i_{\mathrm{F}}^{\mathrm{V}} = z F l_{\mathrm{tpb}}^{\mathrm{V}} \left(k_{\mathrm{f,ct}} \prod_{j \in R_{\mathrm{f,ct}}} \theta_j^{\nu'_j} - k_{\mathrm{r,ct}} \prod_{j \in R_{\mathrm{r,ct}}} \theta_j^{\nu''_j} \right)$	–
	$k_{\mathrm{f,ct}} = k_{\mathrm{f,ct}}^0 \exp\left(-\frac{E_{\mathrm{f,ct}}^{\mathrm{act}}}{RT}\right) \exp\left(-(1-\alpha)\frac{zF}{RT}\Delta\phi_{\mathrm{an}}\right)$	
	$k_{\mathrm{r,ct}} = k_{\mathrm{r,ct}}^0 \exp\left(-\frac{E_{\mathrm{r,ct}}^{\mathrm{act}}}{RT}\right) \exp\left(\alpha\frac{zF}{RT}\Delta\phi_{\mathrm{an}}\right)$	
Relationship cathode $i_{\mathrm{F}}^{\mathrm{V}} - \Delta\phi_{\mathrm{ca}}$	$i_{\mathrm{F}}^{\mathrm{V}} = i_{\mathrm{O}_2}^{\mathrm{V}} \frac{(p_{\mathrm{O}_2}/p_{\mathrm{O}_2}^0)^{1/4}}{1+(p_{\mathrm{O}_2}/p_{\mathrm{O}_2}^0)^{1/2}} \left[\exp\left(\frac{0.5F\eta_{\mathrm{act}}}{RT}\right) - \exp\left(-\frac{0.5F\eta_{\mathrm{act}}}{RT}\right)\right]$	–
	$\eta_{\mathrm{act}} = \Delta\phi_{\mathrm{ca}} - \Delta\phi_{\mathrm{cquil,ca}}(p_{\mathrm{O}_2})$	
	$\Delta\phi_{\mathrm{equil,ca}} = -\frac{\Delta G_{\mathrm{ca}}}{2F} - \frac{RT}{2F} \ln \frac{a(\mathrm{O}_{\mathrm{O}}^{\mathrm{x}})}{a(\mathrm{O}_2)^{1/2} a(\mathrm{V}_{\mathrm{O}}^{\bullet\bullet})}$	
Gas-phase transport in supply channels (x dimension, anode and cathode)		
Continuity	$\frac{\partial \rho}{\partial t} = -\frac{\partial(\rho v)}{\partial x} + \frac{P_{\text{chem}}^{\text{cha}}}{A^{\text{cha}}} \sum \dot{s}_i^{\text{cha}} M_i$	$\rho(x=0) = \rho_{\text{in}}$; $v(x=0) = v_{\text{in}}$; $Y_i(x=0) = Y_{i,\text{in}}$; $p(x = L^{\text{cha}}) = p_{\text{out}}$
Momentum conservation	$\frac{\partial(\rho v)}{\partial t} = -\frac{\partial(\rho v v)}{\partial x} - \frac{\partial p}{\partial x} - \frac{P_{\text{h}}^{\text{cha}}}{A^{\text{cha}}} \tau_{\text{w}}$	
Species conservation (all $i \in S_g$)	$\frac{\partial(\rho Y_i)}{\partial t} = -\frac{\partial(\rho v Y_i)}{\partial x} - \frac{\partial j_i^{\text{diff}}}{\partial x} + \frac{P_{\text{chem}}^{\text{cha}}}{A^{\text{cha}}} \dot{s}_i^{\text{cha}} M_i$	
Ideal gas law	$p = \rho R T \sum_i \frac{Y_i}{M_i}$	–
Porous electrode mass transport (y dimension, anode and cathode)		
Species conservation (all $i \in S_g$)	$\frac{\partial(\varepsilon c^{\text{g}} X_i)}{\partial t} = -\frac{\partial J_i^{\text{diff}}}{\partial y} - \frac{\partial J_i^{\text{flow}}}{\partial y} + \sum_{k \in S_k} A_k^{\text{V}} \dot{s}_i^{\text{A}}$	$\left.\frac{\partial J_i^{\text{diff}}}{\partial y}\right\|_{y=0} = \left.\frac{\partial J_i^{\text{flow}}}{\partial y}\right\|_{y=0} = 0$; $J_i^{\text{diff}}(y=L) + J_i^{\text{flow}}(y=L) = \dot{s}_i^{\text{cha}}$
Diffusive fluxes: Stefan–Maxwell law (all $i \in S_g$)	$\frac{\partial(c^{\text{g}} X_i)}{\partial y} = \sum_{j \in S_g} \frac{X_i J_j^{\text{diff}} - X_j J_i^{\text{diff}}}{D_{ij}^{\text{eff}}}$	–
Pressure-driven porous flux: Darcy flux (all $i \in S_g$)	$J_i^{\text{flow}} = X_i c^{\text{g}} \frac{B}{\mu} \frac{\partial p}{\partial y}$	–
Potential distribution (y dimension)		
Cell voltage	$E = \phi_{\text{elde,ca}} - \phi_{\text{elde,an}}$	$\phi_{\text{elde,ca}} = 0$
Potential step (anode and cathode)	$\Delta\phi = \phi_{\text{elde}} - \phi_{\text{elyt}}$	Continuity of ϕ_{elyt} over porous cathode, solid electrolyte and porous anode
Coupled ionic and electronic charge transport (anode and cathode)	$\frac{\partial}{\partial y}\left(\sigma_{\text{elyt}} f_\sigma \frac{\partial(\Delta\phi)}{\partial y}\right) = -(i_{\mathrm{F}}^{\mathrm{V}} + i_{\mathrm{dl}}^{\mathrm{V}})$	
Ionic charge transport (solid electrolyte)	$\frac{\partial}{\partial y}\left(\sigma_{\text{elyt}} \frac{\partial \phi_{\text{elyt}}}{\partial y}\right) = 0$	

Figure 3.5: Summary of the governing equations of the DENIS model [155].

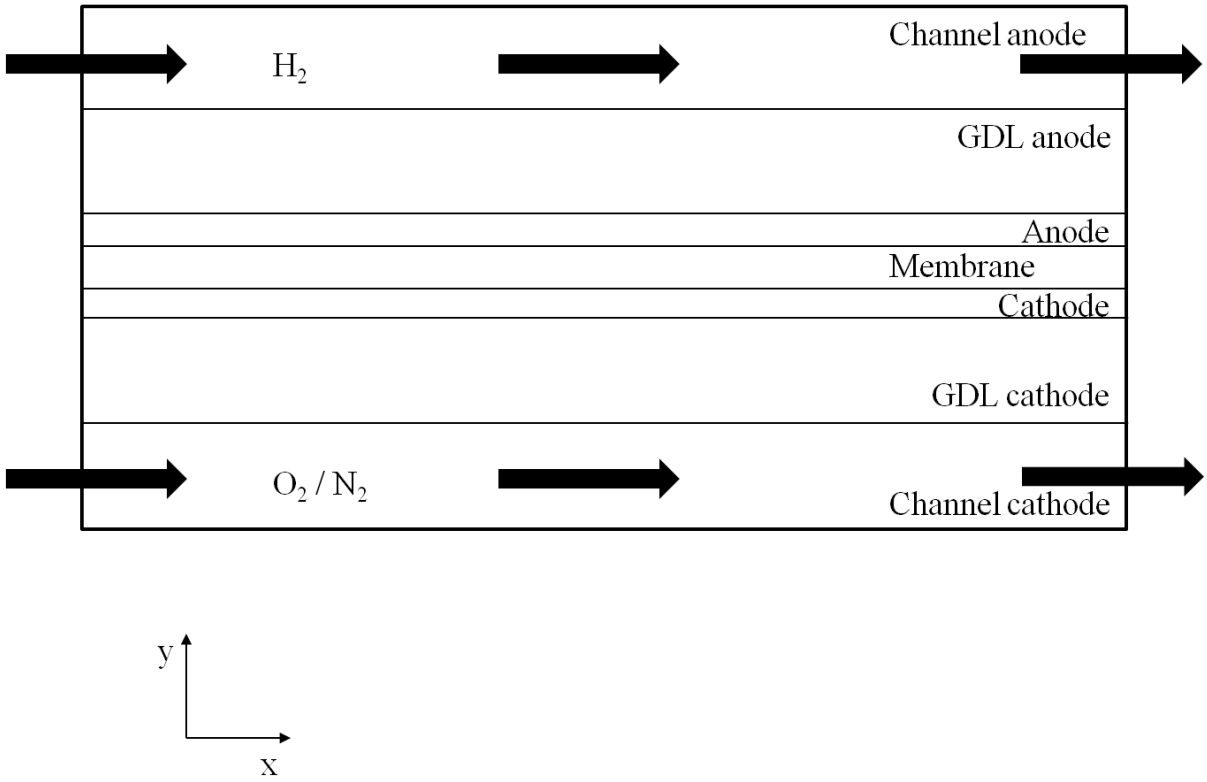

Figure 3.6: Schematic representation of the 2D model DENIS

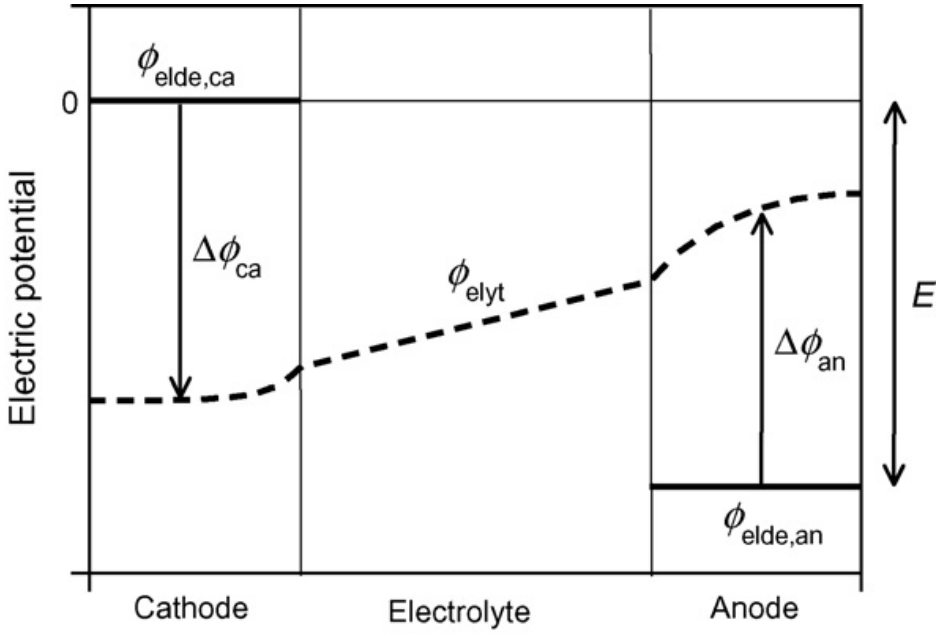

Figure 3.7: Detailed contributions of each cell part to the calculation of the voltage

3.3.2.2 Electrochemical calculations

DENIS considers porous electrodes (described by volume-specific parameters). All the calculations related to the electrochemistry are performed using the Cantera package, developed by Goodwin at CalTech [138]. It has been coupled over the last years to the DENIS environment in order to treat complex problems.

At the anode side, we consider the same mechanism than the one presented in the previous part (see Section 3.2.4.1). The calculation with Cantera requires the knowing of several kinetic parameters, which may either be parameterized or taken from experimental work

At the cathode side, because of current numerical stability issues (which are on the way of being fixed), the approach used in MEMEPhys® does not converge well. For that reason, we used rather a global reaction as on Reaction 1.2, however slightly modified, as we added an adsorption step of oxygen on the catalyst (Reaction 3.15 and Reaction 3.16).

Adsorption of oxygen $O_2 + (Pt) \longrightarrow O_2(Pt)$ Reaction 3.15

Half-cell reaction at the cathode $O_2(Pt) + 4\,H^+ + 4\,e^- \longrightarrow 2\,H_2O + (Pt)$ Reaction 3.16

Cantera is given a definition of the different phases, species and reactions which will have to be considered. Then from the kinetic parameters of the input file and physical parameters given from the DENIS core (concentration, temperature, pressure etc), Cantera calculate the net rate of progress (ROP_{net}) of the reactions (either chemical or electrochemical). From this ROP_{net} it is possible to get the production rate of electron through

$$\frac{d[e^-]}{dt} = -ROP_{net} \text{ and} \qquad 3.41$$

$$I = F \cdot \frac{d[e^-]}{dt} \qquad 3.42$$

The current through the electrode and into the solution may thus be defined in terms of the electron generation rate. Alternatively, the rate of progress for global electrode reactions may be defined in terms of the current density, *i*, in Butler-Volmer equation as

$$i = i_0 \cdot \left(\exp\left[\frac{(1-\beta^e)\cdot F \cdot \eta_s}{R \cdot T} \right] - \exp\left[\frac{-\beta^e \cdot F \cdot \eta_s}{R \cdot T} \right] \right) \quad 3.43$$

where i_0 is the exchange current density, β^e is the symmetry factor for the transition state and η_s is the overpotential (represents the departure from the equilibrium potential at the specific conditions of the electrode).

3.3.3 Gas transport and channel model in DENIS

In this section, the transport models of mass and charge are described. We are using a quasi-1D+1D-description that covers two length scales, as shown in Figure 3.6:

- gas-phase flow in the gas chamber above the PEMFC electrodes (mm–cm scale, *x* dimension)
- gas-phase and charge transport within the porous electrodes (µm–mm scale, *y* dimension)

Every individual scale is modeled in one dimension, and the scales are coupled through appropriate boundary conditions. This allows capturing all relevant physicochemical processes, while keeping computational cost to a reasonable level as compared to a full 2D model [155].

Gas-phase flow is modeled using 1D representation of the Navier–Stokes equations. The porous electrodes are treated as continuum of the three involved phases gas-phase, electrode and electrolyte. The transport within each of the three phases (gas species, electrons and oxygen ions, respectively) is described using effective transport coefficients. Gas-phase transport in the porous electrodes is modeled by two parallel transport pathways: Stefan–Maxwell diffusion and Darcy viscous flow. For the diffusion pathway, modified Bosanquet diffusion coefficients are used that account for both, free-molecular and Knudsen diffusion.

The transport of the gaseous reactants and products takes place through convection and diffusion in the gas chamber above each electrode. These gas transport situations are modeled with one dimensional representations of the transient Navier–Stokes equations (conservation of mass – Equation 3.44, momentum – Equation 3.45 and species-Equation 3.46).

$$\frac{\partial \rho}{\partial t} = -\frac{\partial(\rho v)}{\partial x} + \frac{P_{\text{chem}}^{\text{cha}}}{A^{\text{cha}}} \sum \dot{s}_i^{\text{cha}} M_i \,, \quad 3.44$$

$$\frac{\partial(\rho v)}{\partial t} = -\frac{\partial(\rho v v)}{\partial x} - \frac{\partial p}{\partial x} - \frac{P_{\text{h}}^{\text{cha}}}{A^{\text{cha}}} \tau_{\text{w}} \,, \quad 3.45$$

$$\frac{\partial(\rho Y_i)}{\partial t} = -\frac{\partial(\rho v Y_i)}{\partial x} - \frac{\partial j_i^{\text{diff}}}{\partial x} + \frac{P_{\text{chem}}^{\text{cha}}}{A^{\text{cha}}} \dot{s}_i^{\text{cha}} M_i \quad 3.46$$

.

As previously mentioned, DENIS was first designed for simulations of SOFC technology [135, 136, 155, 156]. Even if the role of the electrodes, electrolyte and gas channel remains the same compared to PEFC technology, one aspect is different comparing both cell designs. In a PEMFC a GDL is needed for a good gas supply at the catalyst layer and a good evacuation of the produced liquid water at the cathode side (see Section 1.1.2). In SOFC technology, a current collector is needed to drive the electron outside out the cathode to the anode. This can be seen as a conductive porous structure, defined through porosity, tortuosity and thickness. Even if from its use it differs from the GDL, its properties can be adapted so that it is representative of a GDL. The only assumption we have to make is the non-presence of liquid water in the porous media representing the GDL. The modeling of the transport phenomena is the same; only the characteristics of the media are modified.

3.4 Comparison MEMEPhys® / DENIS electrode models

This part summarizes the properties of each model as used in this PhD thesis work, their common points and their differences. For clarity purposes, the points we discussed are presented in Table 3.2.

Property	DENIS	MEMEPhys®
Programming language	C	C, Matlab / Simulink
Solver	Limex [140]	Simulink ode23s Simulink
Physical approach	Equilibrium thermodynamics	Non-equilibrium thermodynamics
Electrochemistry Anode	Butler-Volmer-based elementary kinetics Production of H_2O_2	Ab initio-based elementary kinetics Production of H_2O_2 Nanoscale electrochemical double layer structure explicity simulated
Electrochemistry Cathode	Butler-Volmer-based global kinetics	Ab initio-based elementary kinetics Nanoscale electrochemical double layer structure explicitly simulated
Discretization	Two dimensional discretization (1D + 1D) • Along the gas channel	Membrane discretized (1D + 1D) • Local discretization inside the electrodes carbon agglomerates

	• In transversal direction (from gas channel cathode to gas channel anode)	• Discretization along the GDL+MEA thickness
Scaling	Multi-scale model: • description of gas transport along the channel at the macro-scale • description of transport phenomena in the electrodes and the electrolyte at a micro-scale	Multi-scale model: • description of gas and water transport in the channel and the GDL at a macro-scale • description of nano-scale reaction and transport phenomena in the vicinity of the catalyst • description of transport phenomena in the electrodes and the electrolyte at a micro-scale

Table 3.2: DENIS – MEMEPhys® models: comparison of the general features as used in this PhD thesis work.

We had the opportunity to work on a parallel way with two codes. Both are complex and advanced; therefore they differ in some of their assumptions and approach. They are both designed on a modular way, so to make easier any modification on an aspect of the code. Thanks that, it is possible to modify for example the physics used for the transport phenomena in the gas phase without having to change anything in the rest of the code. This modularity was the key, which allowed us to reuse the membrane module in both code. We just had to replace the previous membrane model by the new one and couple it to the rest of the cell. Within the module itself it is also possible to perform modifications without changing the rest of the code.

DENIS offers possibilities, for example in the investigation of gas distribution profiles on electrode surfaces and thus a screening of the areas of the electrode where the electrochemical activity is not optimal. Such a study has already successfully been done in the case of SOFC [136]. A second point is that DENIS is programmed in C and does not depend on any commercial software and the drawbacks linked to their uses. Even if the requirement to program on it is higher than with Matlab for example, we have a higher flexibility for example in the use of the solver.

MEMEPhys® allows simulating a whole cell. It focuses on a precise description of the electrochemical double layer at the surface of the catalyst layer [133, 134]. Its strength lies in its physical approach of the electrochemistry and transport phenomena at multiple scales and in its capabilities to numerically account for the feedback between the reaction and transport processes and materials aging phenomena:

Unlike DENIS and most of the other work published in the literature, MEMEPhys® uses, instead of an top-down modeling approach, a bottom-up approach. The phenomena described at the nano-scale are the causes of the observation at the upper scales (e.g. any Butler-Volmer equation is used, and *ab initio* and microstructural data can be easily integrated). Moreover, the use of non-equilibrium thermodynamics is justified by the fact that fuel cells are continuously fed by gases at different fluxes, depending on the demand and thus, cannot really be considered as system in equilibrium.

3.5 Coupling of the membrane model with the electrodes model

3.5.1 Generalities

As the membrane is sandwiched between the anode and the cathode and because of the continuity principle at the interfaces electrodes / membrane, we have to couple the boundary conditions so that the definition of several inputs and outputs in the model are consistent.

Electrodes are the locations where the electrochemical reactions required for the current production take place, and the reactant are fed through the channel and the GDLs. But in the case of the ORR for example, the proton which are required are produced at the anode and have to diffuse through the membrane. This means that the electrodes models provide boundary conditions to several equations computered by the membrane module. Thus the next chapter aims on explaining how the coupling is made, depending on the simulation environment.

3.5.2 Specifications for the coupling in DENIS

The membrane model was originally developed in C and integrated to the DENIS environment. Thus no changes or adaptation were required to get the model operating. The several parameters which could be needed by the module are directly given by the other modules present in DENIS.

This includes:

- The current density, needed for the calculation of the electro-osmotic drag contribution of the water flux (Equation 2.8)
- The partial pressure of the gases at the anode and the cathode, needed for the application of Henry's law (Equation 2.21)
- The production term of each species are driven by the electrochemistry and the resolution of the diffusion equations through the membrane and degradation are made in the membrane module. Thus a coupling is needed as well, so that the boundary conditions remain time-dependent.

3.5.3 Specifications for the coupling in MEMEPhys®

3.5.3.1 General aspect of the membrane module coupling in MEMEPhys®

The C-module is embedded into MEMEPhys® (Matlab / Simulink environment) through the use of an S-Function (as defined in Section 3.1.3). Thus it is necessary to couple the module to the rest of the model. The module receives inputs from the module and gives outputs as displayed in Figure 3.8. Moreover, some light modifications were made, as parameters were computed both in the S-Function and in the rest of the Simulink model.

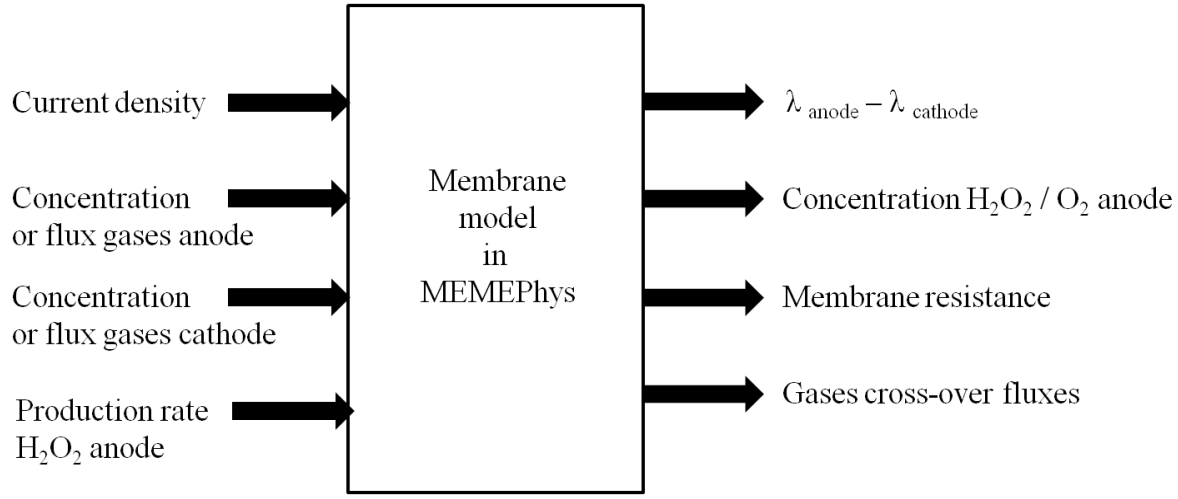

Figure 3.8: Coupling the membrane module into MEMEPhys®

3.5.3.2 Inputs from MEMEPhys® to the membrane module

The first information which has to be given to the membrane module is the current density demanded to the cell. The current density is one of the input parameters when using a MEMEPhys® model. Its value is then directly fed into the S-Function.

The second parameters which have to be given to the module are the boundary conditions for the transport equation. For the diffusion of dissolved gases through the membrane thickness (Equation 2.22), the concentrations of dissolved gases at the electrode / membrane interfaces are needed. This is calculated in DENIS through the expression of Henry's law (Equation 2.21). In the case of ME-MEPhys®, this calculation was already implemented in the GDL model. Thus it is possible to feed directly the value of dissolved gas concentrations into the membrane module. For water transport, the issue is similar. Equation 2.4 allows the calculation of the evolution of the water content λ along the membrane. Equations 2.11 and 2.12 are used in DENIS as boundary conditions, based on the value of

the relative humidity and the production of water from the ORR. As MEMEPhys® describes in the cathode model the electrochemical phenomena and calculates water balance in the catalyst layer; we assume that there is no open gas pore at the electrode / membrane interfaces and, as the thickness of the ionomer is really thin compared to the membrane thickness, the net flux of water in the electrode is represent the boundary conditions for water flux in the membrane model, as presented in Section 2.2.1.1.

Last, as the hydrogen peroxide is produced at the anode side and but decomposed in the membrane, its production rate must be given to the membrane module, in order to be taken into account in the mass balance equation for this component.

3.5.3.3 Outputs from the membrane module to MEMEPhys®

Most of the output we configured are used for post-treatment and are not related to the rest of the model (evolution of porosity, conductivity, concentration profiles etc.). But some of them represent parameters in further calculations in the model.

First for the calculation of the potential in the diffuse layer, the membrane resistance is needed (see Table 3.1). Even if it would have been possible to calculate directly the potential in the membrane module, our choice was rather using the membrane area specific resistance, so that its value can be monitored as well.

The second important information delivered by the membrane module is the concentration of dissolved gases in the electrodes. We assume a continuity of the concentration of species in an electrode and in the membrane at $y = 0$ (cathode side) or $y = L_{\text{membrane}}$ (anode side). In our model and under our assumptions, two concentrations are relevant for the electrochemical calculations, the concentration of hydrogen peroxide and the concentration of dissolved oxygen, both involved in the chemistry of hydrogen peroxide formation. For the same reason, fluxes of dissolved gases over membrane boundaries are required, in order to solve the Fickian diffusion equations in the electrodes.

Last, as the water balance in the electrodes are calculated outside the membrane model (see also Section 3.5.3.2), the values of the water content $y = 0$ (cathode) and $y = L_{\text{membrane}}$ (anode) are needed, so that it can be calculated whether the difference of the water content in the electrode is positive or negative. That will define for example if the membrane dries out (that means water is transferred from the membrane to the electrode).

3.6 Summary

In this chapter we have presented the two preexisting cell models and how our membrane model can be coupled to them. These models are different in the programming and in the physical approach but through the use of C language for the programming of our membrane, we got a generic module easy to embed in both environments.

The next chapter will then deal with the parameterization and the possible uses of this model to help in the comprehension and the interpretation of experimental observables.

CHAPTER 4

Results and discussion

Le modèle étant établi, il est nécessaire de déterminer les paramètres manquants au fonctionnement complet du modèle. Pour cela, des résultats expérimentaux sont nécessaires.

Dans le cadre de cette thèse, la plupart des expériences utilisées sont extraites de la littérature. Les paramètres manquants du modèle (constantes cinétiques) peuvent ainsi être évalués, en comparant les résultats du modèle avec les résultats d'expérience. Chaque étape de la boucle de dégradation est ainsi paramétrisée et validée expérimentalement. Il s'agit :

- **De l'évaluation des constantes cinétiques de l'adsorption de l'oxygène sur le catalyseur à l'anode lors de la production de peroxyde d'hydrogène.**
- **De la validation de la cinétique utilisée dans l'étape de décomposition du peroxyde d'hydrogène en radicaux via les réactions impliquées dans la chimie de Fenton.**
- **De l'évaluation de la constante cinétique associée à l'étape de scission des chaînes pendantes lors de la dégradation chimique de la membrane.**

Cette paramétrisation a été réalisée grâce aux fonctions d'optimisation de MATLAB/Simulink et assure de la fiabilité du modèle et de l'approche adoptée. Au préalable, le modèle d'électrodes a été validé grâce à des expériences réalisées au sein de LCPEM au CEA Grenoble.

Nous avons utilisé notre modèle de dégradation avec couplage des électrodes pour différents modes de fonctionnement et différentes conditions opératoires, représentant diverses applications pouvant être rencontrées lors du fonctionnement d'une pile à combustible. Le type de mode opératoire peut par exemple être un fonctionnement sous courant continu ou une variation périodique des conditions de courant, oscillant entre deux valeurs extrêmes. Différents types de membranes PFSA ont également été simulées dans des conditions. Selon les réactants utilisés lors de la synthèse de la membrane, il est possible de produire une grande gamme de membranes avec masse équivalente et des longueurs de chaînes pendantes variables. En fixant un critère de fin de vie de pile (dans le cadre de cette étude on a fixé la fin de vie de la pile à une diminution de 5 % du potentiel de cellule inital), le modèle permet de déterminer le temps nécessaire à la cellule. Pour finir, après avoir identifié les paramètres pouvant influer la dégradation chimique,

une analyse de sensitivité a pour finir été effectuée.

De simulations effectuées à courant constant, nous observons que la dégradation chimique est moins importante lorsque la densité de courant augmente. La pression ne semble pas avoir d'effet significatif sur la dégradation chimique, au contraire de la température. En quantifiant la dégradation chimique en termes de production d'ions fluoride, une augmentation de 10 °C de la température augmente par deux la dégradation. Une des conséquences de cette dégradation est une augmentation de la résistance de la membrane. A faibles densités de courant, comme la dégradation chimique est plus sévère, l'augmentation de la résistance de la membranse sera plus élevée. Cependant, compte tenu de la contribution de la valeur du courant dans le calcul des pertes ohmiques, l'impact de la dégradation sera moins prononcé lors de l'observation de l'évolution du potentiel de la cellule. En revanche à densités de courant plus élevées, l'augmentation de la résistance de la cellule est moindre, mais la valeur élevée du courant implique une augmentation des pertes ohmiques plus élevées. Ce phénomène explique les résultats observés dans l'étude de la durée de vie de cellule en fixant un critère observable expérimentalement de fin de vie correspondant à une diminution du potentiel de cellule. La durée de vie des piles sous ces conditions est plus courte à hautes densités de courant qu'à faibles densités de courant.

En appliquant une densité de courant oscillant entre deux valeurs à une cellule, le modèle montre que la dégradation chimique observée est une dégradation intermédiaire comprise entre deux états de référence obtenus lors des simulations à courant constants, ce qui traduit une indépendance de la dégradation chimique à des conditions de cyclage.

En ce qui concerne la nature de la membrane PFSA, le modèle ne montre qu'un impact mineur sur la dégradation chimique.

Expérimentalement, il a été observé que lorsque la quantité d'ions fer présente dans la cellule est élevée et dépasse un certain seuil, la dégradation chimique exprimée en termes d'émission d'ions F^- diminue. Eu égard aux différents paramètres que nous pouvons suivre, nous conclûmes qu'un excès d'ions fer dans la cellule va jouer le rôle de piège à radicaux et ainsi protéger la membrane des attaques radicalaires.

L'analyse de sensibilité montre que l'aspect déterminant dans le contrôle de la dégradation chimique de membranes PFSA est les conditions expérimentales, notamment la température et l'humidité relative dans les gaz aux électrodes. Il a également été mis en évidence que la limitation de l'étape de production de peroxyde d'hydrogène à l'anode ne constitue pas un point essentiel dans la dégradation chimique.

4.1 Introduction

This chapter presents the validation of our model and simulation results obtained within MEMEPhys® simulation package, for different experimental conditions and membrane type. We will focus our analysis on the interpretation of several output of the model, as the cell voltage, the membrane resistance or the cumulative fluoride released for example.

When we simulate the behavior of a cell, we give as inputs parameters which not necessarily define a stable state for the cell. The models will then first drive the cell to a stable state and consequently adjust the parameters. We call this phase the numerical preconditioning phase. It usually takes about 20 simulated hours at the beginning and the relevant part for the study of the chemical degradation is then beyond these first 20 hours. This effect can be seen in Figure 4.1, where the first 20 h are needed by the model to reach a steady state.

The second point to be explained is in the calculation of the potential at zero current. OCV is not calculated in MEMEPhys® through Nernst equation but calculated as a potential difference between cathode and anode at zero current. To calculate the cathode potential, the ORR mechanism used in this PhD thesis (as presented in Reaction 3.10 to Reaction 3.14 in Section 3.2.4.2) is the empirical Damjanovic's pathway [152]. Franco showed that the calculation of the cathode potential at zero current with this mechanism mathematically returns multiple solutions [132]. Because of this we consider here that a small current density ($0.04 \cdot 10^{-2}$ A·cm^{-2}) is representative of open circuit. As the application of a non-zero current density will activate the cell, we observe effects on the response of several model parameters. In Figure 4.1, we plotted the evolution of the relative humidity for two current conditions. For a 25 cm² geometric area membrane, we applied 0 A and 1 A absolute current. As is can be seen, the small amount of water produced by applying a non-zero current induces an increase of the relative humidity. The difference remains not so significant, as the high stoichiometry ensures a quick removing of the produced water. Figure 4.2 shows the same simulation with decreased stoichiometries. In that case, the differences are more important. In Figure 4.3, we represented the evolution of the water content in the membrane for the different current conditions. We see that the membrane contains more water and consequently will present better proton conductivity. At 0.04 A·cm^{-2}, the water content is unbalanced compared to OCV conditions. This will then impact the cell resistance.

To mitigate this problem, we will then in this work perform simulations at high stoichiometry, so that our low current simulations are close to what would be expect under OCV conditions.

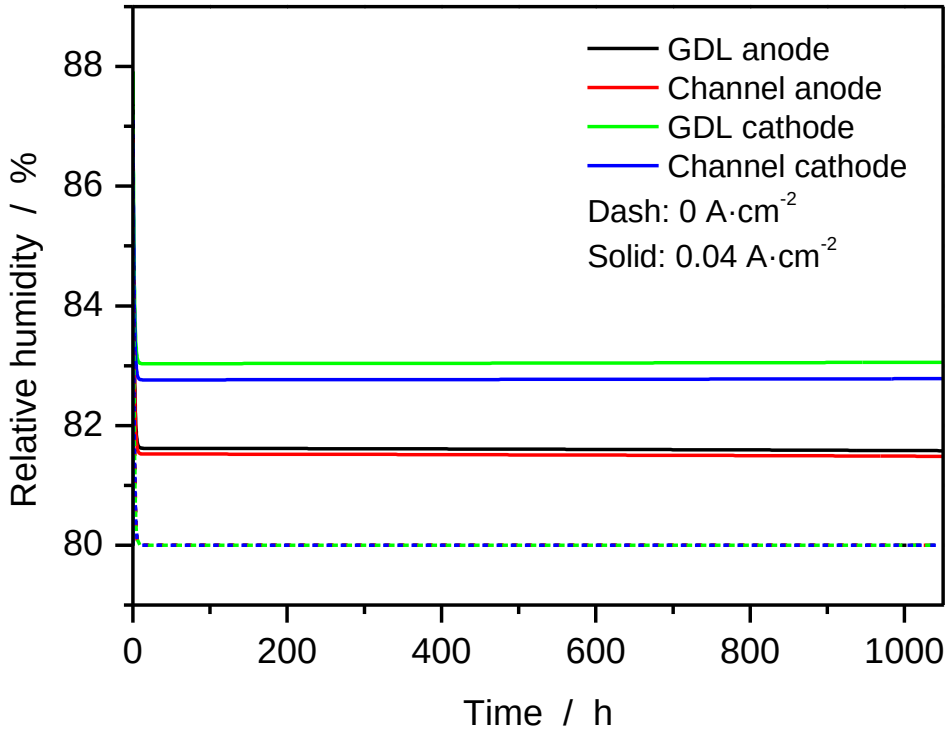

Figure 4.1: Evolution of relative humidity in GDLs and channels for different current densities at 353 K, 2 bar and 15/20 stoichiometry and 80% / 80 % RH anode/cathode.

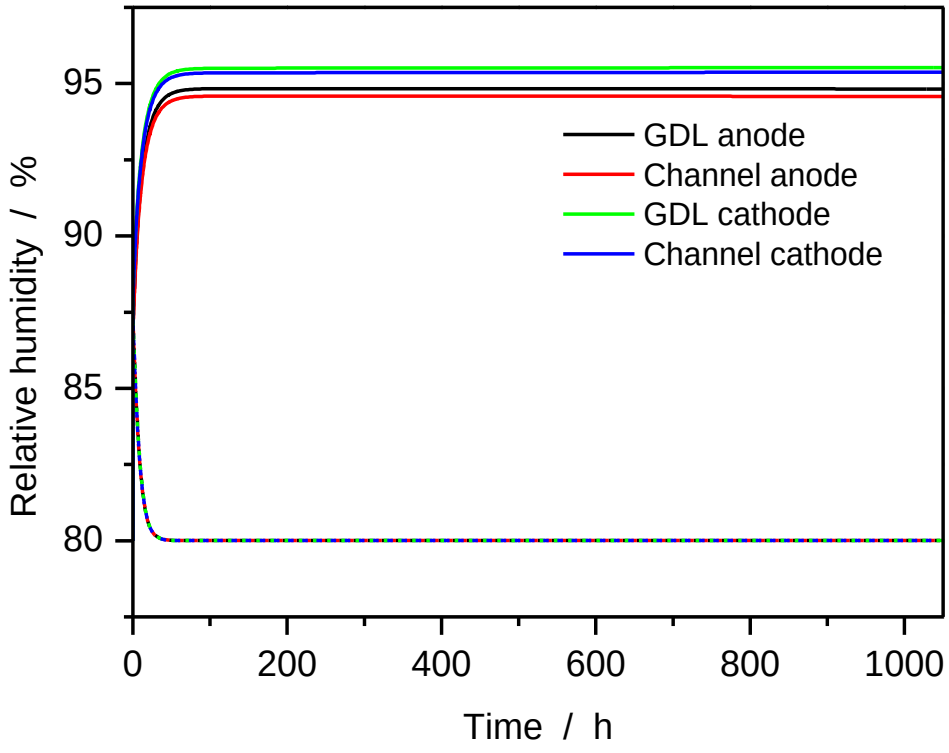

Figure 4.2: Evolution of relative humidity in GDLs and channels for different current densities at 353 K, 2 bar and 2/4 stoichiometry and 80% / 80 % RH anode/cathode.

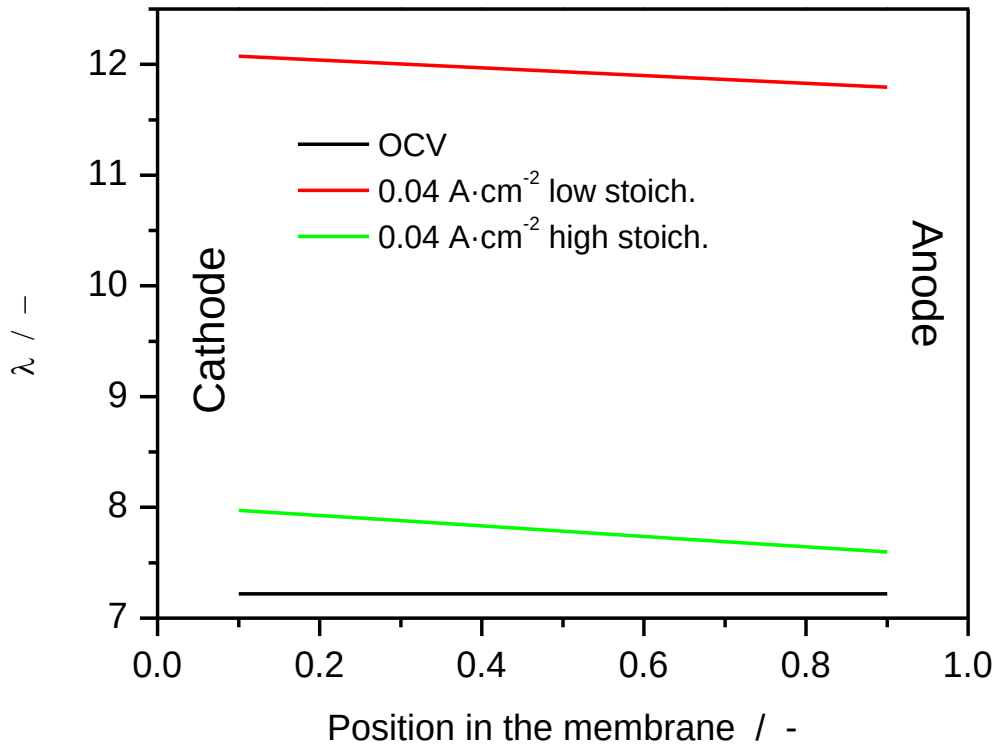

Figure 4.3: Steady-state water profile in the membrane for different current conditions at 353 K, 2 bar and 80% / 80 % RH anode/cathode.

4.2 Model parameterization and evaluation

4.2.1 Presentation of the "standard" cell used in the simulations

In a PEMFC, many parameters having an influence on the response of the cell can be controlled. In the present chapter, we will distinguish the experimental condition parameters from the cell design parameters and the stress applied to the cell (we mean here the current load condition, which we separate from physical experimental parameters). Table 4.1 presents a list of the parameters which can be viewed as potentially relevant for the degradation of the cell. Some of the parameters have an impact rather on the cell performance, other on the chemical degradation. For example, it is obvious that if we increase the platinum load in the electrodes, the performance will be better than for lower load, but that would not necessarily mean that their impact on the chemical degradation is significant.

Experimental condition	Cell design	Applied stress
• Temperature	• Membrane thickness	• Constant current

• Pressure • Relative humidity • Production of irons ions by the system • Gas stoichiometry	• Electrode surface • Platinum load anode • Platinum load cathode	• I_{min} - I_{max} signal • On - off signal • Real automotive cycle

Table 4.1: Variable parameters in the simulations

As the interpretations of results are very complex when varying several parameters at the same time, we focus every time on the impact of one parameter on the response of the cell. For this reason, we define a standard cell, which is the cell whose properties are used in this chapter if no other indications are given. All these parameters are summarized in the Table 4.2.

Parameters	Value	Unit
Membrane thickness	60	µm
Anode thickness	10	µm
Cathode thickness	10	µm
Electrode geometrical area	25	cm^2
Pt load cathode	0.45	$mg \cdot cm^{-2}$
Pt load anode	0.25	$mg \cdot cm^{-2}$
Equivalent weight	1100	$g \cdot eq^{-1}$
Concentration of side chain	1200	$mol \cdot m^{-3}$
GDL thickness	265	µm
Electrochemically active surface area	0.3639	m^{-1}

Table 4.2: Main structural parameters of our *standard* PEMFC

The validation and parameterization of the model is divided into several steps, following the scheme suggested in Figure 2.6. We first validate the performance model, then regarding the degradation model, we validate successively the production of H_2O_2 in the membrane, its decomposition into radicals and at last, the radical attack on the membrane.

4.2.2 Electrochemical model

4.2.2.1 Parameterization of the electrode model

Even if the developed model aims on the prediction of the effect of the chemical degradation of the membrane on the cell, it is first important to ascertain that the results provided by the model without degradation are reliable and lies in a range which is comparable with measurements what could be experimentally observed. The variety of outputs available from experiments is quite low regarding the amount of parameters in such a complex multiscale model as the electrode model used in the ME-MEPhys® approach. However it is possible to get some of the needed parameters through other complementary modeling approaches: as our description of chemical and electrochemical phenomena is based on the elementary kinetics and not on the global kinetics, it is difficult to precisely know the kinetics data linked to these reactions. For that purpose, atomistic tools like density functional theory (DFT) or *ab-initio* calculations are powerful tools to get, for example, an idea of the range of the activation energies for every elementary steps of a given reaction. Ongoing efforts within this direction are being made by Ferreira de Morais *et al.* within Franco's group and became recently available [153].

In this PhD thesis work, the kinetic pathways were assumed and the kinetic parameters for ORR and HOR were fitted. Table 4.3 sums up all the Gibbs activation energies which are used in the simulations of this chapter.

Reaction	Elementary step	$\Delta G_i^{\neq}$ - $\Delta G_{-i}^{\neq}$ / kJ·mol^{-1}	Ref.
HOR	$H_2 + 2\,(Pt) \rightleftharpoons 2\,H(Pt)$	–68 / 68	Fitted
	$H_2 + (Pt) \rightleftharpoons H(Pt) + H^+ + e^-$	34 / –34	Fitted
	$H(Pt) \rightleftharpoons H^+ + e^- + (Pt)$	–53 / 53	Fitted
ORR	$O_2 + 2\,(Pt) \rightleftharpoons 2\,O(Pt)$	–50 / 50	Fitted
	$O(Pt) + H^+ + e^- \rightleftharpoons OH(Pt)$	–67 / 67	Fitted
	$O_2 + H^+ + (Pt) + e^- \rightleftharpoons O_2H(Pt)$	–62 / 62	Fitted
	$O_2H(Pt) + H_2O + 2\,(Pt) \rightleftharpoons 3\,OH(Pt)$	–70 / 70	Fitted
	$OH(Pt) + H^+ + e^- \rightleftharpoons H_2O + (Pt)$	–62 / 62	Fitted

Table 4.3: Gibbs activation energies for elementary steps (chemical and electrochemical) for the HOR and the ORR.

4.2.2.2 Experimental setup

The CEA laboratory of fuel cell components, electrolyzers and modeling (LCPEM) is involved in lot of European projects dealing among other with durability and degradation issues. One of these, named DECODE, focuses on the comprehension and elucidation of degradation mechanisms in PEMFC with special focus on the influence of liquid water [40]. We have received experimental results of this project at LCPEM from Dr. Escribano. In Table 4.4, the main parameters used during the experiment are summed up. The MEA used in this project was not Nafion® but Aquivion E79-03, whose molecular structure is slightly different than the one of Nafion® (see Figure 4.4). Its equivalent weight is 790 $g \cdot eq^{-1}$and it is only 30 µm thick.

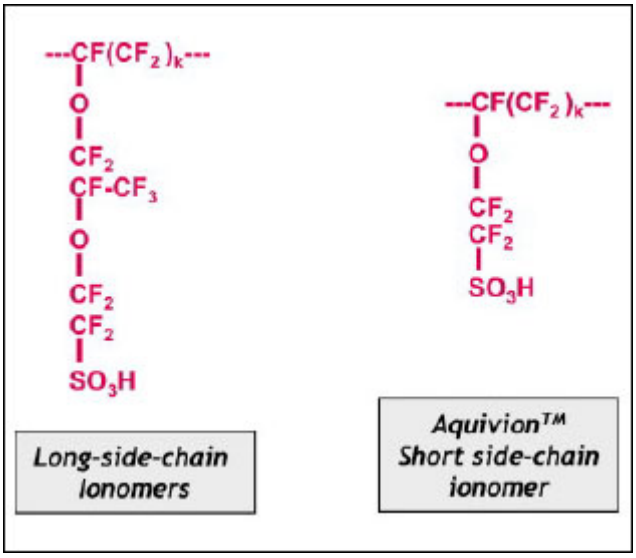

Figure 4.4: Comparison of the chemical structure of Nafion® (left) and Aquivion (right)

As we first regard the performance at the beginning of the experiment, the chemical degradation could not already have occurred. Thus the performance model is still usable, as long the equivalent weight and the membrane thickness used in the simulations still set equal to the experimental values.

Parameters	Value	Unit
Temperature	80	°C
Pressure	1.5	bar
Relative humidity anode	60	%
Relative humidity cathode	40	%
Pt load cathode	0.45	$mg \cdot cm^{-2}$

Pt load anode	0.25	$mg \cdot cm^{-2}$
Membrane thickness	30	µm
Equivalent weight	790	$g \cdot eq^{-1}$

Table 4.4: Parameter used in the experiment displayed in Figure 4.5.

4.2.2.3 Comparison between the experimental and the calculated performance

In Figure 4.5, we present the comparison of experimental results with our simulations results. As we can see, the ranges of the results are comparable.

As it can be seen in Figure 4.5, the range and the trend of the simulated results is in agreement with the experimental data for a current density value between 0.4 and 1.0 $A \cdot cm^{-2}$. Out of this range, a little discrepancy is observed, but we neglect it, as for a PEMFC, the current density value when the cell is working is between this range of 0.4 – 1.0 $A \cdot cm^{-2}$. To parameterize our model, we had to fit the kinetic parameters for the reactions in Table 4.3. As we had only one set of experiment for comparison with our simulations, the combination of possible values for Gibbs energy is countless and we decided to keep the data in Table 4.3 as reference for our calculations, aware that through *ab-initio* calculations, it is possible to get a more reliable estimation of the kinetic parameters we evaluated.

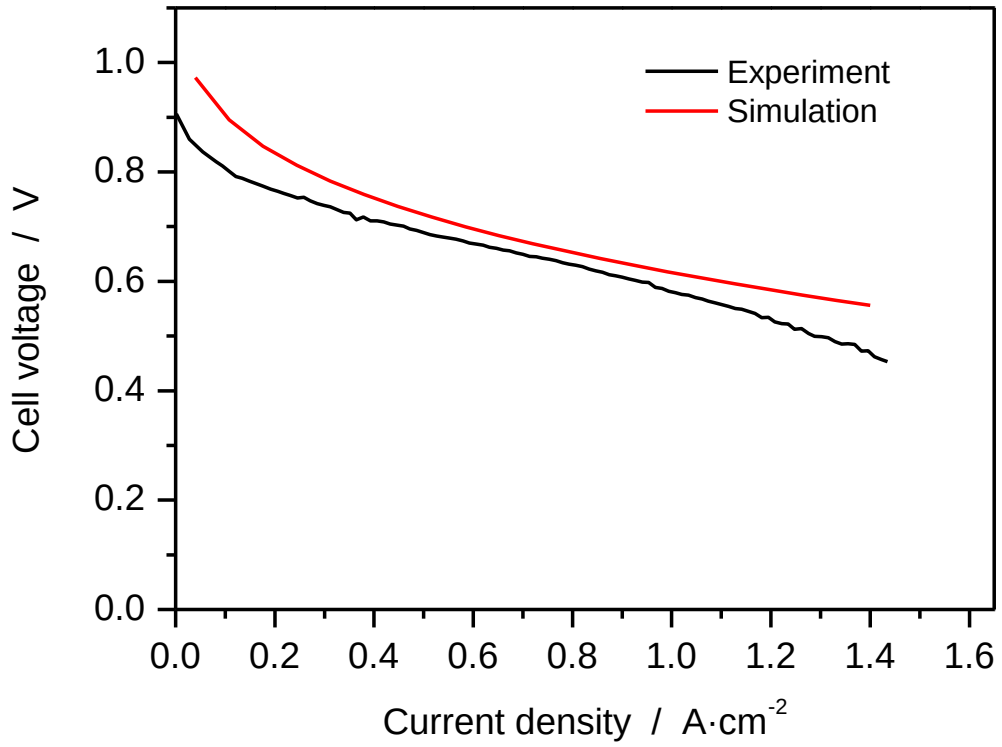

Figure 4.5: Comparison experiment / simulation for validation of the performance model ME-

MEPhys®. Experiment has been carried out at 353 K, 1.5 bar, 40 % / 60 % RH anode / cathode.

This constitutes the starting point for all of our simulations. Modeling does not pretend to simulate the reality with an accuracy of 100%.The main purpose of this work is the modeling of the chemical degradation of the membrane and the evolution of the cell performance, not the absolute value of the cell performance. Thus the starting point of the model can be this approach for cell performance and we can now focus on the validation of our membrane chemical degradation model, before going into prediction studies with our model.

4.2.3 Chemical degradation model

4.2.3.1 Introduction

The performance model developed with the MEMEPhys® approach represents a rigorous physical basis to ensure a good reliability of our membrane degradation model. As it has been reported in Section 1.3, the chemical degradation can be depicted through several experimental observations.

Our membrane degradation model is divided into several parts, respecting Figure 2.6:

- Production of hydrogen peroxide, consequence of the oxygen permeation through the membrane from the cathode to the anode
- Decomposition of the produced H_2O_2 into radicals through the Fenton mechanism
- Attack of the radicals on the membrane, leading to the degradation of the membrane and the releasing of fluoride ions into the cell.

We focus our parameterization and validation on these three points. The aim of this part of the work is the insurance of reliable results about chemical degradation.

4.2.3.2 Production of hydrogen peroxide

4.2.3.2.1 Parameterization based on literature

Several reports in the literature show interest in the presence of hydrogen peroxide in fuel cell [18, 33]. For our parameterization, we choose the experimental results published by Liu and Zuckerbrod [18]. The experiment we refer to is presented in Figure 1.21 in Section 1.3.3. They used Nafion® with different thicknesses and ran the cell under the conditions as presented in Table 4.5 . On a separate way, they measured the CV response of different concentrations of hydrogen peroxide in sulfuric acid conditions so that they somehow had a calibration of the CV measurements. *In situ*, they measured the CV

response of the cell and deduced the concentration of hydrogen peroxide produced in the cell. The advantage of these measurements is that they have been done for several membrane thicknesses. Thus after having parameterized our simulation for a given thickness, we can test it by varying the membrane thickness and comparing the simulations with experiment results.

Parameters	Value	Unit
Current density	OCV	-
Temperature	60	°C
Pressure	1	Bar
Relative humidity anode	100	%
Relative humidity cathode	100	%
Membrane thickness	variable	µm
Equivalent weight	1200	$g \cdot eq^{-1}$

Table 4.5: Experimental parameters used by Liu and Zuckerbrod

4.2.3.2.2 Simulations parameters and assumptions

In Section 2.3.1, we proposed a mechanism describing the H_2O_2 production. For these reactions, we need the activation energies, so that Equation 3.17 can be used. Ferreira de Morais, within Franco's group performed DFT calculations for the oxygen reduction on platinum surface and obtained a set of activation energy values both for H_2O_2 production reaction [84]. The values of these activation energies are given in Table 4.6. However parameters for oxygen adsorption and desorption on the catalyst surface (Reaction 3.6) were not known and parameters found in the literature did not seem to be determined under conditions close to the environment we simulate and thus no good agreement was obtained compared to our objectives. Thus we fitted these values, so that the produced amount of H_2O_2 calculated by the model fits with experimental results. With the genetic algorithm embedded in Matlab, we could set as aim the quantity of hydrogen peroxide for a 30 µm membrane and get the desired parameters.

As in our complete degradation model hydrogen peroxide is decomposed into radicals, we switched off the further degradation steps in the membrane (H_2O_2 decomposition through Fenton's reactions and radical attack on the membrane), so we can follow the concentration of produced H_2O_2. Moreover, considering that the production of hydrogen peroxide is a continuous phenomenon, one could expect that over time the concentration will increase. As we do not know their experiment duration, we de-

cided when to stop the simulation and save the value. This was set to 10 minutes.

Reaction	Elementary step	$\Delta G_i^{\neq}$ - $\Delta G_{-i}^{\neq}$ / kJ·mol^{-1}	Ref.
H_2O_2 formation	$O_2 + (Pt) \rightleftharpoons O_2(Pt)$	30 / 34	Fitted
	$O_2(Pt) + H(Pt) \rightleftharpoons HO_2(Pt) + (Pt)$	publication in preparation	[84]
	$HO_2(Pt) + H(Pt) \rightleftharpoons H_2O_2(Pt) + (Pt)$	publication in preparation	[84]
	$H_2O_2(Pt) \rightleftharpoons H_2O_2 + (Pt)$	pubication in preparation	[84]

Table 4.6: Gibbs activation energies for elementary steps for the H_2O_2 formation

4.2.3.2.3 Comparison between experiment and simulation

To check the domain of validity of our model parameterization, we compared calculated and experimental concentrations of H_2O_2 for different membrane thicknesses.

In Figure 4.6, we represented the comparison between experimental and simulation results. As it can be seen, the trend and the range of the values obtained by simulations are in good agreement with the experimental results. As previously mentioned, the value for a 30 µm thickness shows the best agreement, as the activation energies were fitted for this thickness. It seems that the hydrogen peroxide production is overestimated for thicknesses lower than 30 µm and lightly underestimated between 30 and 120 µm. But globally, if we consider that the thickness range of Nafion® membrane is 30 to 100 µm in the current applications, the simulated values in the desired thicknesses remain close to experimental ones and we can say with a confidence that the model provides reliable concentrations for H_2O_2 concentration. Regarding the degradation loop, the following step is the decomposition of the produced H2O2 through Fenton chemistry. We can now focus on the verification that our assumptions for the Fenton chemistry are justified and lead to results that are still in balance with what can be experimentally observed.

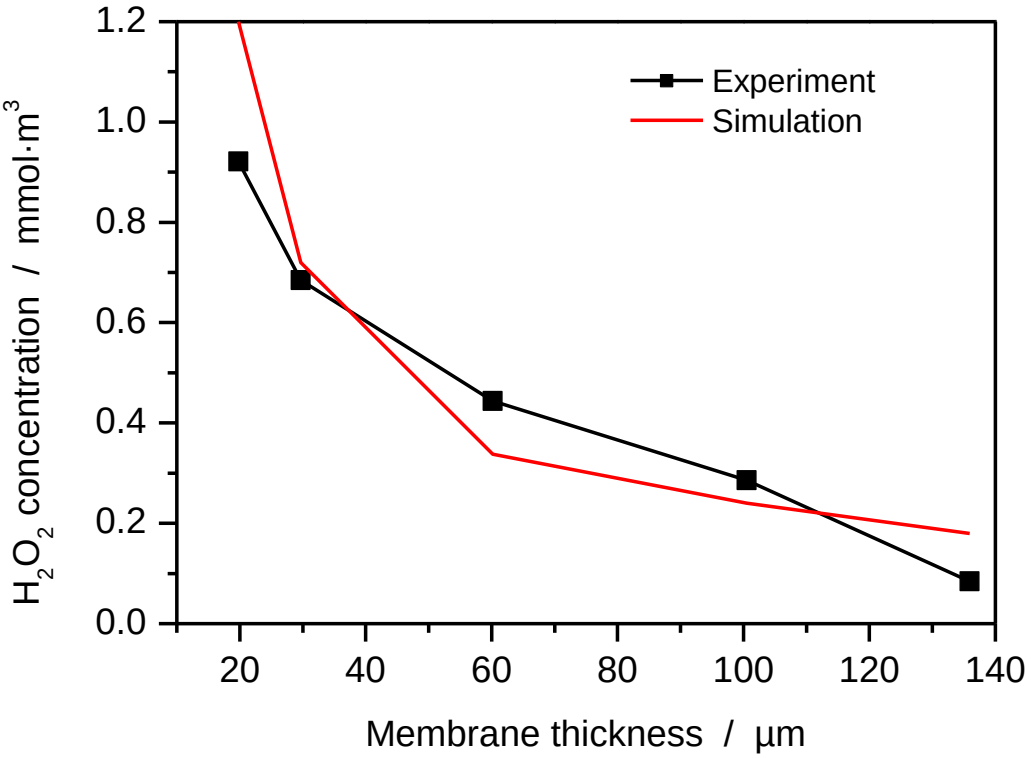

Figure 4.6: Comparison experiment / simulation for the hydrogen peroxide production

4.2.3.3 Fenton chemistry and production of radicals

4.2.3.3.1 Literature experiment

The decomposition of hydrogen peroxide through reaction with iron ions has already been widely studied since the 1890s by Henry Fenton. It is a useful reaction for the oxidation of organic compounds in water, as the produced radicals are highly oxidative species and can attack even the most stabile pollutants in water [23, 24, 157].

But in a PEMFC, this reaction may be dramatic, as the presence of radicals in the system will lead to a chemical attack on the membrane, degrading the cell integrity. However, even if we know that they are present in the system, they are such reactive species that their lifetime lies of about 1 ns. Thus their direct observation is really complex and needs specifically and complex experimental devices like ESR or EPR. Some articles report the results of the application of such methods [28-30, 92]. We took a closer look on the work by Aoki *et al*. [91]. They performed ESR measurements to quantify the amount of radicals produced in the membrane after different treatments. The one of interest for us was conducted on a membrane soaked in Fenton's reagent for 5 minutes (see more precision in Table 4.7). They found out that the quantity of produced radicals is independent of the nature of the membrane.

Parameters	Value	Unit
Temperature	20	°C
Environment	0.3 wt% solution with 2 ppm Fe^{2+} ions	
Experiment duration	5	min

Table 4.7: Experimental parameters used by Aoki *et al*.

4.2.3.3.2 Simulations parameters and modeling assumptions

As Fenton chemistry has been widely investigated, the reaction rates we consider for the decomposition of hydrogen peroxide into radicals (Reaction 2.1 to Reaction 2.5) are available in literature. Table 4.8 reports the kinetic rates at 303 K we have used in our simulations.

Reaction	Elementary step	k_{Fenton}(303 K) / s^{-1}	Ref.
H_2O_2 decomposition	$H_2O_2 + Fe^{2+} + H^+ \rightleftharpoons Fe^{3+} + HO^{\cdot} + H_2O$	$63 \cdot 10^{-3}$	[106]
	$H_2O_2 + Fe^{3+} \rightleftharpoons Fe^{2+} + HOO^{\cdot} + H^+$	$2 \cdot 10^{-6}$	[108]
	$HOO^{\cdot} + Fe^{3+} \rightleftharpoons Fe^{2+} + O_2 + H^+$	$3.3 \cdot 10^{2}$	[107]
	$H_2O_2 + HO^{\cdot} \rightleftharpoons H_2O + HOO^{\cdot}$	$3.3 \cdot 10^{4}$	[105]
	$HO^{\cdot} + Fe^{2+} + H^+ \rightleftharpoons Fe^{3+} + H_2O$	$3.3 \cdot 10^{5}$	[104]

Table 4.8: Kinetic rates of Fenton's chemistry used in our model

Aoki soaked a membrane without any other cell parts. To compare our simulation results with his experimental ones, we ran our membrane model alone. As the production of iron ions and hydrogen peroxide are both linked to electrodes, we modified the code so that it was possible to run simulations with non-zero initial conditions for the concentration of iron ions and hydrogen peroxide and thus, simulated a membrane in a batch with defined concentrations of iron ions and hydrogen peroxide.

As the results of Aoki *et al*. showed results independent to membrane, we ran the simulations with the standard value of our membrane thickness.

4.2.3.3.3 Comparison between experiment and simulations

In Figure 4.7, we present the results of Aoki *et al*. The second balk is the one of interest for us. The absolute amount of HO radical produced after 5 minutes is estimated at 20-30 nmol. The modeling

results are shown in Figure 4.8. After 5 min, the simulation shows a very low HO radical concentration. Simultaneously, the concentration of HO_2 radical increases up to 0.13 mmol·L^{-1}.

To compare with the results of Aoki, we convert them into an absolute amount of radical. Considering our standard cell membrane with 25cm² geometric area and 60 µm thickness, this leads to an absolute amount of $0.13 \cdot 60 \cdot 10^{-6} \cdot 25 \cdot 10^{-4} = 19.50 \cdot 10^{-9}$ mol = 19.50 nmol. This is a good agreement with Aoki's work. But it remains explaining why our HO_2 radical concentration value and not our HO radical concentration is comparable to the work of Aoki *et al*.

They are using spin trap reagent (DMPO) in their experiment. This molecule reacts quickly with HO radicals to form DMPO-OH adduct, thus the radicals do not have the possibility to evolve after reactions of Table 4.8. In our case, the HO radicals are not trapped and can then be involved in other reactions of the Fenton's chemistry. More particularly in Reaction 2.4: HO radicals can react with a quite high kinetic rate with H_2O_2 to form HO_2 radicals. This explains why we compared the total amount of radicals in our model with HO radical amount measured by Aoki.

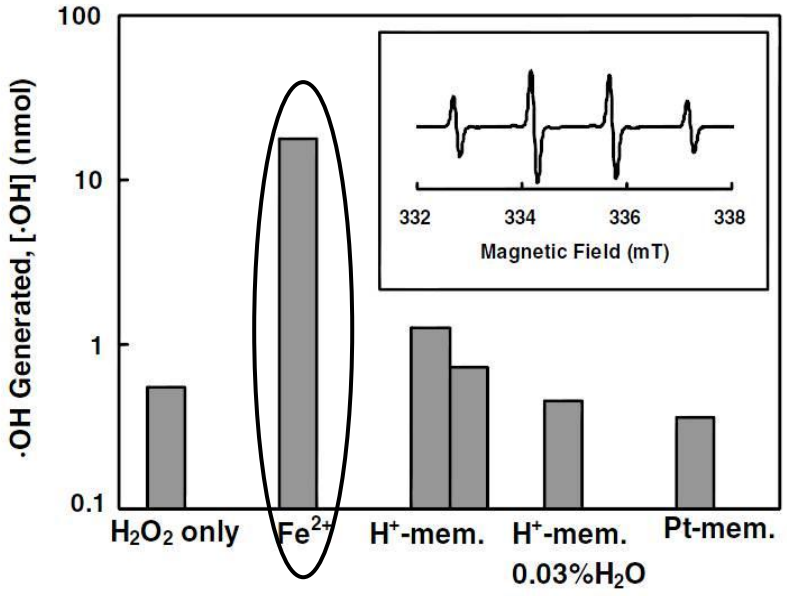

Figure 4.7: Hydroxyl radical generated in membrane in different solutions [91]

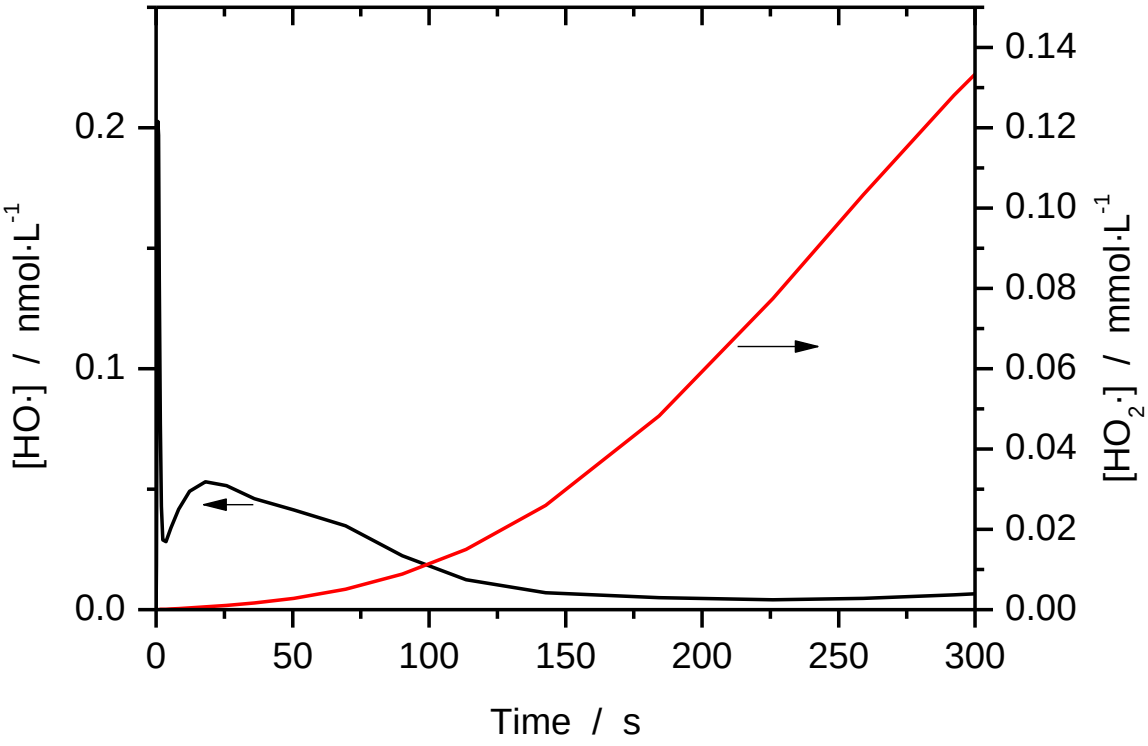

Figure 4.8: Evolution of the radical concentration in a Nafion® membrane starting from conditions given in Table 4.7.

The kinetic rates for the Fenton's reactions are usually given in the literature at room temperature, as these reactions are used for waste water treatment. In our case, as we will operate at higher temperature, we should take into account the thermal effects on the Fenton's chemistry. For that, we use a simplified approach to calculate the reaction rate at any temperature knowing the reaction rate at a reference temperature as

$$k_{\text{Fenton}}(T) = \frac{T}{T_{\text{ref}}} \cdot k_{\text{Fenton}}(T_{\text{ref}}) . \qquad 4.1$$

Equation 4.1 is derived from the definition of the reaction rate. As a first approach, we can consider that the ratio $k_{\text{Fenton}}(T) / T$ is constant and thus is possible to estimate the temperature dependence of the reaction rate knowing a reference value. Considering the production of radicals, we see that our model is validated. Radicals are produced at very low concentrations in the cell and they can react through many ways. However we are now sure that the absolute amount which is produced by the model is in a correct range.

To complete our degradation model, one essential parameter is missing, that one related to the effec-

tive reaction of the membrane degradation.

4.2.3.4 Degradation of the membrane and releasing of fluoride ions

4.2.3.4.1 Experimental studies

For our parameterization, the experimental results we choose were published by Young *et al*. [16]. They measured over time the cumulative production of fluoride ions of a cell under accelerated test conditions, as mentioned in Table 1.4. A summary of the experimental parameters are given in Table 4.9. During their experiment, they sometimes shut down the cell for running extra analysis. We removed the part were the cell was not operating anymore and got a shorter experiment for our validation (the duration of the experiment was reduced from 450 h to about 290 h, as it can be seen in Figure 4.9). This was also used for our parameterization.

Parameters	Value	Unit
Current density	OCV	
Duration	450 (corrected 290)	h
Pressure	2	bar
Temperature	90	°C
Membrane thickness	60	µm
Equivalent weight	1100	$g \cdot eq^{-1}$
Relative humidity	100	%
Pt load cathode	0.60	$mg \cdot cm^{-2}$
Pt load anode	0.30	$mg \cdot cm^{-2}$

Table 4.9: Experimental parameters used by Young *et al*. for the determination of cumulative fluoride ions released under AST.

Last they plotted the cumulative release of fluoride ions, and our model computes instantaneous concentration. Thus we had to integrate our output signal to be able to compare experiment and modeling results.

4.2.3.4.2 Simulations parameters and modeling assumptions

As assumed in Section 2.3.2, side chain degradation is supposed to drive the production kinetic of fluoride ions, which is one of the most reported measurements in the literature to follow the chemical degradation of the membrane. According to Equation 2.27, to get the concentration of fluoride ions, we have to determine the evolution of the side chain concentration in the membrane. For that purpose, one parameter is still needed, and this is the last one to determine to complete our degradation model.

The value of the kinetic constant of the side chain degradation we are searching is used in Equation 2.25. The rewriting of Equation 2.25 applied to side chains in the membrane leads to Equation 4.2,

$$\frac{\partial c_{\text{sidechain}}}{\partial t} = k_{\text{DEG}} \cdot c_{\text{HO}\cdot} \cdot c_{\text{sidechain}} \cdot \qquad 4.2$$

It has been shown that iron ions do have an important impact on the chemical degradation of the cell, as they play a key role in the Fenton chemistry (Reaction 2.1 to Reaction 2.5 in Section 2.3.1). However it is difficult to predict if iron ions will be produced by the system, as the origin of the iron ions remains a widely open question. Our assumption here is that the iron ions are produced by the bipolar plate at the cathode, where the simultaneous presence of water, metallic iron and a high potential could lead to the oxidation of iron metal into iron ions. To model that in a simple way, we add a constant source term for iron ions at the cathode / membrane interface, noted $\dot{S}_{Fe^{2+}}$, which is then included in the mass balance equation and thus taken into account in Equation 2.26. Its value will vary depending on the system we will simulate: Low values for cell with low end-plate degradation (for example), higher values for high end-plate degradation. For the purpose of our parameterization, we choose the value of $3 \cdot 10^{-5}$ mol·m^{-3}·s^{-1}.

4.2.3.4.3 Comparison between experiment and simulations

We had two unknown parameters and only one experiment result to exploit. By setting the production term of iron ions at the cathode, we eliminate one parameter. To determine then the missing reaction rate constant, we proceeded through the same analytical procedure as for the missing Gibbs activation energies in Section 4.2.3.2. We used the optimization toolbox of Matlab, and set as end value the cumulative fluoride amount measured by Young et al. at the end of their experiment (450 h real, 290 h if we ignore the shutdown phase). Setting a fixed rate of production of iron ions at the cathode of $3 \cdot 10^{-5}$ mol·m^{-3}·s^{-1}, the best compromise we found for the side chain scission reaction rate was 4.5 s^{-1}. This value depends on the rate of iron production. If more information were provided concerning the production of iron by the system, we may have parameterized our model on a more reliable way.

Young *et al*. carried out their experiment a high temperature (for a common Nafion® membrane), that is to say 90 °C. As we simulate cases where the temperature is up to 30 °C lower as well, we have to take into account the thermal effects for the chemical degradation. From the value of 4.5 s^{-1} we got from the parameterization, we deduced an approximation of Gibbs activation energy for the degrada-

tion reaction. For that, we inserted into Eyring's equation (Equation 3.17) the reaction rate constant which was found for 363 K. We found out a Gibbs activation energy of roughly –84 $kJ \cdot mol^{-1}$. Table 4.10 presents the calculated values for the kinetic rate of the degradation in dependence on the temperature. As it can be seen, the degradation is about two times faster when the temperature increases of 10 °C, which cannot be neglected in our further simulations.

Temperature / K	k_{DEG} / s^{-1}
333	0.325
343	0.820
353	1.960
363	4.480

Table 4.10: Thermal evolution of the side chain degradation kinetic rate

In Figure 4.9, we can see that with the value of kinetic rate for the chemical attack of radicals on side chain, we obtain a good agreement in shape and range of the total amount of fluoride released by the cell. In the literature, we found numerous experiments, all presenting different cells under different conditions. The specificity of these experiments is that usually the presence of iron ions is neither controlled nor identified. But the fact is that the membrane degrades. We choose this set of experiment because its comprehension is easier compared to other measurements for two reasons:

- The experimental parameters were completely described and given
- The representation of the results as cumulative fluoride release gives a good representation of the degradation. Other literature sources give their results as fluoride emission rate (in $mol_{F^-} \cdot cm^{-2} \cdot h^{-1}$), which is less explicit than the integrate form of the results.

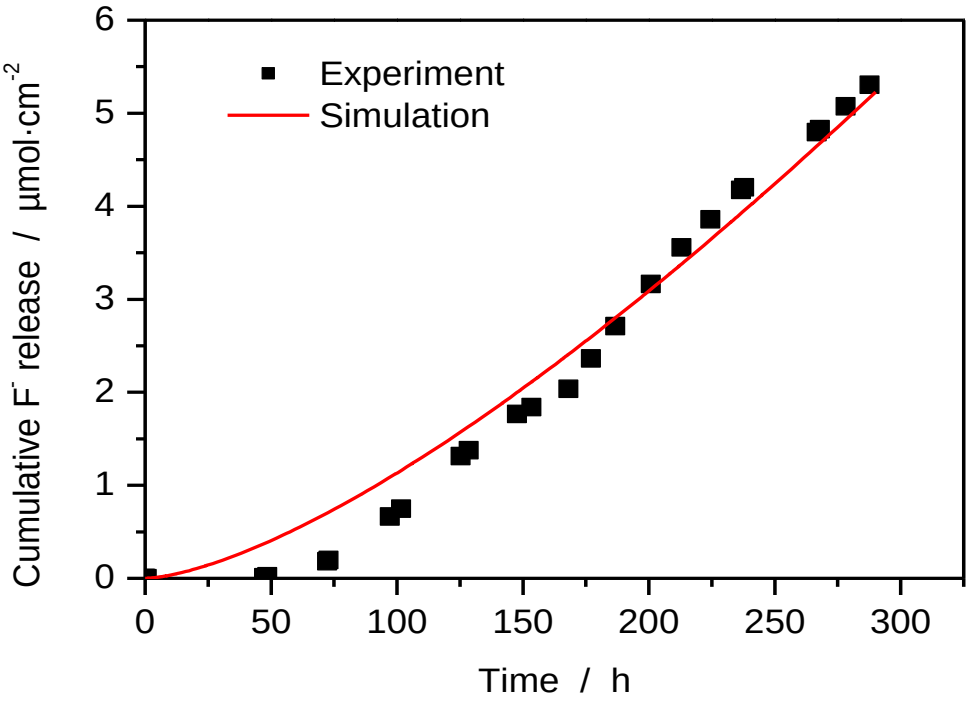

Figure 4.9: Comparison experiment / simulation for the cumulative production of fluoride ion

We are now sure that the use of our model would not give results that are unrealistic. We aim then our work on the prediction of trends with the help of our model.

The results in the next part do not pretend to give accurate results of what would be experimentally observed, but rather pretend to give trends on cells behaviors under different architectures, stresses and experimental conditions, that could constitute some guidelines for engineering enhancement of the PEMFC durability.

4.2.4 Influence of experimental conditions on chemical degradation

An increase of the temperature translates into a higher degradation rate of the membrane. As a first approximation, we can say that an increase of 10 K of the temperature will double the effect of the cumulative fluoride production, which refers to the thermal evolution of the side chain degradation kinetic rate (Table 4.10). This confirms the importance of thermal effects on the different kinetic rates of the model. This result is in agreement with experimental work which can be found in the literature. Kodama *et al*. presented results were they degraded ex-situ Nafion® membranes in hydrogen peroxide [158, 159]. Even if the range of their results cannot be compared with our modeling results (we simulated the operation of a complete fuel cell), the trend is in agreement with the evolution of the degradation with temperature what we get from the simulations. If we compare the evolution between 60 °C

and 80 °C on one side and beyond 80 °C on the other side, we see a difference in the slope of the degradation with temperature. This is also observed in our simulations. This indicates that the degradation processes accelerate at high temperature. The comparison between their experiments and our simulations is given in Figure 4.10

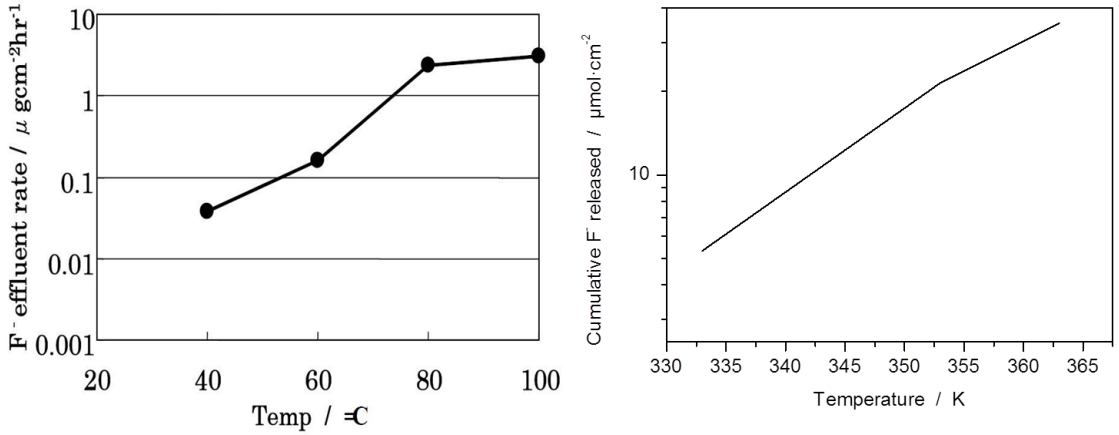

Figure 4.10: (left) F^- effluent rate from Nafion® 112 (7.2cm × 7.2cm) in 1wt% H_2O_2, 8 h with 10ppm Fe2+ [158, 159], (right) Simulated evolution of the fluoride release with temperature (production of Fe^{2+} set to 10^{-3} mol·m^{-3}·s^{-1}, duration 500 h).

This was also observed by Chen and Fuller [37]. As they did not display their results logarithmic axes, the increased degradation while the temperature increases is easier to be seen and we compared their results with our simulations in Figure 4.11.

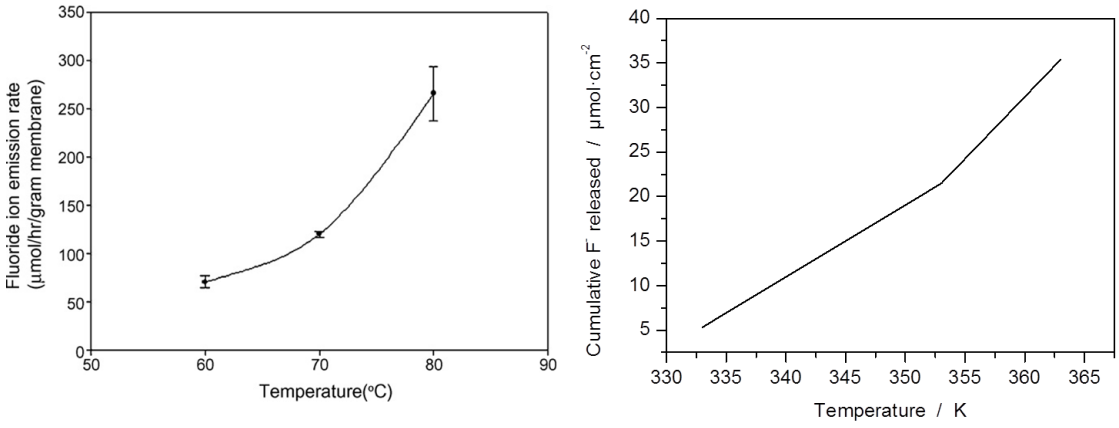

Figure 4.11: (left) Degradation rates under different temperatures (Fe^{2+} fixed at 30 ppm) [37], (right) Simulated evolution of the fluoride release with temperature (production of Fe^{2+} set to 10^{-3} mol·m^{-3}·s^{-1}, duration 500 h).

4.2.5 Validity of the model

We propose in this work prediction tool for evolution of PEMFC performance when chemical degradation is taken into account in the cell. This phenomenon is very difficult to treat, as its occurrence is barely predictable because of the need of iron ions in the system. Even if the chemical degradation of the membrane is an actor of cell failure, it is not the major contributor for cell failure [70]. Thus it is more difficult to give rise to its impact on the degradation of cell performance. However, through the simulated fluoride emission, it is possible to see how severely the membrane is attacked.

Like every modeling work, it relies on assumptions and approximations. The purpose of this Section is to analyze the reliability of the results we obtained in this chapter.

The model we developed in this thesis is to our knowledge the first one in the literature which explicitly correlates the chemical degradation of the cell and their impact on the cell properties and performances. As the model is complex and multiscale, it requires lot of parameters which are not necessarily available in the literature. To solve this problem, comparisons with similar system allow knowing the range of missing parameters, for example the diffusion coefficients of species in PFSA membrane.

The core of the performance model, the electrodes, are complex and relies as well on the knowledge of kinetics parameters which are the results of atomistic simulations, and thus, if the data are not available, fitting remains the only way to complete the electrodes models. In an updated model, thanks the work of Ferreira de Morais *et al.* the ORR mechanism is better known [84, 153].

The last point which should be noticed on our model is the quantification of the influence of iron ions. To reproduce experimental results, we had to simulate cells whose iron ions production is unrealistic. We assume the cause is our assumption on the Fenton chemistry. We assume only a limited number of possibilities for the iron to react. In a real system, possibilities are higher, as the iron ions could react in a more complex way, as displayed in Appendix B.

But our model returns results which are consistent with experimental observations made. We validated the model by reducing as much as possible the number of parameters to fit fitting lot of parameters and rely on data available in the literature. The degradation model, even if it has been simplified, provides good agreement with experimental results. As our modeling work is flexible, any improvement can then be implemented to make the simulations more accurate.

4.3 Impact of chemical degradation on cell performance under constant current load

4.3.1 Introduction

The simplest applications one could imagine for a PEMFC are the stationary ones. The power demanded to the cell is always the same and operating conditions are defined by the polarization curve of the cell. We have to ensure that the cells are stable over time under these conditions or at least, that the degradation of their performances remains in a range which remains acceptable.

We simulated our reference cell for different experimental conditions (relative humidity, temperature, stoichiometry, current density) and we followed different effects of time on cell parameters.

4.3.2 Impact of the chemical degradation on cell potential and membrane resistance

4.3.2.1 At low current density

The first impact that we consider is the one of the temperature in the cell. We simulated the run of a cell for over 500 h under a constant current density.

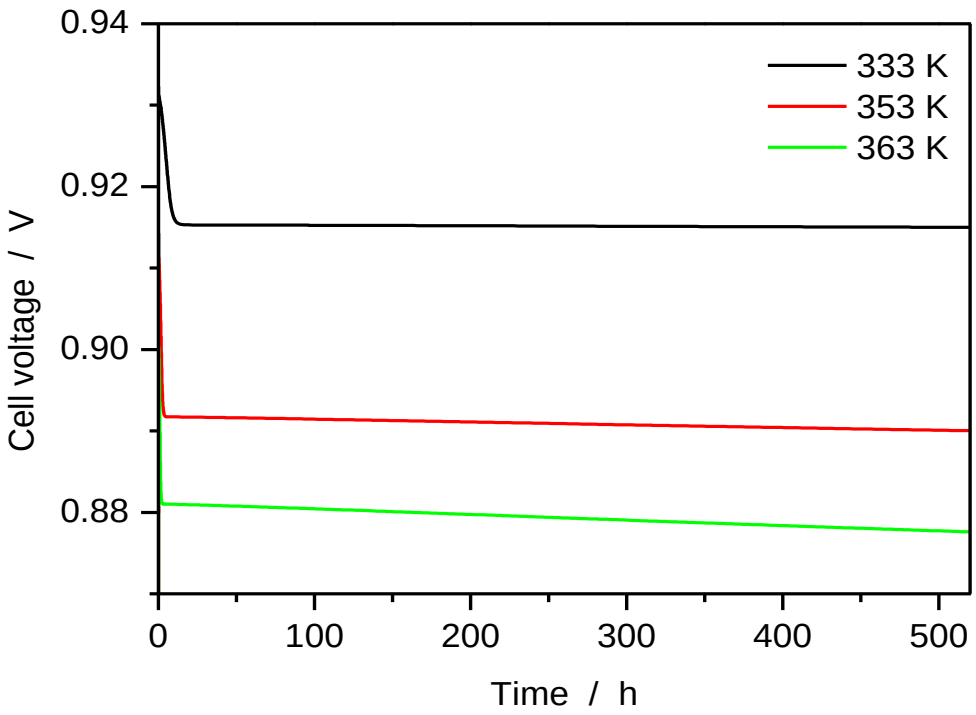

Figure 4.12: Evolution of the cell voltage at low current density at 0.04 $A \cdot cm^{-2}$, 2 bar, 50% relative humidity at anode and cathode, stoichiometry 8/16 anode / cathode and a production of iron ions of $2 \cdot 10^{-5}$ $mol \cdot m^{-3} \cdot s^{-1}$.

Figure 4.12 shows the evolution of the cell voltage at a given relative humidity. We observe that the cell voltage decreases with increasing temperature. This is in contradiction with the laws of kinetics, saying that with increasing temperature, the reaction rate of HOR and ORR would be faster. Moreover the thermal effects are taken into account as well in our degradation model. So how could one explain this divergence from the theory?

At every temperature, we set the relative humidity constant in both electrodes. The relative humidity is defined as the ratio of the partial pressure of water vapor to the saturated water vapor pressure. In Figure 4.13, we represented the evolution of the water saturated vapor pressure with temperature. As it can be seen, there is a strong dependence of temperature. Thus, considering the same relative humidity at 333 K and 363 K and the strong variation of saturated vapor pressure, the partial pressure of water vapor will increase with increasing temperature. Our simulation are isobar, the total pressure is constant at each side. The global pressure is defined as the sum of the oxygen partial pressure and the water partial pressure at the cathode side. If the water partial pressure increases with temperature, the partial pressure of oxygen will decrease to balance this effect and keep the pressure constant. In Figure 4.14, the profiles of dissolved oxygen in the membrane are represented. The value at the cathode side is directly linked to the partial pressure of oxygen through Henry's law (Equation 2.21).

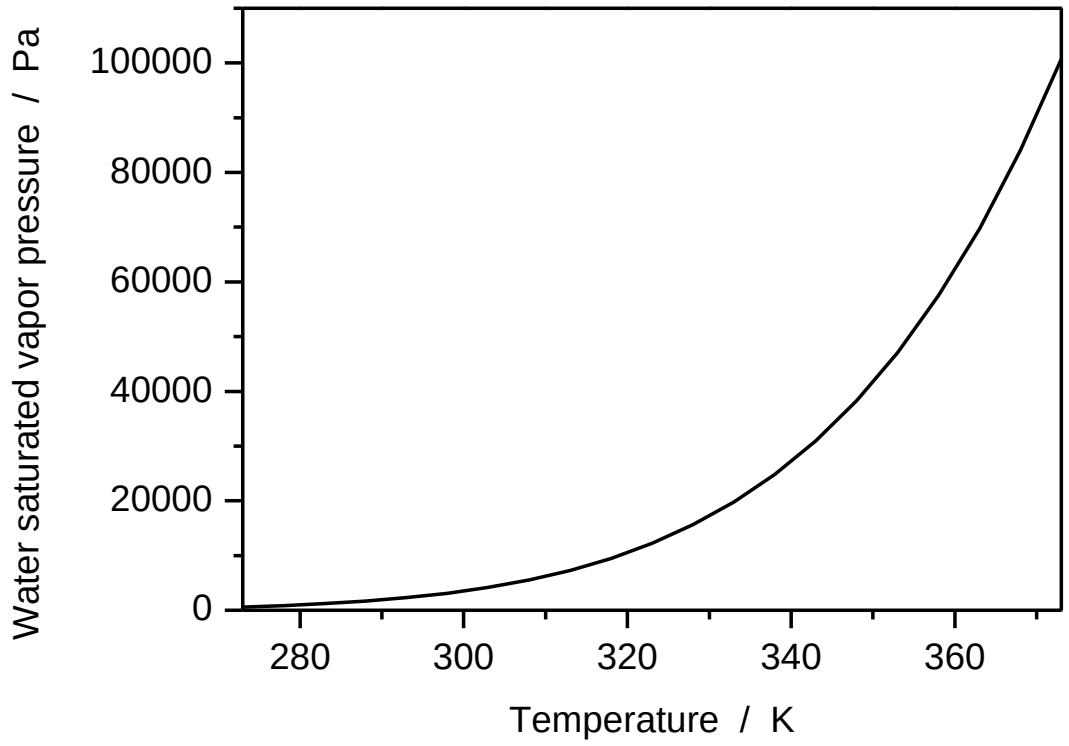

Figure 4.13: Evolution of the water saturated vapor pressure with temperature from 0 °C to 100 °C.

But if we compare Figure 1.15 and Figure 4.12, we see that our modeling predictions show no significant changes in the cell potential at the low current density over time, whereas the experimental results show on the contrary a diminution of the cell potential. Our degradation model takes into account the evolution of the cell resistance over time, and its changes are responsible for the performance degradation of the cell. As this effect is purely an ohmic one, it is obvious that when the current density applied is set close to 0, changes in the ohmic contribution of the potential are negligible. Thus the cause of potential degradation under low current density conditions cannot be attributed to the chemical degradation of the membrane.

A possible explanation for this observation could be the simultaneous presence of oxygen (because of its permeation through the membrane) and hydrogen at the anode side. This would imply the formation of a mixed potential which negatively impact on the cell potential. As one of the consequences of the degradation is a loss of matter and thus an increase of transport phenomena, the increased oxygen cross-over would then explain the degradation of the cell potential at low current density. This remains a hypothesis, as the model does not currently take this into account, we could not predict it.

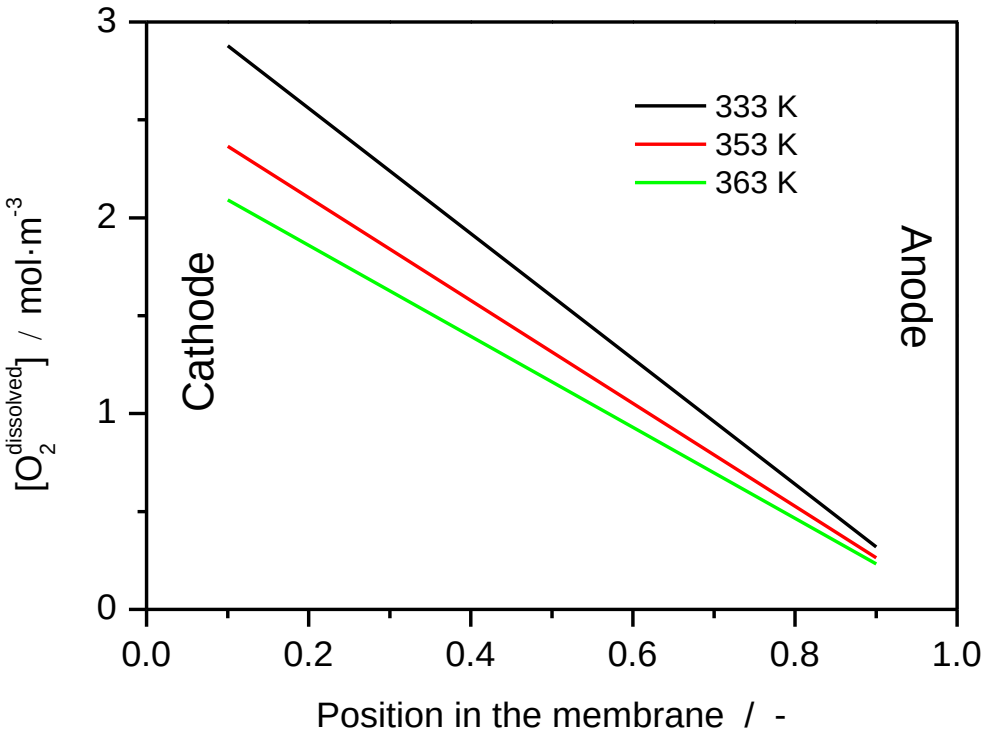

Figure 4.14: Dissolved oxygen concentration profile at 0.04 $A \cdot cm^{-2}$, 2 bar, 50% relative humidity at anode and cathode, stoichiometry 8/16 anode / cathode and a production of iron ions of $2 \cdot 10^{-5}$ $mol \cdot m^{-3} \cdot s^{-1}$.

In our simulations, we observe under low current conditions a small decrease of the cell voltage (Figure 4.12). This is due to the increase in the ohmic losses. But as the absolute current applied is 1 A, this potential decrease is not significant. As previously mentioned, the mixed potential allows explaining the potential decrease at OCV, as no oxygen reacts and the permeation of oxygen to the anode is enhanced. With increasing current density, this mixed potential decreases, as the permeation is not so large and oxygen is consumed, but the ohmic losses increases, as the current is higher.

Because of the different sources of cell potential degradation depending on current density, we do not choose potential degradation as parameter to monitor the chemical degradation of the membrane but the evolution of the membrane resistance.

In Figure 4.15 (a), we plot the evolution of the membrane resistance with time for our low current density experiment. Two different phases are identified. The first fast increasing of the membrane resistance is due to the driving of the system to stable conditions (this is usually due to approximation in the choice of start conditions).

During the second phase (Figure 4.15 (b)), the membrane resistance increase is weaker. As mentioned in Section 4.1, a small amount of water is produced in our low current conditions and depending on the temperature; the humidification of the membrane will be different depending on the temperature. The water profile in the membrane is shown in Figure 4.16. We see strong differences in the humidification, having an impact on the value of the membrane resistance.

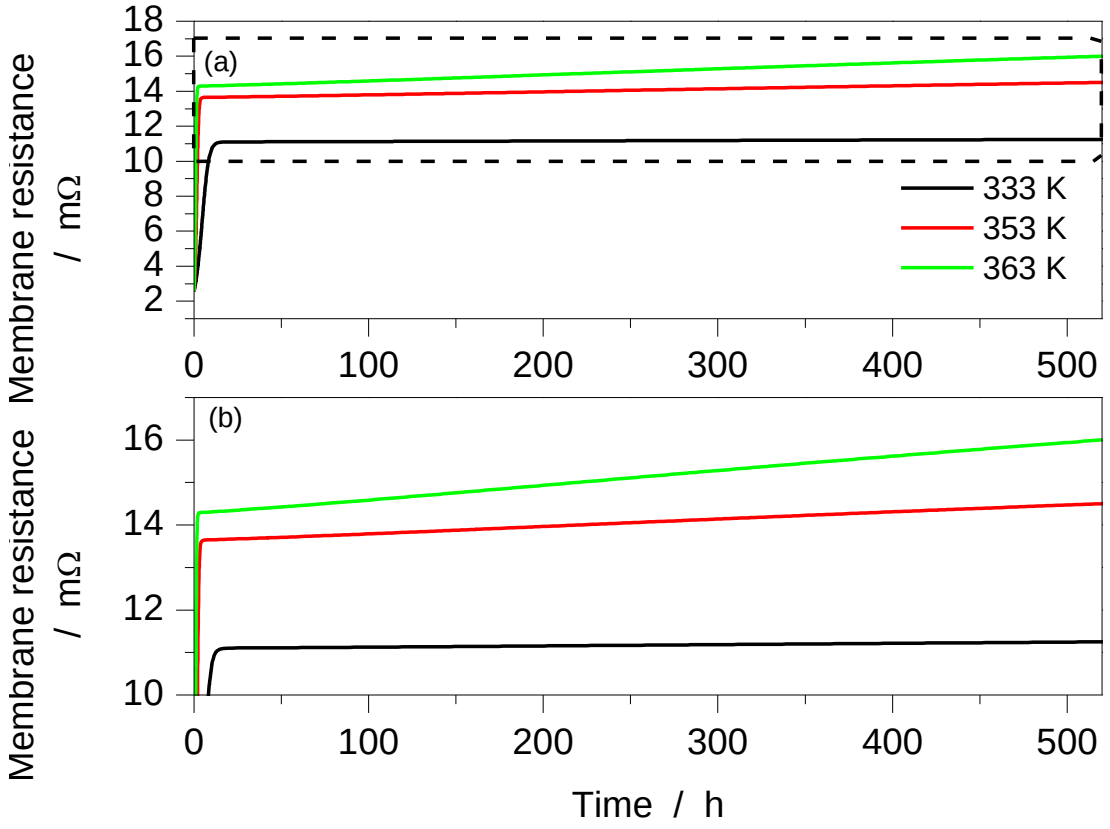

Figure 4.15: Evolution of the membrane resistance at 0.04 A·cm^{-2}, 2 bar, 50% relative humidity at anode and cathode, stoichiometry 8/16 anode / cathode and a production of iron ions of 2·10^{-5} mol·m^{-3}·s^{-1} (a) Complete signal (b) Zoom in the dashed area.

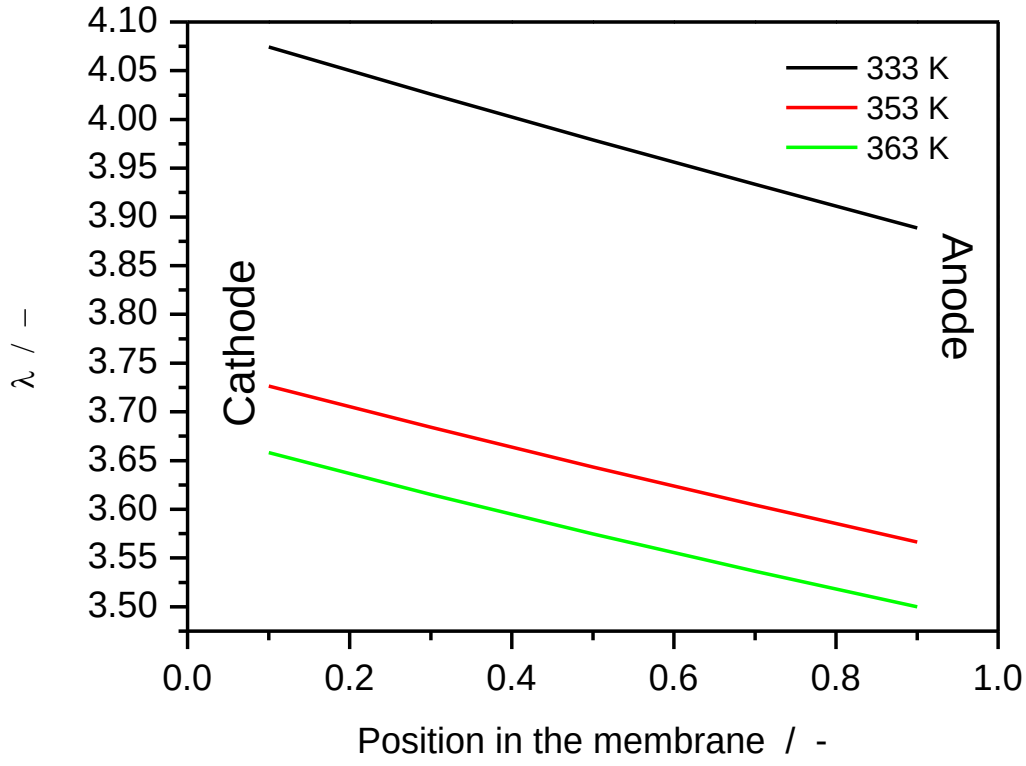

Figure 4.16: Water profile at 0.04 A·cm^{-2}, 2 bar, 50% relative humidity at anode and cathode, stoichiometry 8/16 anode / cathode and a production of iron ions of 2·10^{-5} mol·m^{-3}·s^{-1}.

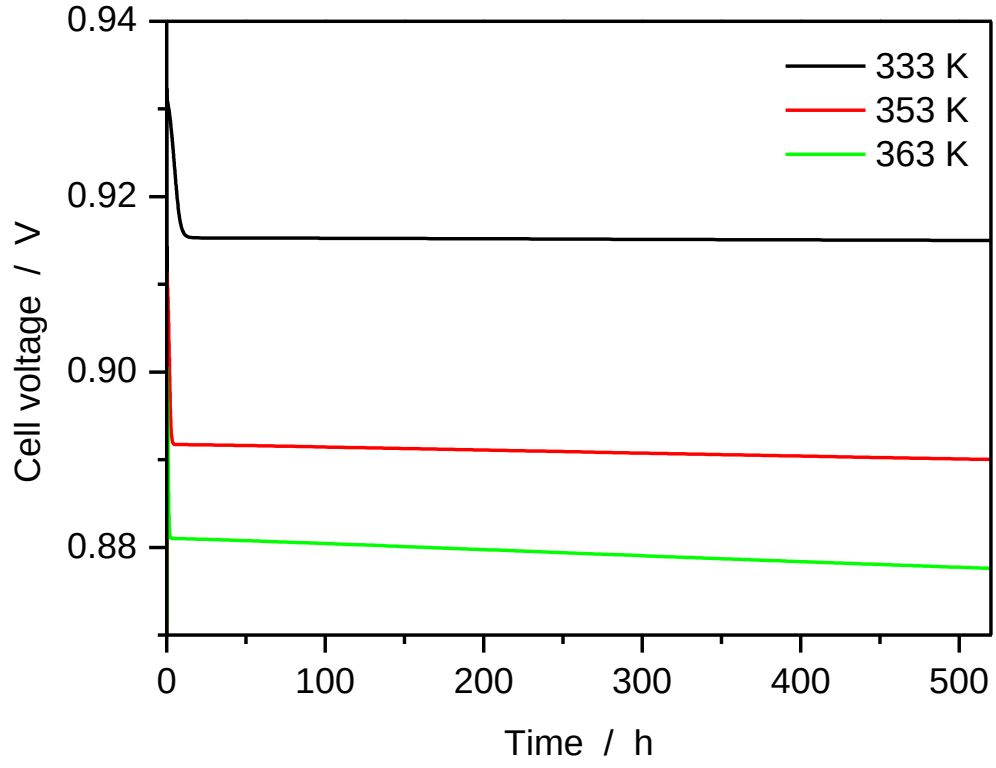

Figure 4.17:Evolution of the cell voltage at low current density at 0.04 A·cm^{-2}, 2 bar, 50% relative humidity at anode and cathode, stoichiometry 8/16 anode / cathode and a production of iron ions of

$2 \cdot 10^{-5}$ mol·m^{-3}·s^{-1}.

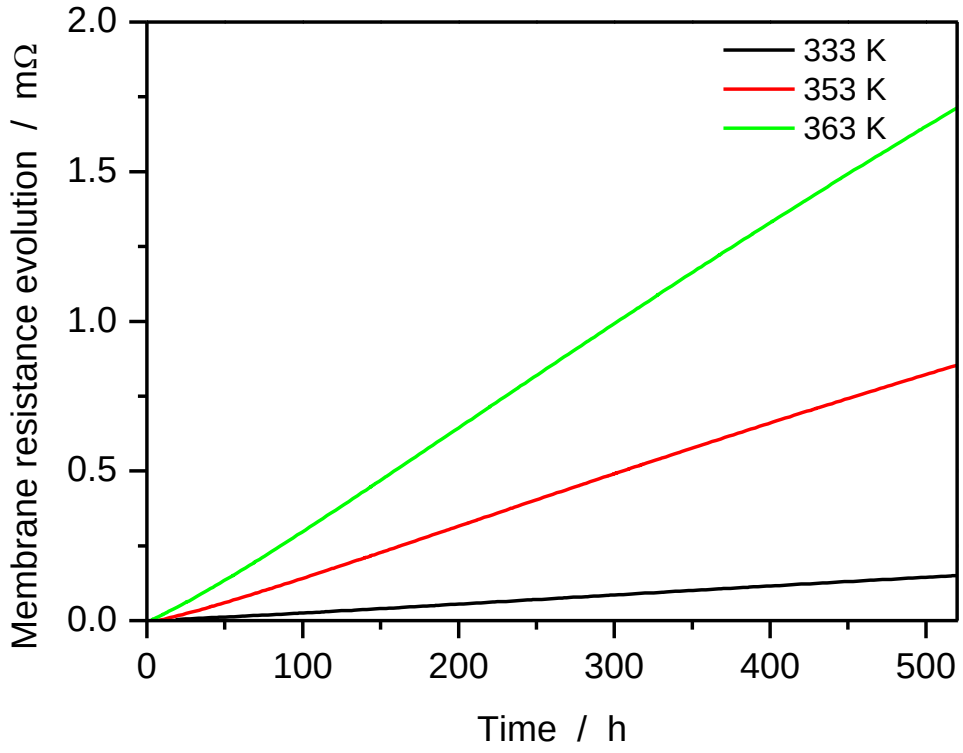

Figure 4.18: Net evolution of the membrane resistance at 0.04 A·cm^{-2}, 2 bar, 50% relative humidity at anode and cathode, stoichiometry 8/16 anode / cathode and a production of iron ions of $2 \cdot 10^{-5}$ mol·m^{-3}·s^{-1}.

To get rid of the problem linked to humidification, we focus only on the resistance increase over time. We take as reference the value of the cell resistance after the first phase. The evolution of the membrane resistance is displayed in Figure 4.18. It is barely present at 333 K, but at 353 K and at 363 K, it becomes more important. The increase of membrane resistance after 500 h at low current density and 363 K is about 1.7 mΩ. This corresponds to an increase of the specific resistance of 42.5 mΩ·cm². This prediction could be validated by comparing EIS measurements on cell before and after operation.

4.3.2.2 At non-zero current density

In this part, we ran simulations of the same cell as previously under 0.6 A·cm^{-2}. It represents standard conditions for a PEMFC.

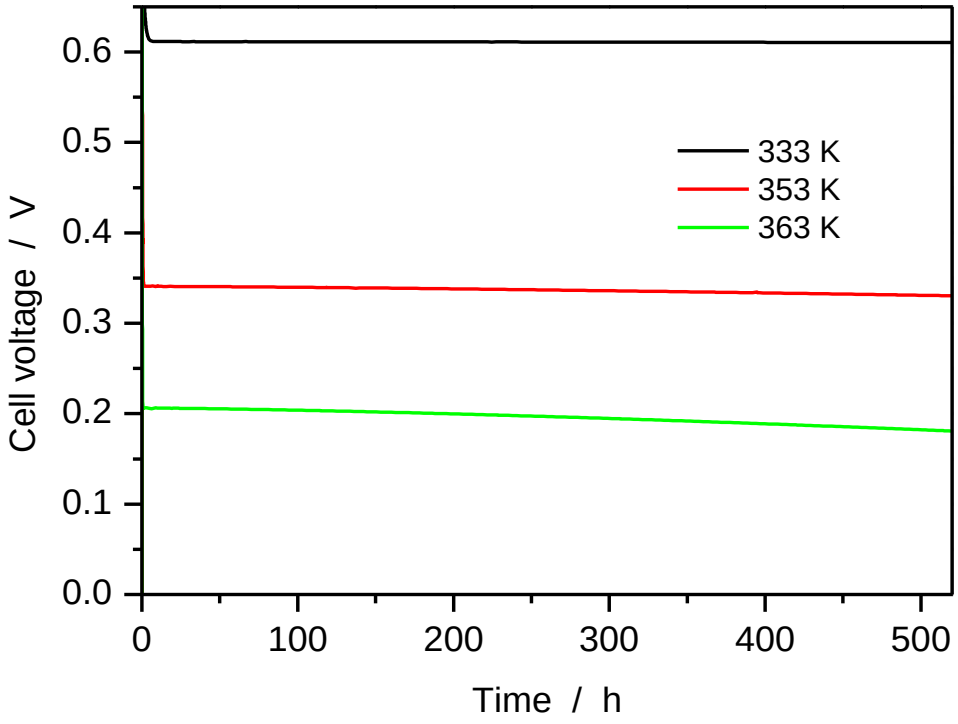

Figure 4.19: Evolution of the cell voltage at 0.6 $A \cdot cm^{-2}$, 2 bar, 50% relative humidity at anode and cathode, stoichiometry 8 / 16 anode / cathode and a production of iron ions of $2 \cdot 10^{-5}$ $mol \cdot m^{-3} \cdot s^{-1}$.

In Figure 4.19, we displayed the evolution of the cell voltage for the same condition as in Section 4.3.2.1 with a constant current density set to 0.6 $A \cdot cm^{-2}$ for different temperatures. Same as with low current density, the voltage drop increases with increased temperature. As the current applied is higher than in Section 4.3.2.1 (15 A for 25 cm^2 membrane geometric area), the ohmic voltage loss induced by an increased membrane resistance will increase as well.

Figure 4.20 shows the calculated evolution of the membrane resistance for several temperatures. We observe that the resistance increases as the temperature increases. This trend can be understood from the calculated temperature dependence of water profile along the membrane reported in Figure 4.21. We see that at lower temperature, the membrane is more humidified than at 80 °C or 90 °C.

At low temperature the membrane resistance increase is not significant. However this effect becomes more important with increasing temperature. In Figure 4.22, we plot the comparison of modeling results at different temperatures and current densities. We notice that at a constant temperature, the membrane resistance increases less when the current density increases.

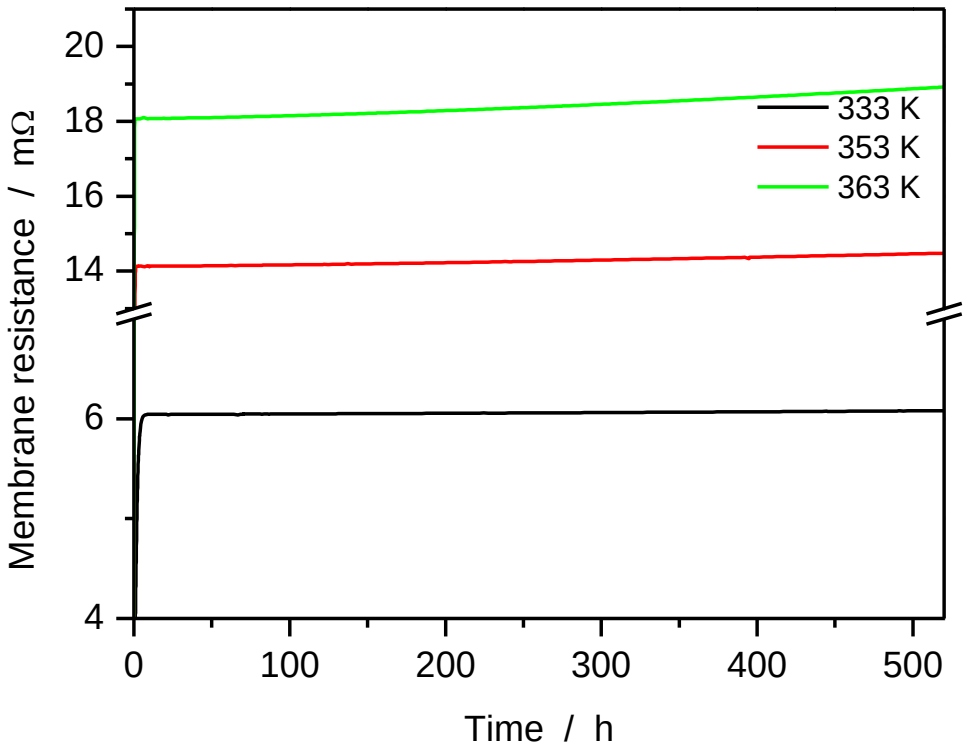

Figure 4.20: Evolution of membrane resistance at 0.6 A·cm^{-2}, 2 bar, 50% relative humidity at anode and cathode, stoichiometry 8 / 16 anode / cathode and a production of iron ions of 2·10^{-5} mol·m^{-3}·s^{-1}.

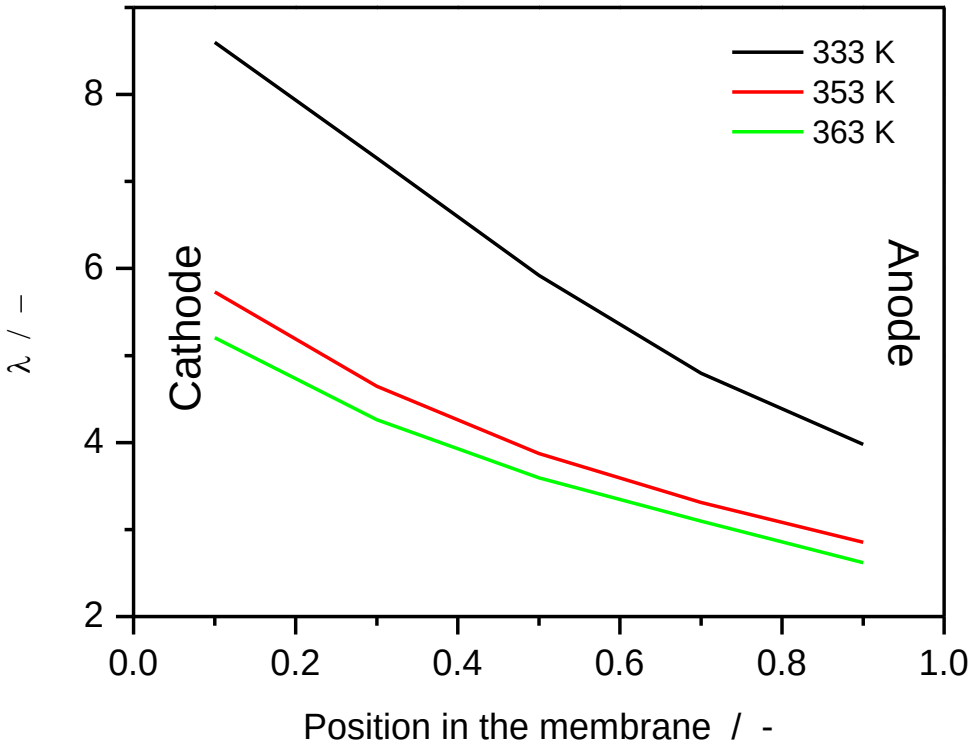

Figure 4.21: Water content profile in the membrane at 0.6 A·cm^{-2}, 2 bar, 50% relative humidity at

anode and cathode, stoichiometry 8 / 16 anode / cathode and a production of iron ions of $2 \cdot 10^{-5}$ $mol \cdot m^{-3} \cdot s^{-1}$

In Figure 4.22, we can see that the membrane resistance barely increases over time under these conditions, and that the resistance increase rate increases as the temperature increases.

However, compared to the low current density case, we observe a smaller increase of the chemical degradation of the membrane. We observe an increase of the membrane resistance of about 0.85 mΩ. Under the same conditions at 0.04 $A \cdot cm^{-2}$, the increase of membrane resistance was 1.9 mΩ. To explain this, we investigate the concentration of several species responsible for degradation, dissolved oxygen, hydrogen peroxide and HO radicals. The profiles of these species are shown in Figure 4.23. We see that when the current density increases, the concentration of the species involved in the membrane degradation decreases. As these concentrations decrease, the membrane will be less susceptible of being attacked, and the cell performance is expected to be less impacted.

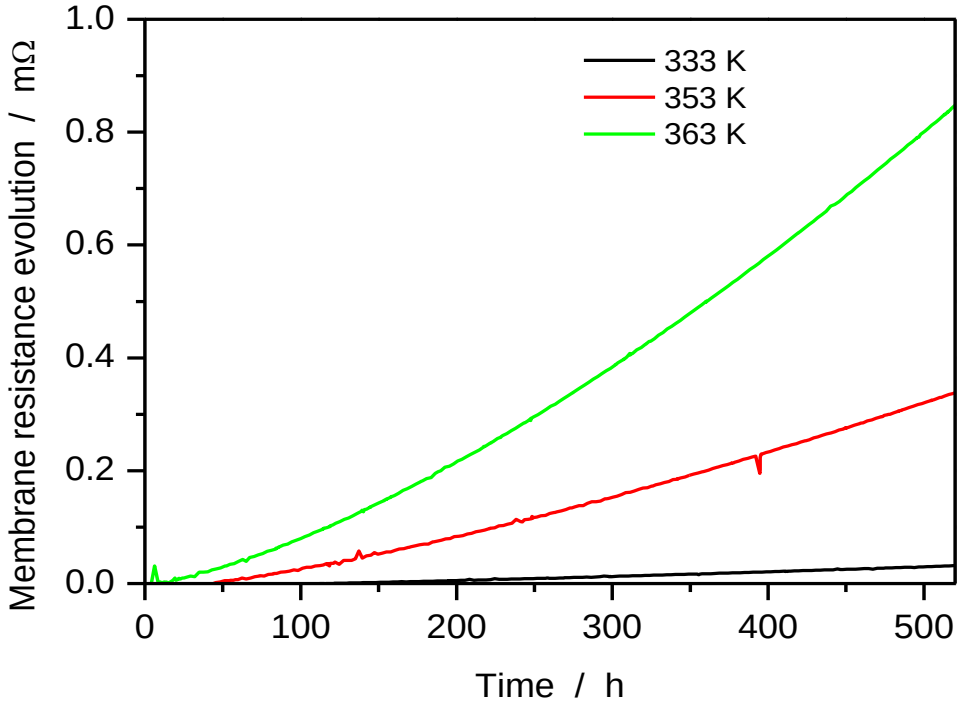

Figure 4.22: Evolution of membrane resistance at 0.6 $A \cdot cm^{-2}$, 2 bar, 50% relative humidity at anode and cathode, stoichiometry 8/16 anode / cathode and a production of iron ions of $2 \cdot 10^{-5}$ $mol \cdot m^{-3} \cdot s^{-1}$.

In the last two sections, we show that running a PEMFC at high temperature and low current density enhances the chemical degradation processes in the membrane. This leads to an increase of the mem-

brane resistance. This resistance increase induces a decrease of the cell potential which can be significant if the current applied is high enough. However, membrane resistance is also influenced by the water content in the membrane. Thus, to uncorrelate the humidification effect from the degradation effect on the membrane resistance, we focus the next section of our work on a parameter representative of the degradation: the cumulative fluoride ions release.

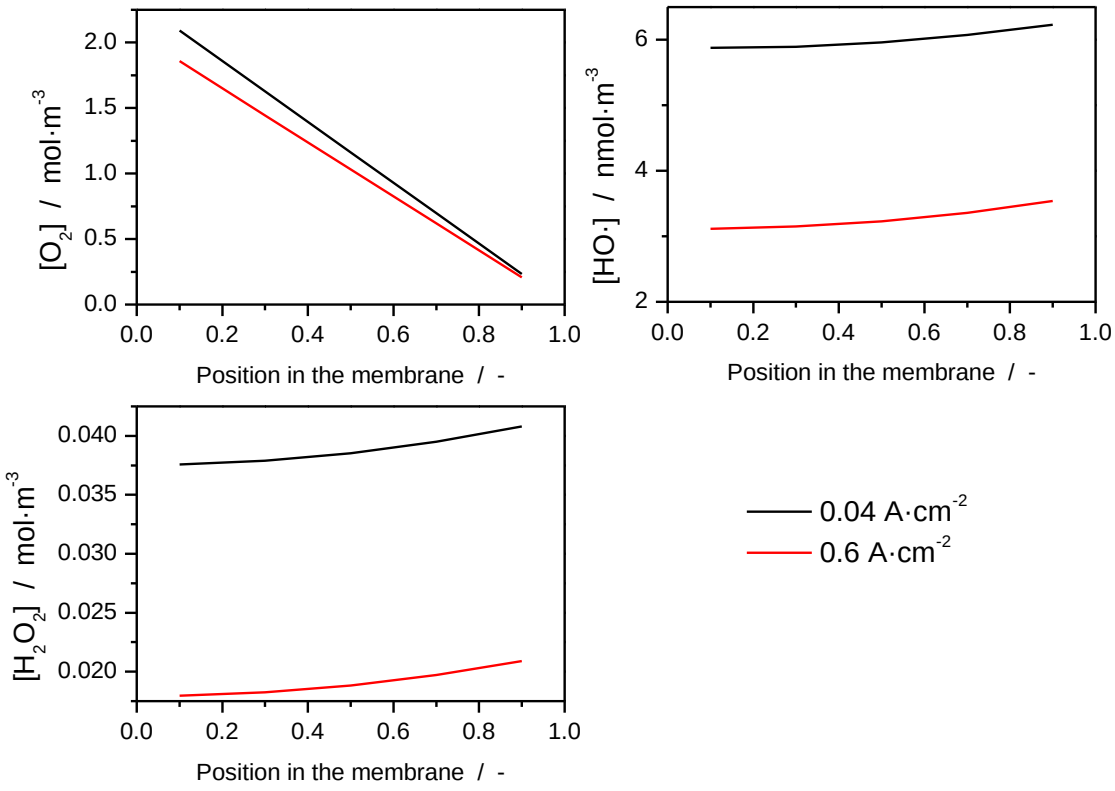

Figure 4.23: Concentration profiles of different species at 0.6 $A \cdot cm^{-2}$, 2 bar, 50% relative humidity at anode and cathode, stoichiometry 8/16 anode / cathode and a production of iron ions of $2 \cdot 10^{-5}$ $mol \cdot m^{-3} \cdot s^{-1}$

4.3.2.3 Impact of degradation on chemical composition

As mentioned in Section 4.1, the stoichiometry of the reactants has a certain impact on the humidification of the membrane.

In Figure 4.24, we compare the calculated degradation of a cell whose reactants are fed at low and high stoichiometry and under OCV conditions. It appears that lower stoichiometry enhances the degradation of the cell. This is the consequence of humidification differences in the membrane: as case 2 / 4 is higher humidified as case 8 / 16, this may mean that if the relative humidity increases, the membrane would be more degraded; this point will be further inquired in the next paragraphs.

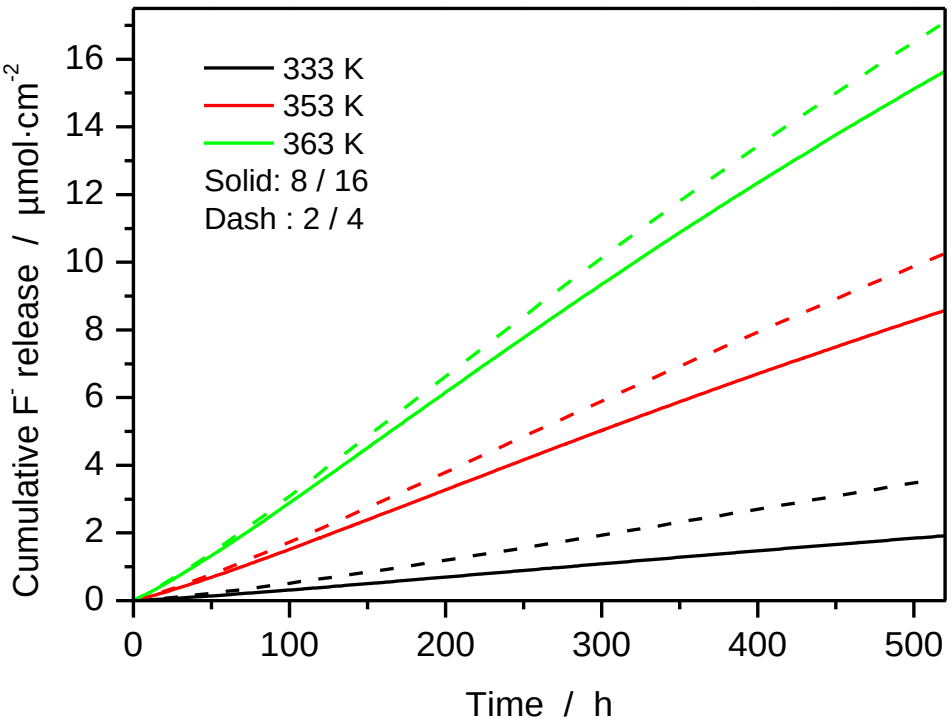

Figure 4.24: Cumulative fluoride ions released by the cell at $4 \cdot 10^{-2}$ A·cm^{-2} and different stoichiometry.

In Figure 4.25, we displayed the impact of the relative humidity on the chemical degradation of the cell. We see that the membrane degrades more at higher relative humidity. The temporal evolution of the fluoride is driven by Equation 4.2. As the kinetic rate is only temperature dependent, the source of the differences is assumed to be the produced radical concentration. Thus we need a closer look on the evolution of different concentrations in the membrane with the humidity.

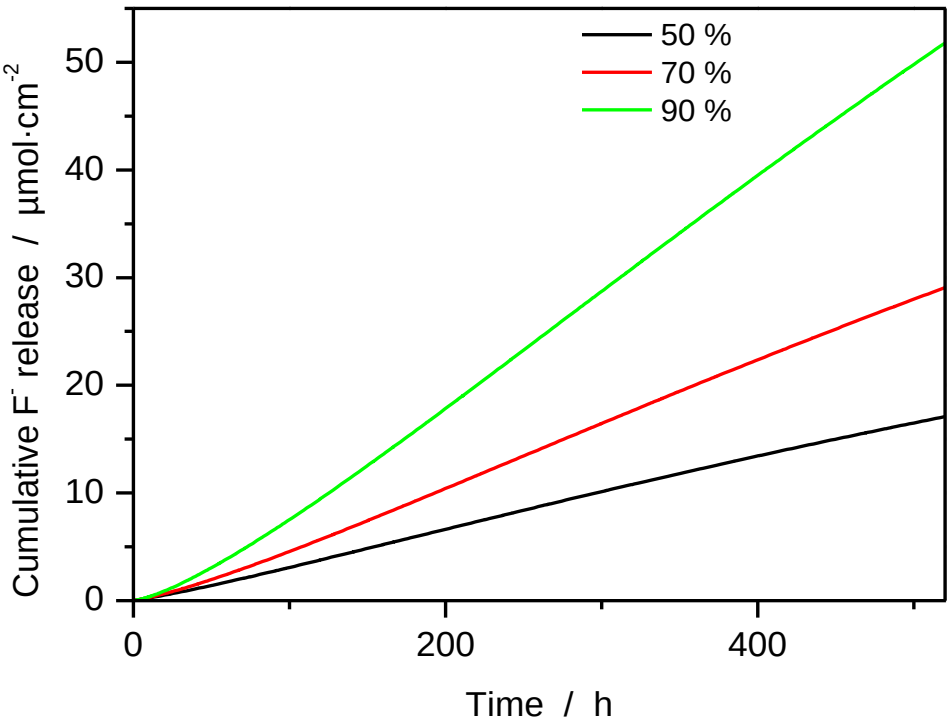

Figure 4.25: Evolution of the degradation with relative humidity at 0.04 $A \cdot cm^{-2}$, 2 bar, stoichiometry 2/4 anode / cathode and a production of iron ions of 10^{-3} $mol \cdot m^{-3} \cdot s^{-1}$.

In Figure 4.26, we displayed the profiles after 500 h for dissolved oxygen and hydrogen peroxide in the membrane. As the oxygen comes into the membrane at the cathode side, it is normal that the concentration of oxygen is much higher at the cathode side. We see that the concentration of oxygen decreases with increasing humidity. This behavior is explained by the fact that at constant pressure, if we increase the relative humidity (i.e. ratio of water in the gas), the corresponding ratio (i.e. partial pressure) of oxygen will decrease. According to Henry's law (Equation 2.21), it is then normal that the concentration of dissolved oxygen decreases. But the range of the concentration remains close of each other, which can then not alone explain the dependence of degradation on relative humidity.

However if we observe the evolution of the concentration of H_2O_2, we see that higher relative humidity greatly enhances the formation of H_2O_2. Thus more radicals will be produced and the membrane will be more subject of being degraded. Experimental works reports in the literature provide contradictory observations. Chen and Fuller showed that with increasing relative humidity, the concentration of H_2O_2 will increase [36]. However in another publication they present another trend where the concentration of H_2O_2 decreases with increasing relative humidity, implying a lower fluoride production [34]. Thus it is difficult to conclude anything about the coherence of the trend we simulate. If we yet refer to

the publications using an accelerated stress test, we may assume that high relative humidity enhances the chemical degradation of the membrane [160].

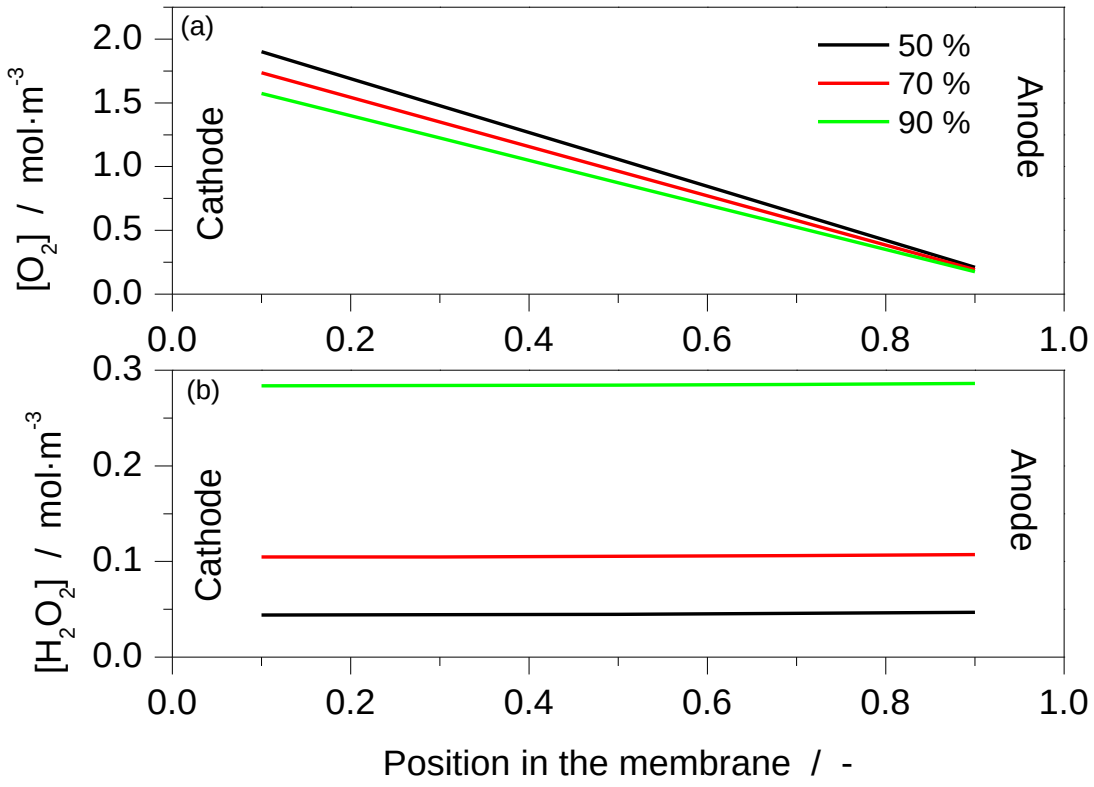

Figure 4.26: Concentration profile of (a) O_2 and (b) H_2O_2 in the membrane for different relative humidity after 500 h at 0.04 $A \cdot cm^{-2}$, 2 bar, stoichiometry 2/4 anode / cathode and a production of iron ions of 10^{-3} $mol \cdot m^{-3} \cdot s^{-1}$.

Thus we performed the same simulations with a current density which is often taken as a operating condition for PEMFC, 0.6 $A \cdot cm^{-2}$.

As explained in Section 4.3.2.2, running a PEMFC at low current density will degrade it faster than at high current density. But as the membrane resistance increase can, generally speaking, be an effect of the water content as well, we have to compare the cumulative fluoride emissions for different cases. Figure 4.27 shows the calculated concentrations of F^- as function of the current density and the temperature.

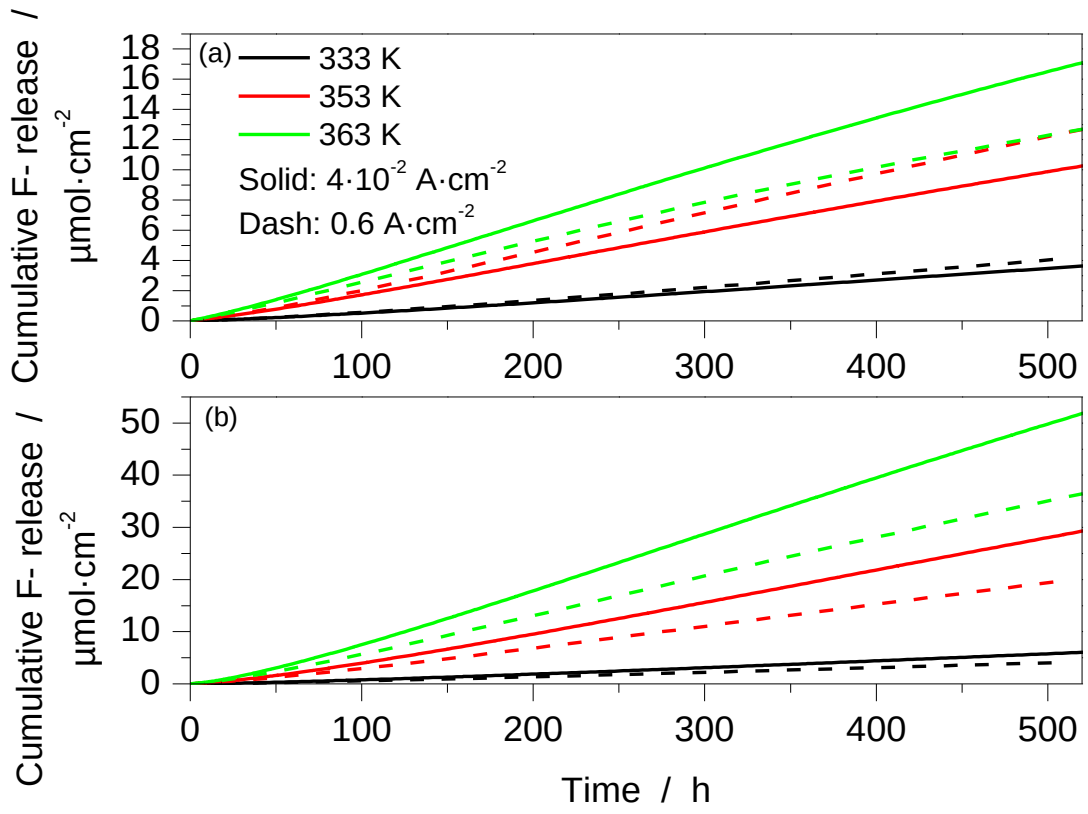

Figure 4.27: Cross influence of membrane chemical degradation with current density and relative humidity (a) 50 % and (b) 90%.

If we increase the relative humidity (Figure 4.27 (b)), we see that the membrane degradation is lower at the higher current densities. This effect is more significant when the temperature increases. At 333 K, the chemical degradation is almost the same at low current density and 0.6 A·cm^{-2} whereas it decreases of 30 % at 353 K. For a relative humidity of 50 % RH, this observation is however not valid (Figure 4.27 (a)). In that case, water management in the membrane is the key parameter which explain such a behavior.

To explain the reason of the trend we observe at 50 % RH, we analyze the evolution of the relative humidity in the GDL for the cases displayed in Figure 4.27. These are displayed in Figure 4.28. At OCV, as no water is produced, the relative humidity in GDL at the anode and the cathode are close. At 0.6 A·cm^{-2}, water is produced at the cathode and anode dries through the drag of water along with protons. For this reason, the humidity difference between anode and cathode is higher. For each temperature, the relative humidity in the GDL at the anode and the cathode increase with the current density; except the anode for 363 K, which is drier with increasing current density. This is the reason for the higher rate of degradation observed. With a too low flow of reactant, the electrodes are more humidified. And combined with the production of water and water motion in the membrane, the mem-

brane is more humidified and thus the degradation is more significant.

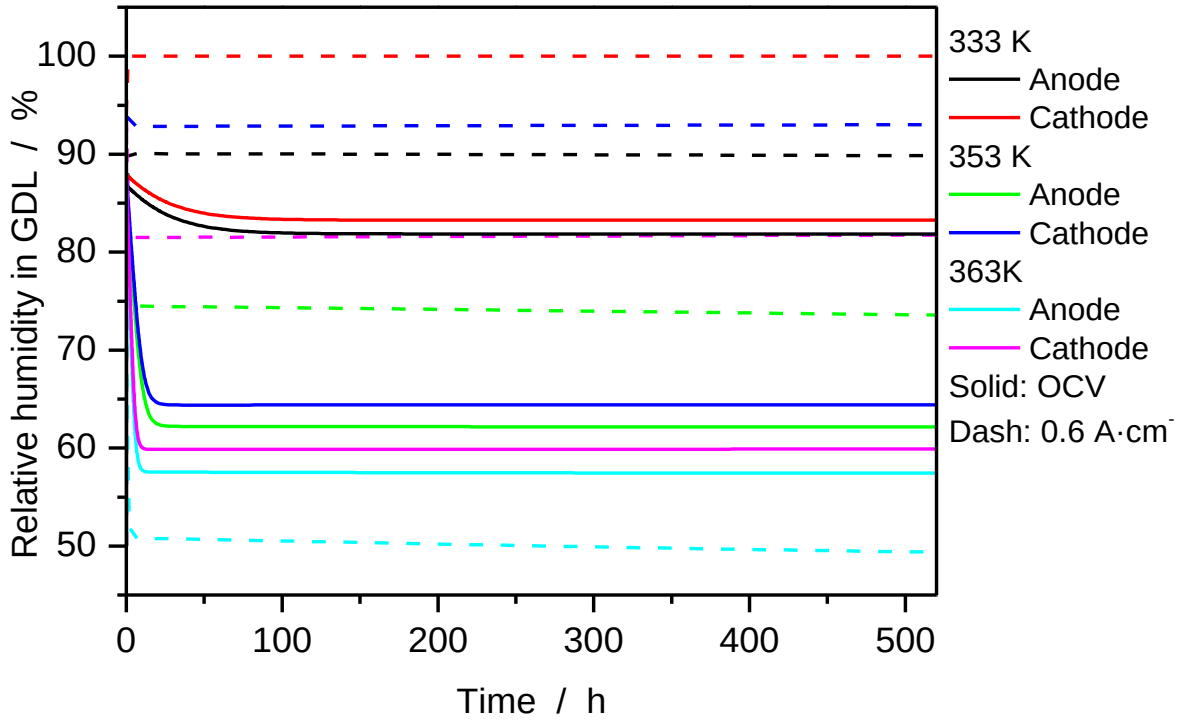

Figure 4.28: Evolution of the relative humidity in the GDL in dependence on the temperature and the current density for a start condition of 50 %, stoichiometry 2 / 4.

To confirm this assumption, we run the same simulation with increased stoichiometry. This should reduce the humidity and thus, we should observe a trend in adequacy to the experimental observations. In Figure 4.29, we plotted the results of the same simulation as in Figure 4.27 (b) for a stoichiometry of 8 /16. We see that for lower temperatures, the trend is reversed and higher current density will decrease the chemical degradation. Considering the fact that a low stoichiometry corresponds to the inlet of the cell and high stoichiometry the outlet, we can say that with increasing current density and below 353 K (estimated), the membrane is more degraded at the inlet than at the outlet.

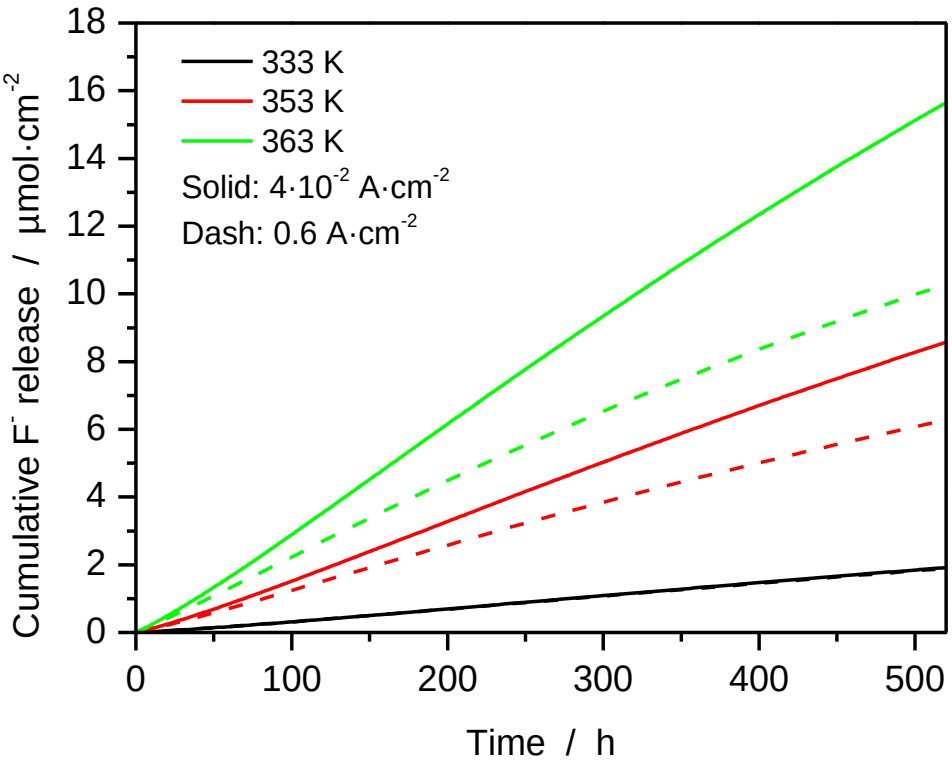

Figure 4.29: Evolution of chemical degradation of the membrane with temperature and current density for a 50 % relative humidity and 8/16 stoichiometry.

4.3.3 Impact of the chemical degradation on cell performance: Evolution of the polarization curve

4.3.3.1 Presentation of the simulations

As our model is able to predict the evolution of the cell voltage, it is interesting to use it in order to predict the evolution of the polarization curve. It is obvious that the performance degradation is not only due to the increasing of the membrane resistance (Figure 1.12 and Figure 1.13). For example platinum dissolution and carbon corrosion are others possible sources for the performance degradation [161-167]. Thus our model will allow separating the contribution of the performance losses due to the membrane degradation and, coupled with other degradation model, a real evaluation of performance losses on polarization curves can be made [3-5].

The current profile we applied to the simulated cell is displayed in Figure 4.30 (a) and (b). We let the system stabilizing during 20 hours, to ensure an equilibrium humidification of the cell (see Section 4.1) and then, we slowly increase the current density up to 1 $A \cdot cm^{-2}$, and after every increase of the current density, we let the response of the cell stabilizing during 10 min. When we run the cell at 0.6 $A \cdot cm^{-2}$, we first drive the cell to low current density and then proceed to the establishment of the polarization curve. After a certain time (500 h), we simulate a second polarization curve. As the mem-

brane is expected to be chemically degraded during these 500 h, the second polarization curve should show degraded performance regarding the cell potential. We vary several parameters in these studies: The stoichiometry, the current density, the simulated time, the temperature and the production source of ferrous ions.

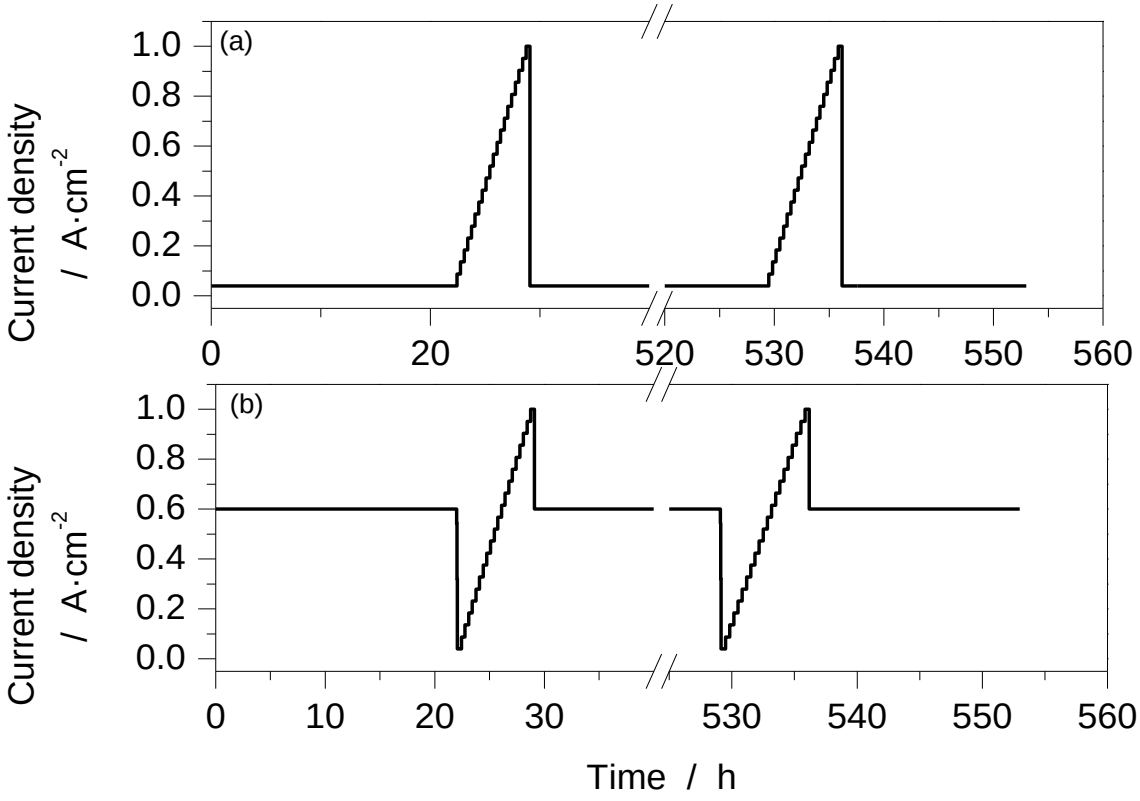

Figure 4.30: Current profiles used for the establishment of polarization curves before and after operation of a cell 500 h at (a) $4 \cdot 10^{-2}$ A·cm^{-2} and (b) 0.6 A·cm^{-2}.

4.3.3.2 Evolution of the polarization curve under low current density conditions

First, to ensure that the only cause for degradation in the model lies in the chemical degradation of the membrane, we run a simulation when no iron is produced. In Figure 4.31, the initial polarization curve and the degraded one are represented. As it can be seen, there is no decrease of the performance over time. That means that any degradation in the performance in further calculation can be attributed to the chemical degradation of the membrane.

Regarding the amount of fluoride ions which are released in the cell (Figure 4.24, Figure 4.25, Figure 4.27, and Figure 4.29), we can expect that a cell which operated at 333 K will not be severely damaged, not enough to really impact on the cell potential. This is confirmed by the observation of Figure 4.32. The cell potential remains unchanged even after 500 h. This would then mean, if an experiment

shows a potential decreases, this could not be attributed to a chemical degradation of the membrane.

First, to ensure that the only cause for degradation in the model lies in the chemical degradation of the membrane, we run a simulation where no iron is produced. In Figure 4.31, we show the evolution of the polarization curve over 500 h for a cell kept under a constant current of 0.04 A·cm–2 at 333 K where no iron ions are produced. We observe over time no changes in the performance. We increase the production term of iron at the cathode and observe the long-time response of the cell. We choose experimental conditions which were identified as extremely aggressive for the cell, a high relative humidity, a high temperature and a low stoichiometry. We simulated the operation of our standard cell for 500 h with three production rate of ferrous ions. These values were chosen according to the study made in Section 4.5. We chose a second case with a moderate degradation (iron production rate of 10^{-5} $mol \cdot m^{-3} \cdot s^{-1}$ and a case where the degradation is supposed to be the worst (10^{-3} $mol \cdot m^{-3} \cdot s^{-1}$ – see Figure 4.47).

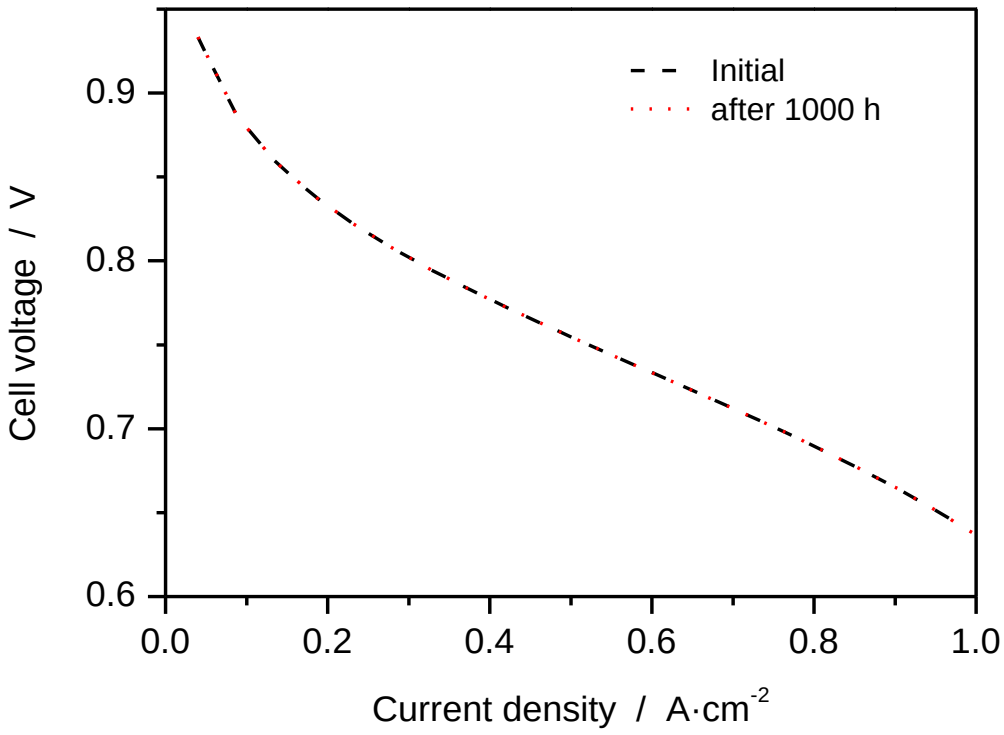

Figure 4.31: Evolution of cell performance over 500 h at 0.04 $A \cdot cm^{-2}$, 333 K, 2 bar, 90% relative humidity at anode and cathode, stoichiometry 2/4 anode / cathode for an iron-free system

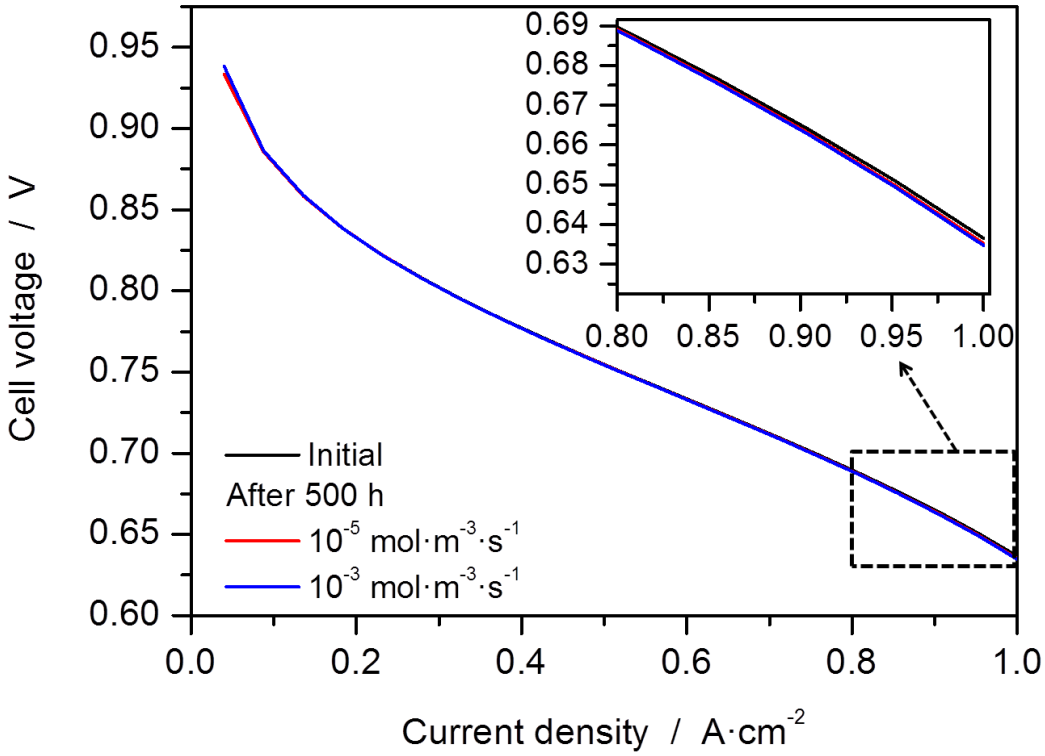

Figure 4.32: Evolution of cell performance over 500 h at 0.04 A·cm^{-2}, 333 K, 2 bar, 90% relative humidity at anode and cathode, stoichiometry 2/4 anode / cathode with iron ions production.

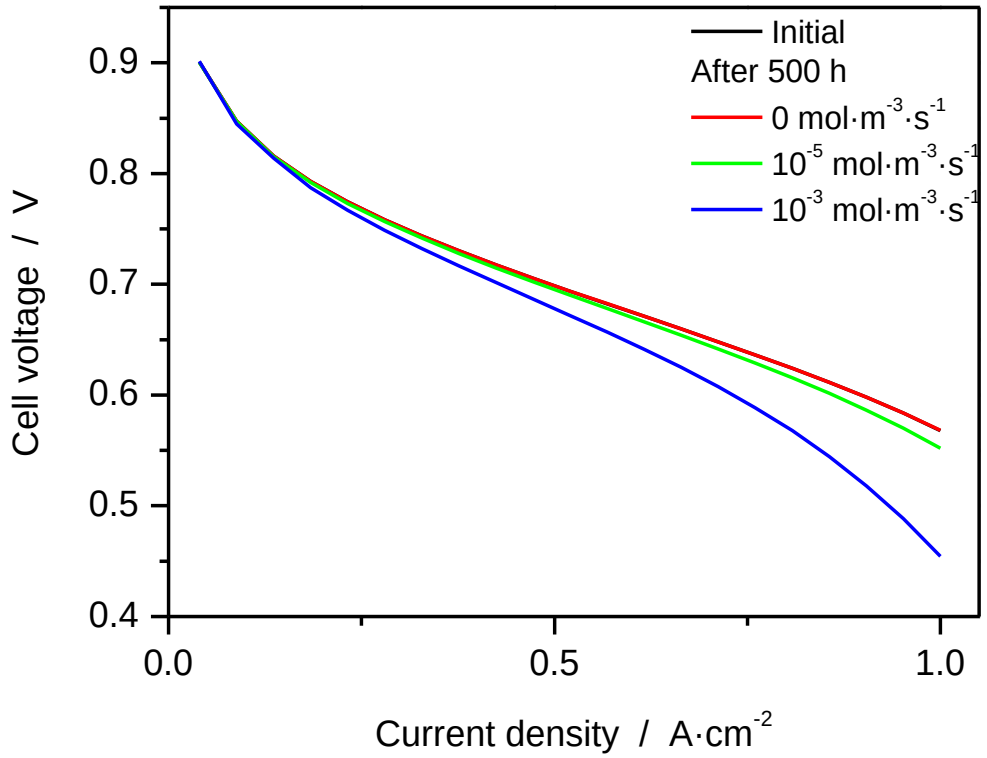

Figure 4.33: Evolution of cell performance over 500 h at 0.04 A·cm^{-2}, 363 K, 2 bar, 90% relative humidity at anode and cathode, stoichiometry 2/4 anode / cathode with iron ions production.

From the observation of Figure 4.33, we see that the impact of the increase of the membrane resistance on the cell voltage is, under the most aggressive simulated conditions, about 100 mV at 1 $A \cdot cm^{-2}$ after 500 h. As such conditions of ferrous ions production is quite unrealistic (and because a PEMFC is never let 500 h in an idle mode), we can say that it is almost unthinkable that a cell fails after 500 h only because of the chemical degradation of its membrane.

4.3.3.3 Evolution of the polarization curve under higher current density

We may now see how the cell behaves if it operates 500 h under a non-zero load, as this is closer to reality than idle operating conditions.

In Figure 4.34, we represent the evolution of the polarization curve after 500 h for a cell which operated at 0.6 $A \cdot cm^{-2}$ and whose iron production varies. In agreement with the observation of cumulative fluoride release, the membrane is less degraded if the demanded current is not zero. The voltage losses are respectively 65.57 mV (high iron production) and 11.21 mV (low iron production) at 1.0 $A \cdot cm^{-2}$ after 500 h. As previously indicated, these values are given for a cell subject to release a lot of iron in the cell. If we reduce the production of ferrous ions by two order of magnitude (Figure 4.35), the voltage losses are reduced to 15 mV (0.04 $A \cdot cm^{-2}$) and 12 mV (0.6 $A \cdot cm^{-2}$) at 1.0 $A \cdot cm^{-2}$ after 500 h. This represents a reducing of the performance of about 2 %, which remains acceptable for a further operation of the cell.

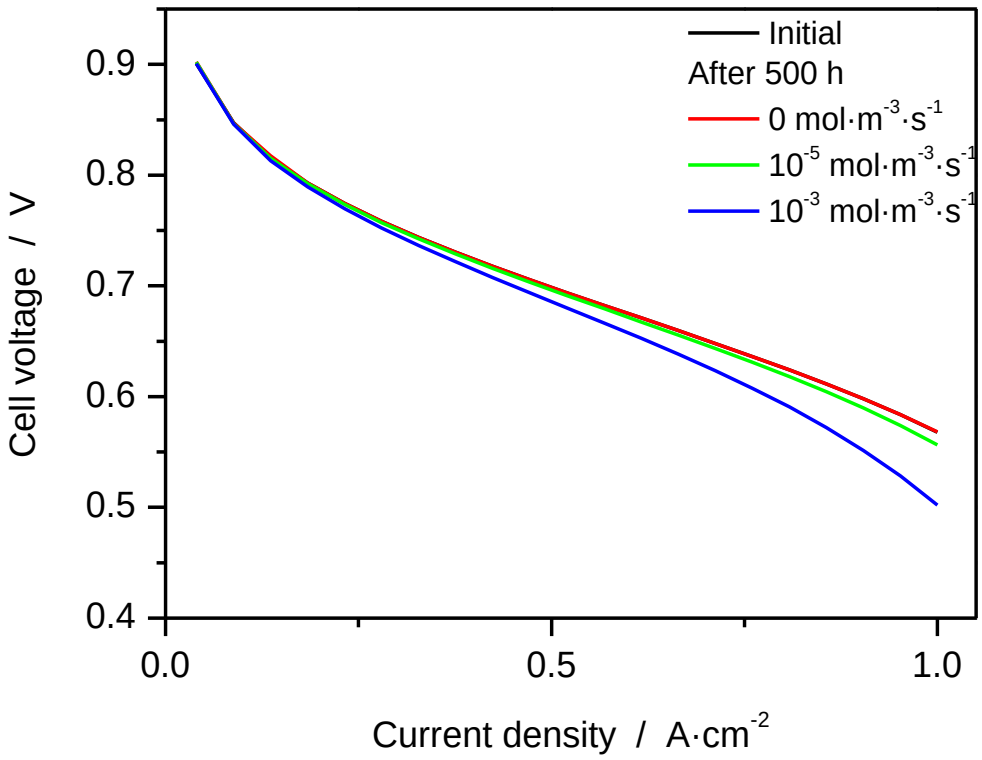

Figure 4.34: Evolution of cell performance over 500 h at 0.6 A·cm^{-2}, 363 K, 2 bar, 90% relative humidity at anode and cathode, stoichiometry 2/4 anode / cathode with iron ions production

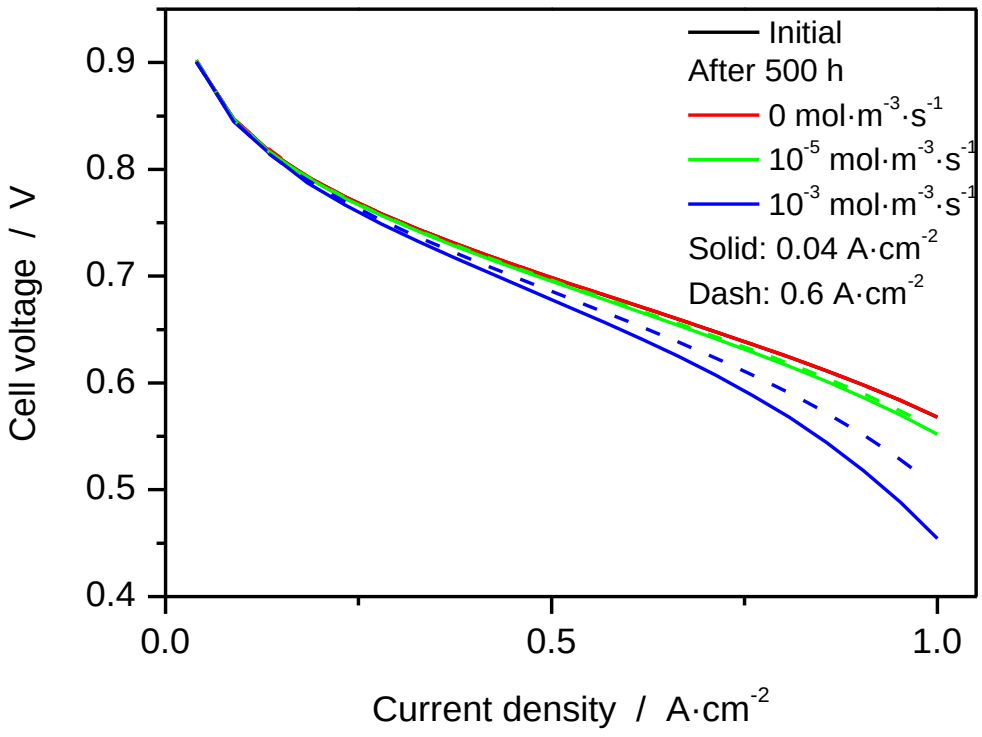

Figure 4.35: Evolution of cell performance over 500 h at 0.04 A·cm^{-2} and 0.6 A·cm^{-2}, 363 K, 2 bar,

90% relative humidity at anode and cathode, stoichiometry 2/4 anode / cathode with iron ions production.

In Figure 4.35, we compared the two cases we studied. The performances of the cell operated at low current density are clearly more degraded than the one operated at high current density.

4.3.3.4 Comparison with experiment

We can compare our evolution of polarization curve with experimental data as well. The experiment mentioned in Section 4.2.2.2 was carried out during over 500h. In Figure 4.36, we report these comparisons. Several remarks can be made. As no information can be provided from experimentalists about the real amount of iron which penetrates the system, the comparison is rather qualitative. First the OCV did not changed during the test, this means that if a mixed potential was present at the beginning of the experiment, it did not increase with degradation. After 500 h, the potential decreases at 1 $A \cdot cm^{-2}$ from 579 mV to 527 mV, which means a decrease of 52 mV. This represents the total losses of the cell, including contribution of all possible degradation sources, like carbon corrosion, platinum dissolution and membrane degradation.

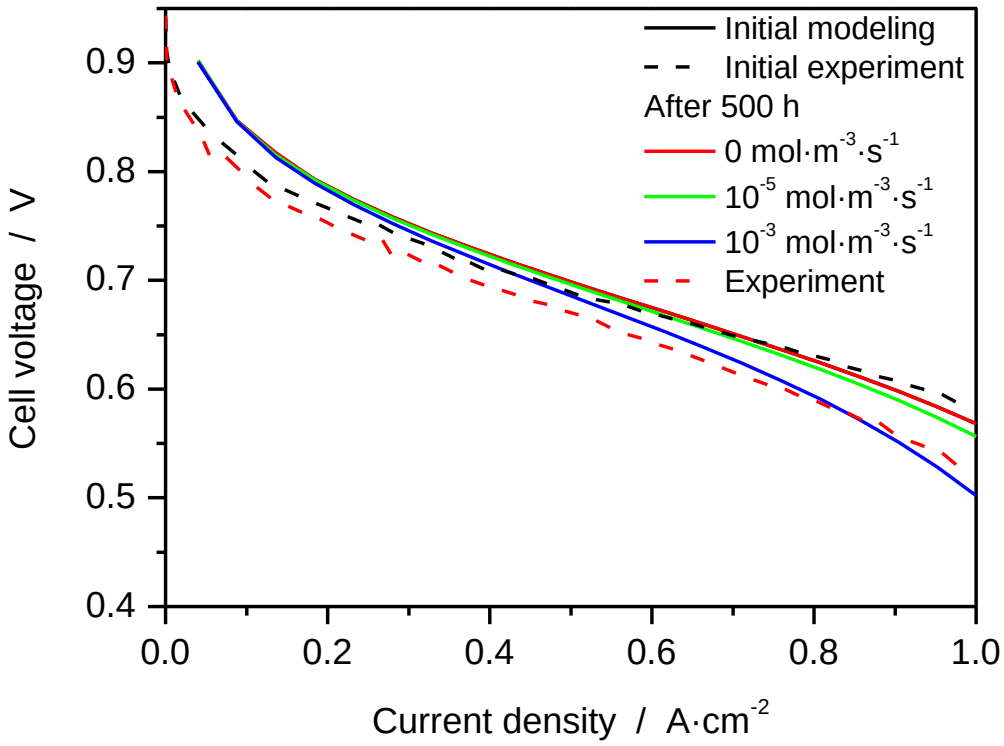

Figure 4.36: Comparison between modeling results and experimental results for the evolution of the polarization curve after 500 h at 0.6 $A \cdot cm^{-2}$.

From the modeling results, we have the possibility to uncorrelate the impact of the membrane degradation over the whole performance decreases. Assuming an iron ion production of 10^{-3} mol·m^{-3}·s^{-1}, the voltage drop over 500 h in the experiment would be only attributed to the membrane degradation. However, several studies show that the main contributor to potential decrease is rather the electrode degradation [73, 168]. If we consider now a lower iron ion production like 10^{-5} mol·m^{-3}·s^{-1}, we see that the potential decrease due to the chemical degradation is much lower. Moreover, at that production rate and after 500 h, the net weight of iron released in the membrane is 151.2 µg. This value seems realistic compared to the weight of a bipolar plate.

4.3.4 Localization of the degradation in the membrane

Thanks to its 1D discretization, our model also allows to spatially resolve the state of degradation of the membrane along its thickness.

We recall that ferrous ions are produced at the cathode side and the hydrogen peroxide at the anode side. In Figure 4.37, we normalized the concentration of species impacting on chemical degradation of the cell and plotted their profile along the membrane. We did this normalization in the concentration because of the high concentration differences observed in the cell (from few nmol·m^{-3} for radicals up to 10^{-1} mol·m^{-3} for dissolved gases). We observe that the region with the highest concentration is located in the middle of the cell, and close to the electrodes, the concentration is the lowest. This means that the degradation rates exhibit trends higher values close to the electrodes (close to the production source of the species involved in the membrane degradation) as in the middle of the cell, where the concentrations are lower. However, the variation of the concentration is too low to really talk about regions in the vicinity of the electrodes which are more degraded than the middle of the membrane. We assume this is due to diffusion coefficients of the species in the Nafion®, which have been to the usually set to standard and maybe over-estimated values when unknown from the literature. Nevertheless the model adapted with optimized parameters could then help to explain the phenomenon of membrane thinning, as displayed in Figure 1.19: the membrane thinning is not linear with the released fluoride, but reaches a limit even if more fluoride are released by the system. The model could help to give clues for a understanding of the phenomena. According to Figure 1.19, it may be expected over time that first anode and cathode side are degraded, inducing a membrane thinning. With continuous degradation, maybe the diffusion processes could be responsible for a motion of the area of higher degradation inside the cell, reducing the membrane thinning phenomenon.

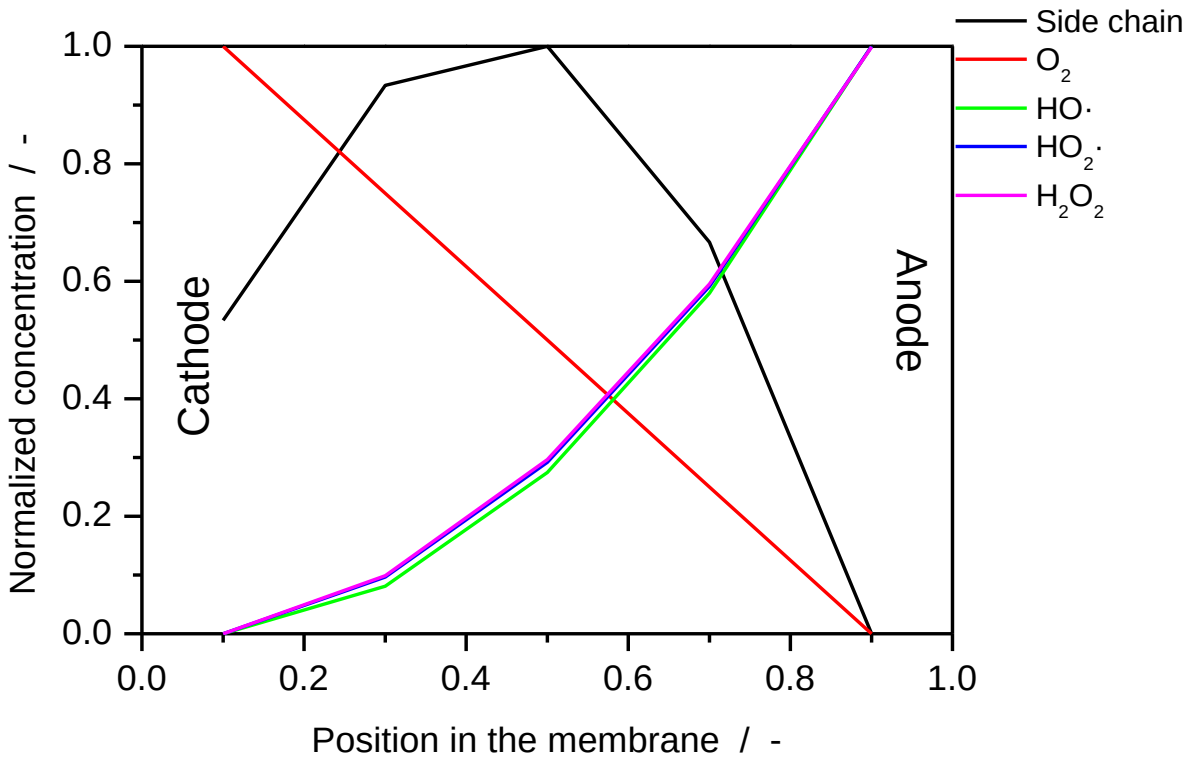

Figure 4.37: Profile of normalized concentrations along the membrane after 500 h for the species acting in the chemical degradation of the membrane at 0.6 A·cm^{-2}, 363 K, 2 bar, 90% relative humidity at anode and cathode, stoichiometry 8/16 anode / cathode and 10^{-3} mol·m^{-3}·s^{-1}.

4.4 Impact of chemical degradation on cell performance under cyclic current operation

4.4.1 Introduction to the necessity of the use of current cycles

During stationary applications, a PEMFC would not be used without any interruptions or variations in the power it is asked to deliver. Thus we focus our attention on stationary cycles which may be more representative of the operation of a real fuel cell system. We consider two different cases, which we identified as realistic for the use which can be made of a commercial PEMFC:

- On-off conditions, when the cell can either be at low current density or under middle current load
- I_{min}-I_{max}, when the needs in energy are oscillating between middle current and a higher one.

4.4.2 On-off cycle of a PEMFC

4.4.2.1 Description of the cycle

If we imagine a stationary system which is used only during the half of the day (for example power supply during the night to make up for a solar energy system), the cell will run during several hours and then be shut down, to be restarted after several hours, as the example displayed in Figure 4.38..

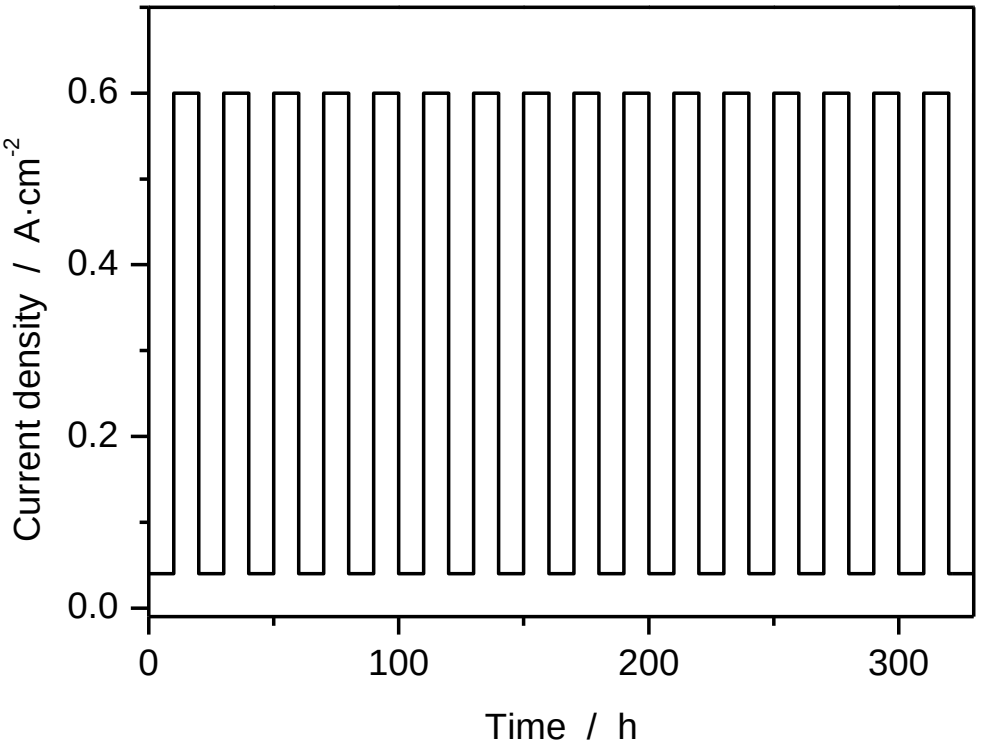

Figure 4.38: Current density profile used to simulate an on - off operation of a PEMFC

4.4.2.2 Behavior of a PEMFC under on-off conditions

We want to see here if the cell responds more like a cell operated under on-off conditions or rather under 0.6 $A \cdot cm^{-2}$. Every 10 hours, the cell is shut down for 10 hours, and then restarted for 10 h.

The evolution of the cell potential is given in Figure 4.39. For simplicity reasons, we illustrate here the evolution of the reference cases taken as simulations under constant current density as in Section 4.3. The PEMFC design we simulated is our standard cell with the simulation conditions given in Table 4.11. We can see that the potential remains stable over time and the potential is in agreement to the reference cases. We notice small overshoots and undershoots when the current density increases, respectively decreases. The source of this behavior is presented in Figure 4.40, where the temporal evolution of the water content in every compartment of the discretization is reported.

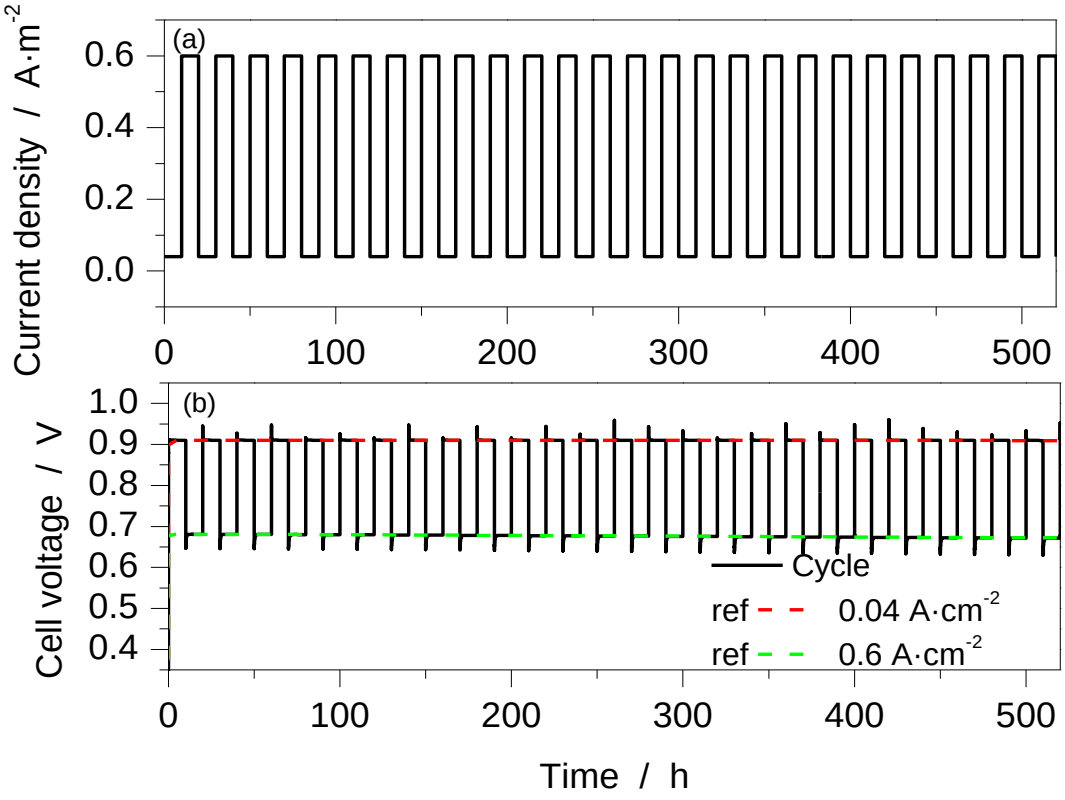

Figure 4.39: Evolution of the current density (a) and cell voltage (b) over time

Parameters	Value	Unit
Pressure	2	bar
Temperature	80	°C
Stoichiometry A / C	15 / 20	-
Relative humidity A / C	80 / 80	%
Production of Fe^{2+}	10^{-3}	$mol \cdot m^{-3} \cdot s^{-1}$

Table 4.11: Conditions used for the on - off simulations

In Figure 4.40 we notice that each potential overshoot correspond to an overshoot in the water content at the anode side, and each potential undershoot correspond to an undershoot in the water content at the anode side. Thus the transient behavior observed in the potential after each current density variation is due to the time needed by the cell to re-equilibrate its water content. By increasing quickly the current density, more protons are instantaneously required at the cathode side and thus the electro-osmotic drag term increases quickly with the proton flux. The drag of water will induce lower water

content at the anode side. As back-diffusion is a slower process, it lasts a certain time to get back to a steady-state condition for water.

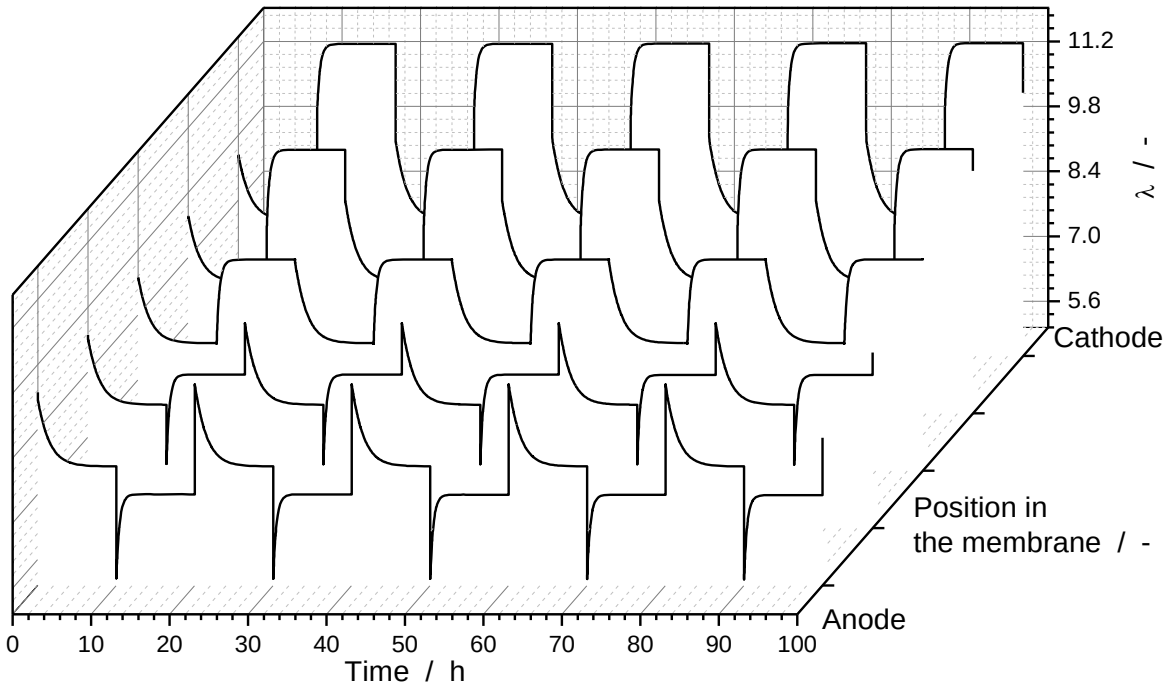

Figure 4.40: Evolution of the water content in each compartment in the membrane.

Moreover, a local disequilibrium in the water content will have an impact on the membrane resistance. In Figure 4.41, the temporal evolution of the membrane resistance is represented. We see indeed that for every water content overshoot, a decrease of the membrane resistance is observed, which is obvious, as with better humidification the proton conductivity of the membrane will be higher. We observe that the membrane resistance increases as well and the values of the membrane resistance of the cycle follow perfectly the evolution of the references cases. How will it impact on the real chemical degradation of the cell?

We have to focus our attention on the fluoride emission by the cell. In Figure 4.42, we represented the cumulative fluoride emission under cycling conditions as well as the two extreme cases, when no cycling occurs. We observed that the degradation is located between a cell operating only at low current density or only at 0.6 $A \cdot cm^{-2}$. We see that the cumulative fluoride emission of a cell subjected to a cycle is between the one of low current density and 0.6 $A \cdot cm^{-2}$.

In summary, when applying an on - off cycle to a PEMFC, the notice a degradation of the membrane. Variations of water content during the switch phases impact the cell voltage signal, as they induce

overshoots and undershoots in the cell voltage. Membrane resistance increases over time in proportion which is similar to cases where no cycle but a constant current density is applied. Last the chemical degradation state of the membrane is located between the degradation of our reference cases of low and high constant current density.

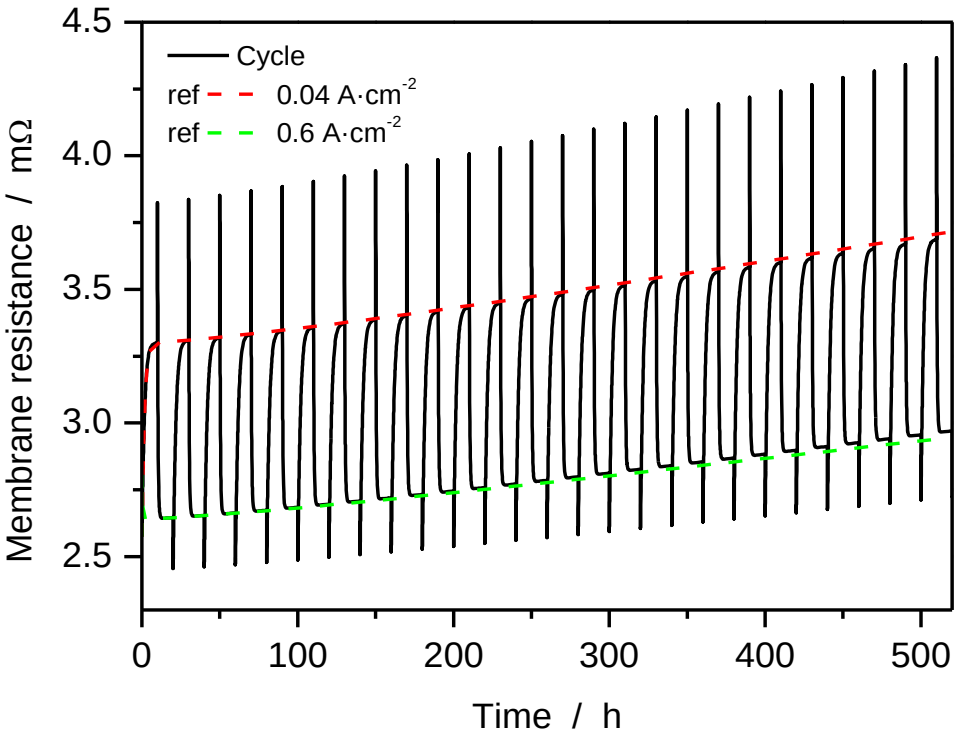

Figure 4.41: Evolution of the membrane resistance for different operating conditions

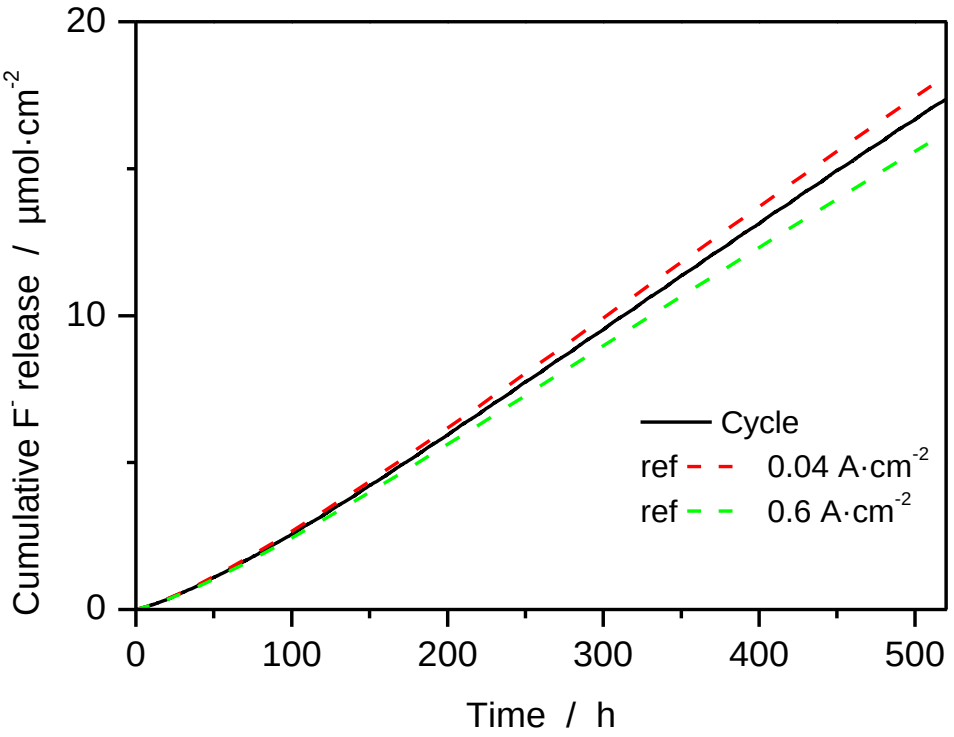

Figure 4.42: Cumulative fluoride release for different operating conditions

4.4.3 I_{min}–I_{max} cycle of a PEMFC

4.4.3.1 Description of the cycle

We focus now on a case when the PEMFC is operated in two different states, either at 0.6 A·cm^{-2} or at 1.2 A·cm^{-2}. The profile used and the response of the cell are given in Figure 4.43. It may correspond to a constant use and peak in the needs of energy because of the switch on of more devices on the PEMFC stack for example. In Table 4.12, we summarize the conditions used in the simulation. We managed to run the simulation for more than 500 h, for a severely attacked membrane.

4.4.3.2 Behavior of a PEMFC under I_{min}–I_{max} conditions

We take now a closer interest on what would happen if we do not oscillate between low current density and 0.6 A·cm^{-2} but between 0.6 A·cm^{-2} and 1.0 A·cm^{-2}. In Figure 4.43, the applied operating conditions and the response of the cell are displayed. To make the comparison easier, we plotted as reference the cases of constant current density condition. We see, like in the previous case (Section 4.4.2.2), that the cycle condition follows the same behavior as the corresponding constant current. We

observe a slight decrease of the cell potential at 1.0 A·cm^{-2}, comparable to the cases observed in Section 4.3.2. The only remarkable point is a potential undershoot when the cell goes from 0.6 A·cm^{-2} to 1.0 A·cm^{-2} and a potential overshoot in the opposite direction. To explain this phenomenon, we investigate water management in the cell over time, as made in the previous section.

In Figure 4.44, we show the evolution of the water content depending on experimental conditions and position in the membrane for the first 100 h for a better representation. Analogous to the previous case of Section 4.4.2, we see that the potential shot coincide with peak in water content in the membrane on the anode side. Close to the cathode side, the changes in the water content with changes of the current density are smoother. That would mean that the membrane resistance would consequently change. In order to check this, we plotted in Figure 4.45 the temporal evolution of the membrane resistance. This behavior is explained by the quick increase of the need in proton at the cathode when the current density increased. The electro-osmotic contribution of the water flux increases quickly and the diffusion processes are not quick enough to balance instantaneously this effect. Thus water depletion is temporarily observed at the anode side.

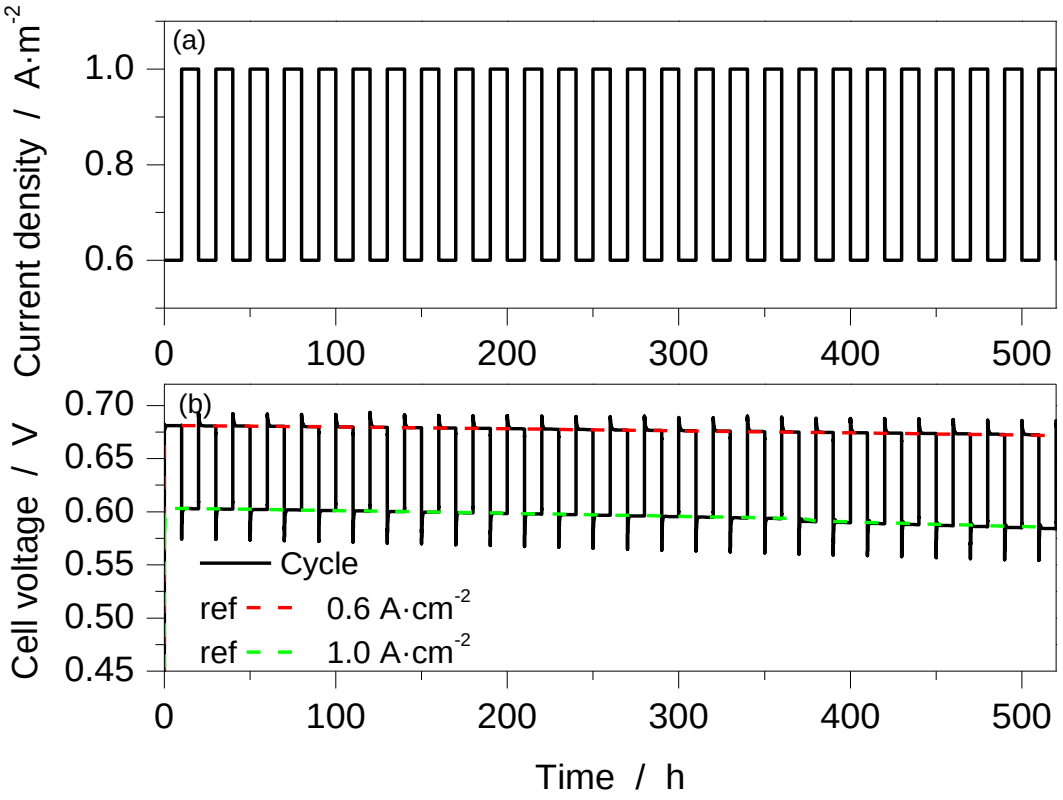

Figure 4.43: Current density cycle applied to the cell (a) and response in cell voltage (b), compared to cases when the current density is kept constant.

Parameters	Value	Unit
Pressure	2	bar
Temperature	80	°C
Stoichiometry A / C	15 / 20	-
Relative humidity A / C	80 / 80	%
Production of Fe^{2+}	10^{-3}	$mol \cdot m^{-3} \cdot s^{-1}$

Table 4.12: Conditions used for the I_{min}–I_{max} simulations

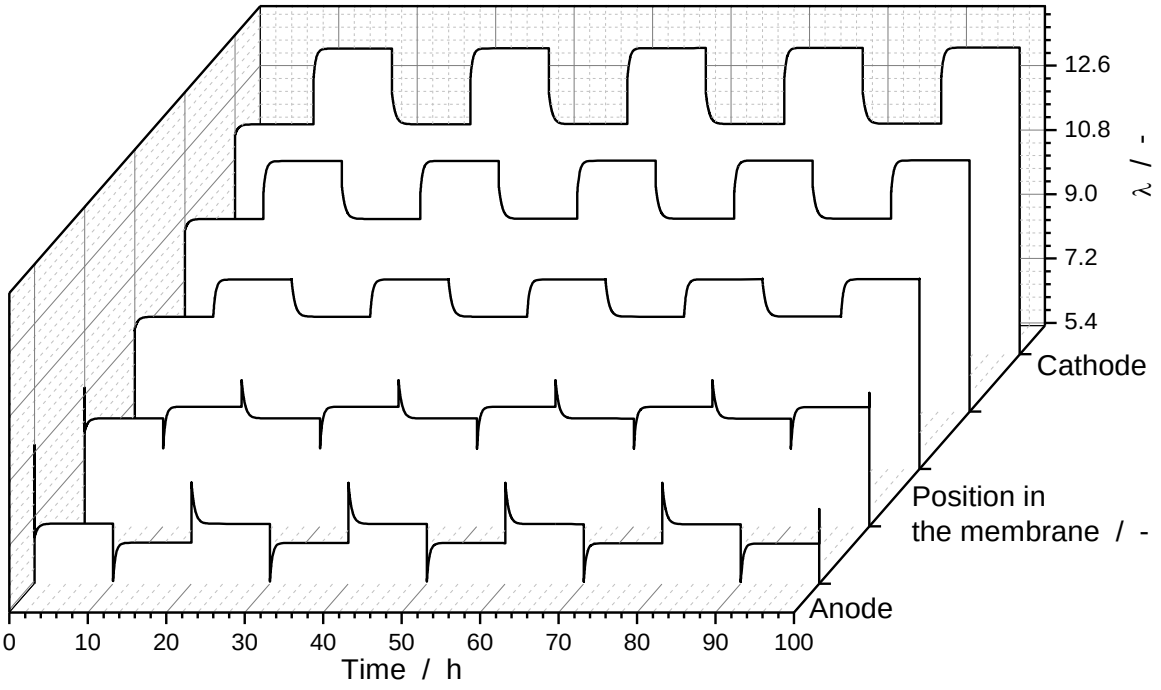

Figure 4.44: Evolution of the water content in every compartment of the membrane during I_{min}–I_{max} cycles.

In Figure 4.45, we observe an increase of the membrane resistance over time. To be sure that the membrane effectively degrades and that the increased resistance is not due to water effect, we plotted in Figure 4.46 the evolution of the accumulated fluoride concentration in the system for cases which are treated here. We see that the amount of fluoride ions released during the degradation is between the extreme of the cycle we applied to the cell. We come then to the same conclusion as for the on -

off cycle we studied previously.

Last, we want to see which conditions are more aggressive for the cell: cycling or a keeping under constant current. As we deliberately set the iron ions production to a value that stimulates degradation, differences are all the more enhanced. In Figure 4.46, we plotted the evolution of the fluoride in the system for cases which are treated here.

Of course, all these observations are given by the model and should be compared to experimental results, in order to check their validity.

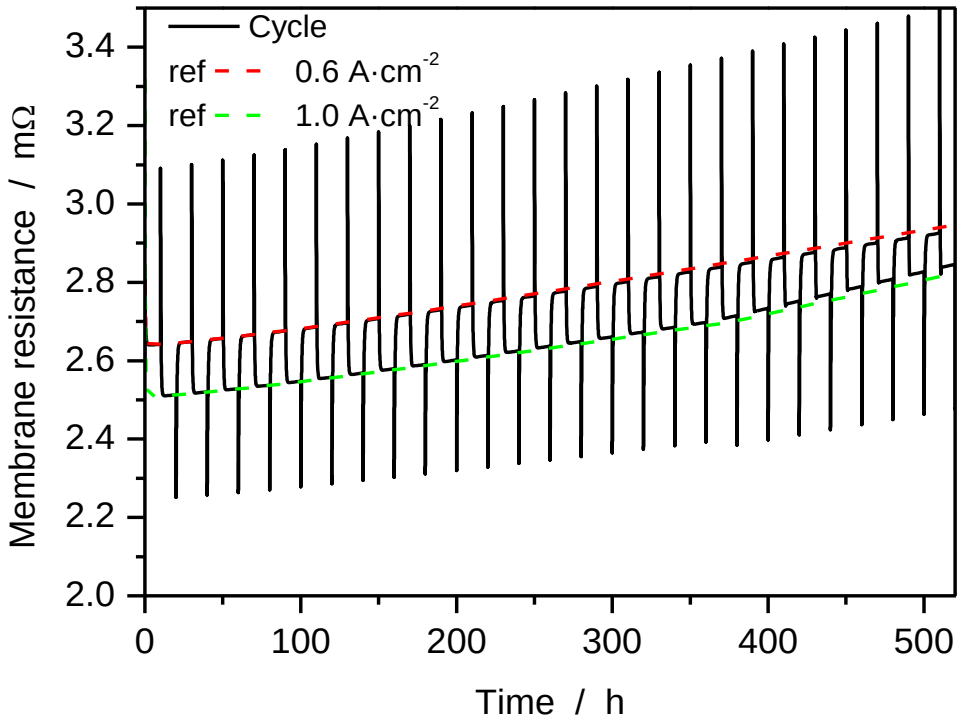

Figure 4.45: Evolution of membrane resistance under I_{min}–I_{max} cycles.

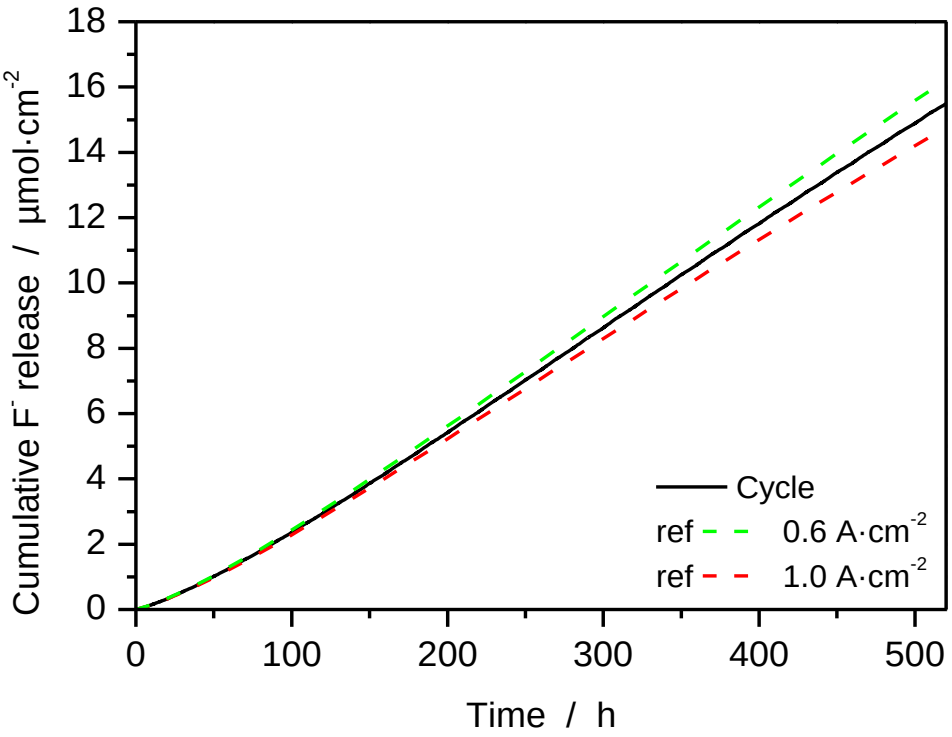

Figure 4.46: Cumulative fluoride release for different operation conditions

4.5 Impact of the presence and the amount of iron ions on degradation

As it has been previously mentioned (see in Section 2.3.1 and Section 4.2.3.3), iron ions are the key parameter for the decomposition of hydrogen peroxide into radicals. Thus we focus in this chapter our attention on the influence of the presence of iron ions and their concentration on the membrane degradation.

The production of iron ions in the real system can be random and difficult to model. For this reason, we simulate the degradation behavior of the cell under different production terms of iron ions at the cathode side. We vary this term in a range from 10^{-7} up to 1 $mol \cdot m^{-3} \cdot s^{-1}$. As the simulation runs for 500 h or 1000 h, this corresponds to a net release of iron in the membrane (25 cm^2 and 60µm thickness) from $2.7 \cdot 10^{-8}$ mol up to $2.7 \cdot 10^{-1}$ mol over time or 15 µg to 15g. The upper limit of iron weight in the membrane is far too high for a real system. This case is then unrealistic, however simulated. It should be taken as a virtual cell in a system highly subjected to end-plate degradation. We assume that these ions can neither precipitate in the membrane nor react on any other way than those described in Section 2.3.1.

In Figure 4.47, we plot the cumulative fluoride release in the membrane after 500 h operation at differ-

ent temperatures (more simulation parameters in the table embedded in Figure 4.47). We choose a low current density

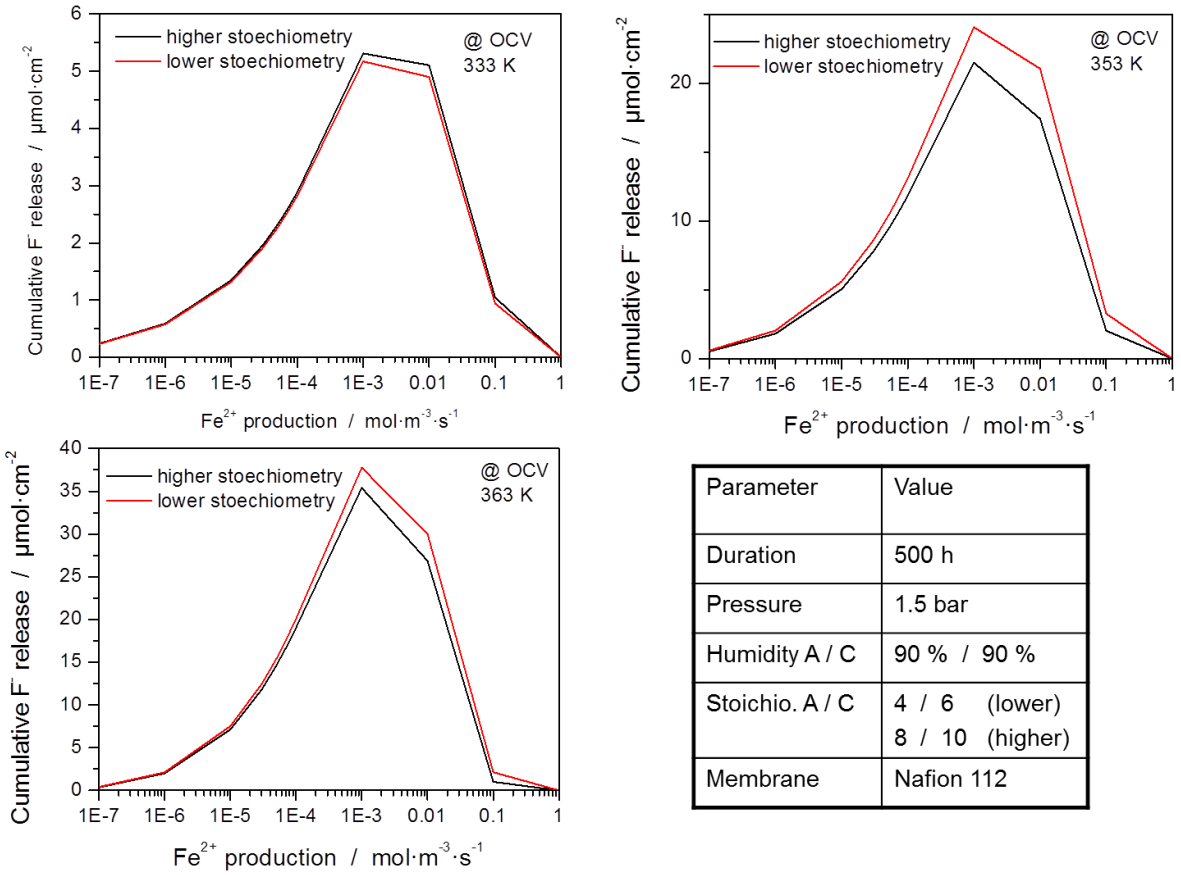

Parameter	Value
Duration	500 h
Pressure	1.5 bar
Humidity A / C	90 % / 90 %
Stoichio. A / C	4 / 6 (lower) 8 / 10 (higher)
Membrane	Nafion 112

Figure 4.47: Dependence of the fluoride production on the iron ions production for different temperatures

Beyond these temperature effect, one particularity of our simulate results have to be noticed. Logic would expect that if we always increase the production term of iron ions in the membrane, the membrane would be worse and worse degraded and would fail faster (potential collapse, consequence of short circuit involved by the disappearance of the electrolyte). But in Figure 4.47, we observe a very interesting phenomenon. Under very aggressive conditions, the membrane is less degraded than under moderate conditions. This could be a very interesting phenomenon if it were experimentally proved. We searched for published results that could confirm what we get through simulations.

On the previously mentioned contributions, Kodama *et al.* presented also results which indicates a similar trend as our modeling results [158, 159]. They studied the degradation of Nafion® in hydrogen peroxide. They found out that under very aggressive conditions, the degradation effects are drastically prevented (see in Figure 4.48).

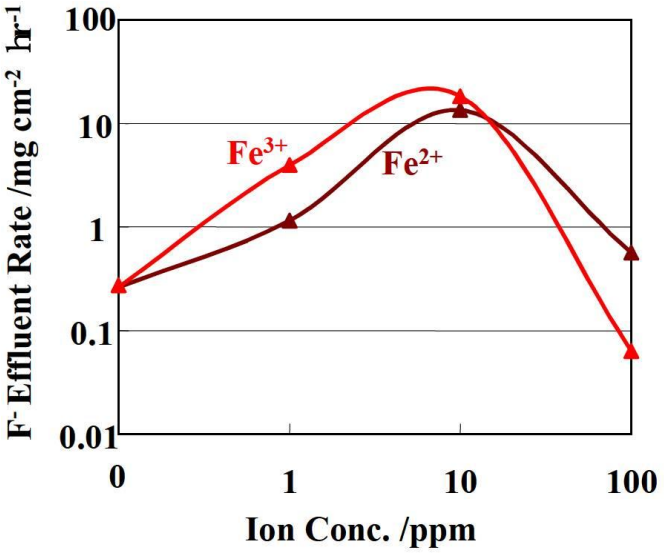

Figure 4.48: F^- effluent rate from Nafion® 112 (7.2cm × 7.2cm) in 1wt%H_2O_2, 100ºC × 8 h with iron ions [159]

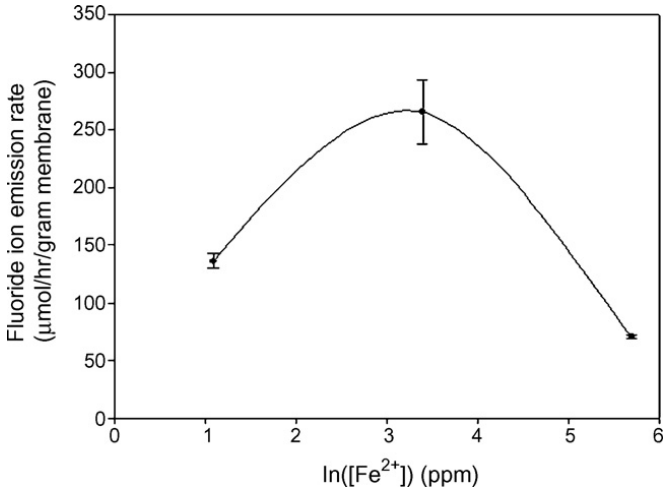

Figure 4.49: Effect of Fe^{2+} concentration on membrane degradation [37]

Kodama *et al*. measured the fluoride concentration with an ion-selective electrode. Few years later, Chen and Fuller investigated through XPS Nafion® degradation and measured the produced fluoride ions through ion chromatography (IC) [37]. As they studied the impact of the ferrous ions concentration, they observed the same trend as Kodama (Figure 4.49). This trend was criticized by Schiraldi *et al*., and assumed to be an experimental error due to the existence of Fe^{3+} in Fenton's reagent when using commercial ion-selective electrodes [31, 37]. This argument was refuted by Chen and Fuller, responding that such an error could not occur in their experiment using IC. They rather thought that the observed decreasing in the fluoride production was due to the presence, at high concentration of

iron ions, of macromolecules containing bound fluoride as degradation products, which could not be measured by IC. On the contrary, lower concentrations of iron ions would rather lead to fluoride ions as main degradation product, explaining the difference they observed.

In our model, we consider only one degradation product: fluoride ions. Thus the explanation given by Chen and Fuller could not be the reason for our observations. This observation has to be a consequence of the model assumptions. Lower membrane degradation means either that less radicals have been produced by the cell, or the radicals did not react with the side chains themselves but with other species in the membrane. This is the first step to the explanation we propose for this iron dependence on the degradation of a PFSA membrane.

If we consider that the hydrogen peroxide production is independent of the concentration of iron ions, which is logical, Reaction 2.4 cannot be the source of the protection of the membrane against radicals. However, if we have a look at Reaction 2.5, HO radicals can react with ferrous ions in acidic media to form ferric ions and water. This leads us to think that if the concentration of iron ions is too high, it will be easier for the radicals to react with them than attacking the side chain of the membrane.

The typical side chain concentration we used in our simulation is 1200 $mol \cdot m^{-3}$. If we look in Figure 4.47, we locate a maximal chemical degradation of the membrane for an iron ions production of about 10^{-3} $mol \cdot m^{-3} \cdot s^{-1}$. After the 500 h of our simulations, this would mean a net concentration of iron ions of $10^{-3} \cdot 500 \cdot 3600 = 1800$ $mol \cdot m^{-3}$. We assume then that when the total concentration of iron ions introduced into the system is close to the initial concentration of side chain, the degradation is maximal. Beyond this point, the iron ion concentration will progressively hidethe side chain and prevent the radical attack on the membrane. More calculation should be carried out to justify this hypothesis, for example by increasing the simulation time and seeing if our hypothesis is correct.

A second hypothesis which can be made is related to the production of hydrogen peroxide at the anode. If iron ions and H_2O_2 are produced at similar rates, ferrous ions will not have the possibility to accumulate and the radicals will react with the membrane.

If iron ions are produced slower than H_2O_2, H_2O_2 will not be completely decomposed into radicals, leading to a decelerated attack on the membrane.

If irons ions are produced much faster than H_2O_2, H_2O_2 will be completely decomposed and ferrous ions will be available for further reaction with the produced radicals. If the concentration of ferrous ions becomes too high, the radicals will preferentially react with iron than with the membrane, which will protect it.

In Figure 4.50, our hypothesis is confirmed. We observe that for a low production of Fe^{2+}, hydrogen peroxide is more present in the membrane and the rate of degradation increases. When we pass the limit of 10^{-2} $mol \cdot m^{-3} \cdot s^{-1}$ the concentration of iron ions severely increases and this corresponds to the

point where the membrane degradation slows down. That would then confirm our second hypothesis.

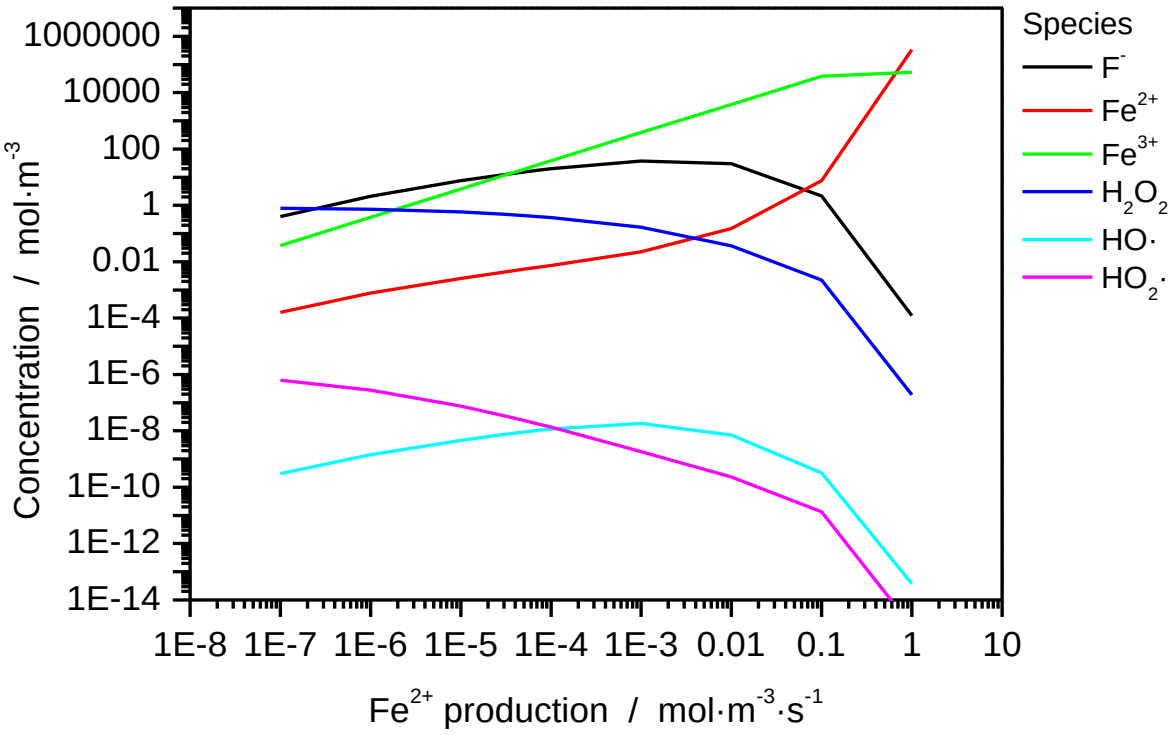

Figure 4.50: Simulated evolution of the concentration of different species during degradation (500h, low current density, 363 K).

We can notice in this study that the chemical degradation of a PFSA membrane is strongly temperature dependent. Even if lower temperatures do not provide as good performances as higher temperature, the durability of the membrane is improved. According to our simulations, running a cell at 60 °C instead of 90 °C could reduce the chemical degradation by a factor 4, which is not negligible.

Moreover, in a cell severely polluted by ferrous ions, the chemical degradation which we simulate is close to zero. However, ferrous ions have a high affinity to the side chain of the PFSA membrane, which is currently not taken into account in our present model. Thus the negative impact of iron ions on the conductivity of the membrane is not regarded. But from a chemical stability point of view, it seems that in presence of hydrogen peroxide and a high quantity of iron ions, Nafion® is more chemically stable than in moderate conditions.

4.6 Degradation of other PFSA membranes

Until now, all the simulations we made used parameters of Nafion®. Even if Nafion® has been a stand-

ard in fuel cell technology, providing gas impermeability, a good thermal, mechanical and chemical stability and a high proton conductivity, many other products came over the years on the market of electrolytes for low–temperature PEMFC (see Table 1.2). They are all PFSA membranes, but they differ in the chemical structure (equivalent weight, length of side chain). Thus the F / S ratio "41" which was used in the model for the Nafion® description would not suit to a membrane with shorter side chains, for example like Aquivion (Figure 4.4), whose equivalent weight is also lower than for Nafion®.

With help of the data from Table 1.2, we run simulations with different kind of PFSA membrane, to see how the chemical structure impact on the chemical degradation of the membrane. This was made under the assumption that the kinetic rate of attack of radicals on the ether functions bonding side chains to the back bone is independent of the chemical structure. This could only be checked by performing experiments with several membranes and following the fluoride emission rate.

In Table 4.13, we present the membrane parameters that we used in our study. We want to determine, under constant current conditions, which membrane is the most resistant to chemical degradation. The calculation of the ratios F / S was performed considering a general structure for PFSA membranes as shown in Figure 1.3 and the (*m*, *n*, *x*, *y*) values given in Table 1.2.

Membrane	EW / $g \cdot eq^{-1}$	Ratio F / S	Thickness / µm
Aciplex	1100	20	25
Dow	800	14	125
Aquivion	870	35	30
Nafion®	1100	41	60

Table 4.13: Parameters of membranes simulated in this study

For this study, we can separate membranes into several classes:

- Low and high equivalent weight
- Low and high fluoride content

Under these points, we sort out as:

- Aciplex: High EW, low F / S ratio
- Dow: Low EW, low F / S ratio
- Aquivion: Low EW, high F / S ratio

- Nafion®: High EW, high F / S ratio.

In Figure 4.51, we plotted the low current density voltage (for $4 \cdot 10^{-2}$ A·cm^{-2}) for the different cells with membranes as defined in Table 4.13. We see that low EW membranes have better performance than high EW membranes. This cell voltage difference is however too small to take the OCV (or in this case voltage at low current density) value as valid criteria in the choice of the membrane when a cell is designed. Our interest here is to see how these membranes behave regarding their chemical degradation. For that purpose we plotted in Figure 4.52 the cumulative fluoride release rate for every membrane we considered.

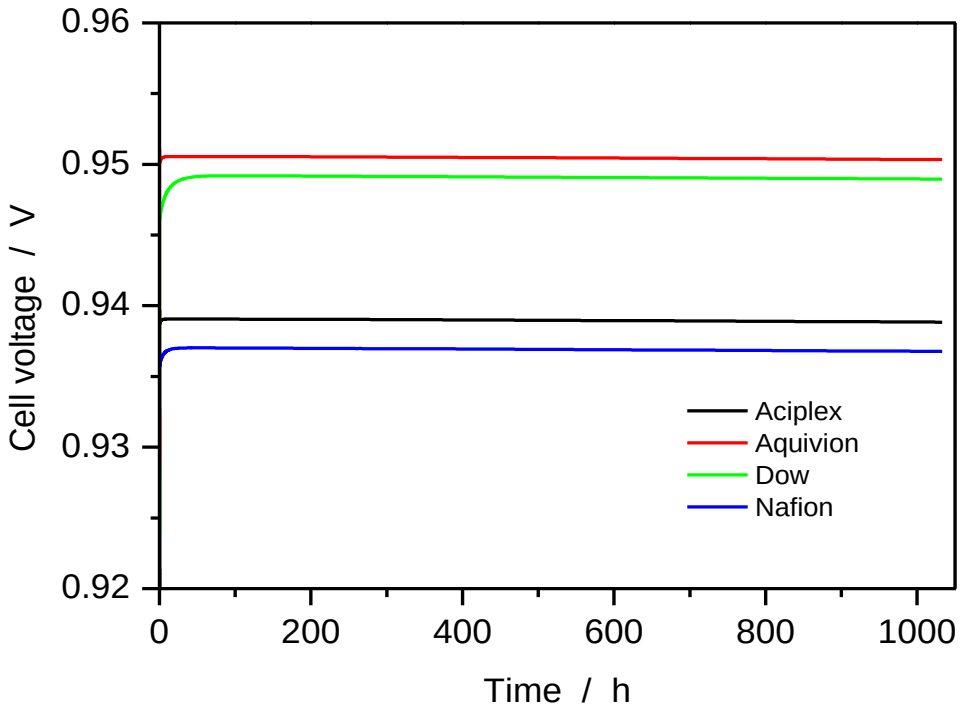

Figure 4.51: Comparison of cell voltage for different membranes at $4 \cdot 10^{-2}$ A·cm^{-2}, 333 K, 90 % relative humidity, 2 bar and 10^{-3} mol·m^{-3}·s^{-1} Fe^{2+} production.

As it can be seen, membranes with lower fluoride to side chain ratio would degrade less than membranes with higher fluoride to side chain ratio. However, we assume in these calculations that the concentration of side chains and the density of the membrane are not dependent on membrane type, which is incorrect. It is difficult to find exact data on different membranes, mostly because of confidentiality. However we found sufficient information both for Aquivion and Nafion®. Thus we simulate this time more precisely these two membranes with the same parameters as given on Table 4.13, completed with parameters of Table 4.14. Moreover, we neglect the humidification effect on the membrane volume, what was previously taken into account. Thus we suppose that the volume of the membrane remains constant over time and is not subjected to the variations of humidity in the cell.

Membrane	Side chain concentration / $mol \cdot m^{-3}$	Density / $kg \cdot m^{-3}$
Aquivion	2367	2060
Nafion®	1800	2240

Table 4.14: Extra parameters regarded for the accurate study of the influence of membrane type.

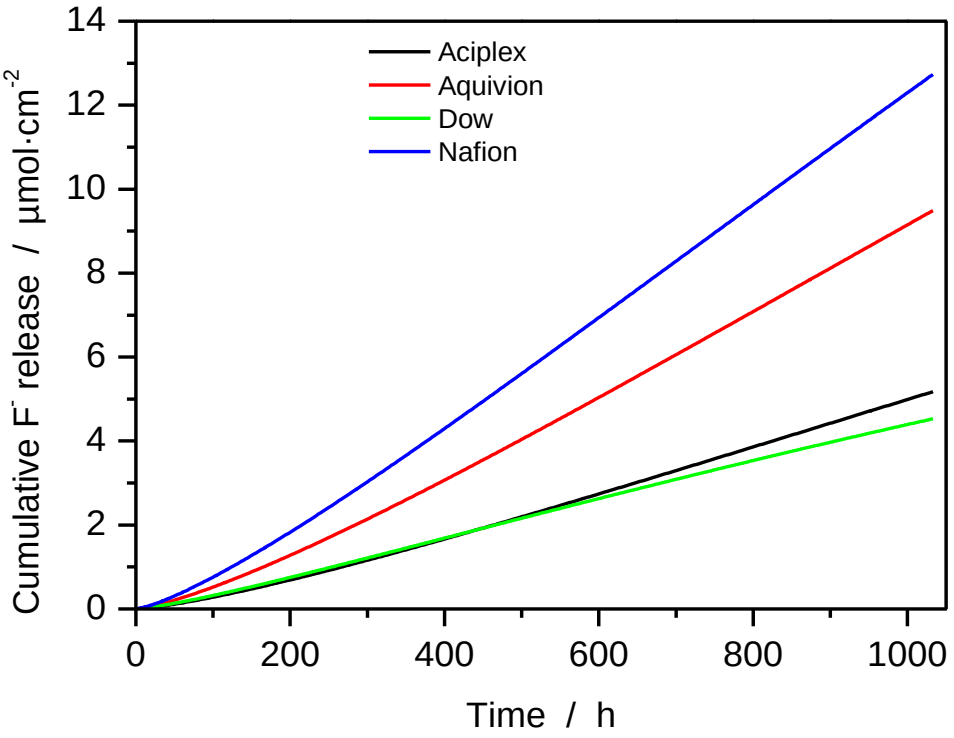

Figure 4.52: Comparison of cumulative fluoride production for different membranes at $4 \cdot 10^{-2}$ $A \cdot cm^{-2}$, 333 K, 90 % relative humidity, 2 bar and 10^{-3} $mol \cdot m^{-3} \cdot s^{-1}$ Fe^{2+} production.

In Table 4.14, the initial concentration of side chain is calculated as the ratio between the density of the membrane and the equivalent weight. As we observe, a decrease of the EW will increase the concentration of side chain and as Aquivion contains less fluoride than Nafion®, it may be comprehensible that the polymer has a lighter densityas well.

The results of our simulation concerning the membrane degradation are given in Figure 4.53 (b). In Figure 4.53 (a), we report for comparison the results for membranes considering the first assumptions we made. What we notice in that case, is that the chemical degradation of both membranes is similar. We observe that with real membrane parameters, the degradation behavior is strongly impacted. When in the simple case we only changed one single parameter, we should have seen more precisely the

physical properties of membranes, which remain sometimes very difficult to access.

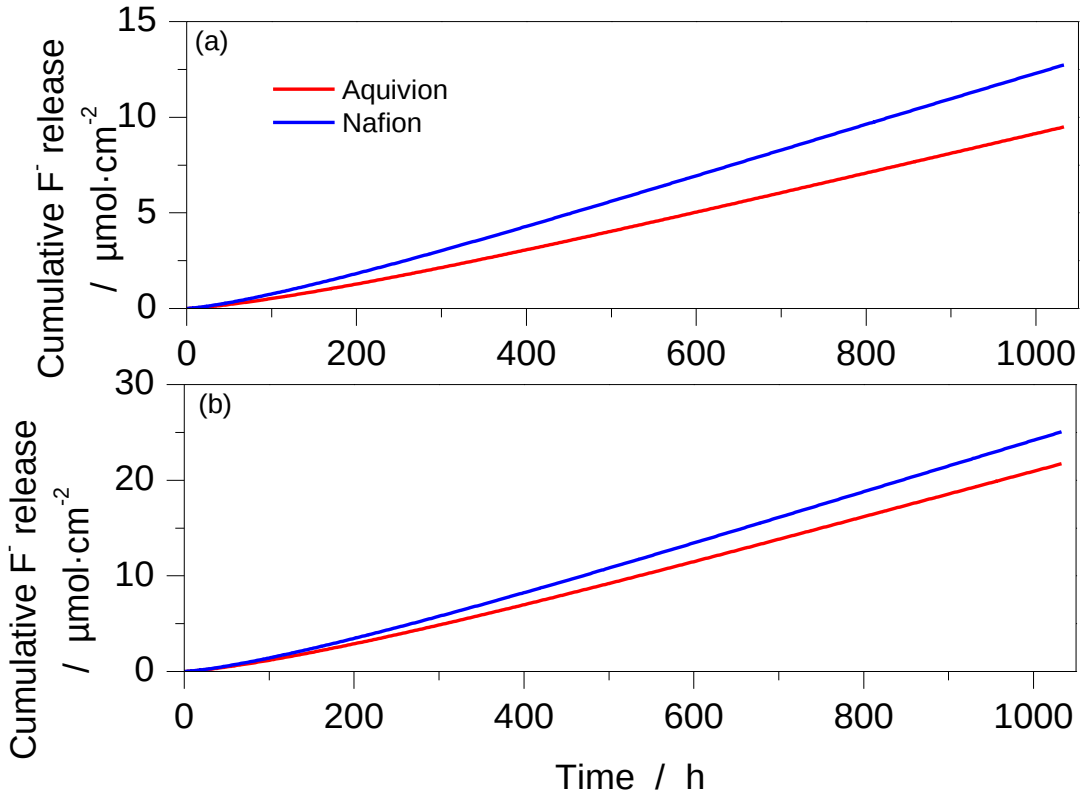

Figure 4.53: Comparison of cumulative fluoride production for different membranes at $4 \cdot 10^{-2}$ A·cm^{-2}, 363 K, 90 % relative humidity, 2 bar and 10^{-3} mol·m^{-3}·s^{-1} Fe^{2+} production (a) Simple case and (b) Complete case.

The chemical degradation of Nafion® 112 and Aquivion E87-03 is comparable. Over 1,000 h, they seem to degrade at similar rates, but physical properties of Aquivion should to make it more resistant to radicals attack, according to our model's prediction. As mentioned in Section 1.2, PFSA membranes are really complex objects whose study requires the best technology available. It cannot be summarized to a simple model to ascertain on their resistance against chemical degradation. However, this trend could be experimentally observed. As manufacturers aim on producing more resistant products with same performance, it may be expected that in a few years, the results we obtained through simulation exaggerate the real trend. But in that case, the degradation mechanism would remain the same and only kinetics parameters might change, assuming known membrane properties.

4.7 Prediction of long-term cell durability

In the previous sections, we have presented our simulation results upon the chemical degradation of

the single cell over 500 h, a duration which is reasonable at the laboratory scale, but still too short for a real stationary application. As the chemical degradation induces a decrease of the cell potential, we want now to evaluate the time needed for the cell potential to decrease to a point when the cell is considered as failed (durability). Different criteria can be taken for the durability of the cell. In our current study, we define the "end-of-life" (EoL) of the cell as the loss of 5% of the initial cell potential (potential after 20 h).

In Figure 4.54, we display the evolution of the durability with current density and temperature. We observe that the resistance increases and the durability decreases as the temperature increases. Another interesting feature is that the durability decreases as the current density increases.

We see as well that increased current density will shorten the durability of the cell.

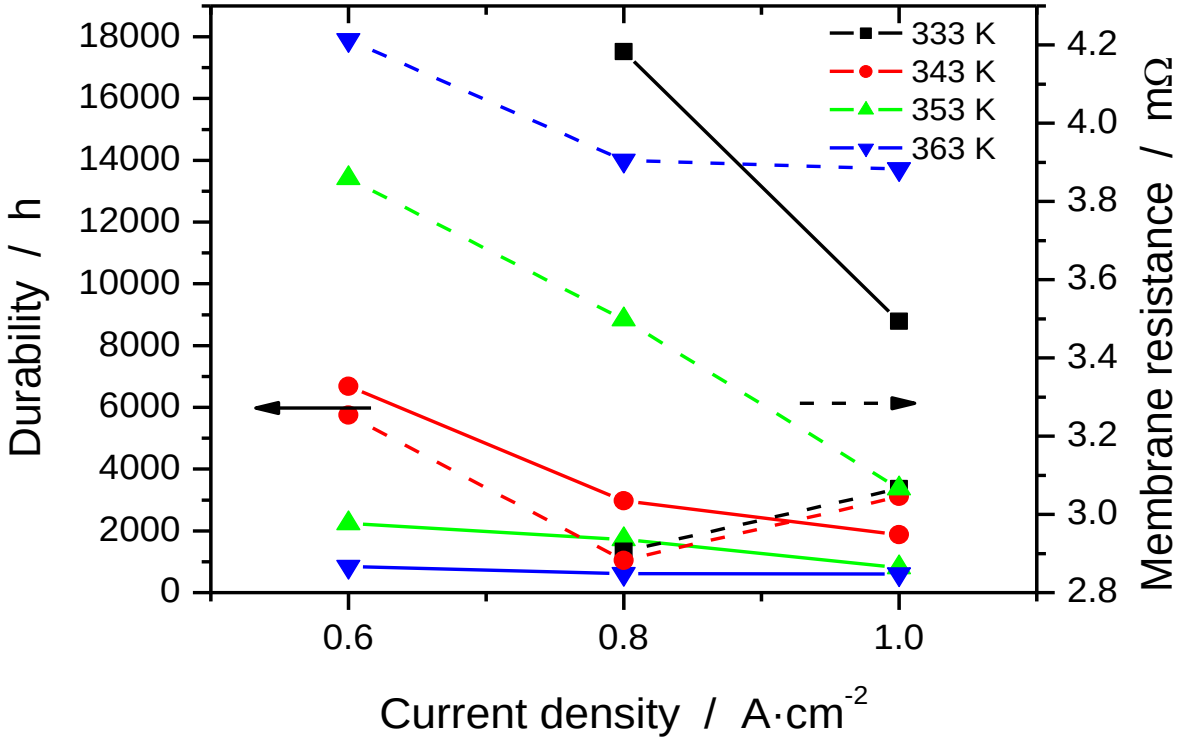

Figure 4.54: Evolution of durability and membrane resistance at EoL with current density and temperature.

As the cell voltage decrease is due to an increase of the ohmic resistance, it is interesting to check the evolution of the cell resistance. As we can see in Figure 4.54, no direct correlation can be made between the membrane resistance at EoL when the durability criterion is reached and the durability of the cell. At high temperature, the membrane resistance decreases with increasing current density when the durability criterion is reached. However at low temperature, the membrane resistance increases. From this, it cannot be concluded that the membrane degradation is more significant at higher current

density for low temperature, as the membrane resistance calculation depend on the temperature, the water content and the degradation state of the membrane. For this reason, in Figure 4.55 we represent the chemical degradation of the cell through the cumulative fluoride emission, which depends only on the stage of the membrane decomposition.

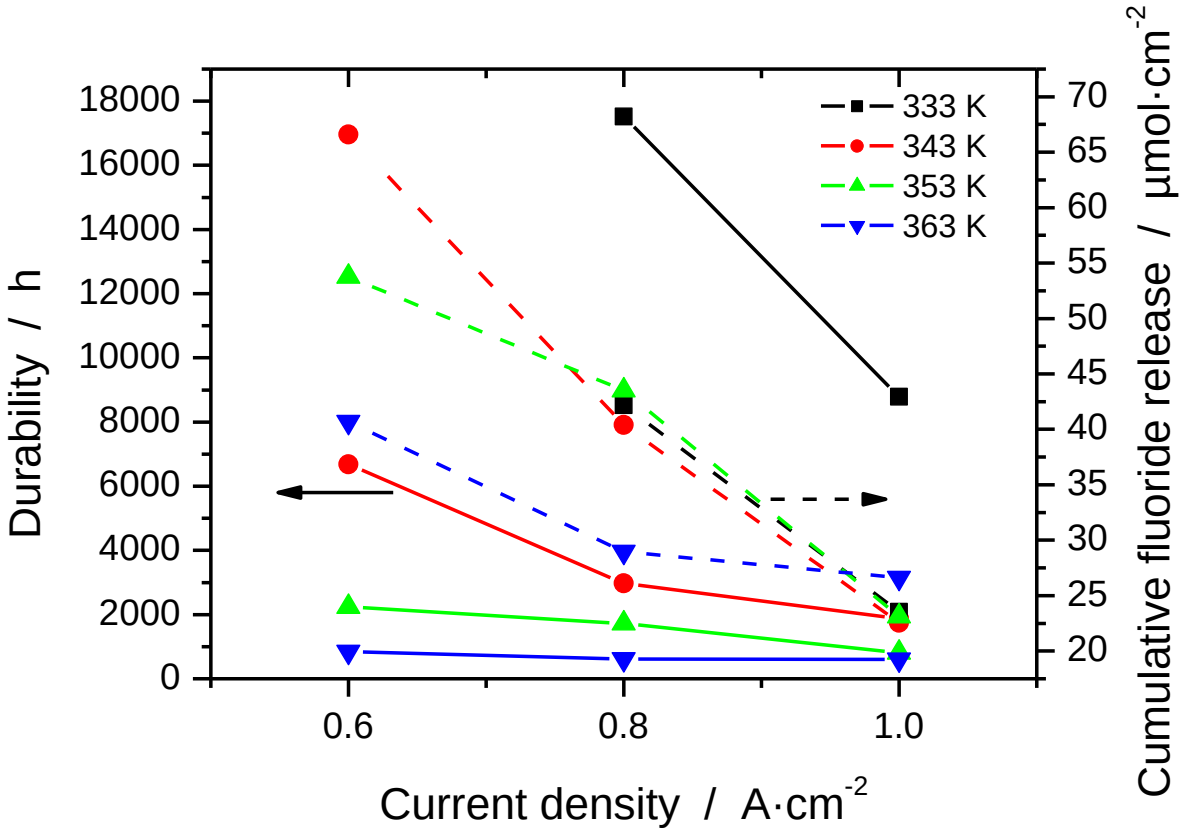

Figure 4.55: Evolution of durability and cumulated fluoride emission at EoL with current density and temperature.

We see in Figure 4.55 that at 0.6 $A \cdot cm^{-2}$ the degree of the membrane decomposition decreases as the temperature decreases when durability criterion is reached. When we increase the current density, the chemical degradation decreases and the variation of the results is smaller. We attribute the observation of a higher degradation at 0.8 $A \cdot cm^{-2}$ and 353 K to an uncertainty on the choice of the data taken when EoL was reached (not every time step was recorded).

We see that the chemical degradation of the membrane is consistent with the other simulations presented all along this manuscript. The degradation is not so significant when the cell operates at higher current density; however, at a given temperature, the durability can be severely reduced (more particularly at low temperature). But the evolution of the membrane resistance in Figure 4.54 is still not explained. As mentioned, water content and degradation impact on the membrane resistance at a given

temperature. As the evolution of the chemical degradation is in agreement with previous conclusions, we focus on the water content profile at EoL. These evolutions are presented in Figure 4.56.

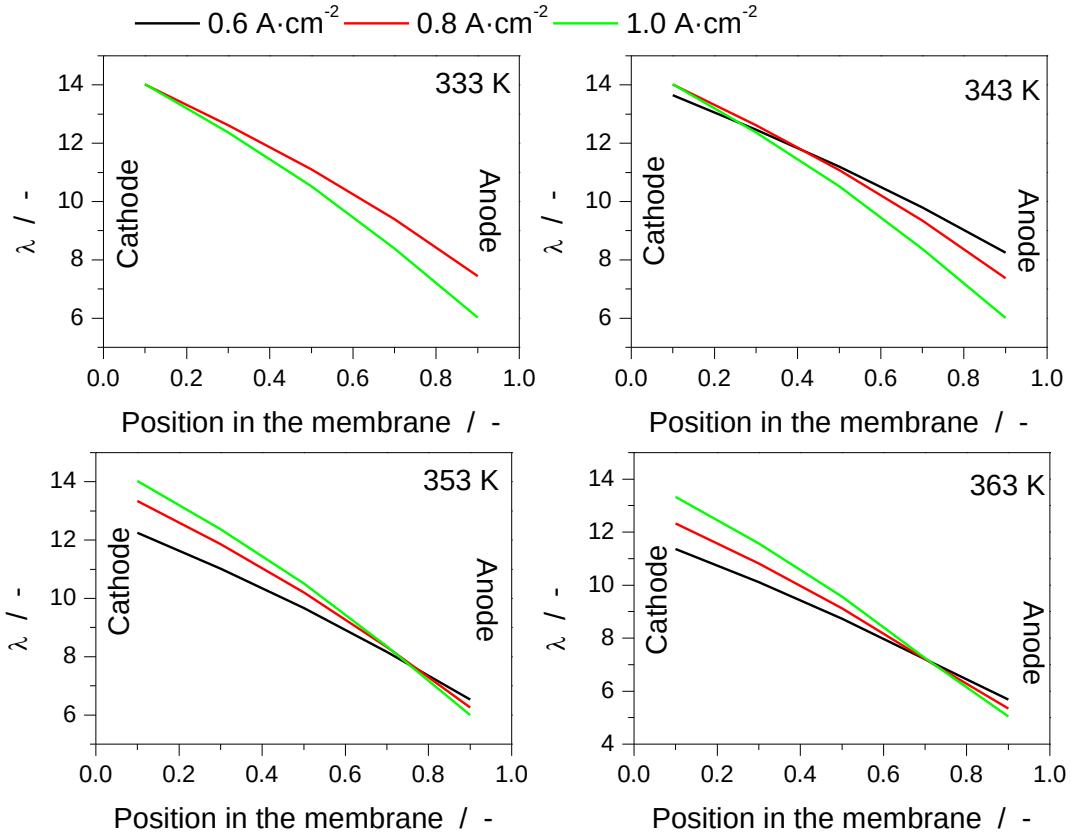

Figure 4.56: Water content profile in the membrane at EoL

For 333 K and 353 K, we see that the membrane contains less water when current density increases. As dry conditions are unfavorable for appropriate proton conductivity, the proton conductivity decreasse with the current density and thus, the membrane resistance increases. At high temperature, the total amount of water in the membrane increases with increasing current density, thus the trend in the membrane resistance evolution is respected.

It should be underlined that the irreversible cell potential degradation is of a real fuel cell can be also other degradation mechanisms, such as the ionomer degradation in the catalyst layers, catalyst dissolution or the catalyst carbon support corrosion [16]. Our model does not intend to predict the real durability of a fuel cell, but only the effects due to the membrane. In future work, this model will be coupled it with the models of other aging phenomena [2-5]. This will allow deeper insights into possible competitions and synergies between processes.

4.8 Strategies for mitigating membrane degradation

4.8.1 Sensitivity analysis

In order to identify the parameters having the highest impact on the chemical degradation, a sensitivity analysis was performed at standard conditions, defined in Appendix C. The target of the analysis was the variation of the membrane area specific resistance over 500 h. Each single model parameters P_i was consecutively increased by 10% from its standard values $P_{i,0}$ to $P_i = 1.1 \cdot P_{i,0}$. The resulting relative change in the variation of the membrane area specific resistance

$$\partial\left(\Delta R_{\text{spec}}\right) = \frac{\Delta R_{\text{spec}}\left(P_i\right) - \Delta R_{\text{spec}}\left(P_{i,0}\right)}{\Delta R_{\text{spec}}\left(P_{i,0}\right)} \qquad 4.3$$

is related to the relative change in the parameter $P_i = 0.1$.

The factor f_{rel}

$$f_{\text{rel}} = \frac{\partial\left(\Delta R_{\text{spec}}\right)}{0.1} \qquad 4.4$$

is the relative sensitivity of the current density with respect to changes in parameter P_i [169]. The result of this analysis is given in Figure 4.57. To identify the potential parameters relevant for the chemical degradation, we refer to Figure 2.6 and isolate any parameter which could impact the chemical degradation of the membrane. We separated the parameters into 5 groups: experimental conditions, parameters related to permeation of oxygen in the membrane, production of H_2O_2, decomposition of H_2O_2, and degradation of the membrane.

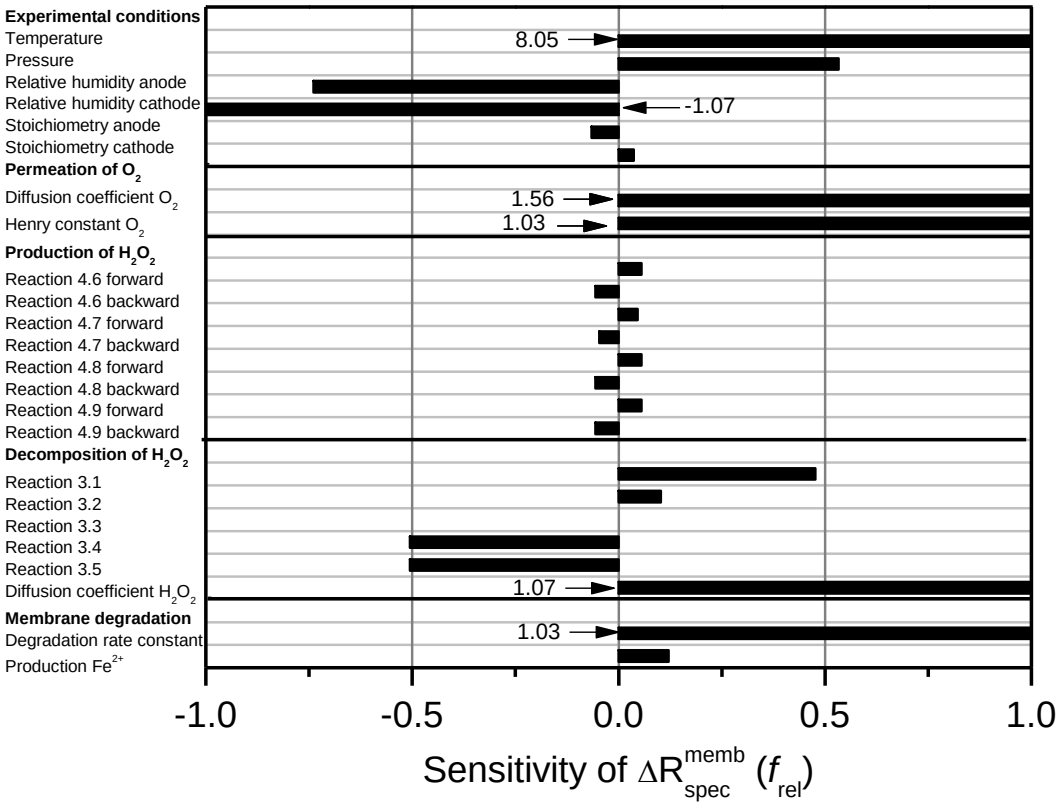

Figure 4.57: Sensitivity analysis of our chemical degradation model. A positive sensitivity means that an increase of the parameter increases the degradation. A value of 1.0 means that the area specific resistance degradation is directly proportional to the parameter.

Experimental conditions – We investigate the effect of temperature, pressure, relative humidity in the electrode and stoichiometry of the gases. Relative humidities have almost a direct proportionality with the evolution of the membrane area specific resistance. The stoichiometry of the gases and pressure variations has a small impact on the resistance variation. However, temperature has an important impact on the evolution of the cell resistance, which can be explained by temperature dependence of the kinetic parameters.

Permeation of oxygen through the membrane – For this process we pay particular attention on the two steps involved in the diffusion of dissolved oxygen within the membrane. The model presents a quasi-linearity between degradation and both, Henry's constant for the dissolution of oxygen from the gas phase into the water of the membrane and the diffusion coefficient of dissolved oxygen within the membrane.

Production of H_2O_2 – We vary here the different reaction rate constants of the steps of hydrogen peroxide production (forward and backward reactions). The influence of these rates is relatively small and no significant impact in the change of the membrane area specific resistance is noticed.

Decomposition of H_2O_2 into radicals – We focus here on the Fenton reactions within the chemical degradation model, the production rate of iron ions and the diffusion of hydrogen peroxide in the membrane. The diffusion coefficient of hydrogen peroxide has a proportional impact on the membrane area specific resistance degradation. Regarding Fenton steps, Reaction 2.1, Reaction 2.4 and Reaction 2.5 are rate determining for the variation of membrane area specific resistance. Modifications in the iron ions production rate show no significant impact on the evolution of the resistance. However it has to be noticed that this conclusion had to be correlated with Figure 4.47, as depending on the initial conditions, an increased iron production can induce either a smaller or a larger degradation.

Decomposition of the membrane – The only parameter implied in the radical attack on the PFSA membrane is the reaction rate constant associated to the attack of the side chain by radicals. It shows proportionality with the evolution of the membrane specific area resistance.

To conclude, cell temperature is the key parameter to be regarded in membrane chemical degradation. Increased temperature has a severe impact on the degradation of the membrane. However, increased relative humidity at the cathode side will reduce the chemical degradation on a proportional way. Regarding steps involved in membrane chemical degradation, dissolution of oxygen and diffusion steps (both oxygen and hydrogen peroxide) show a certain influence on the chemical degradation of the cell. Reducing the diffusion coefficient of oxygen by 10 % would for example be enough to reduce the degradation by 10 % as well. At last, the degradation rate constant of the radical attack on the side chain is important to be reduced, as it is a key factor of the chemical degradation of the membrane.

4.8.2 Experimental conditions preventing the PFSA membrane chemical degradation

We performed a large set of simulations. Several simulations parameters were analyzed and thus, we are able to propose optimized conditions, to prevent a membrane from the chemical degradation and thus, help to solve one potential problem for the cell.

All the experimental parameters are in continuous interaction, but on the basis of our model, water management is the key aspect to control the operation of the cell and thus to optimize performance and lifetime of the PEMFC. High relative humidity will confer the cell a good humidification, improving transport processes (proton conduction) but improving gas permeation as well between the electrodes, what would imply a higher chemical degradation. A too low relative humidity, on the contrary, will inhibit the proton conduction and moreover the membrane is highly susceptible to dry out, which would mean mechanical failures, which are not taken here into account but have to be kept in mind [170].

According to the laws of kinetics, an increase of the temperature accelerates the kinetics of reactions. This is true unfortunately for both the reactions useful for the cell and the parasitic reactions (inducing

the degradation). Moreover, temperature strongly impacts the water management of the cell, as its increases the saturation pressure of vapor as well. That means that it is more difficult at high temperature for vapor to condense and humidify the membrane. This induces a lower level of humidification of the membrane and lower performances, as the water content is directly related to the proton conductivity. Usually, PEMFCs are used at 70 – 80 °C. It appears according to our simulations that it is a good compromise as well.

A further parameter we analyzed is the iron ions production rate in the system. Iron is a cheap material which is used in numerous parts of the cell. It may be the main element of the bipolar plates, coated with gold or a layer of polymer. Our assumption is that defects in the coating are responsible for the possible corrosion of bipolar plate by water at the cathode side, where the cell potential is high. For a weak to moderate degradation of the plate, the chemical degradation of the PEM will drastically increase, causing irreversible damages to the membrane. If the plate is severely attacked then it is possible that the cause of the failure of the cell would not be the membrane degradation but a failure of bipolar plates. Thus the use of iron-free bipolar plate (for example graphite) should prevent and even inhibit the formation of radicals and thus the membrane degradation.

4.8.3 Operating conditions for a higher durability of the PFSA membrane

In our simulations, we regarded two different types of dynamic cycles which are usually applied on test bench to PEMFC: One oscillating between a low and a moderate operating point and the other between moderate and high current density operating conditions. In each case, the degradation of the membrane is moderate compared to reference cases when the membrane is run several hundreds of hours at a constant low current density.

These cycles therefore do not really have an impact on the chemical degradation of the cell. But quick changes in the current density induce an unbalanced water profile in the membrane for short durations. This could have a negative impact not on the membrane degradation itself but on other degradation phenomena occurring at the anode side.

4.8.4 Type of membranes which are the less sensitive to chemical degradation

As mentioned in Section 4.6, the resistance of PFSA membranes is independent of the choice of the membrane. However, relying of our study on well-parameterized membranes, we propose the use of PFSA membranes with low *EW* and fluoride content for PEMFC technology. They are less susceptible of being degraded. In Figure 4.58, we present the possible interactions between the key parameters which can be adjusted by the design of a new generation of membrane.

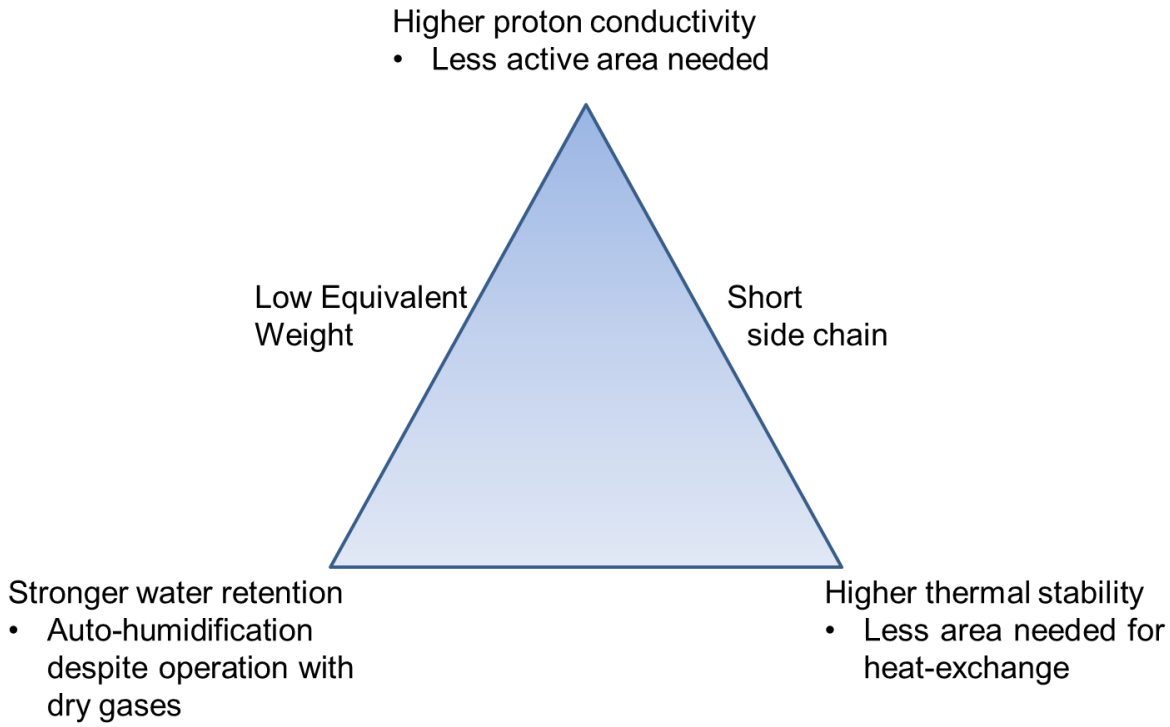

Figure 4.58: Advantages of membrane with low equivalent weight and short side chain (like Aquivion)

4.9 Outlook: Simulations of the membrane model in DENIS environment

Even if the implementation of our membrane chemical degradation model in DENIS has been also done, the model has still to be validated. The coupling with the electrodes and the gas channels / GDL is ready to be used within mono-phasic conditions (no liquid water). However, for reliable and useful simulations, it is necessary to carry out the same parameterization and validation made for MEMEPhys® (see Section 4.1). To date, this has not been completed but is an on-going work. As the electrochemical model used in DENIS is more macroscopic than the one used in MEMEPhys®, the parameters of MEMEPhys® are not directly usable in DENIS.

This is an important task to do as the stoichiometry influence along the gas channel as it has been presented in Section 4.3 can be solved with the 2D model developed in DENIS. With boundary conditions evolving along the gas channel, it will be possible to get a mapping of the degradation in the membrane surface, and underline the real localization of the degradation in the membrane depending on the cell design (co-flow, counter-flow etc.). Moreover, as the impact of the chemical degradation on the cell performance is due to the evolution of the membrane resistance, the same conclusions can be then made. It should be noted that the membrane performance model (i.e. without degradation) was already used in a publication with the DENIS environment [137].

CHAPTER 5

Summary and conclusions

Degradation of PEMFCs is one of the main issues of this promising technology. The durability of a PEMFC system is influenced by the irreversible materials degradation phenomena occurring in the components of the cell; therefore, a detailed understanding of the degradation mechanisms is required in order to design more durable cell components. These phenomena can have different origins and consequences and this PhD thesis focused on the chemical degradation of the membrane. There is strong experimental evidence for changes in the membrane structure during the cell operation (e.g. thinning by SEM, release of degradation by-products such as organic fragments from the membrane or fluoride ions in outlet water of the cell) and its proton conductivity loss over time.

In order to simulate the membrane behavior within a complete PEMFC, the membrane model is numerically connected with pre-existing models describing in a detailed way the processes occurring within the electrodes, the GDLs and the gas channels, within the software tool developed by Franco *et al.* at CEA (MEMEPhys® model). The membrane model was developed in a modular and flexible way in order to be easily embeddable in other simulation software, such as the DENIS package developed by Bessler *et al.* at DLR.

Because the membrane resistance is strongly influenced by the fluctuations of relative humidity in the GDLs, the evolution of membrane resistance on short time scales cannot be reliably considered as a sign for the chemical degradation of the membrane. One unambiguous sign of chemical degradation, which is also widely reported in literature, is the presence of fluoride ions in the water evacuated out of the cell. Consequently, we have simulated fluoride release as one of the major indicators of degradation.

We parameterized and validated our performance and degradation model using available experimental data from literature. The degradation model shows good agreement with experimental data regarding the production of hydrogen peroxide (in dependence to the membrane thickness as well), the produced radicals coming from the decomposition of hydrogen peroxide, and the amount of fluoride ions pro-

duced through the degradation of the membrane through radical attack. This constituted the basis of detailed parameter studies we presented, showing that the experimental conditions (e.g. gas stoichiometry, relative humidity and temperature) have a strong influence on the degradation. We highlighted the importance of each condition under different working conditions.

Based on our study of behavior of a cell under constant current load at different temperatures, we noticed that when keeping the relative humidity of the cell constant at each temperature, the degradation increases as the temperature increases. If the applied current increased, the performance degradation decreases, and, according to the model, is even inexistent at lower temperature. As the model allowed 1D spatial resolution within the membrane, we could identify the location of more or less severe degradation. Under our assumptions (hydrogen peroxide produced at the anode, iron ions at the cathode), less degradation was found in the center of the membrane, while the boundaries towards the electrodes were more degraded. The difference remains however small, as the membrane we simulated as reference case was thin.

We then simulated conditions where the current load periodically oscillated between two values. As it could be expected, the degradation of this mix of two states was about in the middle of degradation of the two extreme cases, where the cell would be run over the same time at a constant current load. This indicates that dynamic operation does not impact the chemical degradation in comparison to stationary operation The plots of the cell voltage under periodic switching of current density showed overshoots and undershoots. The model suggested that these effects were due to local imbalance of the water content. This causes variations in the membrane resistance, and thus impacts the cell potential.

We further studied the influence of the concentration of iron ions on the degradation. We found out under all the simulation conditions used that when the production of iron ions thus increased, the chemical degradation, after having increased to a maximum value, becomes less for highly corroded system. The explanations we proposed for this behavior was either a relationship between the concentration of side chain in the cell and the one of free iron ions, or that the radicals react another way than with side chain, so that the membrane is being protected.

The model can be applied to any type of PFSA membrane, as long as the chemical structure and the physicals properties (thickness, equivalent weight, and density) are known. We compared four different PFSA membranes available on the current market. They differed in equivalent weight (low or high) and side chain length (short or long). The prediction of the model allows us to suggest that regarding the instantaneous performances, membranes with lower equivalent weight offers higher performance. Regarding the chemical degradation, membranes with shorter side chains are less subjected of being degraded, thus would be more stable over time.

Long-term experiments were also simulated. We run the cell for 20,000 h at middle and high current

density and at different temperatures. We fixed as end-of-life condition an arbitrary decrease of 5 % of the initial cell voltage. It came out that the durability decreases with increased temperature and current density. As we considered only chemical degradation of the membrane, the cell potential decrease is due to an increase of the ohmic loss in the membrane. This explained that high current trend to reduce the durability of the cell, even if our simulations showed in these cases that the membrane degraded less than at end of life at lower current density.

Regarding the mitigation of the membrane chemical degradation, we concluded that the most important parameter is the temperature at which the cell is operated. The higher the temperature, the more severe is the chemical degradation of the membrane. Humidifications of the gases are relevant as well in the reduction of the chemical degradation. At high relative humidity, the chemical degradation decreases. Moreover, oxygen dissolution and diffusion in the membrane are a key parameter in the degradation as well. As the membrane degrades, the effective diffusion coefficient is expected to increase which is used in the model. Sensitivity analysis revealed that an increased diffusion of oxygen induces more chemical degradation of the membrane. We came to the same conclusion regarding the diffusion coefficient of hydrogen peroxide in the membrane. At last, it seems that decomposition of hydrogen peroxide through Fenton mechanism is, beside permeation of oxygen in the membrane, a key step in the chemical degradation of the membrane.

Even if this PhD work focused on theory, we always keep in mind that modeling results remain hypothetical predictions unless there is experimental validation. Vice versa, experimentally observed behavior cannot be improved if it is not fully understood, which requires theoretical models. Hand in hand, we are convinced that both, modeling and experiment, have more in common than one could think, and they are two necessary tools applied to the same cause.

Appendix A: On Nafion® and the determination of the chemical structure of a PFSA membrane

The development of Nafion®, the first used PFSA membrane, began in the early 1960s. The research group who worked on it aimed first on studying monomers for copolymerization with TFE, the monomer used in Teflon [170].

One of the acid fluorides studied, based on the reaction product of TFE and sulfur trioxide, led to an unusual TFE copolymer containing branches with pendant sulfonic acid groups. The synthesis process is described in Figure A.1

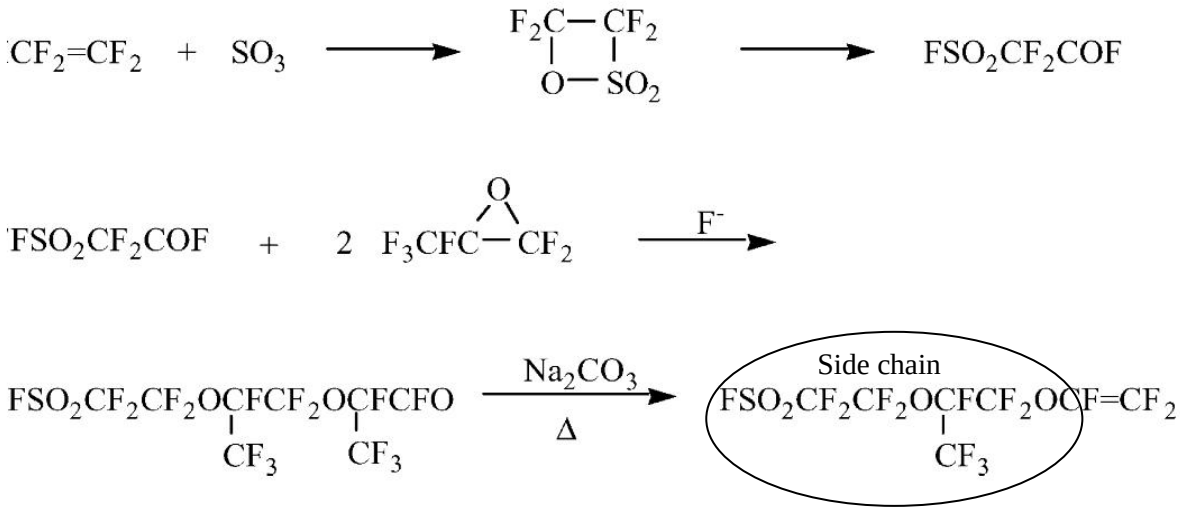

Figure A.1: Synthesis process for Nafion® membrane comonomer [170].

Nafion® derivatives are first synthesized by the copolymerization of tetrafluoroethylene (TFE) (the monomer in Teflon) and a derivative of a perfluoro (alkyl vinyl ether) with sulfonyl acid fluoride (see Figure A.2).

We took the example of Nafion®, but basically, the syntheses of all PFSA membranes are similar. The chemical structure of the side chain will however change. We refer to Figure 1.3 for the general structure of PFSA membranes. A PFSA membrane will differ from the other through the set of parameters (x, y, m, n). m and n are known by knowing the structure of the membrane comonomer. y is usually set to 1. So the only parameter which is still missing is x, giving an information about the frequency of the repetition of a side chain. Through gravimetric analysis, it is possible to determine the equivalent weight of a membrane. The equivalent weight is defined as the mass of dry polymer per sulfonate acid group.

Assuming that EW is known and *m*, *n* and *y* as well, we can write

$$\begin{aligned} EW &= x\cdot(2\cdot12+4\cdot19)+y\cdot(2\cdot12+3\cdot19)+m\cdot(16+3\cdot12+6\cdot19)+n\cdot(12+2\cdot19)+32+16\cdot3+1 \\ &= 100\cdot x+81\cdot y+166m+50\cdot n+81 \end{aligned}$$

This gives the Equation 1.2 for the determination of *x* parameter for a membrane.

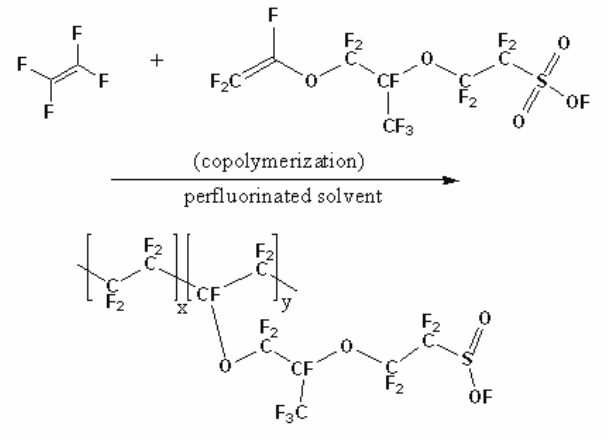

Figure A.2 : Production reaction of a Nafion® [40]

Appendix B: About Fenton chemistry, its application and its complexity

In 1894, Henry Fenton published a work about the oxidation of tartric acid in presence of iron [21]. This was the start of a promising way to treat industrial waste water.

We know under Fenton's reagent a solution of hydrogen peroxide and iron ions. This reagent is used to oxidize contaminants or waste water. I can be used for example to oxidize remaining organic compounds from water, especially for waste water of chemical plants. A part of the organic pollution in such water can be biologically degraded (Biochemical Oxygen Demand) but some refractory organic pollution can still remain. The addition of Fenton's reagent in this water will induce the oxidation of the remaining pollution.

As mentioned in this PhD thesis, the simultaneous presence of hydrogen peroxide and iron ions produces radicals, one of the most oxidizing species which can be found. These are the responsible of the degradation of any stable compound in waste water. They are also responsible for the degradation of PFSA membrane, as discussed earlier.

Test based on Fenton reagents are often used to simulate peroxide attack on PFSA membranes. We recall the main reaction occurring in the Fenton medium

$$H_2O_2 + Fe^{2+} + H^+ \rightleftharpoons Fe^{3+} + HO^{\cdot} + H_2O$$

However, the mechanism of the Fenton process is far more complex as it is assumed in the previous reaction. In Figure B.1, a more complete mechanism (in alkaline conditions) is presented with the corresponding reaction rate constant. As it can be seen, even without the presence of Nafion® in the system, the possible interaction between iron, hydrogen peroxide and the different products is really complex. To reproduce faithfully the behavior of all these species in the fuel cell, we decided to keep some of them. Through this, we ensure that the radicals which are produced during the main reaction of the Fenton chemistry will not only react with the membrane. This induces a lower attack on the membrane and more accurate simulations compared to more simple assumptions, like considering only the disproportionation of hydrogen peroxide.

1	$Fe^{2+} + H_2O_2 \rightarrow Fe^{3+} + {}^{\bullet}OH + OH^-$	63
2	$Fe^{2+} + {}^{\bullet}OH \rightarrow Fe^{3+} + OH^-$	3×10^8
3	$H_2O_2 + {}^{\bullet}OH \rightarrow HO_2{}^{\bullet} + H_2O$	3.3×10^7
4	$Fe^{2+} + HO_2{}^{\bullet} \rightarrow Fe^{III}(HO_2)^{2+}$	1.2×10^6
5	$HO_2{}^{\bullet} \rightarrow O_2{}^{\bullet -} + H^+$	$1.58 \times 10^5\ s^{-1}$
6	$O_2{}^{\bullet -} + H^+ \rightarrow HO_2{}^{\bullet}$	1×10^{10}
7	$Fe^{2+} + O_2{}^{\bullet -} + H^+ \rightarrow Fe(HO_2)^{2+}$	1×10^7
8	$Fe^{3+} + H_2O \rightleftarrows FeOH^{2+} + H^+$	$K = 2.9 \times 10^{-3}\ M$
9	$Fe^{3+} + H_2O \rightleftarrows Fe(OH)_2{}^{+} + 2H^+$	$K = 7.62 \times 10^{-6}\ M^2$
10	$2Fe^{3+} + 2HO_2 \rightleftarrows Fe_2(OH)_2{}^{4+} + 2H^+$	$K = 8 \times 10^{-4}\ M$
11	$Fe^{3+} + H_2O_2 \rightleftarrows Fe(HO_2)^{2+} + H^+$	$K = 3.1 \times 10^{-3}(^*)$
12	$FeOH^{2+} + H_2O_2 \rightleftarrows Fe(OH)(HO_2)^{+} + H^+$	$K = 2.0 \times 10^{-4}$
13	$Fe(HO_2)^{2+} \rightarrow Fe^{2+} + HO_2{}^{\bullet}$	$2.7 \times 10^{-3}\ s^{-1}$
14	$Fe(OH)(HO_2)^{+} \rightarrow Fe^{2+} + HO_2{}^{\bullet} + OH^-$	$2.7 \times 10^{-3}\ s^{-1}$
15	$Fe(III)(^{**}) + HO_2{}^{\bullet} \rightarrow Fe^{2+} + O_2 + H^+$	$< 2 \times 10^3$
16	$Fe(III) + O_2{}^{\bullet -} \rightarrow Fe^{2+} + O_2$	5×10^7
17	$HO_2{}^{\bullet} + HO_2{}^{\bullet} \rightarrow H_2O_2 + O_2$	8.3×10^5
18	$HO_2{}^{\bullet} + O_2{}^{\bullet -} + H^+ \rightarrow H_2O_2 + O_2$	9.7×10^7
19	${}^{\bullet}OH + HO_2{}^{\bullet} \rightarrow H_2O + O_2$	7.1×10^9
20	${}^{\bullet}OH + O_2{}^{\bullet -} \rightarrow OH^{\bullet} + O_2$	1×10^{10}
21	${}^{\bullet}OH + {}^{\bullet}OH \rightarrow H_2O_2$	5.2×10^9
22	$H^+ + SO_4{}^{2-} \rightleftarrows HSO_4{}^-$	$1 \times 10^2\ M^{-1}$
23	$HSO_4{}^- + {}^{\bullet}OH \rightarrow H_2O + SO_4{}^{\bullet -}$	1.7×10^6
24	$SO_4{}^{\bullet -} + H_2O_2{}^{\bullet} \rightarrow HSO_4{}^- + HO_2{}^{\bullet}$	1.2×10^7
25	$SO_4{}^{\bullet -} + HO_2{}^{\bullet} \rightarrow HSO_4{}^- + O_2$	3.5×10^9
26	$SO_4{}^{\bullet -} + Fe^{2+} \rightarrow SO_4{}^{2-} + Fe^{3+}$	9.9×10^8

Figure B.1: Fenton process reactions by Namkung [25]

Appendix C: Sensitivity analysis of the chemical degradation model

Sensitivity analysis is the investigation of th potential changes and errors and their impacts on conclusions to be drawn from the model. We use this approach in our work in order to check the impact of several models parameters on an output of the model. In our case, we focus our attention on the variation of the area specific resistance of the cell (in mΩ·cm²). We run a simulation with parameters taken as reference.

Experimental parameters

Temperature	353 K
Pressure	2 bar
Relative humidity Anode	80
Relative humidity Cathode	80
Stoichiometry Anode	15
Stoichiometry Cathode	20
Current density	$4 \cdot 10^{-2}$ A·cm^{-2}

Permeation of O_2 through the membrane

D_{0,O_2}	3.1·10–7 m²·s^{-1}
E_{act,O_2}^{Diff}	- 2768 J·mol^{-1}

Decomposition of hydrogen peroxide.

Production of iron ions	10^{-3} mol·m^{-3}.s^{-1}
Fenton #1	$63 \cdot 10^{-3}$
Fenton #2	$2 \cdot 10^{-6}$
Fenton #3	$3.3 \cdot 10^{2}$

Fenton #4	$3.3 \cdot 10^4$
Fenton #5	$3.3 \cdot 10^5$

Appendix D: Parameters used during the simulations

Parameters used during the simulations

In our simulations, lot of parameters has been used, and some of them are redundant and not modified during our investigation on the chemical degradation of the PFSA membrane. In this appendix, these parameters are given.

Parameters used in Chapter 2:

Parameters used in the transport model

K_1	1000	1st acidity constant of sulfuric acid
K_2	200	2nd acidity constant of sulfuric acid
l_G	$0.255 \cdot 10^{-9}$ m	Mean step distance for Grotthus diffusion
l_Σ	$0.255 \cdot 10^{-9}$ m	Mean step distance for surface diffusion
M_{H_2O}	$18 \cdot 10^{-3}$ kg·mol^{-1}	Molar mass of water
R_f	$0.254 \cdot 10^{-9}$ m	Effective radius of fixed anion groups
R_i	$0.143 \cdot 10^{-9}$ m	Radius of hydronium ion
R_w	$0.141 \cdot 10^{-9}$ m	Radius of water molecule
s	0.0122	Swelling coefficient
v	20	number of water molecules surrounding one hydronium
z_{H+}	1	Charge
α_{memb}	0.4	Ratio between water flux and effective water flux in the membrane
β_{memb}	8.5 mol·m^{-2}·s^{-1}	Proportionality coefficient between water flux into the membrane and water content difference over electrode / membrane interface
δ	$0.143 \cdot 10^{-9}$ m	Distance between proton in hydronium ion an proton-accepting water molecule
ε_r	6	Relative permittivity of the membrane

η	0.000355 Pa·$^{-1}$	Viscosity of water
θ_F	$\pi/12$	Final angle diffusing proton and an adjacent water molecule
θ_I	$\pi \cdot 107/180$	Initial angle between diffusing proton and adjacent water molecule
μ_W	$0.61 \cdot 10^{-29}$ C·m^{-1}	Dipole moment of liquid water

Henry's constants, diffusion coefficients and related activation energies for the motion of species in the membrane

H_{0,O_2}	$12.8 \cdot 10^{-6}$ mol·m^{-3}·Pa^{-1}
E_{act,O_2}^{Henry}	– 10808 J·mol^{-1}
H_{0,H_2}	$7.6 \cdot 10^{-6}$ mol·m^{-3}·Pa^{-1}
E_{act,O_2}^{Henry}	– 4157 J·mol^{-1}
D_{0,O_2}	$3.1 \cdot 10^{-7}$ m²·s^{-1}
E_{act,O_2}^{Diff}	– 2768 J·mol^{-1}
D_{0,H_2}	$4.1 \cdot 10^{-10}$ m²·s^{-1}
E_{act,H_2}^{Diff}	– 2602 J·mol^{-1}
$D_{0,i}$	10^{-7} m²·s^{-1} (default values for all the others species)
$E_{act,i}^{Diff}$	0 J·mol^{-1}(default values for all the others species)

Fenton's reaction rate constant

Reaction 2.1	$63 \cdot 10^{-3}$ m^3·mol^{-1}·s^{-1}
Reaction 2.2	$2 \cdot 10^{-6}$·mol^{-1}·s^{-1}
Reaction 2.3	$3.3 \cdot 10^{2}$·mol^{-1}·s^{-1}
Reaction 2.4	$3.3 \cdot 10^{4}$·mol^{-1}·s^{-1}
Reaction 2.5	$3.3 \cdot 10^{5}$·mol^{-1}·s^{-1}

Parameters used in Chapter 3:

$\Delta G_{c,1}^{0}$	1000 J·mol^{-1}
$\Delta G_{c,2}^{0}$	1000 J·mol^{-1}
d	$2 \cdot 10^{-10}$
$\varepsilon_{CL,anode}$	$6 \cdot \varepsilon_0$
$\varepsilon_{CL,cathode}$	$4 \cdot \varepsilon_0$
ε_{DL}	$20 \cdot \varepsilon_0$

References

[1] D.M. Bernardi, M.W. Verbrugge, *"A Mathematical Model of the Solid-Polymer-Electrolyte Fuel Cell"*, Journal of The Electrochemical Society, **139** (1992) 2477-2491.

[2] A.A. Franco, PEMFC degradation modeling and analysis, in: C. Hartnig, C. Roth (Eds.) Polymer electrolyte membrane and direct methanol fuel cell technology (PEMFCs and DMFCs), Woodhead, Cambridge, UK, 2011.

[3] A.A. Franco, M. Gerard, *"Multiscale Model of Carbon Corrosion in a PEFC: Coupling with Electrocatalysis and Impact on Performance Degradation"*, Journal of The Electrochemical Society, **155** (2008) B367-B384.

[4] A.A. Franco, S. Passot, P. Fugier, C. Anglade, E. Billy, L. Guetaz, N. Guillet, E. De Vito, S. Mailley, *"Pt_xCo_y Catalysts Degradation in PEFC Environments: Mechanistic Insights"*, Journal of The Electrochemical Society, **156** (2009) B410-B424.

[5] A.A. Franco, M. Tembely, *"Transient Multiscale Modeling of Aging Mechanisms in a PEFC Cathode"*, Journal of The Electrochemical Society, **154** (2007) B712-B723.

[6] Scientific modelling, http://en.wikipedia.org/wiki/Scientific_modelling

[7] A.A. Franco, PEMFC degradation modeling an analysis, in: C. Hartnig, C. Roth (Eds.) Polymer electrolyte membrane and direct methanol fuel cell technology, vol. 1, Woodhead, Cambridge, UK, 2011.

[8] A.A. Franco, M. Guinard, B. Barthe, O. Lemaire, *"Impact of carbon monoxide on PEFC catalyst carbon support degradation under current-cycled operating conditions"*, Electrochimica Acta, **54** (2009) 5267-5279.

[9] K. Malek, A.A. Franco, *"Microstructure-Based Modeling of Aging Mechanisms in Catalyst Layers of Polymer Electrolyte Fuel Cells"*, The Journal of Physical Chemistry B, **115** (2011) 8088-8101.

[10] T.D. Gierke, G.E. Munn, F.C. Wilson, *"The morphology in nafion perfluorinated membrane products, as determined by wide- and small-angle x-ray studies"*, Journal of Polymer Science: Polymer Physics Edition, **19** (1981) 1687-1704.

[11] H.G. Haubold, T. Vad, H. Jungbluth, P. Hiller, *"Nano structure of NAFION: a SAXS study"*, Electrochimica Acta, **46** (2001) 1559-1563.

[12] L. Rubatat, A.L. Rollet, G. Gebel, O. Diat, *"Evidence of Elongated Polymeric Aggregates in Nafion"*, Macromolecules, **35** (2002) 4050-4055.

[13] K. Schmidt-Rohr, Q. Chen, *"Parallel cylindrical water nanochannels in Nafion fuel-cell membranes"*, Nat Mater, **7** (2008) 75-83.

[14] H.L. Yeager, A. Steck, *"Cation and Water Diffusion in Nafion Ion Exchange Membranes: Influence of Polymer Structure"*, Journal of The Electrochemical Society, **128** (1981) 1880-1884.

[15] J. Healy, C. Hayden, T. Xie, K. Olson, R. Waldo, M. Brundage, H. Gasteiger, J. Abbott, *"Aspects*

of the Chemical Degradation of PFSA Ionomers used in PEM Fuel Cells", Fuel Cells, **5** (2005) 302-308.

[16] A.P. Young, J. Stumper, S. Knights, E. Gyenge, *"Ionomer Degradation in Polymer Electrolyte Membrane Fuel Cells"*, Journal of The Electrochemical Society, **157** (2010) B425-B436.

[17] O. Antoine, R. Durand, *"RRDE study of oxygen reduction on Pt nanoparticles inside Nafion®: H2O2 production in PEMFC cathode conditions"*, Journal of Applied Electrochemistry, **30** (2000) 839-844.

[18] W. Liu, D. Zuckerbrod, *"In Situ Detection of Hydrogen Peroxide in PEM Fuel Cells"*, Journal of The Electrochemical Society, **152** (2005) A1165-A1170.

[19] V.A. Sethuraman, J.W. Weidner, A.T. Haug, S. Motupally, L.V. Protsailo, *"Hydrogen Peroxide Formation Rates in a PEMFC Anode and Cathode"*, Journal of The Electrochemical Society, **155** (2008) B50-B57.

[20] R. Andreozzi, A. D'Apuzzo, R. Marotta, *"A kinetic model for the degradation of benzothiazole by Fe^{3+}-photo-assisted Fenton process in a completely mixed batch reactor"*, J. Hazard. Mater., **B80** (2000) 17.

[21] H.J.H. Fenton, *"LXXIII.-Oxidation of tartaric acid in presence of iron"*, Journal of the Chemical Society, Transactions, **65** (1894) 899-910.

[22] W. Gernjak, T. Krutzler, A. Glaser, S. Malato, J. Caceres, R. Bauer, A.R. Fernández-Alba, *"Photo-Fenton treatment of water containing natural phenolic pollutants"*, Chemosphere, **50** (2003) 71-78.

[23] P.L. Huston, J.J. Pignatello, *"Degradation of selected pesticide active ingredients and commercial formulations in water by the photo-assisted Fenton reaction"*, Water Research, **33** (1999) 1238-1246.

[24] J. Kiwi, C. Pulgarin, P. Peringer, *"Effect of Fenton and photo-Fenton reactions on the degradation and biodegradability of 2 and 4-nitrophenols in water treatment"*, Applied Catalysis B: Environmental, **3** (1994) 335-350.

[25] K.C. Namkung, P. Sharratt, *"Fenton and Photo-Fenton Processes for Treatment of Aqueous Wastes"*, UMIST.

[26] C.C. Winterbourn, *"Toxicity of iron and hydrogen peroxide: the Fenton reaction"*, Toxicol. Lett., **82/83** (1995) 6.

[27] M. Danilczuk, F.D. Coms, S. Schlick, *"Visualizing Chemical Reactions and Crossover Processes in a Fuel Cell Inserted in the ESR Resonator: Detection by Spin Trapping of Oxygen Radicals, Nafion-Derived Fragments, and Hydrogen and Deuterium Atoms"*, The Journal of Physical Chemistry B, **113** (2009) 8031-8042.

[28] M.K. Kadirov, A. Bosnjakovic, S. Schlick, *"Membrane-Derived Fluorinated Radicals Detected by Electron Spin Resonance in UV-Irradiated Nafion and Dow Ionomers: Effect of Counterions and*

H2O2", The Journal of Physical Chemistry B, **109** (2005) 7664-7670.

[29] M. Kitazawa, A. Nosaka, Y. Nosaka, *"Radical formation in polymer electrolyte fuel cell components as studied by ESR spectroscopy"*, Journal of Applied Electrochemistry, **38** (2008) 491-496.

[30] A. Panchenko, H. Dilger, J. Kerres, M. Hein, A. Ullrich, T. Kaz, E. Roduner, *"In-situ spin trap electron paramagnetic resonance study of fuel cell processes"*, Physical Chemistry Chemical Physics, **6** (2004) 2891-2894.

[31] D.A. Schiraldi, *"Perfluorinated Polymer Electrolyte Membrane Durability"*, Journal of Macromolecular Science, Part C: Polymer Reviews, **46** (2006) 315-327.

[32] T. Xie, C.A. Hayden, *"A kinetic model for the chemical degradation of perfluorinated sulfonic acid ionomers: Weak end groups versus side chain cleavage"*, Polymer, **48** (2007) 5497-5506.

[33] C. Chen, T. Fuller, *"H_2O_2 Formation under Fuel-Cell Conditions"*, ECS Transactions, **11** (2007) 1127-1137.

[34] C. Chen, T.F. Fuller, *"The effect of humidity on the degradation of Nafion® membrane"*, Polymer Degradation and Stability, **94** (2009) 1436-1447.

[35] C. Chen, T.F. Fuller, *"XPS Analysis of Polymer Membrane Degradation in PEMFCs"*, Journal of The Electrochemical Society, **156** (2009) B1218-B1224.

[36] C. Chen, T.F. Fuller, *"Modeling of H_2O_2 formation in PEMFCs"*, Electrochimica Acta, **54** (2009) 3984-3995.

[37] C. Chen, G. Levitin, D.W. Hess, T.F. Fuller, *"XPS investigation of Nafion membrane degradation"*, Journal of Power Sources, **169** (2007) 288-295.

[38] L. Gubler, S.M. Dockheer, W.H. Koppenol, *"Radical (HO·, H· and HOO·) Formation and Ionomer Degradation in Polymer Electrolyte Fuel Cells"*, Journal of The Electrochemical Society, **158** (2011) B755-B769.

[39] A.A. Shah, T.R. Ralph, F.C. Walsh, *"Modeling and Simulation of the Degradation of Perfluorinated Ion-Exchange Membranes in PEM Fuel Cells"*, Journal of The Electrochemical Society, **156** (2009) B465-B484.

[40] http://en.wikipedia.org/wiki/Henry%27s_law

[41] F. Fouda-Onana, N. Guillet, Method for depositing a metal onto a porous carbon layer, in, France, 2009.

[42] H. Pu, W.H. Meyer, G. Wegner, *"Proton transport in polybenzimidazole blended with H3PO4 or H2SO4"*, Journal of Polymer Science Part B: Polymer Physics, **40** (2002) 663-669.

[43] S.J. Paddison, T.A. Zawodzinski Jr, *"Molecular modeling of the pendant chain in Nafion"*, Solid State Ionics, **113-115** (1998) 333-340.

[44] A. Vishnyakov, A.V. Neimark, *"Molecular Simulation Study of Nafion Membrane Solvation in Water and Methanol"*, The Journal of Physical Chemistry B, **104** (2000) 4471-4478.

[45] K. Malek, M. Eikerling, Q. Wang, T. Navessin, Z. Liu, *"Self-Organization in Catalyst Layers of Polymer Electrolyte Fuel Cells"*, The Journal of Physical Chemistry C, **111** (2007) 13627-13634.

[46] S. Schlick, G. Gebel, M. Pineri, F. Volino, *"Fluorine-19 NMR spectroscopy of acid Nafion membranes and solutions"*, Macromolecules, **24** (1991) 3517-3521.

[47] N.G. Boyle, V.J. McBrierty, A. Eisenberg, *"NMR investigation of molecular motion in Nafion membranes"*, Macromolecules, **16** (1983) 80-84.

[48] Q. Chen, K. Schmidt-Rohr, *"^{19}F and ^{13}C NMR Signal Assignment and Analysis in a Perfluorinated Ionomer (Nafion) by Two-Dimensional Solid-State NMR"*, Macromolecules, **37** (2004) 5995-6003.

[49] Q. Chen, K. Schmidt-Rohr, *"Backbone Dynamics of the Nafion Ionomer Studied by ^{19}F-^{13}C Solid-State NMR"*, Macromolecular Chemistry and Physics, **208** (2007) 2189-2203.

[50] J.A. Elliott, D. Wu, S.J. Paddison, R.B. Moore, *"A unified morphological description of Nafion membranes from SAXS and mesoscale simulations"*, Soft Matter, (2011).

[51] G. Gebel, O. Diat, *"Neutron and X-ray Scattering: Suitable Tools for Studying Ionomer Membranes"*, Fuel Cells, **5** (2005) 261-276.

[52] J. Halim, F.N. Büchi, O. Haas, M. Stamm, G.G. Scherer, *"Characterization of perfluorosulfonic acid membranes by conductivity measurements and small-angle x-ray scattering"*, Electrochimica Acta, **39** (1994) 1303-1307.

[53] K.A. Page, F.A. Landis, A.K. Phillips, R.B. Moore, *"SAXS Analysis of the Thermal Relaxation of Anisotropic Morphologies in Oriented Nafion Membranes"*, Macromolecules, **39** (2006) 3939-3946.

[54] E.J. Roche, M. Pineri, R. Duplessix, A.M. Levelut, *"Small-angle scattering studies of nafion membranes"*, Journal of Polymer Science: Polymer Physics Edition, **19** (1981) 1-11.

[55] A. Eisenberg, B. Hird, R.B. Moore, *"A new multiplet-cluster model for the morphology of random ionomers"*, Macromolecules, **23** (1990) 4098-4107.

[56] W.Y. Hsu, T.D. Gierke, *"Elastic theory for ionic clustering in perfluorinated ionomers"*, Macromolecules, **15** (1982) 101-105.

[57] W.Y. Hsu, T.D. Gierke, *"Ion transport and clustering in nafion perfluorinated membranes"*, Journal of Membrane Science, **13** (1983) 307-326.

[58] K.A. Mauritz, R.B. Moore, *"State of Understanding of Nafion"*, Chemical Reviews, **104** (2004) 4535-4586.

[59] D. Gierke T, Y. Hsu W, The Cluster-Network Model of Ion Clustering in Perfluorosulfonated Membranes, in: Perfluorinated Ionomer Membranes, vol. 180, AMERICAN CHEMICAL SOCIETY, 1982, pp. 283-307.

[60] M. Fujimura, T. Hashimoto, H. Kawai, *"Small-angle x-ray scattering study of perfluorinated ionomer membranes. 1. Origin of two scattering maxima"*, Macromolecules, **14** (1981) 1309-1315.

[61] M. Fujimura, T. Hashimoto, H. Kawai, *"Small-angle x-ray scattering study of perfluorinated*

ionomer membranes. 2. Models for ionic scattering maximum", Macromolecules, **15** (1982) 136-144.

[62] M.H. Litt, Proc. 1997 ACS San Francisco Meeting, San Francisco, 1997.

[63] G. Gebel, *"Structural evolution of water swollen perfluorosulfonated ionomers from dry membrane to solution"*, Polymer, **41** (2000) 5829-5838.

[64] Z. Siroma, N. Fujiwara, T. Ioroi, S. Yamazaki, K. Yasuda, Y. Miyazaki, *"Dissolution of Nafion membrane and recast Nafion film in mixtures of methanol and water"*, Journal of Power Sources, **126** (2004) 41-45.

[65] L. Rubatat, G. Gebel, O. Diat, *"Fibrillar Structure of Nafion: Matching Fourier and Real Space Studies of Corresponding Films and Solutions"*, Macromolecules, **37** (2004) 7772-7783.

[66] A.Z. Weber, J. Newman, *"Transport in Polymer-Electrolyte Membranes"*, Journal of The Electrochemical Society, **150** (2003) A1008-A1015.

[67] A.Z. Weber, J. Newman, *"Transport in Polymer-Electrolyte Membranes"*, Journal of The Electrochemical Society, **151** (2004) A311-A325.

[68] B. Chu, C. Wu, W. Buck, *"Light-scattering characterization of poly(tetrafluoroethylene). 2. PTFE in perfluorotetracosane: molecular weight distribution and solution properties"*, Macromolecules, **22** (1989) 831-837.

[69] B. Rosi-Schwartz, G.R. Mitchell, *"Extracting force fields for disordered polymeric materials from neutron scattering data"*, Polymer, **37** (1996) 1857-1870.

[70] R. Borup, J. Meyers, B. Pivovar, Y.S. Kim, R. Mukundan, N. Garland, D. Myers, M. Wilson, F. Garzon, D. Wood, P. Zelenay, K. More, K. Stroh, T. Zawodzinski, J. Boncella, J.E. McGrath, M. Inaba, K. Miyatake, M. Hori, K. Ota, Z. Ogumi, S. Miyata, A. Nishikata, Z. Siroma, Y. Uchimoto, K. Yasuda, K.-i. Kimijima, N. Iwashita, *"Scientific Aspects of Polymer Electrolyte Fuel Cell Durability and Degradation"*, Chemical Reviews, **107** (2007) 3904-3951.

[71] H. Tang, S. Peikang, S.P. Jiang, F. Wang, M. Pan, *"A degradation study of Nafion proton exchange membrane of PEM fuel cells"*, Journal of Power Sources, **170** (2007) 85-92.

[72] M. Inaba, T. Kinumoto, M. Kiriake, R. Umebayashi, A. Tasaka, Z. Ogumi, *"Gas crossover and membrane degradation in polymer electrolyte fuel cells"*, Electrochimica Acta, **51** (2006) 5746-5753.

[73] M. Schulze, N. Wagner, T. Kaz, K.A. Friedrich, *"Combined electrochemical and surface analysis investigation of degradation processes in polymer electrolyte membrane fuel cells"*, Electrochimica Acta, **52** (2007) 2328-2336.

[74] S. Zhang, X.-Z. Yuan, J.N.C. Hin, H. Wang, K.A. Friedrich, M. Schulze, *"A review of platinum-based catalyst layer degradation in proton exchange membrane fuel cells"*, Journal of Power Sources, **194** (2009) 588-600.

[75] S.S. Kocha, J. Deliang Yang, J.S. Yi, *"Characterization of gas crossover and its implications in PEM fuel cells"*, AIChE Journal, **52** (2006) 1916-1925.

[76] E.H. Jung, U.H. Jung, T.H. Yang, D.H. Peak, D.H. Jung, S.H. Kim, *"Methanol crossover through*

PtRu/Nafion composite membrane for a direct methanol fuel cell", International Journal of Hydrogen Energy, **32** (2007) 903-907.

[77] A.C. Fernandes, E.A. Ticianelli, *"A performance and degradation study of Nafion 212 membrane for proton exchange membrane fuel cells"*, Journal of Power Sources, **193** (2009) 547-554.

[78] V.O. Mittal, H.R. Kunz, J.M. Fenton, *"Is H_2O_2 Involved in the Membrane Degradation Mechanism in PEMFC?"*, Electrochemical and Solid-State Letters, **9** (2006) A299-A302.

[79] M.O. Davies, M. Clark, E. Yeager, F. Hovorka, *"The Oxygen Electrode"*, Journal of The Electrochemical Society, **106** (1959) 56-61.

[80] E. Yeager, *"Dioxygen electrocatalysis: mechanisms in relation to catalyst structure"*, Journal of Molecular Catalysis, **38** (1986) 5-25.

[81] I. Morcos, E. Yeager, *"Kinetic studies of the oxygen--peroxide couple on pyrolytic graphite"*, Electrochimica Acta, **15** (1970) 953-975.

[82] E. Yeager, *"Electrocatalysts for O_2 reduction"*, Electrochimica Acta, **29** (1984) 1527-1537.

[83] E. Yeager, P. Krouse, K.V. Rao, *"The kinetics of the oxygen--peroxide couple on carbon"*, Electrochimica Acta, **9** (1964) 1057-1070.

[84] R. Ferreira de Morais, A.A. Franco, P. Sautet, D. Loffreda, *"Water vs Hydrogen Peroxide Formation on Pt(111) From a First-Principles Study. 2. Coverage Kinetics"*, (in preparation).

[85] R. Ferreira de Morais, P. Sautet, D. Loffreda, A.A. Franco, *"A multiscale theoretical methodology for the calculation of electrochemical observables from ab initio data: Application to the oxygen reduction reaction in a Pt(111)-based polymer electrolyte membrane fuel cell"*, Electrochimica Acta, **In Press, Corrected Proof** (2011).

[86] V.R. Stamenkovic, B. Fowler, B.S. Mun, G. Wang, P.N. Ross, C.A. Lucas, N.M. Marković, *"Improved Oxygen Reduction Activity on Pt3Ni(111) via Increased Surface Site Availability"*, Science, **315** (2007) 493-497.

[87] Y. Wang, P.B. Balbuena, *"Ab Initio Molecular Dynamics Simulations of the Oxygen Reduction Reaction on a Pt(111) Surface in the Presence of Hydrated Hydronium $(H_3O)^+(H_2O)_2$: Direct or Series Pathway?"*, The Journal of Physical Chemistry B, **109** (2005) 14896-14907.

[88] Y. Wang, P.B. Balbuena, *"Potential Energy Surface Profile of the Oxygen Reduction Reaction on a Pt Cluster: Adsorption and Decomposition of OOH and H_2O_2"*, Journal of Chemical Theory and Computation, **1** (2005) 935-943.

[89] A. Pozio, R.F. Silva, M. De Francesco, L. Giorgi, *"Nafion degradation in PEFCs from end plate iron contamination"*, Electrochimica Acta, **48** (2003) 1543-1549.

[90] F.N. Büchi, M. Inaba, T.J. Schmidt, J. Scherer, D. Münter, R. Ströbel, Influence of Metallic Bipolar Plates on the Durability of Polymer Electrolyte Fuel Cells, in: Polymer Electrolyte Fuel Cell Durability, Springer New York, 2009, pp. 243-255.

[91] M. Aoki, H. Uchida, M. Watanabe, *"Decomposition mechanism of perfluorosulfonic acid*

electrolyte in polymer electrolyte fuel cells", Electrochemistry Communications, **8** (2006) 1509-1513.

[92] A. Panchenko, H. Dilger, E. Möller, T. Sixt, E. Roduner, *"In situ EPR investigation of polymer electrolyte membrane degradation in fuel cell applications"*, Journal of Power Sources, **127** (2004) 325-330.

[93] B. Vogel, E. Aleksandrova, S. Mitov, M. Krafft, A. Dreizler, J. Kerres, M. Hein, E. Roduner, *"Observation of Fuel Cell Membrane Degradation by Ex Situ and In Situ Electron Paramagnetic Resonance"*, Journal of The Electrochemical Society, **155** (2008) B570-B574.

[94] H. Liu, H.A. Gasteiger, A. Laconti, J. Zhang, *"Factors Impacting Chemical Degradation Of Perfluorinated Sulfonic Acid Ionomers"*, ECS Transactions, **1** (2006) 283-293.

[95] F.N. Büchi, M. Inaba, T.J. Schmidt, M. Inaba, Chemical Degradation of Perfluorinated Sulfonic Acid Membranes, in: Polymer Electrolyte Fuel Cell Durability, Springer New York, 2009, pp. 57-69.

[96] F.N. Büchi, M. Inaba, T.J. Schmidt, H. Liu, F.D. Coms, J. Zhang, H.A. Gasteiger, A.B. LaConti, Chemical Degradation: Correlations Between Electrolyzer and Fuel Cell Findings, in: Polymer Electrolyte Fuel Cell Durability, Springer New York, 2009, pp. 71-118.

[97] T. Kinumoto, M. Inaba, Y. Nakayama, K. Ogata, R. Umebayashi, A. Tasaka, Y. Iriyama, T. Abe, Z. Ogumi, *"Durability of perfluorinated ionomer membrane against hydrogen peroxide"*, Journal of Power Sources, **158** (2006) 1222-1228.

[98] S. Kundu, M.W. Fowler, L.C. Simon, R. Abouatallah, N. Beydokhti, *"Open circuit voltage durability study and model of catalyst coated membranes at different humidification levels"*, Journal of Power Sources, **195** (2010) 7323-7331.

[99] T. Madden, D. Weiss, N. Cipollini, D. Condit, M. Gummalla, S. Burlatsky, V. Atrazhev, *"Degradation of Polymer-Electrolyte Membranes in Fuel Cells"*, Journal of The Electrochemical Society, **156** (2009) B657-B662.

[100] S. Kundu, L.C. Simon, M.W. Fowler, *"Comparison of two accelerated Nafion degradation experiments"*, Polymer Degradation and Stability, **93** (2008) 214-224.

[101] T. Ishimoto, R. Nagumo, T. Ogura, T. Ishihara, B. Kim, A. Miyamoto, M. Koyama, *"Chemical Degradation Mechanism of Model Compound, $CF_3(CF_2)_3O(CF_2)_2OCF_2SO_3H$, of PFSA Polymer by Attack of Hydroxyl Radical in PEMFCs"*, Journal of The Electrochemical Society, **157** (2010) B1305-B1309.

[102] S.M. Dockheer, L. Gubler, P.L. Bounds, A.S. Domazou, G.G. Scherer, A. Wokaun, W.H. Koppenol, *"Damage to fuel cell membranes. Reaction of HO· with an oligomer of poly(sodium styrene sulfonate) and subsequent reaction with O_2"*, Physical Chemistry Chemical Physics, **12** (2010) 11609-11616.

[103] M.W. Fowler, R.F. Mann, J.C. Amphlett, B.A. Peppley, P.R. Roberge, *"Incorporation of voltage degradation into a generalised steady state electrochemical model for a PEM fuel cell"*, Journal of Power Sources, **106** (2002) 274-283.

[104] G.V. Buxton, L. Clive, W. Greenstock, P. Helman, A.B. Ross, *"Critical review of rate constants for reactions of hydrated electrons, hydrogen atoms and hydroxyl radicals in aqueous solution"*, J. Phys. Chem. Ref. Data, **17** (1988) 513-886.

[105] H. Christensen, K. Sehested, H. Corfitzen, *"Reactions of hydroxyl radicals with hydrogen peroxide at ambient and elevated temperatures"*, The Journal of Physical Chemistry, **86** (1982) 1588-1590.

[106] J. De Laat, H. Gallard, *"Catalytic Decomposition of Hydrogen Peroxide by Fe(III) in Homogeneous Aqueous Solution: Mechanism and Kinetic Modeling"*, Environmental Science & Technology, **33** (1999) 2726-2732.

[107] F. Haber, J. Weiss, The Catalytic Decomposition of Hydrogen Peroxide by Iron Salts, in, 1934, pp. 332-351.

[108] S.-S. Lin, M.D. Gurol, *"Catalytic Decomposition of Hydrogen Peroxide on Iron Oxide: Kinetics, Mechanism, and Implications"*, Environmental Science & Technology, **32** (1998) 1417-1423.

[109] T.E. Springer, T.A. Zawodzinski, S. Gottesfeld, *"Polymer Electrolyte Fuel Cell Model"*, Journal of The Electrochemical Society, **138** (1991) 2334-2342.

[110] M. Eikerling, Y.I. Kharkats, A.A. Kornyshev, Y.M. Volfkovich, *"Phenomenological Theory of Electro-osmotic Effect and Water Management in Polymer Electrolyte Proton-Conducting Membranes"*, Journal of The Electrochemical Society, **145** (1998) 2684-2699.

[111] W. Weppner, R.A. Huggins, *"Determination of the Kinetic Parameters of Mixed-Conducting Electrodes and Application to the System Li[sub 3]Sb"*, Journal of The Electrochemical Society, **124** (1977) 1569-1578.

[112] S. Motupally, A.J. Becker, J.W. Weidner, *"Diffusion of Water in Nafion 115 Membranes"*, Journal of The Electrochemical Society, **147** (2000) 3171-3177.

[113] T.A. Zawodzinski, M. Neeman, L.O. Sillerud, S. Gottesfeld, *"Determination of water diffusion coefficients in perfluorosulfonate ionomeric membranes"*, The Journal of Physical Chemistry, **95** (1991) 6040-6044.

[114] T.V. Nguyen, R.E. White, *"A Water and Heat Management Model for Proton-Exchange-Membrane Fuel Cells"*, Journal of The Electrochemical Society, **140** (1993) 2178-2186.

[115] M. Ise, K.D. Kreuer, J. Maier, *"Electroosmotic drag in polymer electrolyte membranes: an electrophoretic NMR study"*, Solid State Ionics, **125** (1999) 213-223.

[116] T.A. Zawodzinski, J. Davey, J. Valerio, S. Gottesfeld, *"The water content dependence of electro-osmotic drag in proton-conducting polymer electrolytes"*, Electrochimica Acta, **40** (1995) 297-302.

[117] S. Ge, B. Yi, P. Ming, *"Experimental Determination of Electro-Osmotic Drag Coefficient in Nafion Membrane for Fuel Cells"*, Journal of The Electrochemical Society, **153** (2006) A1443-A1450.

[118] T.F. Fuller, J. Newman, *"Experimental Determination of the Transport Number of Water in*

Nafion 117 Membrane", Journal of The Electrochemical Society, **139** (1992) 1332-1337.

[119] C. Vallieres, D. Winkelmann, D. Roizard, E. Favre, P. Scharfer, M. Kind, *"On Schroeder's paradox"*, Journal of Membrane Science, **278** (2006) 357-364.

[120] M.H. Eikerling, P. Berg, *"Poroelectroelastic theory of water sorption and swelling in polymer electrolyte membranes"*, Soft Matter, **7** (2011) 5976-5990.

[121] M. Holz, *"Electrophoretic NMR"*, Chemical Society Reviews, **23** (1994) 165-174.

[122] F. Meier, G. Eigenberger, *"Transport parameters for the modelling of water transport in ionomer membranes for PEM-fuel cells"*, Electrochimica Acta, **49** (2004) 1731-1742.

[123] A. Ohma, S. Yamamoto, K. Shinohara, *"Membrane degradation mechanism during open-circuit voltage hold test"*, Journal of Power Sources, **182** (2008) 39-47.

[124] K. Hongsirikarn, X. Mo, J.G. Goodwin Jr, S. Creager, *"Effect of H_2O_2 on Nafion properties and conductivity at fuel cell conditions"*, Journal of Power Sources, **196** (2010) 3060-3072.

[125] M. Aoki, H. Uchida, M. Watanabe, *"Novel evaluation method for degradation rate of polymer electrolytes in fuel cells"*, Electrochemistry Communications, **7** (2005) 1434-1438.

[126] E.T. Denisov, T.G. Denisova, T.S. Pokidova, Handbook of Free Radical Initiators, in: Handbook of Free Radical Initiators, John Wiley & Sons, Inc., 2005, pp. i-xxii.

[127] F. Haber, J. Weiss, *"Über die Katalyse des Hydroperoxydes"*, Naturwissenschaften, **20** (1932) 948-950.

[128] S. Prager, *"Diffusion in Inhomogeneous Media"*, Journal of Chemical Physics, **33** (1960) 122-127.

[129] H. Yasuda, C.E. Lamaze, L.D. Ikenberry, *"Permeability of solutes through hydrated polymer membranes. Part I. Diffusion of sodium chloride"*, Die Makromolekulare Chemie, **118** (1968) 19-35.

[130] S. Koter, *"Transport of simple electrolyte solutions through ion-exchange membranes--the capillary model"*, Journal of Membrane Science, **206** (2002) 201-215.

[131] P. Choi, N.H. Jalani, R. Datta, *"Thermodynamics and Proton Transport in Nafion"*, Journal of The Electrochemical Society, **152** (2005) E123-E130.

[132] A.A. Franco, Un modèle physique multiéchelle de la dynamique électrochimique dans une pile à combustible à électrolyte polymère – Une approche Bond Graph dimension infinie, in, Université Claude Bernard, Lyon-1 France, 2005.

[133] A.A. Franco, P. Schott, C. Jallut, B. Maschke, *"A Dynamic Mechanistic Model of an Electrochemical Interface"*, Journal of The Electrochemical Society, **153** (2006) A1053-A1061.

[134] A.A. Franco, P. Schott, C. Jallut, B. Maschke, *"A Multi-Scale Dynamic Mechanistic Model for the Transient Analysis of PEFCs"*, Fuel Cells, **7** (2007) 99-117.

[135] W.G. Bessler, S. Gewies, *"Gas Concentration Impedance of Solid Oxide Fuel Cell Anodes"*, Journal of The Electrochemical Society, **154** (2007) B548-B559.

[136] W.G. Bessler, S. Gewies, C. Willich, G. Schiller, K.A. Friedrich, *"Spatial Distribution of*

Electrochemical Performance in a Segmented SOFC: A Combined Modeling and Experimental Study", Fuel Cells, **10** (2009) 411-418.

[137] M.P. Eschenbach, R. Coulon, A.A. Franco, J. Kallo, W.G. Bessler, *"Multi-scale simulation of fuel cells: From the cell to the system"*, Solid State Ionics, **192** (2011) 615-618.

[138] D. Goodwin, Proc. 203rd Meeting of the Electrochemical Society, Paris, France, 2003.

[139] A.-L. Rollet, O. Diat, G. Gebel, *"A New Insight into Nafion Structure"*, The Journal of Physical Chemistry B, **106** (2002) 3033-3036.

[140] P. Deuflhard, E. Hairer, J. Zugck, *"One-step and extrapolation methods for differential-algebraic systems"*, Numerische Mathematik, **51** (1987) 501-516.

[141] R. Ehrig, U.Nowak, L.P.Oeverdieck, in: H.-J. Bungartz, F. Durst, C. Zenger (Eds.) High performance Scientific and Engineering Computing.

[142] M. Eikerling, A.A. Kornyshev, A.A. Kulikovsky, Physical Modeling of Fuel Cells and their Components, in: Encyclopedia of Electrochemistry, Wiley-VCH Verlag GmbH & Co. KGaA, 2007.

[143] M. Inaba, M. Uno, J. Marayama, A. Tasaka, K. Katakura, Z. Ogumi, *"Hydrogen oxidation on partially immersed Nafion-coated electrodes"*, Journal of Electroanalytical Chemistry, **417** (1996) 105-111.

[144] D.A. Harrington, B.E. Conway, *"ac Impedance of Faradaic reactions involving electrosorbed intermediates I. Kinetic theory"*, Electrochimica Acta, **32** (1987) 1703-1712.

[145] L. Bai, D.A. Harrington, B.E. Conway, *"Behavior of overpotential deposited species in Faradaic reactions. ac Impedance measurements on H_2 evolution kinetics at activated and unactivated Pt cathodes"*, Electrochimica Acta, **32** (1987) 1713-1731.

[146] D.A. Harrington, B.E. Conway, *"Kinetic theory of the open-circuit potential decay method for evaluation of behaviour of adsorbed intermediates: Analysis for the case of the H2 evolution reaction"*, Journal of Electroanalytical Chemistry and Interfacial Electrochemistry, **221** (1987) 1-21.

[147] R.M.Q. Mello, E.A. Ticianelli, *"Kinetic study of the hydrogen oxidation reaction on platinum and Nafion covered platinum electrodes"*, Electrochimica Acta, **42** (1997) 1031-1039.

[148] N.M. Markovic, B.N. Grgur, P.N. Ross, *"Temperature-Dependent Hydrogen Electrochemistry on Platinum Low-Index Single-Crystal Surfaces in Acid Solutions"*, The Journal of Physical Chemistry B, **101** (1997) 5405-5413.

[149] H. Eyring, *"The Activated Complex in Chemical Reactions"*, J. Chem. Phys., **3** (1935) 107.

[150] U.A. Paulus, T.J. Schmidt, H.A. Gasteiger, R.J. Behm, *"Oxygen reduction on a high-surface area Pt/Vulcan carbon catalyst: a thin-film rotating ring-disk electrode study"*, Journal of Electroanalytical Chemistry, **495** (2001) 134-145.

[151] N.M. Markovic, H.A. Gasteiger, P.N. Ross, *"Oxygen Reduction on Platinum Low-Index Single-Crystal Surfaces in Sulfuric Acid Solution: Rotating Ring-Pt(hkl) Disk Studies"*, The Journal of Physical Chemistry, **99** (1995) 3411-3415.

[152] A. Damjanovic, D.B. Sepa, M.V. Vojnovic, *"New evidence supports the proposed mechanism for O2 reduction at oxide free platinum electrodes"*, Electrochimica Acta, **24** (1979) 887-889.

[153] R. Ferreira de Morais, P. Sautet, D. Loffreda, A.A. Franco, *"A multiscale theoretical methodology for the calculation of electrochemical observables from ab initio data: Application to the oxygen reduction reaction in a Pt(111)-based polymer electrolyte membrane fuel cell"*, Electrochimica Acta, **56** (2011) 10842-10856.

[154] P. Schott, P. Baurens, *"Fuel cell operation characterization using simulation"*, Journal of Power Sources, **156** (2006) 85-91.

[155] W.G. Bessler, S. Gewies, M. Vogler, *"A new framework for physically based modeling of solid oxide fuel cells"*, Electrochimica Acta, **53** (2007) 1782-1800.

[156] S. Gewies, W.G. Bessler, *"Physically Based Impedance Modeling of Ni/YSZ Cermet Anodes"*, Journal of The Electrochemical Society, **155** (2008) B937-B952.

[157] E. Oliveros, O. Legrini, M. Hohl, T. Müller, A.M. Braun, *"Industrial waste water treatment: large scale development of a light-enhanced Fenton reaction"*, Chemical Engineering and Processing: Process Intensification, **36** (1997) 397-405.

[158] K. Kodama, F. Miura, N. Hagesawa, M. Kawasumi, Y. Morimoto, 2005.

[159] K. Kodama, F. Miura, N. Hasegawa, M. Kawasumi, Y. Morimoto, *"Degradation of Nafion Membranes in Hydrogen Peroxide"*, ECS Meeting Abstracts, **502** (2006) 1185-1185.

[160] S. Zhang, X. Yuan, H. Wang, W. Mérida, H. Zhu, J. Shen, S. Wu, J. Zhang, *"A review of accelerated stress tests of MEA durability in PEM fuel cells"*, International Journal of Hydrogen Energy, **34** (2009) 388-404.

[161] S. Maass, F. Finsterwalder, G. Frank, R. Hartmann, C. Merten, *"Carbon support oxidation in PEM fuel cell cathodes"*, Journal of Power Sources, **176** (2008) 444-451.

[162] L.M. Roen, C.H. Paik, T.D. Jarvi, *"Electrocatalytic Corrosion of Carbon Support in PEMFC Cathodes"*, Electrochemical and Solid-State Letters, **7** (2004) A19-A22.

[163] H. Tang, Z. Qi, M. Ramani, J.F. Elter, *"PEM fuel cell cathode carbon corrosion due to the formation of air/fuel boundary at the anode"*, Journal of Power Sources, **158** (2006) 1306-1312.

[164] K. Yasuda, A. Taniguchi, T. Akita, T. Ioroi, Z. Siroma, *"Platinum dissolution and deposition in the polymer electrolyte membrane of a PEM fuel cell as studied by potential cycling"*, Physical Chemistry Chemical Physics, **8** (2006) 746-752.

[165] X. Wang, R. Kumar, D.J. Myers, *"Effect of Voltage on Platinum Dissolution"*, Electrochemical and Solid-State Letters, **9** (2006) A225-A227.

[166] W. Bi, G.E. Gray, T.F. Fuller, *"PEM Fuel Cell Pt/C Dissolution and Deposition in Nafion Electrolyte"*, Electrochemical and Solid-State Letters, **10** (2007) B101-B104.

[167] V.A.T. Dam, F.A. de Bruijn, *"The Stability of PEMFC Electrodes"*, Journal of The Electrochemical Society, **154** (2007) B494-B499.

[168] M. Schulze, M. Lorenz, N. Wagner, E. Gülzow, *"XPS analysis of the degradation of Nafion"*, Fresenius' Journal of Analytical Chemistry, **365** (1999) 106-113.

[169] M. Vogler, A. Bieberle-Hutter, L. Gauckler, J. Warnatz, W.G. Bessler, *"Modelling Study of Surface Reactions, Diffusion, and Spillover at a Ni/YSZ Patterned Anode"*, Journal of The Electrochemical Society, **156** (2009) B663-B672.

[170] S. Banerjee, D.E. Curtin, *"Nafion perfluorinated membranes in fuel cells"*, Journal of Fluorine Chemistry, **125** (2004) 1211-1216.